INSTITUTO DE ASTRONOMIA, GEOFÍSICA E CIÊNCIAS ATMOSFÉRICAS
DA UNIVERSIDADE DE SÃO PAULO

OBSERVATOIRE ASTRONOMIQUE DE STRASBOURG

THESIS

to obtain the title of

DOCTOR OF PHILOSOPHY

of the Universities of São Paulo, Brazil, and Strasbourg, France
Speciality : ASTROPHYSICS

Defended by
Adriana MANCINI PIRES

Population Study of Radio-Quiet and Thermally Emitting Isolated Neutron Stars

Thesis Advisors:
Christian MOTCH and Eduardo JANOT PACHECO
defended in November 2009

Jury :

Reviewers :	Didier BARRET	-	Director of Research CNRS (CESR, France)
	Jean HEYVAERTS	-	Professor (UdS, France)
	Jorge HORVATH	-	Professor (IAG-USP, Brazil)
Advisers :	Christian MOTCH	-	Director of Research CNRS (UdS, France)
	Eduardo JANOT PACHECO	-	Professor (IAG-USP, Brazil)
Examiners :	João BRAGA	-	Director of Research (INPE, Brazil)
	Marcos DIAZ	-	Professor (IAG-USP, Brazil)
	Bettina POSSELT	-	Researcher (Harvard-Smithsonian CfA, US)
	Roberto TUROLLA	-	Professor (Universitá di Padova, Italy)

A meus queridos pais; a meus queridos Greg e Liza.

Acknowledgements

It is a great pleasure to thank those who contributed to make my work possible. Foremost, I am heartily thankful to Christian Motch, whose guidance, attentive help and patience during all these years enabled me to accomplish a task which at first seemed so big. I am equally thankful to Eduardo Janot Pacheco, for his support and helpful advising, and for trusting in my capabilities. It is a pleasure to thank my collaborators, especially Roberto Turolla and Sergei Popov. I cannot imagine how my PhD would have been without the friendship of Rubens and Laerte, with whom I have shared much more than the office at IAG. To Bettina Posselt, a special thanks for the discussions and evening spent over tartes flambées while we were both at the Strasbourg Observatory. For help on the scientific side, I am in debt to many people of the Observatory, especially Christian Boily, for his help with the Galactic potential, and Nicolas Grosso, for discussions regarding the source 2XMM J104608.7-594306 and Chandra data; to Patrick Guillout, for the compilation of finding charts for the proper motion project as well as for singing and dancing Brazilian sambas every time he came into my office; to the other PhD students, Fabien Grisé and François-Xavier Pineau among them, for their help with the photometry and cross-correlations. From the Brazilian side, I would also like to express my gratitude to Marcos Diaz and Jorge Horvath, for accompanying my work. For making life in Strasbourg even more pleasant, I am thankful to Maxime Viallet for the regular petite pause for tea; to Jean Heyvaerts, Anabela Gonçalves Darbon and Chantal Rameau for their kindness. Pour les bons moments, à Sophie et aux gamines du foot. I could not thank enough Laurence Boirin: without her my stay in France would have been not nearly half as charming; pour notres soirées de cinéma à l'Odyssée et de bière à l'Epicerie. From São Paulo, a special thanks to meu querido baiano Raimundo. To all my friends from university: Gabi, Cecilia, Pri and Jairo, Bel, Kika, Laura, Denison and Tati. Para a Ru, por me aturar por mais de 14 anos... e para meus amigos da época do colégio, Preta, Thata e Leo. Ao Dodô, Vera, Letícia e D. Ottilia, por todo o carinho.

Nothing at all would have been possible without my parents, Iliana and Francisco, or without the love, constant help and wise advice from Greg.

This work was financially supported by FAPESP (grant 04/04950-4), CAPES (grant BEX7812/05-7), Brazil, and the Observatory of Strasbourg (CNRS), France.

Contents

List of Figures

List of Tables

Abstract

Around ten years ago, a highly homogeneous group of seven isolated neutron stars, sharing properties never found together in previously known classes of neutron stars, was identified in the ROSAT All-Sky Survey. This group is now commonly referred to as the "Magnificent Seven" (or M7, for simplicity). Their long spin periods (~ 10 s), high magnetic fields ($B \sim$ few 10^{13} G), soft thermal emission ($kT \sim 40 - 100$ eV) and lack of radio emission and significant magnetospheric activity are unique among all isolated neutron star populations and make them stand apart from ordinary rotation-powered radio pulsars. The M7 are believed to be nearby, with distances of a few hundred parsecs, middle-aged (a few 10^5 yr) and cooling isolated neutron stars, probably born in the OB associations of the Gould Belt. They are locally as numerous as young radio pulsars and thus might represent the tip of an iceberg of a large hidden population of stellar remnants. Striking evidence relates them to other peculiar groups of isolated neutron stars, in particular *magnetars* and *rotating radio transients*, known as RRATs.

The main objective of the thesis is to study the properties of this population of radio-quiet and thermally emitting isolated neutron stars in the Galaxy. This is achieved by further studying the known sample of seven sources, as well as by searching for new candidates and constraining possible populations.

Proper motion determinations are a sensitive diagnostic of the X-ray powering mechanism as well as of population properties. First, the relative velocities with respect to the interstellar medium place constraints on the contribution of accretion to the overall energy budget. Second, the reconstruction of backward trajectories allows an estimate of the kinematic age of the neutron star assuming a birth in the Galactic plane and, more precisely, in one of the nearby OB associations. The flight time can then be compared with the characteristic age derived from spin-down, revealing a possible non-standard braking mechanism or pointing towards a long spin period at birth. Finally, the kinematic age also constrains the cooling mechanism. Proper motion studies of the M7 in the optical have established the three X-ray brightest sources, which have sufficiently bright optical counterparts, as cooling, middle-aged neutron stars, probably originating in the nearby associations of the Gould Belt. During the thesis, we investigated the proper motion of three of the faintest M7 in X-rays with the satellite Chandra. This work allowed us to constrain the neutron star displacement in two cases as well as to accurately determine the high proper motion of a third source, for the first time in X-rays with a significance approaching 10 standard deviations (Motch, Pires, Haberl, & Schwope, 2007, Ap&SS, 308, 217; Motch, Pires, Haberl, Schwope, & Zavlin, 2009, A&A 497, 423).

The search for new isolated neutron star candidates in the serendipitous catalogue of the XMM-Newton Observatory, with more than 120,000 X-ray sources, also had the aim to constrain the spatial density of thermally emitting sources located beyond the Solar vicinity. This work brought the long awaited discovery of a new thermally emitting isolated neutron star with properties similar to those of the seven nearby sources discovered by ROSAT; in particular, the lack of radio emission, the absence of a significant non-thermal component in the source's X-ray spectral energy distribution and a constant X-ray flux over long time scales. On the other hand, the source – which is probably located in the Carina Nebula at a distance of ~ 2.3 kpc – is hotter, more luminous and possibly younger than the other seven sources. In this sense, it may represent an evolutionary missing link between the different classes of magnetars, radio-transient and radio-quiet isolated neutron stars (Pires, Motch, Turolla, Treves, & Popov, 2009, A&A 498, 233). Moreover, deep optical ob-

servations with SOAR and the ESO-VLT were obtained during the work on the thesis to optically identify a handful of isolated neutron star candidates that had been selected from among more than $72,000$ sources (Pires, Motch, & Janot-Pacheco, 2009, A&A, 504, 185).

Finally, population synthesis of Galactic thermally emitting isolated neutron stars constrains the global properties of this population based on the whole sample of XMM-Newton observations. By estimating the density of similar sources at more remote distances in the Milky Way, the final objective is to determine whether the spatial density derived from the group of seven nearby sources is a local anomaly caused by the Sun's current location near regions of active stellar formation in the Gould Belt.

Resumo

O grupo de estrelas de nêutrons isoladas descobertas pelo ROSAT

Há dez anos, sete estrelas de nêutrons isoladas, silenciosas em rádio e compartilhando propriedades peculiares (significativamente distintas daquelas apresentadas por pulsares rádio) foram identificadas nos dados do satélite de raios X ROSAT (ver Haberl 2007; para um *review*). Apesar de inúmeras buscas por objetos similares terem sido conduzidas nos anos subseqüentes à descoberta das sete fontes, nenhum candidato foi confirmado (por exemplo, Rutledge et al. 2003, Chieregato et al. 2005, Agüeros et al. 2006).

As sete fontes são caracterizadas por uma distribuição de energia térmica e pela ausência de emissão magnetosférica. O espectro em raios X é usualmente descrito por um corpo negro a baixas temperaturas, pouco absorvido pela matéria interestelar ($kT \sim 40 - 100\,\mathrm{eV}$ e $N_{\mathrm{H}} \sim 10^{20}\,\mathrm{cm}^{-2}$). Em muitos casos, difusas contrapartidas óticas (com magnitudes na banda B entre 25 e 28) foram detectadas, o que implica elevadas razões entre os fluxos em raios X e no ótico, $\log(f_{\mathrm{X}}/f_{\mathrm{opt}}) \sim 4-5$. A emissão em raios X de seis entre as sete fontes é modulada por variações sinusoidais de amplitude contida entre 1% e 18% e periodicidade da ordem de segundos, o que é associado à rotação da estrela de nêutrons. Estes períodos são mais longos que os observados em pulsares rádio e são distribuídos em un intervalo mais estreito. Devido à fraca absorção interestelar, é esperado que este grupo de estrelas de nêutrons seja constituído de objetos próximos, situados a distâncias inferiores a $\sim 500\,\mathrm{pc}$ na maioria dos casos (Posselt et al. 2007). De fato, paralaxes foram medidas para as duas fontes mais brilhantes graças à observações com o satélite espacial Hubble (Kaplan et al. 2002b; 2007); estes resultados encontram-se em acordo com os deduzidos a partir da distribuição do meio interestelar em função da distância e dos valores de coluna de densidade medidos nos espectros em raios X. As sete fontes não emitem em comprimentos de onda rádio seja de maneira persistente ou transitória (Kondratiev et al. 2008; 2009) e não são associadas a restos de supernovas.

Movimentos próprios de cinco entre os sete objetos foram medidos através de observações óticas com o telescópio ESO-VLT, para as estrelas mais brilhantes. No caso das fontes mais fracas, observações com o satélite de raios X Chandra foram utilizadas (ver referências em Motch et al. 2009). A detecção de deslocamentos anuais de 70 a 200 mas permitiu identificar estas fontes como estrelas de nêutrons de idades interemediárias, por volta de 10^5 a 10^6 anos, originárias das mais próximas associações OB do Cinturão de Gould, e que se encontram em processo de resfriamento. Em particular, os altos valores de movimentos próprios excluem a possibilidade de que estas estrelas possam ser reaquecidas pela acreção da matéria do meio interestelar, uma vez que esta é apenas eficaz a baixas velocidades.

Campos magnéticos intensos, $B \sim 10^{13} - 10^{14}\,\mathrm{G}$ (ver Haberl 2007, van Kerkwijk & Kaplan 2007; para artigos de *review*), são deduzidos a partir da presença de largas linhas de absorção nos espectros X das fontes, assim como da taxa de freamento da rotação da estrela nos casos em que esta é medida (Kaplan & van Kerkwijk 2005a;b, van Kerkwijk & Kaplan 2008, Kaplan & van Kerkwijk 2009). A presença de linhas de absorção é usualmente interpretada no contexto de transições cíclotron de protons (Zane et al. 2001) ou de transições atômicas na atmosfera parcialmente ionizada da estrela de nêutrons (Lai 2001), sob a influência do intenso campo magnético. A ausência do fenômeno de acreção e de atividade magnetosférica intensa permite a observação direta da superfície da estrela de nêutrons e, portanto, a investigação dos processos físicos que ocorrem na atmosfera sob condições extremas de gravidade e campo magnético.

A posição ocupada por estas fontes no diagrama $P - \dot{P}$, intermediária entre as de pulsares rádio "canônicos" e *magnetars*, indica que elas possam estar conectadas de maneira evolutiva a outros grupos de estrelas de nêutrons isoladas. Particularmente, os longos períodos de rotação e os campos magnéticos intensos poderiam indicar que o grupo de sete fontes térmicas evoluiu do de magnetars, composto por estrelas de nêutrons mais jovens e que possuem campos magnéticos ainda mais intensos (Heyl & Kulkarni 1998). O decaimento do campo magnético fornece uma fonte de aquecimento adicional da crosta da estrela de nêutrons, o que pode modificar de maneira significativa a evolução da radiação proveniente da superfície. Por outro lado, se o campo magnético da estrela permanece aproximadamente constante durante sua vida, é possível definir uma relação com os "pulsares de intenso campo magnético" (*high magnetic field radio pulsar*, HBPSR; Zane et al. 2002). Este objetos são mais distantes que as sete fontes térmicas e irradiam uma luminosidade de rotação muito mais elevada ($\dot{E}$). No entanto, se os HBPSRs são mais jovens por um fator 100, então a diferença em $\dot{E}$ pode ser explicada dentro do cenário habitual de evolução de pulsares e do modelo de freamento magnético (Kaplan 2008). Neste caso, as sete fontes descobertas pelo ROSAT poderiam ser pulsares rádio de longos períodos de rotação, nos quais o estreito cone de emissão não cruza a linha de visada. Finalmente, o único pulsar rádio transiório (*rotating radio transient*, RRAT) detectado presentemente em altas energias (McLaughlin et al. 2007), compartilha de maneira surpreendente muitas das propriedades das sete fontes descobertas pelo ROSAT – em particular, a posição no diagrama $P - \dot{P}$ e a presença de uma linha de absorção no espectro térmico em raios X. Esta fonte é no entanto mais quente ($kT \sim 140\,\mathrm{eV}$), mais fraca e provavelmente mais distante ($d \sim 3.6\,\mathrm{kpc}$).

Considerando que em um raio de 1 kpc ao redor do Sol as sete fontes descobertas pelo ROSAT são tão numerosas quanto os pulsares γ e rádio jovens, de idades inferiores a alguns milhões de anos (Popov et al. 2003), conclui-se que estas fontes térmicas silenciosas em rádio representam uma fração considerável da população de estrelas de nêutrons isoladas na Galáxia. No entanto, a proximidade de ricas associações OB na vizinhança solar é um fator importante que deve ser considerado. De fato, o resfriamento de estrelas de nêutrons depende fortemente da massa e, com menor importância, do campo magnético, de maneira que a idade particular das estrelas massivas progenitoras poderia explicar esta forte densidade local de estrelas de nêutrons térmicas. A descoberta de outros membros mais distantes é portanto fundamental para o avanço da compreensão das propriedades globais da população assim como de suas relações com outros grupos de estrelas de nêutrons isoladas na Galáxia.

Objetivos e resultados da tese

O objetivo da presente tese de doutorado é investigar a população de estrelas de nêutrons isoladas térmicas silenciosas em rádio na Galáxia. As propriedades desta população são estudadas através da análise da conhecida amostra de sete fontes, por um lado, assim como através da procura de novos candidatos e da modelização da população, supondo diversos cenários evolutivos possíveis.

A partir do estudo de movimentos proóprios das fontes conhecidas, é possível restringir não apenas a origem da emissão X e da contribuição relativa da acreção à luminosidade da fonte, mas também estimar o lugar de nascimento e a idade cinemática da estrela de nêutrons. Isto é feito reconstituindo-se as trajetórias passadas definidas pela direção do movimento próprio projetada no céu, e então supondo-se que estas estrelas de nêutrons são provenientes do disco Galáctico ou de uma associação OB. O tempo de vôo estimado permite restringir os mecanismos de resfriamento e a comparação entre a idade cinemática e aquela deduzida do freamento da rotação da estrela de nêutrons, a qual é sistematicamente mais elevads. Estes estudos mostram que os mais brilhantes objetos deste grupo são provenientes da região mais próxima do Cinturão de Gould – em particular, da associação Sco OB2 – e possuem idades de alguns 10^5 anos. Os movimentos próprios de três entre as mais fracas fontes foram investigados com o satélite Chandra durante a tese. Este trabalho permitiu restringir o deslocamento da estrela de nêutrons em dois casos para as fontes RX J0806.4-4123 e RX J0420.0-5022 e colocou em evidência, pela primeira vez no domínio de raios X, o movimento próprio de uma terceira fonte, RX J1308.6+2127, com uma precisão jamais obtida anteriormente (Motch, Pires, Haberl, & Schwope, 2007, Ap&SS, 308, 217; Motch, Pires, Haberl, Schwope, & Zavlin, 2009, A&A 497, 423).

A busca por candidatos a estrelas de nêutrons isoladas no catálogo do satélite de raios X XMM-Newton, com mais de 120 mil fontes, teve igualmente como objetivo restringir a densidade espacial de fontes X térmicas situadas a grandes distâncias. Este trabalho levou à bastante aguardada descoberta de uma nova estrela de nêutrons isolada, 2XMM J104608.7-594306, que apresenta propriedades similares às sete fontes descobertas pelo ROSAT – particularmente, a ausência de emissão rádio ou de um componente non-térmico no espectro de raios X e a estabilidade do flux em uma longa escala de tempo. Por outro lado, esta fonte, provavelmente situada na Nebulosa da Carina, a uma distância por volta de 2.3 kpc, é um pouco mais quente e luminosa e possivelmente mais jovem que as outras. Desta forma, ela pode representar um elo entre os diversos grupos de estrelas de nêutrons isoladas que estão presentemente sendo descobertas com a atual geração de satélites de raios X (Pires, Motch, Turolla, Treves, & Popov, 2009, A&A 498, 233). Mais ainda, observações profundas no ótico com o telescópio ESO-VLT e SOAR foram utilizadas para identificar opticamente a amostra de candidatos a estrelas de nêutrons que foram selecionadas entre mais de 72 mil fontes (Pires, Motch, & Janot-Pacheco, 2009, A&A, 504, 185).

Finalmente, o trabalho de modelização da população de estrelas de nêutrons isoladas térmicas na Galáxia permite restringir as propriedades globais dessa população a partir dos resultados obtidos com as observações do satélite XMM-Newton. Este trabalho tem como objetivo determinar se a densidade espacial deduzida do grupo de sete estrelas próximas é uma anomalia causada pela nossa posição atual próxima de zonas ativas de formação recente de estrelas do Cinturão de Gould, estimando a densidade de fontes similares na Via Láctea a maior distância.

Résumé

Le groupe d'étoiles à neutrons isolées découvertes par ROSAT

Il y a environ dix ans, sept étoiles à neutrons isolées silencieuses en radio et partageant des propriétés particulières (très différentes de celles des pulsars radio) ont été identifiées dans les données du satellite observatoire en rayons X ROSAT (voir Haberl 2007; pour un article de revue). Malgré de nombreuses recherches d'objets similaires conduites dans les années suivantes (par exemple, Rutledge et al. 2003, Chieregato et al. 2005, Agüeros et al. 2006), aucun candidat n'a été confirmé depuis la découverte du dernier membre des sept, RX J2143.0+0654 (Zampieri et al. 2001).

Les sept sources sont caractérisées par une distribution d'énergie thermique et par l'absence d'émission magnétosphérique. Le spectre X est habituellement décrit par un corps noir à basse température, peu absorbé par la matière interstellaire ($kT \sim 40 - 100$ eV et $N_{\rm H} \sim$ quelques 10^{20} cm^{-2}). Dans plusieurs cas, des contreparties optiques très faibles et bleues (avec $m_{\rm B} \sim 25 - 28$) ont été détectées, impliquant des rapports de flux très elevés, $\log(f_{\rm X}/f_{\rm opt}) \sim 4 - 5$. L'émission X de six des sept sources est modulée par des variations sinusoïdals d'amplitude comprise entre 1% et 18% à des périodes de l'ordre de quelques secondes que l'on assimile à la rotation de l'étoile à neutrons. Ces périodes sont plus longues que celles observées dans les pulsars radio et sont distribuées dans un intervalle plus étroit.

A cause de la faible absorption interstellaire, on s'attend à ce que ce groupe d'étoiles à neutrons soit constitué d'objets proches, situés à des distances inférieures à $\sim$500 pc dans la majorité des cas (Posselt et al. 2007). En fait, des parallaxes ont pû être mesurées pour les deux sources les plus brillantes avec le télescope spatial Hubble (Kaplan et al. 2002b; 2007); ces résultats confirment les distances déduites à partir de la distribution du milieu interstellaire en fonction de la distance et de la colonne de densité mesurée dans le spectre X. Ces étoiles à neutrons n'émettent pas dans les longueurs d'onde radio soit de manière persistente soit transitoire (Kondratiev et al. 2008; 2009) et ne sont pas associées à des restes de supernova.

Les mouvements propres de cinq des sept objets ont été mesurés à l'aide d'observations optiques avec l'ESO-VLT, pour les étoiles les plus brillantes, et en rayons X avec Chandra, pour les sources les plus faibles (voir références dans Motch et al. 2009). La mesure de déplacements annuels de 70 à 200 mas a permis d'établir que ces sources sont des étoiles à neutrons d'âges intermédiaires ($\sim 10^5 - 10^6$ ans), originaires des associations OB de la ceinture de Gould les plus proches du Soleil, et qui sont en cours de refroidissement. En particulier, les valeurs considérables du mouvement propre excluent la possibilité que ces étoiles puissent être réchauffés par l'accrétion de matière à partir du milieu interstellaire, celle-ci n'étant efficace qu'à basse vitesse.

Des champs magnétiques intenses, $B \sim 10^{13} - 10^{14}$ G (voir Haberl 2007, van Kerkwijk & Kaplan 2007; pour des revues) sont déduits à partir de la présence de raies larges d'absorption dans le spectre X des sources aussi bien qu'à partir du taux de ralentissement de la rotation de l'étoile dans les cas où il est mesurable (Kaplan & van Kerkwijk 2005a;b, van Kerkwijk & Kaplan 2008, Kaplan & van Kerkwijk 2009). Les raies d'absorption sont habituellement interpretées comme dûes à des transitions cyclotron protoniques (Zane et al. 2001) ou atomiques dans l'atmosphère de l'étoile partiellement ionisée (Lai 2001), sous l'influence du fort champ magnétique. L'absence de phénomène d'accrétion et d'activité magnétosphérique intense permet une vue directe de la surface de l'étoile et l'étude de la physique des atmosphères dans des conditions de gravité et de champ magnétique intenses.

La position occupée par ces sources dans le diagramme $P - \dot{P}$, à peu près intermédiaire entre les pulsars radio "canoniques" et les *magnetars*, indique qu'elles pourraient être liées de manière évolutive à d'autres groupes d'étoiles à neutrons isolées. En particulier, les longues périodes de rotation et les champs magnétiques intenses pourraient indiquer que le groupe de sept sources thermiques a évolué à partir de celui composé par les magnétars, étoiles plus jeunes et à encore plus grand champ magnétique (Heyl & Kulkarni 1998). La décroissance du champ magnétique fournit une source additionnelle de chauffage de la croûte de l'étoile à neutrons, qui peut changer de façon significative l'évolution du rayonnement de la surface. Par contre, si le champ magnétique de l'étoile n'avait pas trop changé pendant sa vie, il serait alors possible d'établir un lien avec les "pulsars radio à fort champ magnétique" (*high magnetic field radio pulsar*, HBPSR; Zane et al. 2002). Ces objets sont plus lointains que les sept sources thermiques et rayonnent une énergie de rotation beaucoup plus élevée ($\dot{E}$). Cependant, si les HBPSR sont plus jeunes d'un facteur 100, alors la différence de $\dot{E}$ peut être expliquée par le scénario habituel d'évolution des pulsars et le modèle de ralentissement magnétique (Kaplan 2008). Dans ce cas, les sept sources découvertes par ROSAT pourraient être des pulsars radio de longues périodes de rotation dont le cône d'émission très étroit ne croise pas la ligne de visée. Finalement, le seul pulsar radio transitoire (*rotating radio transient*, RRAT) détecté à hautes énergies jusqu'à présent (McLaughlin et al. 2007), partage de manière remarquable plusieurs propriétés avec les sept sources ROSAT – soient, la position dans le diagramme $P - \dot{P}$ et la présence d'une raie d'absorption dans le spectre X thermique. Cette source est néanmoins plus chaude ($kT \sim 140\,\mathrm{eV}$), plus faible et probablement plus lointaine ($d \sim 3.6\mathrm{kpc}$).

Si on considére que, dans un rayon d'environ 1 kpc du Soleil, les sept sources découvertes par ROSAT sont aussi nombreuses que les pulsars γ et radio jeunes – ayant des âges inférieurs à quelques millions d'années (Popov et al. 2003) – alors, il se peut que ces sources thermiques silencieuses en radio représentent de fait une partie considérable de la population d'étoiles à neutrons isolées présente dans la Galaxie. Cependant, la proximité d'associations OB riches dans le voisinage solaire est un facteur important qui doit être pris en compte. En effet, le refroidissement des étoiles à neutrons dépend fortement de la masse et, dans une certaine mesure, du champ magnétique, de sorte que l'âge particulier des étoiles massives progénitrices pourrait expliquer cette forte densité locale d'étoiles à neutrons thermiques. La découverte d'autres membres plus lointains est donc fondamentale pour l'avancement de la comprehension des propriétés globales de la population ainsi que de ses liens avec les autres groupes d'étoiles à neutrons isolées dans la Galaxie.

Objectifs et résultats de la thése

La présente thèse de doctorat porte sur la population d'étoiles à neutrons isolées thermiques dénuées d'émission radio dans la Galaxie. Les propriétés de cette population sont étudiées par l'analyse de l'échantillon connu des sept sources, d'une part, et d'autre part par la recherche de nouveaux candidats et par la modélisation de cette population supposant plusieurs scénarios évolutifs possibles.

A partir des études du mouvement propre des sources connues, il est possible de contraindre non seulement l'origine de l'émission X et la contribution relative de l'accrétion à la luminosité de la source mais aussi d'estimer le lieu de naissance et l'âge cinématique de l'étoile à neutrons, en reconstituant les trajectoires passées définies par la direction du mouvement projeté sur le ciel, et supposant que ces étoiles sont nées dans le disque Galactique ou dans une association OB. De plus, les temps de vol estimés permettent de contraindre les mécanismes de refroidissement ainsi que la confrontation entre l'âge cinématique et celui déduit du ralentissement de la rotation de l'étoile (qui se trouve être systématiquement plus élévé). Ces études ont montré que les objets les plus brillants de ce groupe sont nés dans la partie la plus proche de la ceinture de Gould, dans l'association Sco OB2 et sont âgées de quelques 10^5 ans. Les mouvements propres de trois sources parmi les plus faibles sources ont été étudiés avec le satellite Chandra pendant la thése. Ce travail a permis de contraindre le déplacement de l'étoile à neutrons dans deux cas pour les sources RX J0806.4-4123 et RX J0420.0-5022 et a mis en évidence pour la première fois dans le domaine des rayons X le mouvement propre d'une troisième source, RX J1308.6+2127, avec une précision jamais obtenue avant (Motch, Pires, Haberl, & Schwope, 2007, Ap&SS, 308, 217; Motch, Pires, Haberl, Schwope, & Zavlin, 2009, A&A 497, 423).

La recherche de nouveaux candidats étoile à neutrons isolée dans le catalogue du satellite de rayons X XMM-Newton, avec plus de 120 mille sources, a eu également comme but de contraindre la densité spatiale des sources X thermiques situées à grandes distances. Ce travail a mené à la découverte très attendue d'une nouvelle étoile à neutrons isolée, 2XMM J104608.7-594306, présentant des propriétés similaires à celles des sept sources découvertes par ROSAT – en particulier, l'absence d'émission radio ou d'un composante non-thermique dans le spectre X et la stabilité du flux sur une longue échelle de temps (Pires & Motch 2008, Pires et al. 2009b). D'un autre côté, cette source, probablement située dans la nebuleuse de la Carène, à une distance d'environ 2.3 kpc, est un peu plus chaude et lumineuse et possiblement plus jeune que les autres. Elle pourrait ainsi devenir un lien entre les diverses groupes d'étoiles à neutrons isolées qui sont en train d'être découvertes avec la génération de satellites X actuelle (Pires, Motch, Turolla, Treves, & Popov, 2009, A&A 498, 233). En outre, des observations optiques profondes avec les telescopes ESO-VLT et SOAR ont été utilisées pour identifier optiquement l'échantillon des candidats étoile à neutrons qui ont été séléctionnés parmi plus de 72 milles sources (Pires, Motch, & Janot-Pacheco, 2009, A&A, 504, 185).

Finalement, le travail de modélisation de la population d'étoiles à neutrons isolées thermiques de la Galaxie permet de contraindre les propriétés globales de cette population à partir du relevé constitué par l'ensemble des observations faites par le satellite XMM-Newton. Ce travail a pour but de déterminer si la densité spatiale déduite du groupe de sept étoiles proches est une anomalie causée par notre position actuelle proche des zones actives de formation récente d'étoiles de la ceinture de Gould en estimant la densité des sources similaires dans la Voie Lactée à plus grande distance.

Chapter 1

Introduction

Contents

1.1 Historical overview

Landau (1932) was the first to speculate on the possible existence of a degenerate star entirely composed of neutrons, formed when the pressure within normal stellar matter becomes high enough. In the framework of the newly established Fermi-Dirac statistics, this "*unheimliche Sterne*", once formed, would not generate energy and could only radiate its remaining store of heat through photon diffusion. The neutron star's presumed limited size of $R \sim 3\,\mathrm{km}$ would, in practice, prevent its observation due to the expected low optical luminosity.

A couple of years after, Baade & Zwicky (1934) realised that, at their maximum brightness, supernova events emit nearly as much light as the "nebula" in which they originate. Wondering what would be the final state following such event, they concluded that a supernova represents the transition of an ordinary star into a compact body of considerably smaller mass – possibly a neutron star – and that a huge amount of energy is released in the process. Within the general theory of relativity and the nuclear physics that was then known, Oppenheimer & Volkoff (1939) soon worked out the first models for the structure of neutron stars, presenting a classic analysis of the theoretical viability of these objects.

In spite of the excitement caused by these early theoretical advances, neutron stars would remain as speculations for nearly a quarter of century until a series of important discoveries were made in radio and high energy astronomy. In the late 1950s, based on the detected X-ray emission from the Solar corona – just a tiny fraction of the Sun's total luminosity – it was generally believed that the much more distant stars would be unobservable in X-rays. In 1962, the unexpected results of the team led by Bruno Rossi and Riccardo Giacconi, who detected strong X-ray sources in the constellations of Scorpio and Cygnus and even a hint of the existence of an X-ray background, were intriguing. Although among the various processes proposed for the generation of the detected X-rays was thermal radiation from the surface of a hot neutron star (Chiu & Salpeter 1964) and, a few years later, accretion onto a neutron star in a close binary system (model proposed for Sco X-1 by Shklovsky 1967), early X-ray observations were not sensitive enough to prove their existence. This was done a few years later by radio astronomers.

In 1967, while using a radio telescope built to look for rapid variations in the radio emission of quasars, Jocelyn Bell came accross a series of extremely precise and fast pulsating radio signals originating from a source located at right ascension $19^{\mathrm{h}}\,20^{\mathrm{m}}$ and declination $+23°$. It became clear that a new kind of celestial object had been discovered when a few more similar sources were detected (Hewish et al. 1968). In particular, the discovery of pulsating radio sources in the Crab and Vela nebulae (Staelin & Reifenstein 1968, Large et al. 1968, Comella et al. 1969) provided striking evidence that neutron stars are born in core-collapse supernovae from a massive main sequence star. The link between these pulsating radio sources, which were called *pulsars*, and fast spinning highly magnetized neutron stars was established by Pacini (1967; 1968) and Gold (1968; 1969), that eventually introduced the concept of the "rotation-powered pulsar": if the neutron star radiates at the expense of its available rotational energy, a gradual lengthening of the period should be observed. In fact, although the measured periods are very stable by most normal standards, pulsars had been discovered to be slowing down by an average of $\sim 3\,\mathrm{s}$ every 10^8 years (e.g. Davies et al. 1969, Durney 1969, Cole 1969). This is understood to be a consequence of the torque exerted by the strong magnetic field on the rotating star, the "magnetic dipole braking model" (Ostriker & Gunn 1969). The injection of relativistic particles into the pulsar magnetosphere and creation of a *pulsar wind nebula* (PWN) is a further source of energy loss.

These exciting radio discoveries triggered subsequent pulsar searches at nearly all wavelengths. The Crab pulsar was discovered to emit pulsed radiation in the optical (Cocke et al. 1969), at X-ray energies in the 1.5 – 10 keV range (Fritz et al. 1969, Bradt et al. 1969) and at γ-ray energies above 0.6 MeV (Hillier et al. 1970). The observations showed that the pulsations are phase-aligned with pulse profiles that are nearly the same at all energies (Fig. 1.1), suggesting a common emission site in the pulsar magnetosphere and a non-thermal origin of the radiation. The Vela pulsar was found to be the brightest persistent γ-ray source in the sky, with pulsations detected for the first time by Thompson et al. (1975). A faint optical object, with $V \sim 23$, was suggested as the pulsar counterpart by Lasker (1976) and then confirmed one year later when pulsations were discovered (Wal-

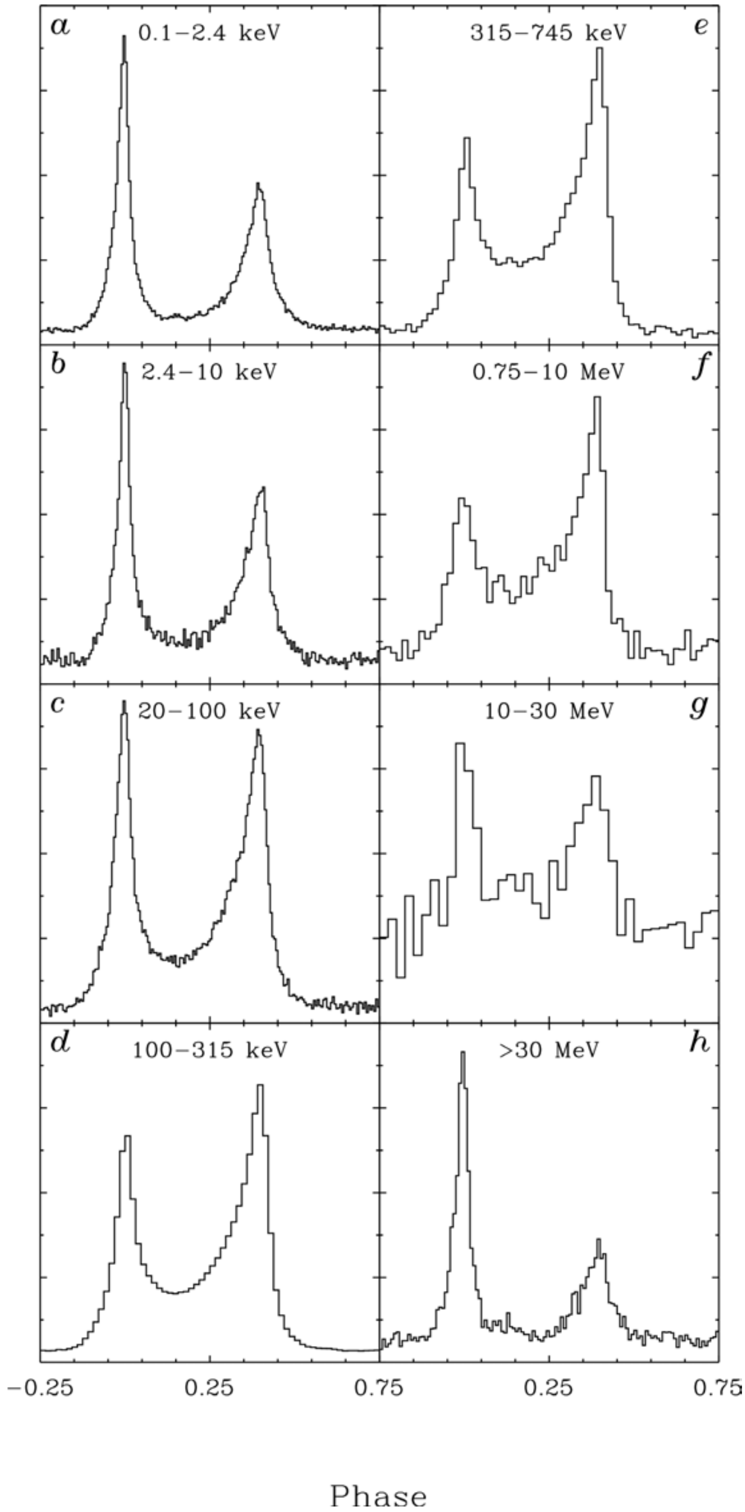

Figure 1.1: The Crab pulse profile at high photon energies. Its characteristic double-peaked shape is observed at all wavelengths (from Kuiper et al. 2001).

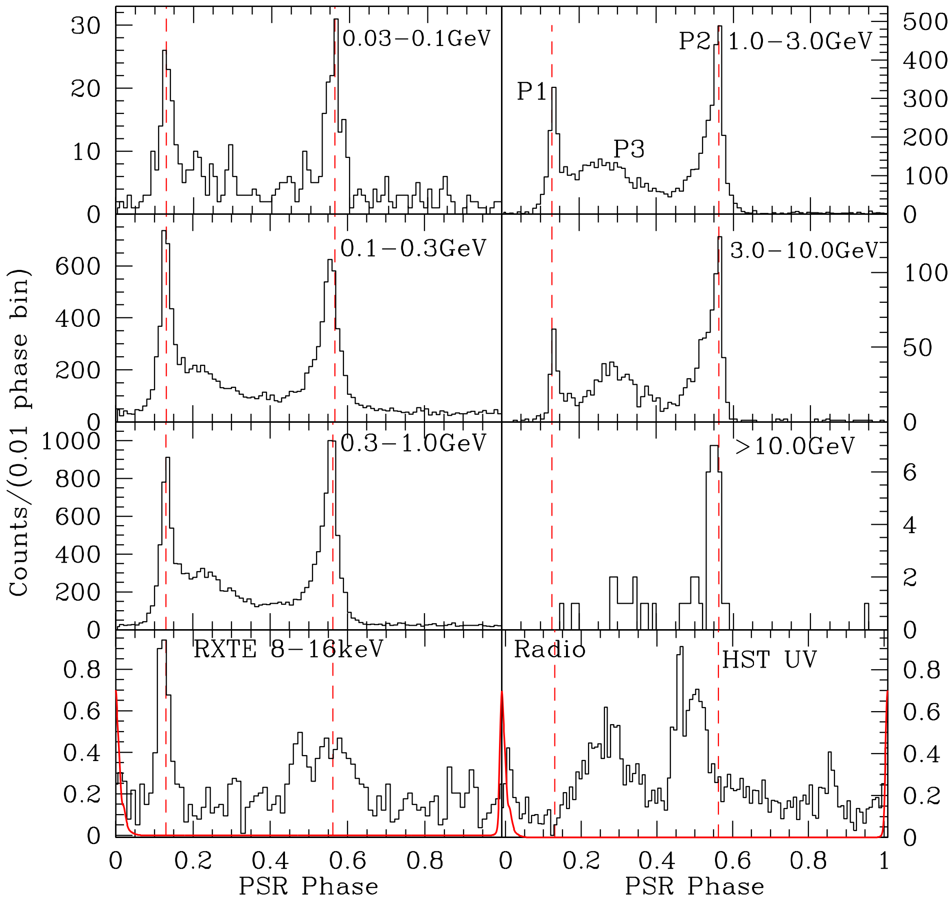

Figure 1.2: The Vela pulse profile at different energies, showing a shift in phase between pulses (from Abdo et al. 2009).

lace et al. 1977). Unlike the Crab, the γ-ray pulses are not phase-aligned with the radio and optical profiles (Fig. 1.2); moreover, the optical counterpart of the Vela pulsar is much fainter than the Crab ($V \sim 16.5$), the luminosity being four orders of magnitude lower, whereas its rotational energy loss is only a factor of 65 lower.

It was soon realised that the emission at long wavelengths is energetically unimportant relative to the power emitted at short wavelengths by a factor of more than two orders of magnitude. This fact, among others, urged the development of more sensitive X-ray and γ-ray observatories that would be suited to perform detailed investigations of pulsar emission mechanisms as well as to survey the sky for yet unknown X-ray and γ-ray sources. In the remainder of this section, we highlight the main contributions of some of these past X-ray missions to the study of neutron stars without, however, reviewing the progress made in the last ten years by current high energy observatories – in particular, the Chandra and XMM-Newton missions – which are extensively discussed throughout this work.

Overview of past high energy missions The first space observatory dedicated entirely to X-ray science was the satellite Uhuru (SAS-1; Giacconi et al. 1971). This mission performed the first all-sky X-ray survey in the 2 – 20 keV energy band, with a sensitivity of 1.5×10^{-11} erg s^{-1} cm^{-2}. Uhuru discovered 339 new X-ray sources, most of them belonging to the group of "accretion-powered binaries" (Lewin et al. 1997, Lewin & van der Klis 2006) – neutron stars or black holes in binary systems that accrete matter from a companion star. Strong X-ray radiation is emitted as the matter spirals in onto the compact object or heats up in an accretion disc. In fact, the strong X-ray sources accidentally detected by rocket flight experiments in the early 1960's belong to this group – Sco X-1, the prototypic low mass X-ray binary (LMXB), consisting of a neutron star and an evolved low mass subgiant (as predicted by Shklovsky 1967 and others) and Cyg X-1, a black hole in a high mass accreting binary system (HMXB). To date, known LMXBs and HMXBs amount to a total number of 187 (Liu et al. 2007) and 114 (Liu et al. 2006) systems, respectively, including objects in the Magellanic clouds.

Of particular interest to the study of isolated neutron stars (INSs) was the operation of the Einstein Observatory (HEAO-2; Giacconi et al. 1979) in the 1980's, the first imaging X-ray telescope. Sensitive in the 0.15 – 4 keV energy range, this mission investigated the soft X-ray radiation from the Crab and Vela pulsars, unveiled the pulsed emission of young neutron stars in the Magellanic clouds and detected the X-ray counterparts of a number of middle-aged and old nearby radio pulsars. Moreover, Einstein identified a handful of faint and soft previously unknown X-ray sources located near the center of supernova remnants (SNRs) RCW 103, PKS 1209-51/52, Puppis A and Kes 73 as neutron star candidates.

The succesful Roentgen Satellite mission (ROSAT, Trümper 1984), launched on June 1990, performed an all-sky survey during the first six months of operation (RASS; Voges et al. 1999), the first one using an imaging telescope. With a sensitivity of 3×10^{-12} erg s^{-1} cm^{-2} in the 0.1 – 2.4 keV energy band, it catalogued more than 150,000 X-ray sources and provided valuable information on fluxes for all known radio pulsars. One of the main outcomes of the ROSAT mission was the discovery of a group of radio-quiet and thermally emitting INSs which, since their discovery in the late 1990s, have raised much interest among the astronomical community. The scope of the present thesis is to investigate the population properties of these thermal X-ray sources in the Milky Way.

In the last ten years of the century – the "decade of space science", in the words of Becker & Pavlov (2002) – several other space missions have greatly contributed to the current understanding of the broad-band emission of neutron stars. In particular, the Extreme Ultraviolet Explorer (EUVE; Bowyer & Malina 1991) observed several neutron stars at very soft X-rays, 0.07 – 0.2 keV. The BeppoSAX (Boella et al. 1997) and Rossi X-ray Timing Explorer (RXTE; Bradt et al. 1993, still in operation) missions have proved to be particularly important to the field of X-ray binaries and accretion-powered pulsars. The γ-ray observatory Compton (CGRO; Kniffen 1990) identified five new γ-ray pulsars to supplement the two that were known before, Crab and Vela. Finally, contrary to the early expectations of the 1930s, the direct observation of very faint optical counterparts of several pulsars and INSs became possible in the 1990s with the Hubble Space Telescope (HST) as well as with the ground-based European Southern Observatory Very Large Telescope (ESO-VLT; see Mignani et al. 2004, for a review).

A few last words must briefly mention the most relevant high energy observatories that are currently in operation. NASA's Chandra is a high spatial resolution X-ray telescope operating in the 0.1 – 10 keV range (Appendix B.1.2). The recently launched Fermi γ-Ray Space Telescope (formerly GLAST; Gehrels & Michelson 1999) is performing an all-sky survey and monitoring γ-ray bursts with unprecedented effective area, field-of-view and sensitivity in the 10 keV to 300 GeV. The International γ-Ray Astrophysics Laboratory (INTEGRAL; Winkler et al. 2003) of the European Space Agency (ESA) aims to produce a complete map of the sky in the soft γ-ray waveband with high spectral and spatial capabilities. The Japanese Suzaku (Mitsuda et al. 2007) is the successor of the ASCA X-ray Observatory and is sensistive in the 0.2 – 600 keV energy range. Swift (Gehrels et al. 2004) is a medium-sized multi-wavelength mission with a fast response to γ-ray bursts and their afterglows in X-rays, UV and optical wavebands. Finally, ESA's XMM-Newton (Appendix B.1.1) is a multi-mirror X-ray mission that operates in the 0.15 – 15 keV energy range with very large collecting area and simultaneous optical observation.

1.2 Number of neutron stars in the Galaxy

Supernovae are at the origin of all elements, from iron to the heavier ones, that are created through explosive oxygen and silicon burning (Woosley et al. 1973, Woosley & Weaver 1986; 1995). They offer both a site for the high temperatures required for nuclear reactions with large Coulomb barriers and a very efficient means of dispersing the products that have been synthesized during stellar evolution into the interstellar medium (ISM).

Common to all types of supernovae is the synthesis of significant amounts of the radioisotope ^{56}Ni during the explosion, which subsequently decays to ^{56}Co and ^{56}Fe, providing energy to the expanding envelope that translates into an almost exponentially decaying lightcurve. Hence the present Galactic iron abundance can in principle trace the number of past supernova events and the number of neutron stars populating the Milky Way. However, the total number of neutron stars cannot be derived with great accuracy since both types of supernova – types I and II, related respectively to the thermonuclear burning of a C-O white dwarf and the gravitational collapse of a massive star – contribute to the iron yield. Obviously, a further complication is that not all type II supernovae leave a neutron star as a remnant since black holes can also form either during the event or later, due to fall-back of the ejected stellar layers. Nonetheless, it is expected that, from the frequency of occurrence of type II supernovae in nearby spiral galaxies of similar type and luminosity (e.g. Cappellaro et al. 1997; 1999), more than 10^8 neutron stars should populate the Milky Way. This estimate may just be a lower limit for the total number of galactic neutron stars since our Galaxy may have experienced phases of enhanced star formation in early epochs.

Another important tracer of the galactic nucleosynthesis is the γ-ray emission resulting from the decay of ^{26}Al (Diehl et al. 2006). This element is mainly produced by massive stars in the disk during either Wolf-Rayet phases and supernova events. Through the measurement of the corresponding 1808.65 keV γ-ray flux in the Milky Way, Diehl et al. (2006) estimated that the galactic core-collapse supernova rate is around 1.9 ± 1.1 events per century, implying again a total population of $\sim 10^8$ neutron stars in the Galaxy.

1.2.1 Radio pulsars and surveys

In spite of the great development of high energy astronomy in the last 30 years, it has always been at radio wavelengths that the vast majority of neutron stars are detected. Since the discovery of the first pulsar, the number of known Galactic objects has grown to nearly 1800 (Manchester et al. 2005[1]). More than half of these have been discovered in the past few years by surveys carried out using the multibeam receiver on the Parkes 64 m radio telescope. These surveys have searched for new pulsars in a range of longitudes in the inner Galactic plane ($|b| < 5°$, the Parkes Multibeam Pulsar Survey, PMPS; Manchester et al. 2001, Lorimer et al. 2006) and in a strip covering higher Galactic latitudes ($|b| < 60°$, the Parkes High Latitude Survey, PH; Burgay et al. 2006). Other important searches are the Swinburne Intermediate Latitude (SIL; Edwards et al. 2001) and High Latitude (SHL; Jacoby 2005) surveys, which together discovered more than 200 new pulsars. The Parkes surveys can be considered the most successful large scale search for pulsars so far undertaken (Lyne 2008). A recent and comprehensive review can be found in e.g. Manchester (2009).

The choice of high radio frequencies, 1.4 – 2.3 GHz, is the best suited for searches in the Galactic plane and at the core of SNRs since these frequencies are much less sensitive to the interstellar scattering. The newly discovered pulsars tend to be young, distant and of high radio luminosity. On the other hand, low frequency surveys (typically 300 – 400 MHz) represent a good option for investigating the low-luminosity tail of pulsars in the Solar neighbourhood, where a population of relatively old objects prevails (Possenti 2007).

Radio surveys at high frequencies are also appropriate for the detection of millisecond pulsars. In these objects, the bulk of the observed pulsar population underwent a phase of spin-up due to mass transfer in binaries. A recent succesful search for these fast-spinning objects has been the Green Bank Globular Cluster (GBGC) survey, which alone discovered more than 60 recycled pulsars in globular clusters. Among these, more than half belong to Terzan 5 (Ransom et al. 2005), including the fastest-spinning pulsar ever detected, PSR J1748-2446ad, with a spin period $P = 1.4$ ms (Hessels et al. 2006). Another exciting object discovered by the GBGC survey is the binary pulsar PSR J1748-2021B in NGC 6440, for which the system total mass might imply the existence of a neutron star heavier than about 1.7 $M_\odot$ (Freire et al. 2008a). Finally, on-going projects, like the Perseus Arm (PA) and Arecibo PALFA surveys are extending the Parkes pulsar surveys to targets outside the Solar radius. Upon completion, it is expected that the PA survey will provide excellent constraints on the radial Galactic distribution of pulsars for $R > R_\odot \cong 8.5$ kpc.

Despite these very succesful radio surveys, it is well known that the observed sample of radio pulsars is heavily biased by selection effects and is not representative of the true population. The expected number of potentially observable active radio pulsars – i.e. those that have not yet crossed the pulsar "death line" (Sect. 1.4.1.1) – is around 10^5 in the Galaxy (Vranesevic et al. 2004, Lorimer et al. 2006, Faucher-Giguère & Kaspi 2006) while only $\sim 2\%$ have actually been detected altogether. In addition to the rather obvi-

[1] See also the ATNF pulsar catalogue webpage, `http://www.atnf.csiro.au/research/pulsar/psrcat`, for an up-to-date list of the known radio pulsars and INSs. Presently, 21 extragalactic sources have been detected in the Magellanic clouds and are not included here.

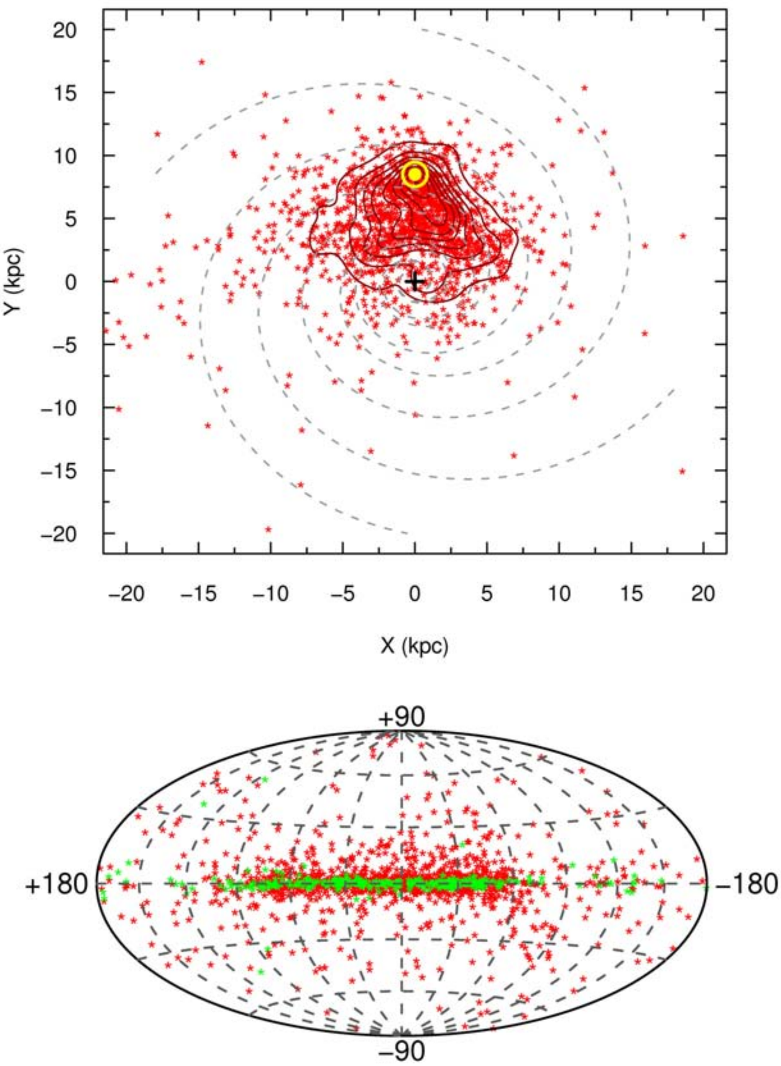

Figure 1.3: *Top:* Projected distribution of the sample of catalogued radio pulsars and INSs in the Galactic plane. The Sun's location is marked in yellow while a cross at $X, Y = 0, 0$ shows the Galactic center. Dashed lines represent a parametrized description of the Galactic spiral arms (Wainscoat et al. 1992). *Bottom:* Hammer-Aitoff projection in galactic coordinates of the same sample. Sources younger than a characteristic age of $\tau_{\rm ch} = 10^6$ yr are shown in green.

ous beaming effect and luminosity geometric dilution, other selection biases that limit the number of detected sources in a given survey are the thermal noise in the receiver, i.e. the "system temperature"; the radio sky background due to synchrotron emitting electrons in the Galactic magnetic field – the "sky temperature", which is fortunately dependent on frequency and thus possible to minimize; propagation effects in the ISM which disperse and broaden the radio pulse, with severe effects for the detectability of fast and/or distant pulsars; the sudden cessation of pulsed emission over several periods, an effect known as

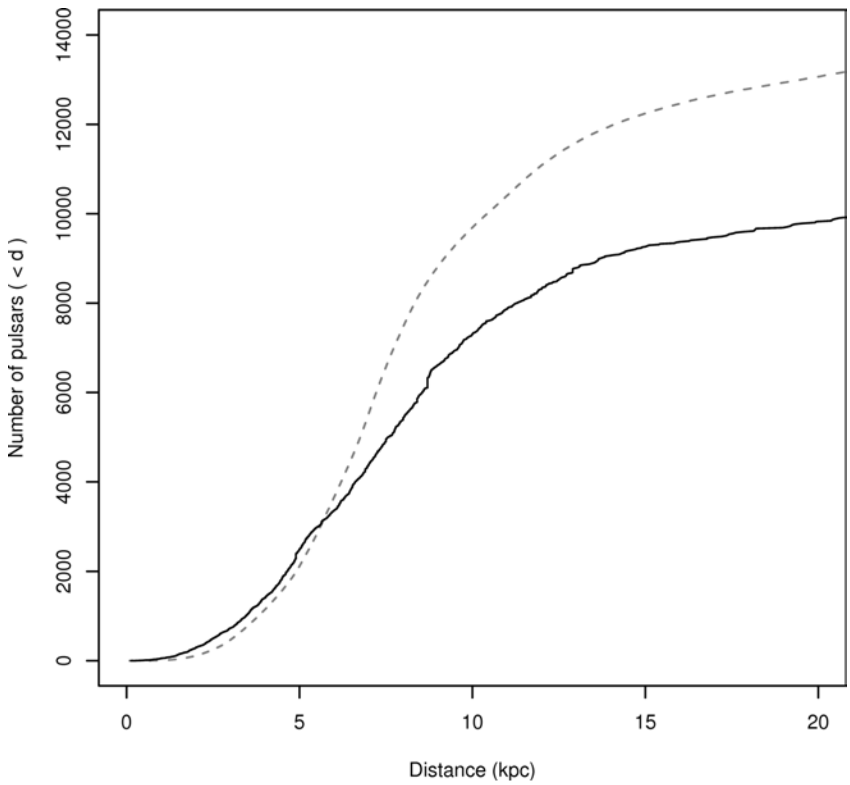

Figure 1.4: Cumulative distribution of pulsars as a function of distance from the Sun projected onto the Galactic plane. The solid line shows the observed sample (around 1800 objects) while the dashed line shows the expected distribution of a population free from selection effects, drawn from a simulation of synthetic neutron stars born in the disk.

"pulse nulling", which requires surveys to preferentially adopt many pointings and long integration times; among others.

To illustrate these selection effects, in Fig. 1.3 we show the spatial distribution of known radio pulsars and INSs from the ATNF catalogue projected in the Galactic plane and in a Hammer-Aitoff sky projection in galactic coordinates. It is evident that most detected objects lie in the Solar vicinity and within a distance of 3 kpc of the Galactic center. Moreover, it is clear that young objects are strongly concentrated in the Galactic plane.

The cumulative distribution of catalogued pulsars as a function of distance from the Sun can be seen in Fig. 1.4, along with the expected distribution for a simulated unbiased population. As can be seen, there is a deficit of remote objects relative to expectations. Distances to radio pulsars and INSs have been determined either directly, through radio or optical parallax, or inferred from known association with SNRs, photoelectric absorption in the spectra of the sources and through a measure of the dispersion of the various wavelengths in the pulsed radio signal: due to interaction with the interstellar electrons, longer radio wavelengths suffer a greater time delay in reaching the Earth than shorter ones. From this "dispersion measure" (DM), the column density of intervening electrons and the distance to the pulsar can be derived adopting a model for the distribution of free electrons in the Galaxy.

1.2.2 Expectations with ROSAT

Thanks to the major contribution to pulsar astronomy of X-ray and γ-ray observatories from Einstein and ROSAT to Fermi, nearly 100 pulsars are now known to emit high energy radiation. Although most of the target sources have been chosen from radio pulsar catalogues, a significant number of objects was previously unknown; some have subsequently been detected at radio wavelengths while others have not.

Many of these pulsars are powered by the rotational energy of the underlying neutron star, with radiative processes that include (*i*) non-thermal emission from charged particles accelerated in the pulsar magnetosphere, (*ii*) extended emission from pulsar-driven synchrotron nebulae and (*iii*) X-ray and γ-ray emission from interaction of relativistic pulsar winds with a close companion star or its wind. Moreover, during its early life the neutron star is very hot and its thermal energy is expected to be responsible for the (*iv*) photospheric emission from the cooling surface. In many pulsars the observed X-ray emission results from the sum of thermal and non-thermal components (see Becker & Aschenbach 2002, Kaspi et al. 2004; for reviews). Although it is not always evident how to discriminate between the different emission scenarios for a given source, it is well established that the spectrum of young rotation-powered pulsars (with ages $\lesssim 10^5$ yr) is dominated by magnetospheric emission, characterized by a power-law over a broad energy band. Old pulsars (age $\gtrsim$ few Myr) exhibit a weak thermal component, probably originating from small heated polar caps, in addition to a dominating power-law. Middle-aged (age $\sim$ few 10^5 yr) pulsars – such as the "Three Musketeers" Geminga, PSR B0656+14 and PSR B1055-52 – show complex spectra that result from the contributions of the cooling surface and polar caps as well as of weak remnant magnetospheric emission.

The number of X-ray detected rotation-powered neutron stars has more than tripled in the last 12 years due to improvements in X-ray sensitivity, in particular from RXTE, Chandra and XMM-Newton, as well as to follow-up observations of newly discovered radio pulsars and millisecond sources in globular clusters. However, excluding these recycled pulsars in binary systems, only young neutron stars are being detected by high energy missions since objects older than at most $10^7 - 10^8$ yr are expected to have both exhausted their internal source of particle production and acceleration as well as cooled down to temperatures undetectable in the X-ray regime. Averaged over the entire lifetime of the Galaxy, this means that INSs are doomed to be cold, dead compact objects for most of their lives.

The launch of ROSAT, a satellite of outstanding sensitivity at soft X-ray energies – 20 times more than any previous survey in X-rays – raised a major expectation in the scientific community that a population of old INSs would be detected through their accretion from the interstellar medium (ISM; Treves & Colpi 1991, Colpi et al. 1993, Blaes & Madau 1993, Madau & Blaes 1994). This idea was first proposed by Ostriker et al. (1970) who estimated that, since the number of old "dead" pulsars should overwhelmingly outnumber active ones, the contribution of accretion from the ISM to the X-ray background would

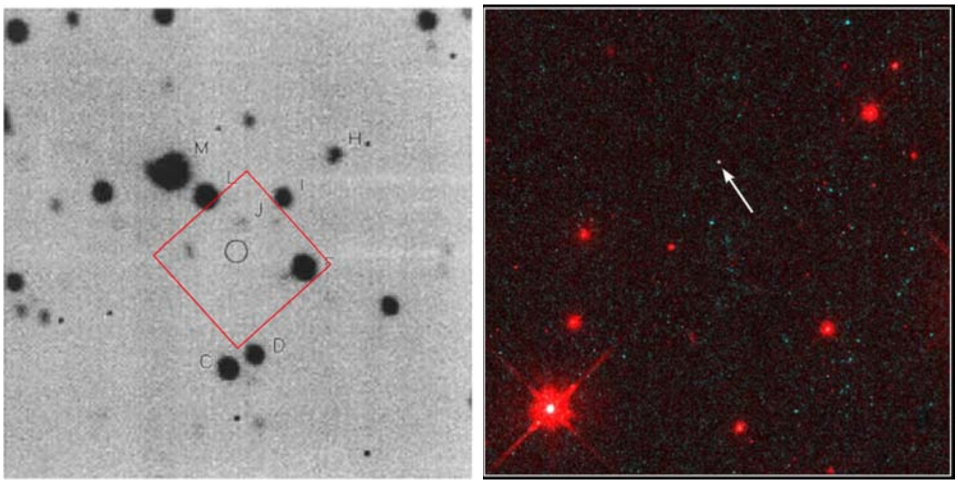

Figure 1.5: Discovery of the first nearby thermally emitting INS candidate RX J1856.5-3754 in ROSAT data. *Left:* Optical finding chart from the time of the discovery showing the blank error circle of the X-ray source (from Walter et al. 1996). The red frame shows the orientation of the Hubble image. *Right:* Hubble image showing the detected optical counterpart of the neutron star (from F. M. Walter's webpage `http://www.astro.sunysb.edu/fwalter/NS/ns.html`).

be significant at soft energies, $\lesssim 0.25\,\text{keV}$, and that the closest neutron stars should be detectable as discrete sources.

Following this idea 30 years later, Treves & Colpi (1991) estimated that about 5000 old INSs should be identifiable in the RASS data, considering the spatial distribution of a total population of 10^9 neutron stars evolving in the Galactic potential for 10^{10} years. Assuming that accretion from the ISM would proceed at the Bondi-Hoyle rate (Appendix A.2), the accreting sources would radiate at soft X-ray energies, $T_{\rm BB} \sim 10^6\,\text{K}$, with a luminosity of $\sim 10^{31}\,\text{erg s}^{-1}$. The authors considered the local density of old neutron stars for four different velocity bins in the range of 25 to $100\,\text{km s}^{-1}$ with corresponding scale heights of around 200 pc, as derived from the calculations of Paczynski (1990) for a population born in the disk. Their results showed that only the low velocity[2] neutron stars among the total population would contribute significantly to the detectable number of accreting sources – the observability decreasing by three orders of magnitude when neutron stars have a mean velocity $v = 100\,\text{km s}^{-1}$ relative to objects with $v = 25\,\text{km s}^{-1}$. These predictions were confirmed by the detailed analysis carried out by Blaes & Madau (1993). The authors investigated the spatial and kinematic properties of the local INS population through Monte Carlo simulations and semianalytic techniques, under a number of similar assumptions – 10^9 neutron stars in the Galaxy, a velocity distribution as observed for young radio pulsars, a blackbody approximation for the emitted spectrum, etc – predicting a number of 2,000 to 10,000 potentially detectable sources, also considering polar cap accretion in addition to the isotropic case.

While discussing their results, Treves & Colpi (1991) stressed the fact that the de-

[2]The accretion luminosity depends on v^{-3}; see Appendix A.2.

tectability of accreting sources is highly dependent on the rather uncertain assumptions that had been made; in particular, they questioned the validity of the application of Bondi-Hoyle theory in the slowly-accreting regime, the influence of the magnetic field on accretion (since it was assumed $B = 10^9$ G), the blackbody approximation and, most importantly, the space and velocity distributions of old neutron stars in the Solar vicinity. All these factors turned out to be of fundamental importance when it was time to confront theoretical expectations with the results obtained with ROSAT.

The evident absence of a large number of unidentified soft X-ray sources in the RASS data was in clear opposition to expectations. In particular, the analysis of the source content resulting from searches in both the Galactic plane (Motch et al. 1997) and in molecular clouds (Danner 1998) called into question the figures predicted for the accretion scenario, which had to be critically reevaluated in the following years in order to explain the paucity of INS candidates (see e.g. Neuhäuser & Trümper 1999, Treves et al. 2000).

Independently of the number, accreting INSs should be identifiable due to the softness of their spectra, low column densities and extremely high X-ray-to-optical flux ratios. Moreover, for the very local sources, moderate proper motions of faint blue optical counterparts should be observable (Ostriker et al. 1970). The first confirmed INS candidate showing the above characteristics, RX J1856.5-3754 (Fig. 1.5), was reported by Walter et al. (1996); six other would be identified in the following 5 years (Haberl et al. 1997; 1998, Schwope et al. 1999, Motch et al. 1999, Haberl et al. 1999, Zampieri et al. 2001). Contrary to expectations, RX J1856.5-3754 is not an old accreting neutron star; quite possibly, the other six are not either. However, they share particular properties which are clearly at variance with the bulk of the population of rotation-powered radio pulsars, and have been nicknamed the "Magnificent Seven" (or M7, for simplicity[3]).

1.3 The group of seven nearby isolated neutron stars

A major outcome of the ROSAT mission was the discovery of a group of radio-quiet thermally emitting INSs, originally identified serendipitously as soft, bright X-ray sources with no obvious optical counterparts. The seven sources share a rather well defined set of properties which have never been encountered together in previously known classes of INSs.

A prime reason to observe and study neutron stars is the hope of constraining the fundamental physics of ultra-dense matter at very extreme conditions of gravity and magnetic field (see Sect. A.1). Unlike radio pulsars detected at X-ray energies, the seven ROSAT-discovered INSs show no evidence for magnetospheric activity and thus provide a direct view of the surface of the neutron star.

1.3.1 Overall observed characteristics

We give in Table 1.1 a summary of the overall observed characteristics of the M7. Reviews can be found in Treves et al. (2000), Motch (2001), Haberl (2004b; 2005; 2007), Kaplan

[3] In this work, the acronym M7 is used to designate the seven ROSAT-discovered radio-quiet and thermally emitting INSs. There is still no general term to address the whole population to which these sources might belong. Other terms currently used in the literature are "XDINS" – X-ray Dim INSs – or simply "INSs".

(2008), Turolla (2009).

A soft blackbody spectrum undergoing low interstellar absorption ($kT \sim 40 - 100\,\mathrm{eV}$ and $N_\mathrm{H} \sim$ few $10^{20}\,\mathrm{cm}^{-2}$) and constant X-ray flux are common to the seven sources, as well as the absence of a non-thermal component extending towards higher energies (characteristic of radio pulsars detected in X-rays). Typical X-ray luminositites are roughly in range 10^{30} to $10^{32}\,\mathrm{erg\,s}^{-1}$. High resolution X-ray spectroscopy of the brightest source RX J1856.5-3754, using the LETG (Low Energy Transmission Grating) and the RGS (Reflection Grating Spectrometer) on board Chandra and XMM-Newton, respectively, produced the striking result that a simple blackbody yields a much better fit to the spectrum of the source than the more physically motivated neutron star atmosphere models that were then available (Burwitz et al. 2001; 2003; see Sect. 1.3.2). In particular, no atomic spectral features that could be used to derive the gravitational redshift and the mass-to-radius ratio of the neutron star were identified in the very high signal-to-noise (S/N) 500 ks Chandra observation.

The gravitational redshift z_g is given by:

$$1 + z_g = \left(1 - \frac{2GM}{Rc^2}\right)^{-1/2} \tag{1.1}$$

where M and R are the neutron star mass and radius, respectively. Since neutron stars are relativistic objects, the apparent radiation temperature T_∞ and radius R_∞, as seen by an observer at infinity, are both affected by the gravitational redshift, i.e.:

$$T_\infty = \frac{T_\mathrm{eff}}{1 + z_g} \tag{1.2}$$

$$R_\infty = R_\mathrm{em}(1 + z_g) \tag{1.3}$$

where R_em is the physical size of the emission region and T_eff is the neutron star effective blackbody temperature.

On the other hand, broad absorption lines in the energy range 0.2 to 0.75 keV were found to be present in the spectra of the other six sources (Haberl et al. 2003; 2004b, van Kerkwijk et al. 2004, Haberl et al. 2004a, Zane et al. 2005), which have typically been modelled by Gaussian absorption lines added to the blackbody continuum. These broad features have complex, phase-dependent shapes and the line depths often exceed 50% (see Fig. 1.6). The two common interpretations are that they are due to either protron cyclotron absorption or atomic transitions in the partially ionised hydrogen atmosphere of the strongly magnetized neutron star. Several sources even show evidence for absorption at multiple (harmonically spaced) energies (Haberl 2007, Schwope et al. 2007) which is puzzling and not well understood, since the flux ratio between the observed lines does not follow what would be expected for cyclotron absorption (see Sect. 1.3.1.1).

Very faint optical counterparts with blue magnitudes roughly in the range of 25 to 28 have been identified for most of the sources (Walter & Matthews 1997, Motch & Haberl 1998, Kulkarni & van Kerkwijk 1998, Kaplan et al. 2002a; 2003, Haberl et al. 2004a, Zane et al. 2008, Schwope et al. 2009, Mignani et al. 2009), implying high X-ray-to-optical flux ratios of $f_\mathrm{X}/f_\mathrm{opt} \sim 10^4 - 10^5$. Relative to radio pulsars, the neutron star spin periods

Table 1.1: Observed properties of the *Magnificent Seven*.

Source	Spin			Spectrum					Astrometry	
RX	P (s)	$\dot{P}$ ($\mathrm{s\,s^{-1}}$)	p_f (%)	N_H ($10^{20}\,\mathrm{cm^{-2}}$)	kT (eV)	f_X ($\mathrm{erg\,s^{-1}\,cm^{-2}}$)	ε_abs (keV)	m_B	μ ($\mathrm{mas\,yr^{-1}}$)	d (pc)
J1856.5−3754	7.06	3.0×10^{-14}	1	0.8	62	1.46×10^{-11}	…	25.2	333	160
J0720.4−3125	8.39	7.0×10^{-14}	11	1.0	87	1.01×10^{-11}	0.3	26.6	108	360
J1605.3+3249	…	…	<3	0.8	93	6.08×10^{-12}	0.4(0.6,0.8)	27.2	155	390
J1308.6+2127	10.31	1.1×10^{-13}	18	1.8	102	3.01×10^{-12}	0.2(0.4)	28.4	220	…
J2143.0+0654	9.43	4.1×10^{-14}	4	3.6	104	2.94×10^{-12}	0.7	27.4	…	430
J0806.4−4123	11.37	…	6	1.1	92	2.38×10^{-12}	0.3(0.6)	>24	<86	250
J0420.0−5022	3.45	…	17	2.1	45	2.22×10^{-13}	0.3	27.5(?)	<123	345

Note: We list the spin period P, period derivative $\dot{P}$, rms pulsed fraction pf, hydrogen column density N_H, blackbody temperature kT, observed flux f_X (0.15 – 12 keV), central energy of any absorption features ε_abs in the X-ray spectrum (and secondary lines, if present), B-band magnitude m_B, proper motion μ and distance d (updated and adapted from Kaplan 2008). Sources are sorted by X-ray intensity, as usual for the M7.

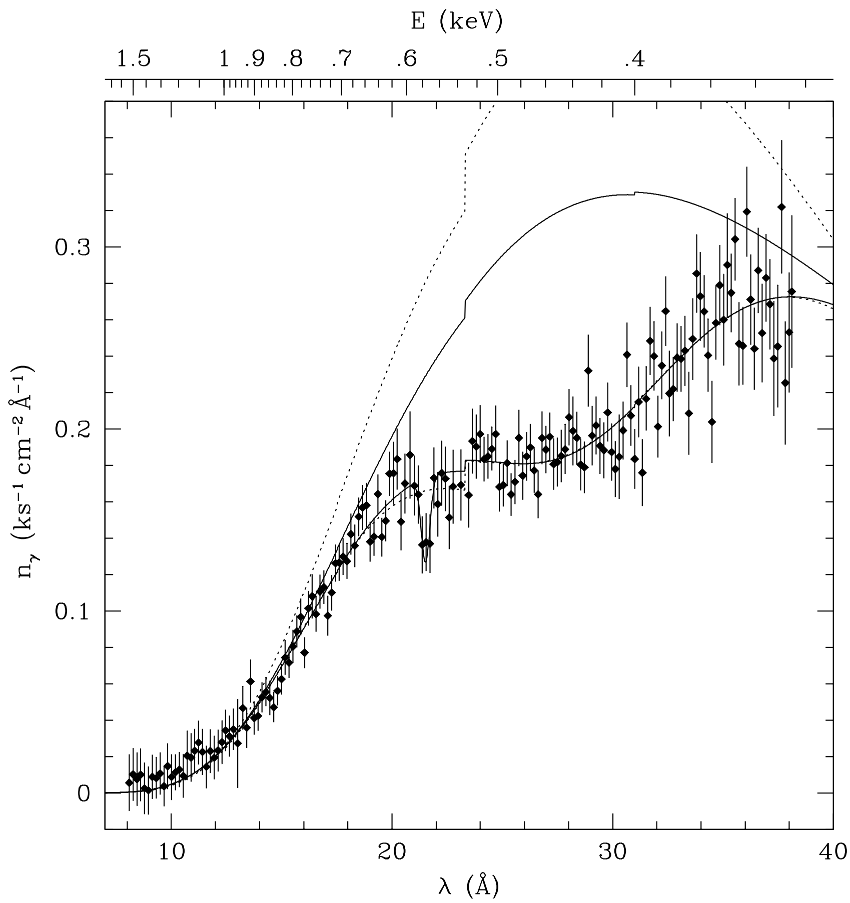

Figure 1.6: RGS spectrum of source RX J1605.3+3249, showing the presence of a broad absorption line (from van Kerkwijk et al. 2004).

are longer and distributed over a much narrower range, $P \sim 3 - 11$ s. Six of the sources show sinusoidal X-ray pulsations with pulsed fractions between $\sim 1\%$ and 18%. To date, only the spin period of source RX J1605.3+3249 remains undetected; the smooth intensity variations should be less than 3% (van Kerkwijk et al. 2004).

The M7 are believed to be nearby (generally, $d \lesssim 500$ pc), as inferred from the distribution of the interstellar medium in the line-of-sight and the equivalent hydrogen column densities measured in their X-ray spectra (Posselt et al. 2007). Furthermore, HST parallaxes are available for the two X-ray brightest members, RX J1856.5-3754 ($d = 161^{+18}_{-14}$ pc; Kaplan et al. 2002b) and RX J0720.4-3125 ($d = 361^{+172}_{-88}$ pc; Kaplan et al. 2007), with results largely consistent with those estimated by Posselt et al. (2007). The seven sources do not show either persistent or transient radio emission to a rather sensitive limiting flux of $\sim 10\,\mu$Jy (Kondratiev et al. 2008; 2009) and are not associated to SNRs. However, unconfirmed claims of faint detection at long wavelengths exist for RX J1308.6+2127 and RX J2143.0+0654 (Malofeev et al. 2007).

Table 1.2: Spectral line parameters and inferred magnetic field of the M7 for proton cyclotron absorption and atomic hydrogen transitions.

Source RX	ε_{abs} (keV)	σ (eV)	EW (eV)	B_{cyc} (10^{13} G)	B_H (10^{13} G)	Ref.
J0720.4−3125	0.27	60	-40	5.6	2.9	(a)
J1605.3+3249	0.40, 0.59, 0.78	90	-95, -75, -70	8.0	4.9	(b, c)
J1308.6+2127	0.23, 0.46	150, 200	-200, -180	4.0	2.3	(d, e)
J2143.0+0654	0.75	30		14	...	(f)
J0806.4−4123	0.46	70	-30	9.2	5.8	(g, c)
J0420.0−5022	0.33	70	-45	6.6	3.8	(g, c)

Note: The approximation of Eq. (1.5) is not valid for RX J2143.0+0654. *Ref.:* [(a)]Haberl et al. 2004b, [(b)]van Kerkwijk et al. 2004, [(c)]Haberl 2007, [(d)]Haberl et al. 2003, [(e)]Schwope et al. 2007, [(f)]Zane et al. 2005, [(g)]Haberl et al. 2004a.

1.3.1.1 Intense magnetic fields

Intense magnetic fields are inferred from several observational constraints: the long spin periods of the sources, the presence of broad absorption lines in the spectra, the detection of a Balmer-dominated nebula around one source and from timing measurements (see Haberl 2007, van Kerkwijk & Kaplan 2007; for reviews).

Spin periods of the order of seconds are similar to those shown by the objects known as *magnetars*[4] – neutron stars which are thought to possess magnetic fields in excess of the quantum critical value, $B_{QED} = m_e^2c^3(e\hbar)^{-1} \sim 4.4 \times 10^{13}$ G, at which the energy between Landau levels of electrons equals their rest mass. The observed emission of magnetars is thought to be powered by the decay of the strong magnetic field (Sect. 1.4.1). Some of the M7 could then be old nearby magnetars, as first suggested by Heyl & Kulkarni (1998). Alternatively, within the standard scenario of pulsar evolution and the magnetic dipole braking model, $\sim 10^6$ yr and $B \sim 10^{13}$ G are required to decelerate a rotation-powered neutron star born with a spin period of milliseconds to the values shown currently by the sample of seven sources, in agreement with their rough age expectations from cooling.

These crude estimates have been confirmed by the presence of absorption lines in the spectra of six of the M7. These features have been tentatively interpreted as proton cyclotron lines in magnetic fields in range $B \sim 10^{13} - 10^{14}$ G, according to:

$$\varepsilon_{cyc} = \frac{\hbar\omega}{1+z_g} = \frac{\hbar}{1+z_g}\frac{eB_{cyc}}{m_pc} \sim 0.63 y_g \left(\frac{B_{cyc}}{10^{14}\,\mathrm{G}}\right) \mathrm{keV} \tag{1.4}$$

where ε_{cyc} is the central energy of the proton cyclotron resonance line, $\omega = eB_{cyc}(m_pc)^{-1}$ is the cyclotron frequency and $y_g \equiv (1+z_g)^{-1}$ is the gravitational redshift factor (Zane et al. 2001). In Table 1.2 the central energies and widths of the measured absorption lines are

[4]Two known observational manifestations of magnetars are the groups of INSs known as AXPs (*anomalous X-ray pulsars*) and SGRs (*soft γ-ray repeaters*); see Sect. 1.4.1.

listed, together with the inferred surface magnetic field estimates. A canonical value for the gravitational redshift is assumed, $z_g \sim 0.3$, for $M = 1.4\,\mathrm{M}_\odot$ and $R = 10\,\mathrm{km}$; c.f. Eq. (1.1). For multiple lines, the lowest energy was considered in order to compute B_{cyc}.

Interestingly, evidence for multiple (harmonically spaced) lines has been found for some of the M7. In particular, while analysing XMM-Newton EPIC pn data of source RX J1605.3+3249, Haberl (2007) reported that the inclusion of the Gaussian absorption feature identified by van Kerkwijk et al. (2004) is not sufficient to obtain an acceptable fit; instead, if two more lines are added at multiply spaced energies, in a ratio 2:3:4, the quality of the fit is significantly improved (from reduced least squares $\chi^2_\nu = 2.4$ to $\chi^2_\nu = 1.4$). Similarly, higher S/N XMM-Newton observations of source RX J1308.6+2127 have required the presence of a second line at an energy which is twice the first one (Schwope et al. 2007). The same situation has been suggested for source RX J0806.4-4123, although the fit with only one line is formally acceptable ($\chi^2_\nu = 1.4$; Haberl 2007).

The interpretation of the multiple features as harmonically spaced cyclotron lines is hampered by the fact that the flux ratio between the observed lines does not follow what would be expected – for cyclotron absorption, the oscillator strength of the first harmonic is smaller than that of the fundamental by a factor $\varepsilon(m_p c^2)^{-1}$ and would thus be unobservable. A tentative alternative explanation would rest upon atomic transitions of the material deposited in the outermost layers of the neutron star: in the temperature and high magnetic field conditions which are thought to prevail in these objects, the atmosphere might be partially ionized due to the large increase of ionization potential (Lai 2001). In particular, hydrogen transitions could account for part or all of the observed broad features. At sufficiently strong magnetic field, the transitions could become harmonically related, in proportion to the proton cyclotron energy (van Kerkwijk & Kaplan 2007).

For hydrogen atmospheres in magnetic fields of the order of 10^{13} G the strongest atomic transition, between the ground state and the lowest excited state, is expected at energy (Zavlin & Pavlov 2002):

$$\varepsilon_{\mathrm{H}} \sim 75\left[1 + 0.13\ln\left(\frac{B_{\mathrm{H}}}{10^{13}\,\mathrm{G}}\right)\right] + 63\left(\frac{B_{\mathrm{H}}}{10^{13}\,\mathrm{G}}\right)\mathrm{eV} \tag{1.5}$$

The corresponding magnetic field estimates B_{H} for the M7 are shown in Table 1.2, considering the central energies of the absorption lines and Eq. (1.5).

Magnetic field strengths can also be inferred from coherent timing solutions, assuming that the measured spin-down ($\dot{P}$) is caused by magnetic dipole braking. It hence provides a further observational constraint that can be confronted with estimates from absorption lines. For two cases, RX J0720.4-3125 (Kaplan & van Kerkwijk 2005a)[5] and RX J1308.6+2127 (Kaplan & van Kerkwijk 2005b), dedicated Chandra observations combined with other archival data allowed the determination of unambiguous phase-coherent timing solutions for a period of at least 5 years. The inferred magnetic fields, $B_{\mathrm{dip}} = 2.4 \times 10^{13}$ G and $B_{\mathrm{dip}} = 3.4 \times 10^{13}$ G, respectively, agree quite well with the intensities inferred from absorption lines.

On the other hand, characteristic ages $\tau_{\mathrm{ch}} = P(2\dot{P})^{-1}$ of 1.9 Myr and 1.5 Myr for RX

[5] See, however, Sect. 1.3.3.

J0720.4-3125 and RX J1308.6+2127 are much larger than would be expected based on cooling: from standard cooling curves (Page et al. 2004a), the observed temperatures correspond to ages of a few 10^5 yr. Even if it is considered that the blackbody temperature likely overestimates the effective temperature – as is clear from the measured "optical excess" (Sect. 1.3.2) – it is not likely to derive ages much in excess of 10^6 yr for the M7; at 1.5 Myr, the effective temperature should be below 20 eV (van Kerkwijk & Kaplan 2007). Furthermore, from proper motion measurements (Sect. 1.3.1.2), it is known that the characteristic ages overpredict by factors of ~ 3 and $\sim 1-2$ the kinematic travel times estimated for these two sources, which are inferred by tracing back the trajectories from their likely birth places (Motch et al. 2003; 2009).

From a detailed analysis using a large amount of data, van Kerkwijk & Kaplan (2008) constrained the spin-down rate of a third source, the X-ray brightest RX J1856.5-3754, and derived a most likely phase-connected solution. The pulsations of this source are so gentle (with fractional amplitude of $\sim 1\%$) that they were only recently discovered in a long XMM-Newton observation (Tiengo & Mereghetti 2007). The spin-down rate implies a magnetic field strength of $B_{\rm dip} = 1.5 \times 10^{13}$ G and a characteristic age of $\tau_{\rm ch} \sim 4$ Myr. However, while the source shows no evidence for the presence of absorption lines in its spectrum which could be used to confront the magnetic field estimate, these values are in contrast to other observational constraints that are available for RX J1856.5-3754. To begin with, an extended cometary-shaped Hα nebula was detected around the position of the source, whose apex is roughly aligned with the direction of motion of the neutron star (van Kerkwijk & Kulkarni 2001). Assuming that the emission nebula is caused by a bow-shock between the neutron star relativistic wind and its surrounding, as has been seen for several radio pulsars (e.g. Chatterjee & Cordes 2002), a magnetic field of similar intensity is inferred, $B_{\rm H\alpha} \sim 1.0 \times 10^{13}$ G; however, the spin-down luminosity $\dot{E}_{\rm H\alpha} \gtrsim 1.0 \times 10^{33}$ is much higher than that inferred from the timing solution, $\dot{E}_{\rm tim} \sim 3.0 \times 10^{30}$ erg s^{-1}. Moreover, the spectral modelling of the source from the optical to X-rays using a consistent description of the partially ionised neutron star atmosphere (Ho et al. 2007) gives a best-fit value of $B_{\rm atm} \sim (3-4) \times 10^{12}$ G, in order to explain the lack of absorption features (Sect. 1.3.2). Finally, the characteristic age is a factor of 10 higher than the kinematic age of the source, derived from the projected direction of motion on the sky and a likely birth place in Sco OB1 (Neuhäuser 2001, Walter 2001, Kaplan et al. 2002b).

Dedicated XMM-Newton observations of RX J2143.0+0654, the neutron star among the M7 with the highest estimated magnetic field value (inferred from an absorption line at energy 0.75 keV), were used to constrain the spin-down rate of the source (Kaplan & van Kerkwijk 2009). A small, marginally significant measurement of $\dot{P} = 4.1 \times 10^{-14}$ s s^{-1} implied a dipole magnetic field of $B_{\rm dip} = 2.0 \times 10^{13}$ G, similar to those derived for the other sources, but well below the cyclotron constraint, $B_{\rm cyc} = 1.4 \times 10^{14}$ G. As noted by Kaplan & van Kerkwijk (2009), the cyclotron interpretation ignores the suppression of spectral lines due to effects of vacuum polarization under magnetic fields in excess of 10^{14} G (Ho & Lai 2004).

In Table 1.3 the derived parameters for the M7 with timing measurements are listed. The total available spin luminosity, $\dot{E}$, is given by the rate of loss of the pulsar rotational kinetic energy, as a fuction of P and $\dot{P}$. The magnetic field $B_{\rm dip}$ and characteristic age $\tau_{\rm ch}$

Table 1.3: Timing parameters for some of the M7.

Source RX	P (s)	$\dot{P}$ ($10^{-14}\,\mathrm{s\,s^{-1}}$)	$\dot{E}$ ($10^{30}\,\mathrm{erg\,s^{-1}}$)	$B_{\rm dip}$ ($10^{13}\,\mathrm{G}$)	$\tau_{\rm ch}$ ($10^{6}\,\mathrm{yr}$)	Ref.
J1856.5−3754	7.06	2.97	3.3	1.5	3.8	(a)
J0720.4−3125	8.39	6.98	4.7	2.4	1.9	(b)
J1308.6+2127	10.31	11.20	4.0	3.4	1.5	(c)
J2143.0+0654	9.43	4.1	1.9	2.0	3.7	(d)

Ref.: [(a)]van Kerkwijk & Kaplan 2008, [(b)]Kaplan & van Kerkwijk 2005a, [(c)]Kaplan & van Kerkwijk 2005b, [(d)]Kaplan & van Kerkwijk 2009.

are inferred assuming spin-down by magnetic dipole radiation.

1.3.1.2 Proper motion studies

The fact that neutron stars are fast moving objects was realised shortly after the discovery of radio pulsars (Gunn & Ostriker 1970). Indeed, radio pulsars have much higher spatial velocity relative to standards of their progenitor population, the massive OB stars – the typical speeds being 400 km s^{-1} against 10 km s^{-1}, respectively. Although there is some consensus that asymmetries occuring in the core-collapse process during the supernova event are responsible for the kick imparted to the newly born neutron star, it is not clear what exact physical mechanism could give origin to such asymmetries. Possible processes include hydrodynamic or convective instabilities as well as asymmetric neutrino emission due to the presence of strong magnetic fields (see Lai et al. 2001; for a summary of possible mechanisms).

Proper motion studies of INSs are important for a number of reasons. First of all, accurate proper motion measurements (together with distance estimates) are crucial to population statistics of radio pulsar velocities (e.g. Hobbs et al. 2005). The physical mechanisms behind neutron star kicks generally only predict a limited range of velocities; therefore, pulsar velocities are used to test the most plausible ones. Many of these assume a correlation between the direction of spatial motion and spin axis which can be constrained for well studied cases such as the Crab (Kaplan et al. 2008; and references therein) and Vela pulsars (e.g. Helfand et al. 2001). Moreover, if high magnetic fields can produce asymmetric neutrino emission which results in extreme space velocities, then proper motions of magnetars may provide a direct probe of this interdependence (Kaplan et al. 2009a, De Luca et al. 2009). Proper motion determinations of young neutron stars can also provide a test for proposed associations between a given radio pulsar or AXP with a SNR, important for an independent age estimate that can be confronted with e.g. characteristic ages from spin-down and age of the remnant.

For the M7, proper motion determinations are a sensitive diagnostic of the X-ray powering mechanism as well as of population properties. First, the relative velocities with respect to the ISM place constraints on the contribution of accretion to the overall energy

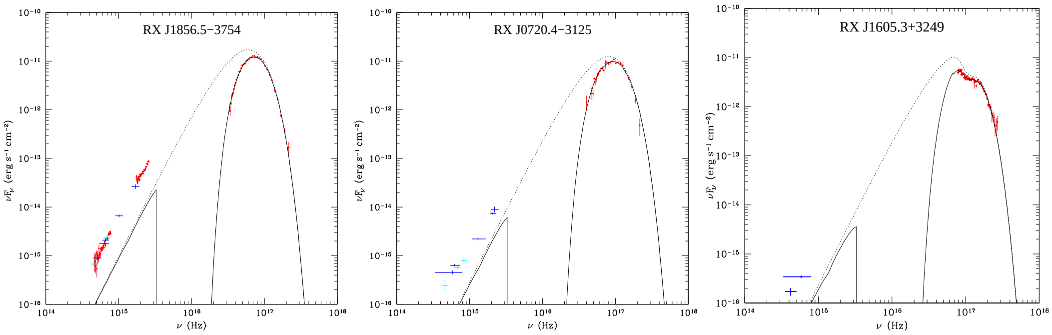

Figure 1.7: Spectral energy ditribution of three of the M7, showing clearly the *optical excess* relative to the blackbody extrapolation (from Kaplan 2008).

budget. Second, the reconstruction of backward trajectories allows an estimate of the kinematic age of the neutron star assuming a birth in the Galactic plane and more precisely in one of the nearby OB associations. The flight time can then be compared with the characteristic age derived from spin-down, revealing a possible non-standard braking mechanism or pointing towards a long spin period at birth. Finally, the kinematic age also constrains the cooling mechanism (Motch et al. 2009).

Proper motion measurements in the optical and in X-rays have established these objects as cooling, middle-aged ($\sim 10^5 - 10^6$ yr) neutron stars, probably originating in the nearby OB associations of the Gould Belt. The determinations lie in range 110 to 330 mas yr^{-1}, implying estimated transverse velocities[6] between 180 and 800 km s^{-1}. Even based on small number statistics, it seems likely that the velocity distribution of the M7 does not differ from that of the population of young radio pulsars (age $\leq 3 \times 10^6$ yr; see Chapter 2).

1.3.2 Understanding surface emission

Thermal emission from INSs is expected to originate immediately at the surface, with the bulk of the energy flux peaking in the soft X-ray band. In principle, by confronting the observed spectra and light curves with theoretical models for neutron star thermal radiation, it should be possible to derive the surface temperature, magnetic field, gravitational acceleration and chemical composition: if distances are known, then the stellar mass, radius and the equation of state (EoS) of neutron star interior could be constrained as well (Appendix A.1). However, initial attempts to model the observed spectra of the M7 have revealed that a single component could not describe the overall spectral energy distribution: the extrapolation of the (best-fit) blackbody model inferred from X-rays to optical wavelengths falls well below the actual detected fluxes: this is known as the “optical excess” (Fig. 1.7).

The overall spectrum has been modelled instead by the superposition of two blackbody components, which were used to describe the optical and X-ray data individually. Within this description, a small and hot emitting region ($kT_{\rm X}^{\infty} \sim 60$ eV and $R_{\rm X}^{\infty} \sim 5$ km, for

[6]However, one has to keep in mind that for most of the M7 accurate distances are not available.

RX J1856.5-3754, Burwitz et al. 2003) would be responsible for the X-ray flux whereas photons arriving from the cooler neutron star surface would be detected in the optical/UV bands ($kT^{\infty}_{\rm opt} \lesssim 30\,$eV and $R^{\infty}_{\rm opt} \gtrsim 18\,$km, again for RX J1856.5-3754; same reference). It was soon realised that these composite models could not work – at least for the case of the brightest member RX J1856.5-3754, since such temperature anisotropy on the surface should be easily detected as temporal intensity variations in the light curve[7], unless requiring either a particular geometrical orientation or strong gravitational deflection (Ransom et al. 2002).

Models of non-magnetized neutron star atmosphere also fail to describe the overall distribution of the sources, in this case overpredicting the optical flux (e.g. Pavlov et al. 2002). Gaseous atmospheres composed of elements heavier than hydrogen and helium seem to be unlikely, due to the lack of large numbers of features and the strong gravitational stratification forces – if any hydrogen is present, it must settle onto the outermost stellar layers. Indeed, light-element thin atmospheres on top of a condensed (blackbody-like) neutron star surface (Motch et al. 2003), which is partially ionized in presence of the rather strong magnetic field (Ho et al. 2007), seem to constitute the most promising route. Depending on the composition, a condensed surface is possible, in the range of expected temperature and magnetic field strengths (Medin & Lai 2007). These models were found to adequately reproduce the overall spectral distribution of the brightest sources RX J1856.5-3754 (Ho et al. 2007) and RX J0720.4-3125 (Pérez-Azorín et al. 2006), using a single component.

The conditions of formation of such a thin hydrogen atmosphere are briefly discussed by Motch et al. (2003) and, in more detail, by Ho et al. (2007). One possible scenario is accretion from the interstellar medium or from a fall-back disk. As noticed by Ho et al. (2007), unreasonable fine-tuning is needed to explain every single case, since the accretion rate onto different neutron stars would have to be finely adjusted in order to fit the required hydrogen layers (for instance, $\sim 0.8\,{\rm g\,s^{-1}}$ for RX J1856.5-3754, and $\sim 0.06\,{\rm g\,s^{-1}}$ for RX J0720.4-3125). Another possibility would be that the layer is a remnant from the formation of the neutron star. Due to the diffusive nuclear burning (Chang & Bildsten 2003), the thickness of a hydrogen envelope depends on the thermal history of the neutron star and the underlying stellar composition. However, since this process is extremely sensitive to temperature, it could well be that all available hydrogen at the surface of the neutron star is consumed early in its cooling history (Chang & Bildsten 2004). Moreover, the magnetic field can influence the lifetime of such a layer (higher magnetic fields decrease the envelope lifetime). Alternatively, the thin layer could be formed by a self-regulating mechanism that is driven by magnetospheric currents. Within this scenario, protons accumulate on the surface of the neutron star as a result of electromagnetic cascades impacting the surface due to acceleration of high energy particles, analogously to proton spallation of CNO elements in accreting systems. The formation of such a layer regulates the cessation of the process, since protons cannot further dissociate into stable nuclei. For magnetized surfaces, the thickness of the formed hydrogen layer may be in agreement with expectations from spectral modelling (see Ho et al. 2007; for details).

[7]Detailed phase-dependent spectral evolution studies, invoking an anisotropic temperature distribution based on polar caps with different temperatures and sizes, and not located at exact antipodal positions, have been carried out for other sources (e.g. Schwope et al. 2005, Zane & Turolla 2006).

As pointed out by van Kerkwijk & Kaplan (2007), Kaplan (2008), even if the unique determination of all astrophysical unknowns (abundances, temperature, magnetic field intensity, gravitational redshift) is difficult while investigating the thermal emission of a single source, one should aim for a self-consistent picture for this particular group of neutron stars – i.e. ideally, it should be possible to understand the spectra of the sources by adopting a single composition and, for a range of temperatures and magnetic field strengths, different ionisation states would be dominant or the formation of a condensate could be favoured, which would then explain the observed differences from source to source.

1.3.3 The long-term variability of RX J0720.4-3125

The second brightest source RX J0720.4-3125 is the only one among the M7 that has been shown to undergo long-term variations in its spectral parameters, at more or less constant flux. The change could be described as an increase in temperature, size of the emission region and equivalent width of the low-energy absorption feature (see spectral hardening in Fig. 1.8). This behaviour has been interpreted as possibly cyclic and related to the star precession (de Vries et al. 2004, Haberl et al. 2006, Hohle et al. 2009). Free precession with time scales of the order of months to years has been invoked for a few radio pulsars (e.g. Cordes 1993, Jones & Andersson 2001, Link 2003, Akgün et al. 2006). Precession occurs when the principal axes of a body (defined through the moments of inertia) revolve periodically around the angular momentum axis, as viewed in an inertial frame. To undergo free precession, a star must be deformed in some way, so that its shape and moment of inertia tensor differ from that of an unstressed fluid body. Such a deformation can be caused by stresses in the stellar crust and core and hence the study of precession can provide invaluable probes into the physics of neutron stars.

Haberl et al. (2006) argued that the time evolution of the spectral changes was consistent with a sinusoidal modulation with period 7.1 ± 0.5 yr and that the arrival-time residuals – obtained when the timing solution is subtracted from the photon arrival-times – could similarly show a cyclic behaviour, with a periodicity of 7.7 ± 0.6 yr. This period would provide evidence that the neutron star is precessing.

Alternatively, van Kerkwijk et al. (2007) suggested a different scenario, where the spectral changes are impulsive, with a sudden change on the neutron star surface accompanied with a simultaneous torque, caused by an accretion or glitch episode. This picture is motivated by the fact that, although the changes seem to be happening over the course of several years, the majority of the variation occurred over a time span of a few months, from May to October of 2003.

New XMM-Newton observations of the source (Hohle et al. 2009) showed that the inferred spectral parameters (kT, $R_{\rm em}$, EW) continue to change. However, they are not following the sinusoidal evolution originally suggested by Haberl et al. (2006) and the inferred timescale under the precession scenario might be longer, perhaps 9 to 12 years. As it is, present data cannot yet significantly constrain the possible precession periodicity and do not favour any of the proposed scenarios. In this respect, the timing solution derived for RX J0720.4-3125 (Kaplan & van Kerkwijk 2005a, van Kerkwijk & Kaplan 2007) might be regarded as preliminary since it depends on the future behaviour of the source; in particular,

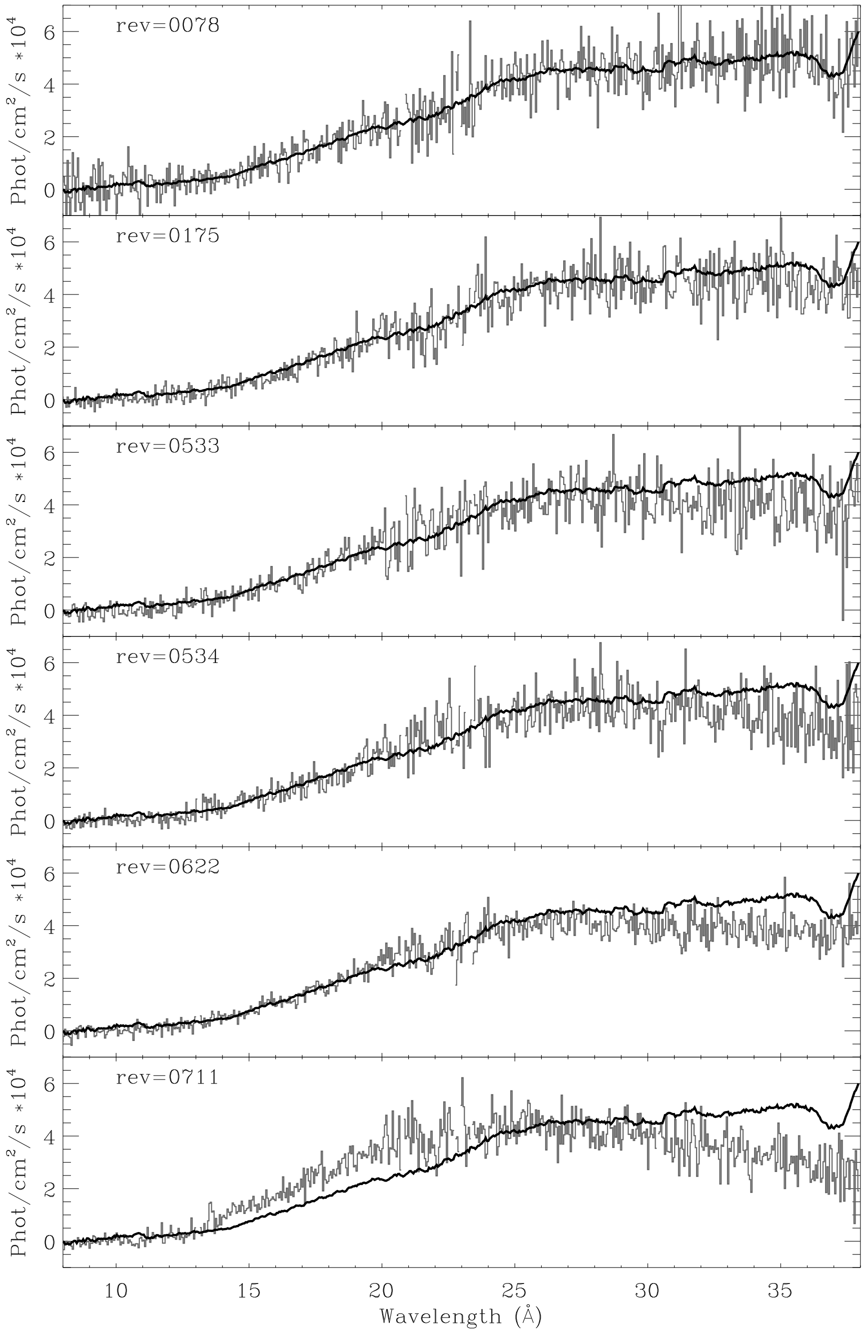

Figure 1.8: RGS spectra of RX J0720.4-3125 covering a period of 3 years (2000 to 2003). The observed spectrum (grey histograms) clearly shows a spectral hardening at more or less constant flux (the black line shows the smoothed spectra of revolution 0078; from de Vries et al. 2004).

as noted by Hohle et al., the phase residuals have trends that show opposite behaviours when more data are included.

1.4 The diversity of isolated neutron stars

The observed population of neutron stars is dominated by radio pulsars. In recent years, however, new and different observational manifestations of INSs have been discovered. While these subpopulations are fewer in number, they may have a significant impact on our understanding of neutron star properties and of matter at extreme physical conditions of gravity and magnetic field. In the following we discuss the current observational picture of INSs, the possible links between the subgroups and in which way population studies can bring information in order to address these issues.

1.4.1 Current observational picture of isolated neutron stars

Radio pulsars are divided into two main classes, the so-called "normal" pulsars with periods of the order of 0.1 to 1 s and the class of the fast-spinning *millisecond pulsars* (MSPs). Most MSPs (which comprise around 10% of the total pulsar population) are in binary systems, while only a few percent of the bulk of radio pulsars have a binary companion. These two main populations are easiliy identifiable in the histogram of Fig. 1.9, where the period distribution of all galactic isolated neutron stars catalogued in the ATNF database and of those with binary companions are plotted.

Other groups of isolated neutron stars include the *rotating ratio transients* (RRATs; McLaughlin et al. 2006, McLaughlin 2009), the magnetar candidates *anomalous X-ray pulsars* and *soft γ-ray repeaters* (AXPs and SGRs; Woods & Thompson 2006, Mereghetti 2008, Hurley 2009), the group of the *Magnificent Seven* or *X-ray dim isolated neutron stars* (XDINS, as they are also referred to), the *central compact objects* in supernova remnants (CCOs; Pavlov et al. 2004, de Luca 2008) and the *high magnetic field radio pulsars* (HBP-SRs). In the following we describe the most important features of these different subgroups of INSs. For that, we first provide a brief description of the evolution of rotation-powered pulsars in the framework of the magnetic dipole braking theory, in order to introduce the relevance of the $P-\dot{P}$ diagram in the classification of observed pulsars and isolated neutron stars.

1.4.1.1 Evolution of rotation-powered pulsars

Pulsars slow down as a consequence of the loss of rotational kinetic energy due to magnetic dipole radiation and acceleration of relativistic particles. The spin-down rate can be expressed as:

$$\dot{P} = \kappa P^{2-n} \tag{1.6}$$

where κ depends on the magnetic field strength at the stellar surface and the neutron star moment of inertia I; n is the so-called braking index. If κ and n are assumed to be constant,

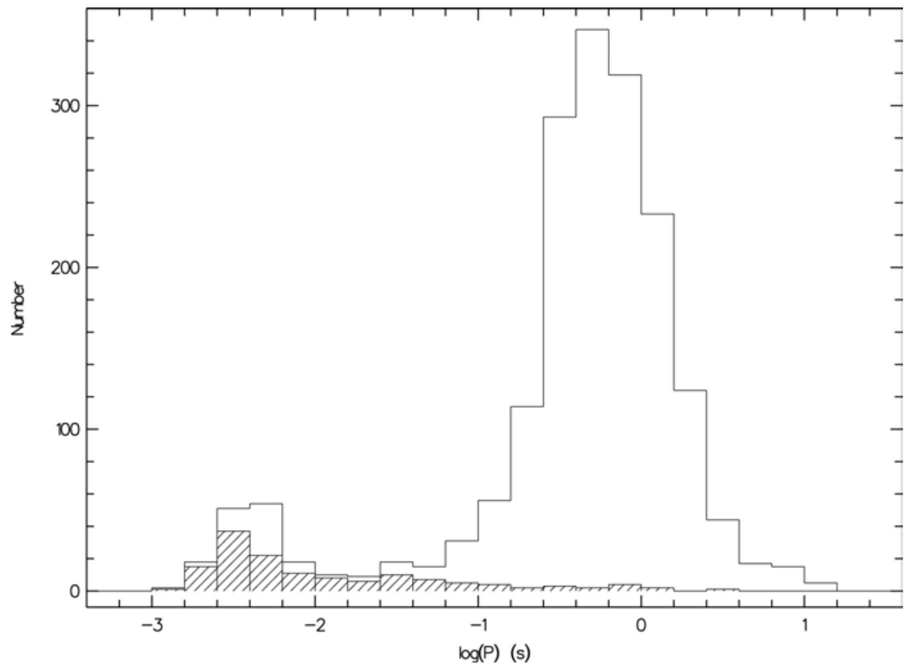

Figure 1.9: Histogram of observed pulsar periods from the ATNF catalogue. Pulsars in binaries are highlighted by hatched lines.

then the braking index can be determined from a measurement of the second time derivative of the period, according to:

$$n = 2 - P\ddot{P}\dot{P}^{-2} \tag{1.7}$$

Integrating Eq. (1.6) above, one finds the pulsar age:

$$\tau = \frac{P}{(n-1)\dot{P}}\left[1 - \left(\frac{P_0}{P}\right)^{n-1}\right] \tag{1.8}$$

where P_0 is the initial spin period of the pulsar. Assuming that the losses are due to pure magnetic dipole braking in vacuum, then $n = 3$ and the constant κ can be written:

$$\kappa = \frac{8\pi^2 B^2 R^6 \sin^2\alpha}{3Ic^3} \tag{1.9}$$

where α is the inclination angle of the dipole magnetic field axis relative to the spin axis. If the neutron star is born rotating much faster than the value at the present time, $P_0 \ll P$, the age in Eq. (1.8) reduces to the so-called pulsar "characteristic time" τ_{ch} for dipole braking, i.e.:

$$\tau_{ch} = \frac{P}{2\dot{P}} \tag{1.10}$$

For the pulsars with measured $\ddot{P}$, n is usually less than 3, indicating that pulsars do not lose energy like perfect dipole rotators in vacuum. In this regard, τ_{ch} overestimates the

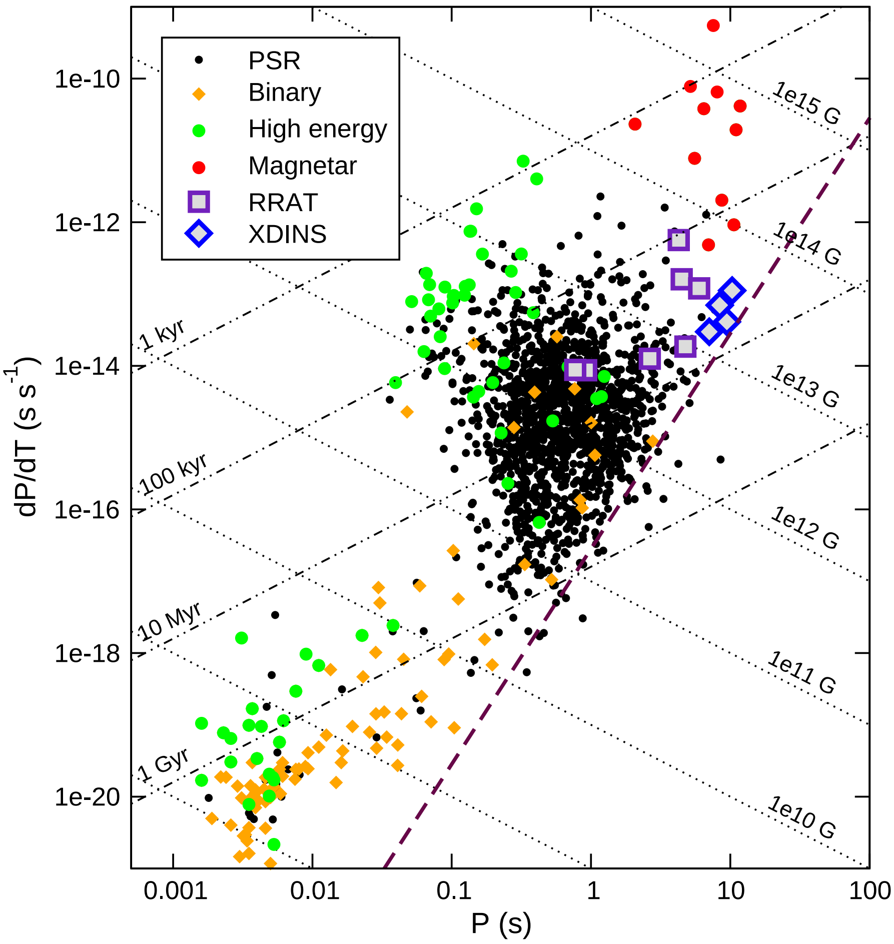

Figure 1.10: $P - \dot{P}$ diagram of pulsars catalogued in the ATNF database. The majority of objects are "normal" radio pulsars (black circles). Pulsars in binaries are denoted by orange diamonds whereas those detected at high energies by green circles. The subgroups of magnetars, XDINS and RRATs can also be seen as red circles, blue filled diamonds and purple filled squares. Lines of constants $B_{\rm dip}$ and $\tau_{\rm ch}$ are plotted with labels, as well as the so-called pulsar "death line" as a thick hashed line.

pulsar true age. The strength of the magnetic field at the neutron star surface can also be estimated, assuming further $\alpha = 90°$ and $I = (2/5)MR^2 \sim 10^{45}\,\mathrm{g\,cm^2}$ (for neutron star canonical mass and radius of $M = 1.44\,\mathrm{M}\odot$ and $R = 10\,\mathrm{km}$):

$$B_{\rm dip} = 3.2 \times 10^{19} (P\dot{P})^{1/2}\ \mathrm{G} \tag{1.11}$$

The loss of rotational kinetic energy can be estimated in a model-independent way, only by means of measuring the pulsar spin period and period derivative:

$$\dot{E} = 4\pi^2 I \frac{\dot{P}}{P^3} \tag{1.12}$$

which, considering again $I = 10^{45}\,\mathrm{g\,cm^{-2}}$, can be written in usual units as $\dot{E} = 4.5 \times 10^{46}(\dot{P}P^{-3})\,\mathrm{erg\,s^{-1}}$.

In the magnetic dipole braking scenario, pulsars are expected to evolve through rotational energy loss towards longer periods. Depending on a combination of the magnetic field strength and period, radio emission is expected to turn off when the pulsar can no longer produce electron-positron pairs. This is generally approximated by the equation of Bhattacharya et al. (1992):

$$\frac{B}{P^2} = 0.17 \times 10^{12}\ \mathrm{G\,s^{-2}} \tag{1.13}$$

Although $\tau_{\rm ch}$ and $B_{\rm dip}$ depend on the validity of the simplifying assumptions discussed above, P and $\dot{P}$ provide useful estimates of important neutron star properties. In this fact resides the utility in population studies of INSs of the so-called $P - \dot{P}$ diagram, which we show in Fig. 1.10.

The two main pulsar populations discussed before cluster in well defined, different regions of this diagram, as do other subgroups such as magnetars, pulsars detected at high energies and XDINS. The positions of the seven RRATs for which the period derivative is known overlap regions occupied both by standard radio pulsars, XDINS and magnetars. Lines of constant characteristic age and magnetic field (under the assumption of magnetic dipole braking model) can be seen in the diagram. The pulsar "death line" below which radio emission is expected to cease is also plotted; one can see that several pulsars presently observed occupy "forbidden" regions of the diagram. Therefore, the death line modelled by Eq. (1.13) shall not be taken at face value.

1.4.1.2 Millisecond (recycled) pulsars

Millisecond pulsars are characterised by very fast rotation, $P \lesssim 50\,\mathrm{ms}$, and low magnetic fields, $B_{\rm dip} \lesssim 10^{10}\,\mathrm{G}$; as so, they occupy the lowest left region of the $P - \dot{P}$ diagram. As can be seen in Fig. 1.10, most of them are in binary systems and many are detected at high energies. They are believed to be relatively old pulsars, with $\tau_{\rm ch} = 0.1 - 10\,\mathrm{Gyr}$, which have been spun up to millisecond periods by angular momentum transfer due to accretion of matter from an originally less massive companion during a late epoch in their lives (e.g Bhattacharya & van den Heuvel 1991). Their low magnetic fields could be explained by Ohmic and/or accretion-induced decay (Cumming 2008). Accretion is therefore thought to be responsible for "recycling" these old pulsars: first, by spinning up the pulsar so radio emission is turned on again once the pulsar is on the left side of the death line; second, by heating areas of the neutron star surface – polar caps or hot spots – which can then emit X-rays. About three quarters of the MSPs are associated with globular clusters, due to the high rate of exchange interactions that occur in the core of these dense gravitational systems. For most of them, the bulk of the high energy radiation is thermal, originating from the hot spots, but a few exhibit almost pure non-thermal X-ray emission believed to be generated in the pulsar magnetosphere. X-rays can also be emitted from shocked pulsar winds with that of the binary companion (see e.g. Zavlin 2007, Grindlay & Bogdanov 2009, Harding 2009).

A schematic view of binary evolution leading to the formation of MSPs either in binaries or in isolation can be seen in the sketch of Fig. 1.11. Basically, the original stellar masses and the fraction of mass ejected in the supernova event mainly determine the final stage of these binary systems. If the system remains bound after the (first) supernova explosion, it can be detected as either a low-mass or high-mass X-ray binary once accretion from the originally less massive star onto the neutron star sets in. Observed radio pulsars in binaries with very eccentric orbits are thought to be the survivors of such explosions. If the secondary star is massive enough, it will also undergo a supernova explosion and, in this case and if the system is not again disrupted, the pair forms a double neutron star system. This kind of system is a natural laboratory for testing theoretical predictions of general relativity, such as the orbital decay through emission of gravitational waves, as in the famous case of the Hulse-Taylor system (Hulse & Taylor 1975). If the secondary is not sufficiently massive, it will transfer mass on a much longer timescale. Tidal forces will tend to circularize the binary orbit and the neutron star will accrete matter and angular momentum at the expense of the orbital angular momentum. Numerous examples of these MSP-white dwarf systems are currently known (for references, see e.g. Lorimer 2008).

1.4.1.3 Magnetars

Two observational manifestations of X-ray pulsars, the AXPs and SGRs, are included in the class of magnetars. In contrast to rotation-powered pulsars, magnetars are INSs thought to be powered by the decay of a strong magnetic field, which is by definition in excess of the quantum critical value of 4.4×10^{13} G (see Sect. 1.3.1.1). Known magnetars display field strengths[8] which are a factor of 10 to 100 times those observed in standard radio pulsars. They can be recognized in the upper right part of the $P - \dot{P}$ diagram in Fig. 1.10.

The two subgroups were independently discovered through different manifestations of their high energy emission. SGRs were originally thought to be a subclass of γ-ray bursts since they were first discovered through the detection of short bursts in the hard X-ray/soft γ-ray band. AXPs, on the other hand, were discovered at soft X-ray energies and were thought to be accreting neutron stars. Further optical/IR/X-ray observations have excluded however the presence of binary companions and have revealed much of the complex and "anomalous" observational behaviour of these pulsars. The observation of the persistent X-ray counterparts of SGRs have allowed these two originally independent subgroups to be linked in one class of peculiar INSs. In particular, AXPs and SGRs show similar luminosities[9], burst behaviour, periods and period derivatives, although SGRs usually have harder spectra below 10 keV.

Magnetars are characterised by an X-ray luminosity of 10^{34} to $10^{36}\,\mathrm{erg\,s^{-1}}$, which is in excess of the spin-down power; they show long spin periods in a narrow range of 2 to 12 s, very short spin-down characteristic times of 10^3 to 10^5 yr and variability at different timescales. The phenomenology of magnetars is complex and includes the emission of giant flares, bursts with the presence of bright spectral lines and QPOs, glitches, timing

[8] Under the magnetic dipole braking model.

[9] There is however some evidence that SGRs might be slightly more luminous than AXPs; see e.g. Mereghetti (2008).

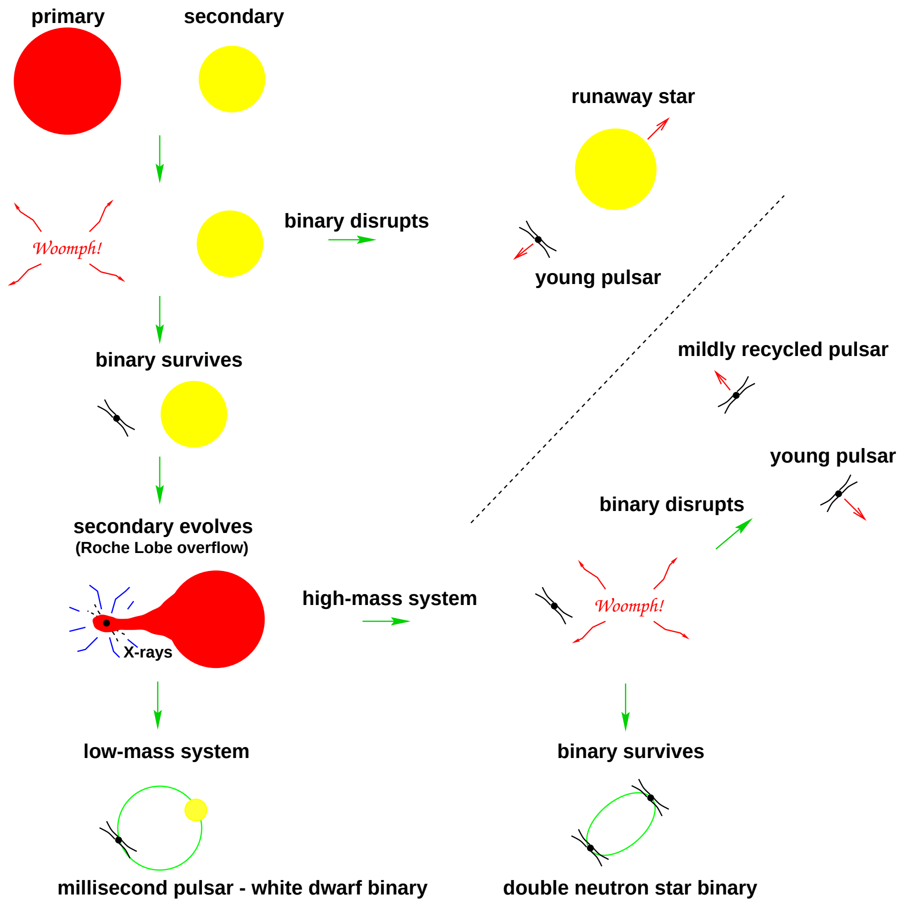

Figure 1.11: Sketch of binary evolution leading to the formation of millisecond radio pulsars either in binary or in isolation (see text for details; from Lorimer 2008).

noise, multiwavelength variability and pulse profile changes. The characteristic distances are a few kiloparsecs and they are mainly distributed in the Galactic plane (therefore, their X-ray emission is highly absorbed). Three transient AXPs and one transient SGR have also been observed. Optical and IR counterparts have been identified for a number of sources. In several cases, an association with a supernova remnant is likely. The majority of them are radio-quiet; only recently the radio emission of a few transient magnetars has been detected (Camilo et al. 2006; 2007). At variance with normal radio pulsars, the radio emission of magnetars has so far been characterised by highly variable fluxes, flatter spectra and varying pulse profiles with time, indicating that the radio emitting regions are more complex than dipolar open field emission. Giant flares seen in SGRs are considered the most compelling evidence for the presence of high magnetic fields.

Below 10 keV, the X-ray spectra of magnetars are usually described by a combination of a blackbody of temperature $kT \sim 0.5$ keV and a steep power-law with photon index $\Gamma \sim 3-4$, although in some cases double blackbodies give fits of similar quality. At these X-ray energies, the emission is believed to be mostly of thermal origin. In addition to the soft X-ray spectrum, a significant flux above 20 keV in the persistent emission of AXPs and SGRs has been detected with INTEGRAL, implying that the luminosity of these objects is dominated by the non-thermal emission (e.g. Kuiper et al. 2004, den Hartog et al. 2006).

The formation of the high magnetic fields is generally understood in the context of the turbulent dynamo amplification that might occur either in the differentially rotating proto-neutron star or in the convective layers of its progenitor star (Thompson & Duncan 1993). Alternative models are based on accretion from fossil disks (e.g. Alpar 2001). In contrast to the magnetar scenario, such models have been proposed to explain several of the peculiar manifestations of AXPs without invoking the presence of a high magnetic field. The accretion scenario is however less favoured relative to the magnetar model due to the fact that the former would imply the observation of a disk component in the optical and NIR wavelengths. Indeed, the observation of a mid-IR counterpart of the AXP 4U 0142+61 with the Spitzer Space Telescope has been interpreted as evidence for the presence of a cool dust disk around the neutron star (Wang et al. 2006b); however, the disk is believed to be truncated at an inner radius of $\sim 3\,R_\odot$ and be rather passive and reprocessing the X-ray emission from the pulsar. Another criticism of the accretion model with residual disks is that they cannot easily account for observed phenomena of bursts and flares. Magnetars might also possess a twisted magnetosphere which would be responsible for the main differences between magnetars and high magnetic field pulsars; in particular, it would explain the presence of the hard tails seen by INTEGRAL (Thompson & Beloborodov 2005).

The origin of high magnetic fields in magnetars has also been investigated under the so-called *fossil field hypothesis*, where magnetars are the remnants of massive and highly magnetized progenitor OB stars. This scenario is motivated firstly by the fact that several AXPs and SGRs are associated with massive star clusters, implying progenitor masses as high as $40\,M_\odot$ (e.g. Muno et al. 2006, Figer et al. 2005, Corbel et al. 1999, Klose et al. 2004). Secondly, there is increasing evidence that more massive main-sequence stars tend to have higher magnetic fluxes than less massive ones (e.g. Petit et al. 2008). Fossil magnetic fluxes may therefore already be present in stellar cores prior to collapse, which favours the formation of super strong magnetic fields either by magnetic flux conservation or by the dynamo mechanism.

1.4.1.4 Rotating radio transients

RRATs are a group consisting originally of 11 transient radio sources that have been discovered in a single dispersed pulse search by McLaughlin et al. (2006), carried out in the 1.4 GHz PMPS data. Due to the transient behaviour of their pulsed emission, these sources have escaped detection in previous radio pulsar searches that only apply standard FFT algorithms. Very recently, in a reprocessing of the PMPS data optimized for the finding of more RRATs, Keane et al. (2009) identified 10 new transient objects which have been confirmed by follow-up observations. It is clear that the inclusion of single pulse searches in radio pulsar survey data can significantly increase the number of known RRATs (see e.g. Hessels et al. 2008, Deneva et al. 2009b). This implies that the population of RRATs might be even larger than initially thought, an issue that we address further in Sect. 1.4.2.

The properties of the sources vary widely. Bursts of radio emission are seen with typical durations of a few milliseconds and occur at intervals ranging from minutes to a few hours. Radio intensities are rather bright with peak flux densities of 0.1 to 10 Jy. Investigations of the bursts' times-of-arrival have revealed underlying periodicities which indicate that RRATs are neutron stars rotating with relatively long spin periods in the range of 0.7 to 7 s. The sources are concentrated in the Galactic plane at distances between ~ 2 to 7 kpc from the Sun and their spatial distribution seems consistent with that of the normal radio pulsar population.

Period derivatives are currently available for seven RRATs (McLaughlin et al. 2009); hence, the usual pulsar properties ($\dot{E}$, $B_{\rm dip}$ and $\tau_{\rm ch}$) can be derived for these sources. The ranges of inferred spin-down luminosities, characteristic ages and magnetic field intensities[10] are 10^{31} to 10^{33} erg s^{-1}, 10^5 to 10^6 yr and 2.7×10^{12} to 5.0×10^{13} G, respectively. As it is, RRATs occupy a somewhat wide region of the $P-\dot{P}$ diagram (Fig. 1.10), which overlaps that of a typical radio pulsar as well as those of the peculiar XDINS and magnetars. Three out of seven of these RRATs have magnetic fields in excess of 10^{13} G; two exhibit long periods and large characteristic ages and therefore lie near the pulsar death line. The remaining two RRATs, in spite of their transient nature, display properties that cannot be distinguished from those of the bulk of normal radio pulsars.

The nature of these sources and the mechanism behind the transient radio emission are not well understood. Some authors have suggested that RRATs are neutron stars that are near the radio emission death line (Zhang et al. 2007). Redman & Rankin (2009) proposed that the radio mechanism might be the same as that behind radio pulse nulling (Sect. 1.2.1). Alternatively, the intermittent emission could also be a consequence of the presence of a circumstellar asteroid belt around the pulsar (Cordes & Shannon 2008). Interestingly, Weltevrede et al. (2006) showed that if the nearby middle-aged pulsar PSR B0656+14 – one of the "Three Musketeers" which is located at ~ 230 pc (Becker & Truemper 1997; see Sect. 3.4.1.2) – were more distant, its burst behaviour would appear similar to those of the RRATs. Keane et al. (2009) explored this idea further, computing the distance boundary at which a known RRAT would have to be placed in order that its transient emission be detected as standard (continuous) pulsar emission, under the assumption that RRATs emit pulses as a power-law function of radio density flux. They concluded that the RRAT emission could be explained as coming from distant ordinary pulsars if the power-law is steep enough; however, this is unlikely to explain all the transient sources if the previous assumption is not valid.

The most active source among the known sample of RRATs is the highly magnetized J1819-1458. At 1.4 GHz it exhibits bursts of radio emission with peak flux density as high as 10 Jy every 2 to 3 min. This high burst rate allowed the determination not only of the RRAT timing solution, placing it right below the locus occupied by magnetars in the $P-\dot{P}$ diagram, but also made possible the determination of an accurate celestial position. As a result, its X-ray counterpart was soon serendipitously discovered in a Chandra observation of the young SNR G15.9+0.2, which is located only $\sim 11'$ away from the RRAT source (Reynolds et al. 2006, Gaensler et al. 2007). Very interestingly, the X-ray source was found to display the same characteristics of a cooling middle-aged neutron star as do the

[10] These last two properties assuming magnetic dipole braking model.

M7. From its radio emission, a characteristic age of $\tau_{ch} = 1.2\times10^5$ yr and a DM distance of $d = 3.8$ kpc are derived. Taking these at face value, the RRAT is expected to be somewhat younger and much more distant than the seven XDINS.

McLaughlin et al. (2007) established the proposed association by means of a dedicated XMM-Newton observation, which confirmed the thermal nature of the X-ray counterpart and unveiled the neutron star spin at the same period as derived from the radio data, $P = 4.26$ s. The pulsed fraction was found to be large, at 34%; in comparison, the neutron star among the M7 with the largest pulsed fraction is RX J1308.6+2127, with $p_f = 18\%$. Similarly to several of the M7, the X-ray spectrum is best fitted by an absorbed blackbody with the addition of a broad absorption feature. The blackbody temperature is however hotter, with $kT = 0.14$ keV, and the central line energy is harder, at ~ 1 keV ($0.3-0.5$ keV). If interpreted as a protron cyclotron absorption, as for the cases of the M7, then the derived magnetic field, $B_{cyc} \sim 2\times10^{14}$ G, is higher than that derived through timing assuming magnetic dipole braking, $B_{dip} = 5\times10^{13}$ G. The analysis of a recent Chandra ACIS-S observation (Rea et al. 2009) confirmed the spectral results of McLaughlin et al. (2007). Rea et al. (2009) also reported evidence for the detection of extended X-ray emission around the RRAT, a possible nebula powered by the pulsar. In spite of recent X-ray searches with Chandra, no X-ray counterpart was found for two other RRATs with longer characteristic times relative to J1819-1458 (Kaplan et al. 2009b).

Also very recently, two unusual glitches that occured over a timescale of five years were reported for this RRAT (Lyne et al. 2009). A glitch is a sudden increase in the rotational frequency of a spinning neutron star, followed by a period of gradual recovery, generally lasting from days to years, where the observed spin period tends to its value before the glitch. Glitches are not completely understood theoretically but are thought to be caused by coupling effects and resulting transfer of angular momentum occuring in the boundary between the neutron star core and crust. Although the glitch magnitude detected in the RRAT is similar to what is observed for radio pulsars and magnetars, the aftermath was an unusual and significant decrease in the spin-down rate, which corresponded to a downward vertical movement of the source in the $P-\dot{P}$ diagram. The dramatic conclusion is, if such glitches occur at a frequency of a few tens of years, the spin-down rate could drop to zero in a timescale of thousands of years and, as a consequence, so could the dipole magnetic field. This would imply that J1819-1458 was originally in the magnetar region of the diagram in the early stages of its life as a neutron star.

1.4.1.5 Central compact objects in SNRs

The highly energetic Crab pulsar[11], with its strong multiwavelength pulsed emission caused by non-thermal process in its magnetosphere, had been regarded for many years as the typical example of a young neutron star of age $\sim 10^3$ to 10^4 yr. This idea has dramatically changed with the discovery of CCOs. CCOs were first observed as faint, point-like, radio-quiet X-ray sources located near the geometrical center of supernova remnants. At present, a total of six sources are usually considered to belong to this group although it is not

[11] As well as the so-called "Crab-like" pulsars, see e.g. Becker & Pavlov (2002), Becker (2009); for reviews

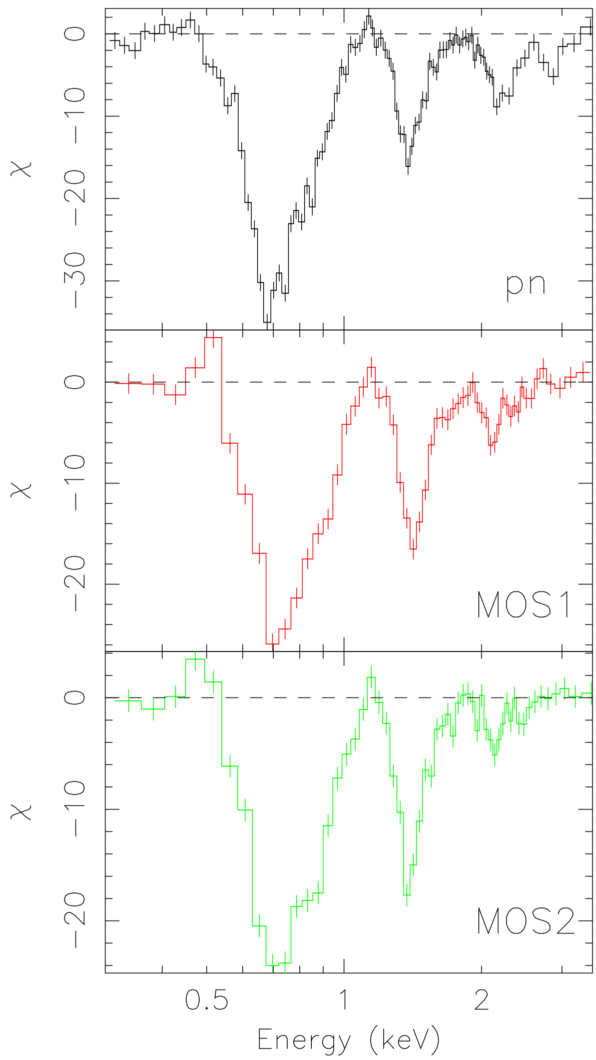

Figure 1.12: Residuals of observed XMM-Newton spectra of the CCO 1E 1207.4-5209 relative to the best-fit continuum model (De Luca et al. 2004). Evidence for harmonically related absorption lines can be seen.

clear whether or not they consist of an homogenous class or even if they should indeed be regarded as a separate subgroup of INSs among the known Galactic population.

Other than being located near the center of SNRs with ages $\leq 10^4$ yr and being quiet at radio wavelengths, the six sources have in common an X-ray luminosity in the range 10^{33} to 10^{34} erg s^{-1} and X-ray spectral properties remarkably different from those of other young rotation-powered pulsars detected at high energies. In general, the X-ray spectra of CCOs are modelled by two blackbody components with temperatures in the range $kT_\infty = (2-7)\times10^6$ K and small sizes of the redshifted emitting areas of $R_\infty = 0.3-5$ km. Spectral absorption lines have been detected in the spectra of one of the sources, 1E 1207.4-5209 (located in the SNR PKS 1209-51/52), with evidence of them being harmonically related at energies 0.7 keV, 1.4 keV, 2.1 keV and 2.8 keV (De Luca et al. 2004), which can be seen in Fig. 1.12. Interpreting these lines in the framework of electron cyclotron absorption yields a significantly low magnetic field strength of $\lesssim 10^{11}$ G.

On the other hand, the six sources show different temporal behaviour. While most of the CCOs exhibit a rather stable X-ray flux at the $5 - 10\,\%$ level, one of the sources, 1E 1613-5055 in RCW 103, shows significant X-ray flux variations and is probably orbiting a low-mass companion in an eccentric binary system with an orbital period of ~ 6.7 h (De Luca et al. 2006). For the other three sources, X-ray pulsations in the range 0.11 to 0.42 s, identified with the neutron star spin period, have been detected. These sources seem to display very stable timing properties with no strong evidence for spin-down over timescales of a few years. This fact implies that these CCOs might have low magnetic field intensities and may have been born rotating at a period close to the present values, again in contrast with the standard picture for rotation-powered pulsars.

1.4.1.6 High magnetic field radio PSRs

The count of radio pulsars with known large inferred dipolar magnetic fields, in excess of 10^{13} G, has been steadily growing in number in recent years. In particular, there are at present a few examples of radio pulsars with magnetic fields in excess of the quantum critical value and yet they do not manifest themselves as magnetars and are not detected at high energies (e.g. McLaughlin et al. 2003; for the very extreme case of PSR J1847-0130). The sources rotate more slowly than ordinary pulsars, tend to be young, with typical characteristic ages up to 10^5 yr, and are located at great distances of several kiloparsecs. Those detected in X-rays are usually faint with the exception of very young sources (ages up to few kiloyears) which show high spin-down luminosities in the range 10^{36} to 10^{37} erg s^{-1}, sometimes powering a pulsar wind nebula. In these cases, the X-ray emission is non-thermal. The other sources detected in X-rays show either thermal and/or non-thermal emission, with X-ray luminosities much fainter than their spin-down power (e.g. Gonzalez et al. 2007, Zhu et al. 2009).

1.4.2 Relations to other groups of isolated neutron stars

The evolution of neutron stars in binaries is considerably affected by mass transfer episodes during periods of close interaction with the companion star. Therefore, the phenomenology of MSPs should not be taken into account when one is interested in the observational manifestations of neutron stars that are as much as possible unaffected by external factors. The properties exhibited by magnetars and ordinary radio pulsars might then be considered the two extreme observational behaviours of the known INS population.

The observational picture discussed above hints at the idea that the magnetic field is the primary characteristic determining the general behaviour of the different manifestations of neutron stars. In particular, the very complex phenomenology exhibited by AXPs and SGRs might very likely be caused by their enormous inferred magnetic fields. Interestingly, Pons et al. (2007a) derived a $T \propto B^{1/2}$ correlation for INSs with both a measurement of the dipolar magnetic field and a blackbody temperature derived from X-ray fits, which they

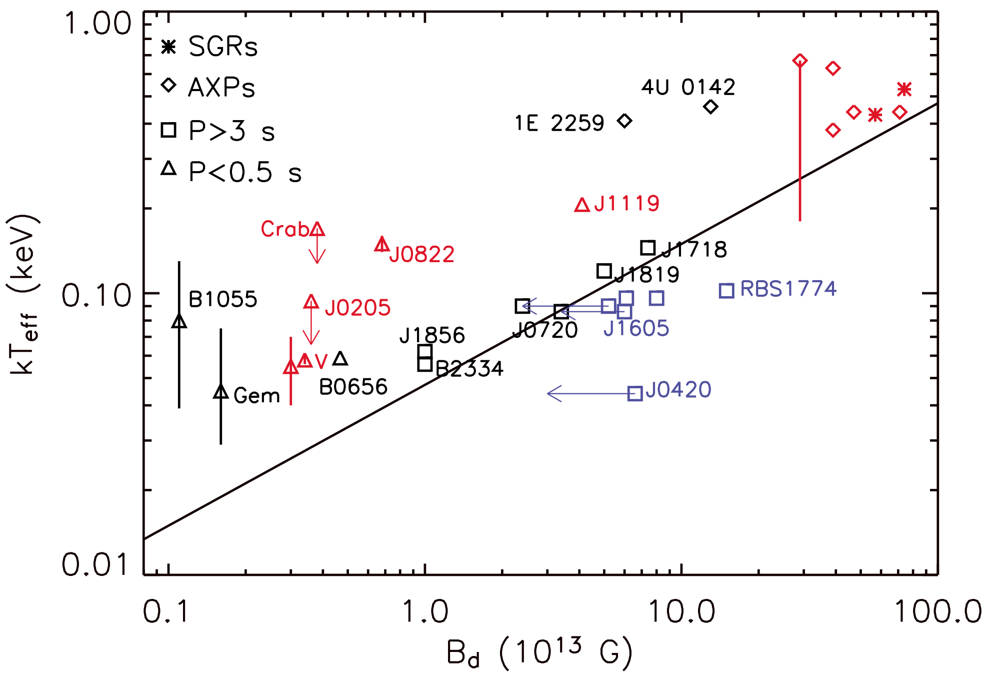

Figure 1.13: Correlation between neutron star temperature and dipolar magnetic field intensity. Magnetar objects SGRs and AXPs are denoted by stars and diamonds, respectively; squares are slowly spinning INSs, $P > 3$ s, whereas triangles are fast spinning INSs, with periods less than 0.5 s. Young neutron stars are represented in red. Magnetic fields estimated from cyclotron lines are shown in blue (from Pons et al. 2007b).

interpreted as a consequence of heating of the neutron star crust through magnetic field decay (Fig. 1.13).

Aguilera et al. (2008) investigated this scenario further by means of 2-d simulations that took into account the anisotropic heat transport and the relevant neutrino emission processes in the inner layers of magnetized neutron stars, in an attempt to find a self-consistent picture suitable to explain the observations. They concluded that magnetic field decay provides an additional source of heating of the neutron star crust that dramatically changes the cooling history of neutron stars with $B \gtrsim 10^{13}$ G. However, the overall picture is much more complex since the observed sample includes several counterexamples of objects that, by their timing parameters only, were expected to show different emission properties than those actually displayed, as in the case of e.g. PSR J1847-0130.

The regions in the $P - \dot{P}$ diagram occupied by the several new subgroups show considerable overlaps with the two extreme classes of magnetars and ordinary radio PSRs. The discovery of RRATs, in particular, is intriguing since these transient radio sources have so far manifested themselves in a variety of ways. The different objects show timing characteristics of either normal radio sources or of a possibly dormant/transient or old magnetar, not to mention that the only source so far detected in X-rays shares unique spectral properties with the radio-quiet M7. In this regard, it seems likely that several of the proposed physical mechanisms mentioned in Sect. 1.4.1.4 are required to explain all the transient sources and the totality of distinct burst behaviours. This would imply that there is no unifying scenario that can account for all of their properties and that the intermitent radio emission might be due to factors both intrinsic and extrinsic to the neutron star as well as to selection biases. With the increasing number of detected new sources, these issues can be addressed and new scenarios can be proposed to explain their unusual radio emission.

On the other hand, the seven nearby XDINS seem to form a rather homogenous class of cooling neutron stars. In particular, the sources show very similar timing and spectral behaviour, with a few exceptions: namely the long-term spectral variations of RX J0720.4-3125 and the absence of absorption lines in the spectra of RX J1856.5-3754. Nonetheless, it is striking that a group of very similar sources, displaying at the same time unique properties that are so different from ordinary radio pulsars, are detected in the very local Solar vicinity, which we discuss further in Sect. 1.5.

The locus occupied by the M7 in the $P - \dot{P}$ diagram is somewhat intermediate between radio pulsars and magnetars and suggests, as for the RRATs, that they could be linked to them. In particular, the similar spin periods and intense magnetic fields raised the possibility that some of the M7 could have evolved from the younger and more energetic magnetar objects (Heyl & Kulkarni 1998). Aguilera et al. (2008) showed that the range of observed temperatures of the M7 is consistent with them being born as magnetars with $B \sim 10^{14} - 10^{15}$ G, provided that their current ages are around 10^6 yr (which is in rough agreement with their age estimates).

Alternatively, if the neutron star magnetic field has not changed substantially over its lifetime, an evolutionary link with the HBPSRs may be suggested (e.g. Zane et al. 2002). Relative to the M7, these objects are generally located at much greater distances and show considerably higher spin-down luminosity. However, if the HBPSRs are a factor of ~ 100 younger, then the difference in $\dot{E}$ may be explained within the standard scenario for pulsar evolution under magnetic dipole braking (Kaplan 2008). With time, the residual thermal emission from the surface is expected to become the dominant source of X-ray emission, once $\dot{E}$ has dropped to values sufficiently low so that the non-thermal power-law component seen in the spectra of HBPSRs and radio pulsars no longer "hides" the thermal emission. The M7 could then be nearby long-period radio pulsars for which the narrow emission beam simply does not sweep over the Earth. This scenario does not seem to be in disagreement with the recent very deep radio limits obtained by Kondratiev et al. (2009) (Sect. 1.3). These authors estimated that at least 40 sources similar to the M7 are required in order that at least one is beamed towards the Earth at the 1σ confidence level. In other words, considering their narrow emission beams (a correlation with long spin periods), the probability that all six sources for which P is known are beamed away from the Earth could be high, up to $\sim 80\%$.

1.5 Searches and population studies

In the light of the newly discovered manifestations of INSs, a point of crucial importance for the ensemble of the Galactic neutron stars is to assess the relative contributions of the various subgroups to the total number of objects populating the Milky Way. A natural side effect of this point is the investigation of the possible links between the subgroups, a subject of high interest on its own (Sect. 1.4.2). If each subgroup is treated independently, a likely consequence is that the Galactic core-collapse supernova rate cannot account for the entire estimated population of neutron stars, an issue recently considered by Keane & Kramer (2008). For instance, both the poorly constrained populations of RRATs and XDINS are estimated to outnumber ordinary radio pulsars whereas these alone are sufficient to account for the total number of past Galactic core-collapse supernovae estimated from the measurements of Diehl et al. (2006) (Sect. 1.2).

Translating into numbers, while the core-collapse supernova rate in the Galaxy is inferred to be around 1.9 ± 1.1 events per century, PSRs, XDINS and RRATs have estimated birthrates of roughly 2.8, 2.1 and 5.6 objects per century[12], respectively, which amounts to ~ 11 core-collapse supernovae occuring every 100 years in order to account for all the subpopulations in an unrelated fashion. With the discovery of more RRATs, Keane et al. (2009) estimated that their birthrate might even be larger, up to four times that of normal radio pulsars. We note nonetheless that in all cases excluding that of PSRs, these estimates are rather crude and not well constrained by observations, given the low number of detected sources.

The birthrate of magnetars, in contrast to those of RRATs and XDINS, is estimated to be small, around 0.3 objects per century in the Galaxy (Gill & Heyl 2007), and is therefore not expected to contribute significantly to the overall count of the neutron star population. However, the existence of transient magnetars, which are believed to possess low X-ray luminosities that currently prevent their observation, also has implications for both the total magnetar birthrate and for the overall neutron star population.

At present, it is not clear whether the subgroup of CCOs represents an homogenous class of sources, or if these neutron stars in fact show distinct properties relative to other INSs. Some evidence indicates however that these radio-quiet sources might be "anti-magnetars", i.e. young low magnetized objects with very low spin-down rates. If this is the case, CCOs should also be considered when accounting for the total neutron star birthrate in the Galaxy.

From the discussion of Sect. 1.4.2, XDINS and RRATs show common properties with both normal radio pulsars and magnetars, as well as with each other. Therefore, and given the problem of "superpopulating" the Galaxy with unrelated neutron stars, it is not only plausible but necessary to invoke links between all of these groups, which may either be geometrical effects or actual evolutionary relations. In particular, if the RRAT population indeed outnumbers the normal radio pulsar population, then not all transient sources can be accounted for as weak or distant ordinary pulsars, as suggested by Weltevrede et al. (2006). In this case, one must also appeal to e.g. an evolution from a magnetar, or to a connexion

[12] See Keane & Kramer (2008) for details. References: Faucher-Giguère & Kaspi (2006), Gill & Heyl (2007), Keane & Kramer (2008), respectively for the estimated birthrates of radio pulsars, XDINS and RRATs.

with a transient AXP or distant XDINS.

In these facts reside the importance of statistical population studies and surveys. On the one hand, populations studies of the known sample represent a means to evaluate birthrates and other important properties of the studied neutron stars; on the other hand, the investigation of individual sources and the finding of other members both contribute to the understanding of possible relations and provide a better sampling of the underlying populations.

1.5.1 Remnants of a local population of massive stars

As mentioned before, it is striking that the M7 represent such an homogeneous group of nearby cooling neutron stars given the diversity of the observed subpopulations and the rather complex current observational picture of INSs. In fact, no other object in the ATNF catalogue exhibits the same properties that define the group with the exception of the RRAT J1819-1458, which is however more distant and fainter than the M7. Therefore, the most important question one might consider regarding population properties of the XDINS is to understand why there are so many cooling INSs with similar periods (and presumably ages and magnetic fields) in such a small volume.

Considering that within 1 kpc the M7 appear in comparable numbers as young ($\lesssim$ few Myr) radio and γ-ray pulsars (Popov et al. 2003), they may represent the only identified members of a large, yet undetected, elusive population of radio-quiet and thermally emitting INSs in the Galaxy. It should be noted, however, that the proximity of the OB associations of the Gould Belt to the Solar vicinity is an important factor that might explain this apparent local overdensity of INSs with similar temperatures, ages and magnetic field intensities. Since neutron star cooling is strongly dependent on mass and, to a lower extent, on magnetic field, a scenario where these stars evolved from a common progenitor population of massive stars could be considered. The discovery of similar sources at greater distances is then mandatory in order to make any progress towards understanding their population properties and evolutionary links with other groups of Galactic INSs.

Population statistics of thermally emitting INSs have been extensively investigated in the past by means of population synthesis. In Popov et al. (2000a), the relative contribution of the populations of both accreting and cooling INSs to the number of detectable sources at a given flux was analysed. The well motivated suggestion that the observed sample of XDINS is a direct consequence of the Sun's proximity to OB associations from the Gould Belt was investigated in Popov et al. (2003; 2005). In particular, the authors concluded that in order to reproduce the observed $\log N - \log S$ obtained with the ROSAT All Sky Survey data, a local "injection" of sources from the nearby massive OB associations is needed in addition to the remnants coming from the disk (see Fig. 1.14). Interestingly, in Popov et al. (2006a), the expected number of sources at a given flux was used to constrain the cooling curves of INSs.

1.5.2 Outside the Gould Belt

In order to fully address the population properties of thermally emitting INSs, one has to consider how numerous they are outside the Solar vicinity and the Gould Belt. For

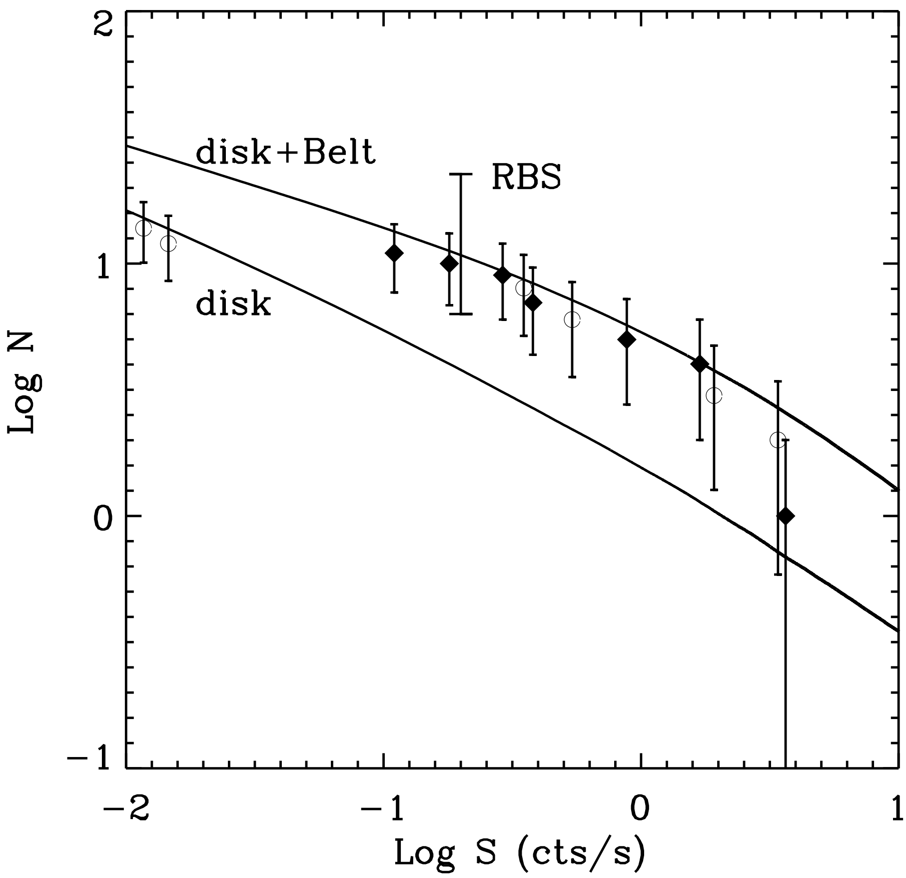

Figure 1.14: $\log N - \log S$ curve of the expected population of cooling INSs, showing the relative contribution of remnants from the Gould Belt, in comparison with disk objects. Observational points are from the RASS (from Popov et al. 2003).

that, investigations at fainter fluxes – which are not in practice feasible with ROSAT – are needed. We have addressed population properties issues of M7-like INSs firstly, by studying further the existing neutron star sample of nearby seven sources by means of a proper motion survey in X-rays and secondly, by searching for new candidates in XMM-Newton data and comparing the observational results with the expected scenarios at larger distances from the Sun.

1.6 Outline of the thesis

The thesis is outlined as follows: in Chapter 2 we describe our proper motion survey in X-rays and results. In Chapter 3 we describe the search for sources similar to the M7 in the XMM-Newton 2XMMp catalogue, the results and the long awaited discovery of a new member. In Chapter 4 we outline the modelling of such a population in the Galaxy and the preliminary results. In Chapter 5 we summarize our results and discuss the main important conclusions and perspectives for future work.

In Appendix A we provide a description of the theory behind thermal emission from young cooling and old accreting isolated neutron stars. In Appendix B are listed technicalities concerning the facilities used in the thesis work, including instruments in X-ray missions and optical telescopes, as well as details about data bases. Additional figures and tables for the chapters can be found in Appendix C. Finally, a list of acronyms used in the thesis manuscript can be found in Appendix D.

CHAPTER 2

Proper motion study of three isolated neutron stars in X-rays

Contents

2.1 Introduction

High proper motions have been detected for the three X-ray brightest isolated neutron stars among the M7 that have bright enough optical counterparts to allow measurements with large telescopes on the ground or with the HST (Neuhäuser 2001, Walter 2001, Kaplan et al. 2002b, van Kerkwijk & Kaplan 2007, Motch et al. 2003, Kaplan et al. 2007, Motch et al. 2005, Zane et al. 2006). However, the remaining sources either have no known optical counterpart or have an optical candidate too faint to allow repeated observations in a reasonable amount of time.

X-ray imaging telescopes of the former generation had an insufficient spatial resolution to detect source displacements on the sky in a reasonable interval of time, even for fast moving objects such as INSs. The advent of high spatial resolution X-ray observatories has made possible the measurement with sufficient accuracy of the proper motions of objects too faint to be detected at other wavelengths. Radio-quiet neutron stars are obviously prime targets for this kind of study.

Up to now, only a limited number of attempts have been made to measure proper motions of neutron stars in X-rays. The first example is the confirmation of the high proper motion of RX J1856.5-3754 (0.34 ± 0.12 mas yr^{-1}, Neuhäuser 2001; see Sect. 2.1.1 below) based on two ROSAT HRI (High Resolution Imager) observations obtained three years apart. A second example is the derivation of an upper limit of ~ 170 mas yr^{-1} on the motion of AXP 1E 2259+586 (Ogelman & Tepedelenlioglu 2005) using ROSAT, Chandra and XMM-Newton data. Another study concerns the CCO in Puppis-A, for which Hui & Becker (2006) derived a proper motion of 107 ± 34 mas yr^{-1} by comparing two Chandra HRC-I observations. This result was later improved to 165 ± 25 mas yr^{-1} by Winkler & Petre (2007), who included a third HRC-I image. Very recently, De Luca et al. (2009) and Kaplan et al. (2009a), using Chandra ACIS-I observations, reported 90% upper limits on the proper motion of two magnetars, SGR 1900+14 and 1E 2259+586, of 54 mas yr^{-1} and 65 mas yr^{-1}, respectively.

In a detailed study of the dynamic structure of the pulsar wind nebula (PWN) surrounding the Vela pulsar, Pavlov et al. (2003) was able to determine the displacement of bright knots moving outwards along the pulsar outer jet. Such an observational achievement was only made possible thanks to the superb spatial resolution of the Chandra cameras as well as to a dedicated monitoring of the pulsar by the satellite, with 13 observations conducted over two years. The apparent speeds of the fast moving observed "blobs" were determined as 0.35 ± 0.06 and 0.51 ± 0.16 fractions of the speed of light, c. Strictly speaking, this study is rather different than the determination of the proper motion of a neutron star as far as observing strategy is concerned, since the implied velocities are in different ranges; the transverse speeds of neutron stars are not as extreme and therefore require a longer time basis in order to detect signifcant motions. On the other hand, there is no need of so many observations to be taken in between: in the case of the blob in Vela, this was crucial given the intrinsic variability of the nebula at short timescales.

We took advantage of the unprecedented spatial resolution of the Chandra Observatory to set up a proper motion survey in X-rays of three of the faintest members of the M7 starting in 2002 and having second epoch observations taking place three to five years after. Observing close to the maximum of the spectral energy distribution, Chandra provides a fast and efficient way of measuring accurate relative positions with respect to the background of active galactic nuclei (AGN). In this chapter we report on the results of this observing campaign, extensively discuss the error budget on the proper motion and present the implications of our findings on the understanding of the properties of this particular group of neutron stars. These results were presented in Motch et al. (2007b; 2008; 2009).

The outline of the chapter is as follows: in the remainder of this introductory section the main results of proper motion studies that were carried out in the optical for sources RX J1856.5-3754, RX J0720.4-3125 and RX J1605.3+3249, the three X-ray brightest M7 (Sect. 2.1.1), are reviewed. In Sect. 2.1.2 the observational properties shown by the three INSs that were targeted for the proper motion study in X-rays, sources RX J1308.6+2127, RX J0806.4-4123 and RX J0420.0-5022, are briefly summarized. We then describe in Sect. 2.2 the Chandra observations and the procedure for data reduction. The analysis and method applied in order to detect displacements are detailed in Sect. 2.3. The discussion of the inherent error budget, by means of extensive simulations and analysis using test fields, is in Sect. 2.4. Actual results are gathered in Sect. 2.5 and discussed in Sect. 2.6.

We refer to Appendix B.1.2 for details about the Chandra Observatory and ACIS instruments, as well as the Proposers' Observatory Guide (POG)[1]. Appendix A.2 provides a brief description of the theory behind the Bondi-Hoyle scenario for spherical accretion from the interstellar medium.

2.1.1 Proper motion studies of the M7 in the optical

RX J1856.5−3754 The X-ray bright RX J1856.5-3754 is believed to be the nearest member of the M7. Due to its proximity, purely thermal soft X-ray emission and bright optical counterpart (for neutron star standards, with $m_{\rm B} = 25.2$), it constitutes one of the favourite targets for investigations that aim at constraining the neutron star EoS, by determining its mass and radius. For reliable radius measurements through broadband spectral modelling, one has to have an independent determination of the distance to the source through, for example, a parallax measurement. As early as 2001, Walter completed the first astrometric study of this neutron star, providing measurements of its annual parallax and proper motion, from observations with the Hubble Space Telescope (HST) and a three-year baseline. The author determined a proper motion of $\mu = 332 \pm 1\,{\rm mas\,yr^{-1}}$ and a parallax of $\pi = 16.5 \pm 2.3\,{\rm mas}$, which implied a distance of 61 pc. Based on these determinations, it was suggested a putative former association with the runaway O star ζ Oph – the stars' projected backward trajectories would coincide in the Upper Sco OB association around 1 Myr ago. The proper motion determination was confirmed independently by ground based (less accurate) ESO-VLT observations, as well as ROSAT HRI images (Neuhäuser 2001).

However, these determinations were called into question one year later by Kaplan, van Kerkwijk, & Anderson, who reanalyzed the HST data and found a much greater distance, $d \sim 140\,{\rm pc}$, implied from a measured parallax of $\pi = 7 \pm 2\,{\rm mas}$. This would therefore exclude the possibility of a former association with ζ Oph (Walter & Lattimer 2002) and imply instead, for a birth in Upper Sco, a younger kinematic age of ~ 0.4 Myr. A proper motion measurement of $\mu = 333 \pm 1\,{\rm mas\,yr^{-1}}$ was, on the other hand, fully consistent with the previous determination, since it is much less subject to systematic uncertainties than parallax measurements with the HST (Kaplan et al. 2007). It is worth mentioning for the sake of completeness that a careful analysis including more data allowed van Kerkwijk & Kaplan to consistently and accurately refine the parallax determination of the source[2], obtaining $\pi = 6.2 \pm 0.6\,{\rm mas}$ and a distance of $d = 161^{+18}_{-14}\,{\rm pc}$. The revised distance implies a neutron star tangential velocity (projected on the sky) of $v_\perp \sim 260\,{\rm km\,s^{-1}}$, which excludes the possibility, for this object in particular, that the X-ray luminosity is powered by accretion from the ISM as originally thought.

RX J0720.4−3125 Making use of the facilities provided by the ESO-NTT 4 m telescope together with the ESO-VLT, Motch, Zavlin, & Haberl were able to determine the proper

[1] http://cxc.harvard.edu/proposer/POG/html/index.html

[2] A revised value of $d \sim 117$ pc was provided by Walter & Lattimer (2002) in between.

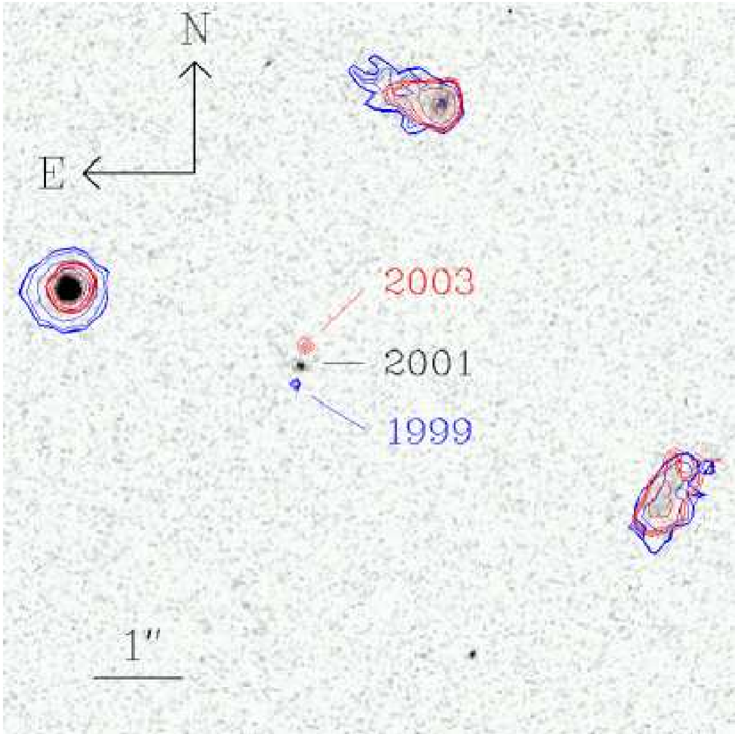

Figure 2.1: Proper motion of the optical counterpart of the INS RX J1605.3+3249, made evident by Subaru and HST observations (from Motch et al. 2005).

motion of the second brightest among the M7, RX J0720.4-3125. The data, taken over a period of six years, revealed a yearly displacement of $\mu = 97 \pm 12$ mas of the optical counterpart ($m_{\mathrm{B}} = 26.6$). Similarly to RX J1856.5-3754, the large proper motion unveiled the nature of the source as a cooling middle-aged INS and confirmed its optical blue counterpart. Later HST observations using a time basis of eight different epochs spread over two years confirmed and refined the results, further providing a parallax determination for the neutron star: $\mu = 107.8 \pm 1.2\,\mathrm{mas\,yr^{-1}}$ and $\pi = 2.8 \pm 0.9$ mas (Kaplan et al. 2007). The inferred distance of $d = 361^{+172}_{-88}$ pc and measured proper motion imply a tangential velocity of $v_\perp = 185^{+88}_{-45}\,\mathrm{km\,s^{-1}}$ and a kinematic age of $t_{\mathrm{kin}} \sim 0.7$ Myr, assuming a most likely birth location in the Trumpler 10 OB association.

RX J1605.3+3249 The optical counterpart ($m_{\mathrm{B}} = 27.2$) of the M7 RX J1605.3+3249 was observed with the Subaru Telescope in 1999 and 2003 by Motch, Sekiguchi, Haberl, Zavlin, Schwope, & Pakull. The analysis of these observations, together with archival HST data, allowed the determination of a high proper motion of $\mu = 145 \pm 13\,\mathrm{mas\,yr^{-1}}$ (see Fig. 2.1), excluding again the possibility that this INS could be re-heated by accretion from the ISM. Assuming that the source is instead a middle-aged neutron star, 10^5 to 10^6 yr, its backward trajectory could well be consistent with a birth near the Sco OB2 association, similar to what was found for RX J1856.5-3754. Motch et al. (2005) argued that at least the brighter members of the ROSAT-discovered group of seven INSs seems to be dominated by the production of the Sco OB2 association, the closest OB association to the Earth and part of the Gould Belt. The above results were updated one year later by Zane, de Luca, Mignani, & Turolla, who included a new HST observation of the source in order to confirm the proper motion determination. The authors obtained $\mu = 155 \pm 3\,\mathrm{mas\,yr^{-1}}$, in agreement with the original measurement, although much more precise. For this source, no parallax measurement is available. However, a distance estimate has been proposed by Posselt et al. (2007), $d \sim 390\,\mathrm{pc}$, based on the determination of the hydrogen column density in the direction of the source (as inferred from fits to its X-ray spectrum), together with a model of the distribution of the ISM. For this distance, the detected proper motion implies a tangential velocity of $v_\perp \sim 290\,\mathrm{km\,s^{-1}}$ and corroborates a likely birth place in the Sco OB2 association, as suggested by Motch et al., as well as their discussion of the role of the Gould Belt as the main provider of neutron stars to the Solar vicinity.

2.1.2 Summary of properties of the Chandra targets

Below, the main observational properties shown by the three M7 which were the object of the proper motion campaign with the Chandra Observatory, and part of the thesis work, are summarized.

RX J1308.6+2127 The source was discovered by Schwope et al. (1999) in a programme aiming at identifying in the optical the brightest ROSAT sources located at high galactic latitudes (Schwope et al. 2000). Its nature as a nearby thermally emitting INS was confirmed when pulsations were found in Chandra data (Hambaryan et al. 2002), as well as from the detection in a deep HST observation of a faint optical counterpart with $m_\mathrm{B} \sim 28.4$ (Kaplan et al. 2002a). Based on new XMM-Newton observations, Haberl (2004a) showed that the pulsations originally detected were in fact the manifestation of the first harmonic of the actual spin period, one of the longest among the M7, $P = 10.31\,\mathrm{s}$. The blackbody temperature is hot for M7 standards, around 100 eV. RX J1308.6+2127 was the first M7 for which significant evidence for the presence of a broad absorption feature had been found (Haberl et al. 2003). More data led Schwope et al. (2007) to argue for the presence of two lines instead of only one, spaced in energy in a ratio 1:2, in order to get an acceptable spectral fit (Sect. 1.3.1.1). Kaplan & van Kerkwijk (2005b) found a coherent timing solution for the source, from Chandra and XMM-Newton observations that covered over five years. The derived spin-down rate, if due to magnetic dipole radiation, would imply $B_\mathrm{dip} = 3.4\times10^{13}\,\mathrm{G}$, a value consistent with that estimated from the energy of the absorption lines, $B_\mathrm{abs} = (2-4)\times10^{13}\,\mathrm{G}$, assuming proton cyclotron absorption or atomic hydrogen transitions.

RX J0806.4-4123 The source was discovered by Haberl et al. (1998) in the ROSAT All-Sky Survey. A gentle intensity modulation of the X-ray light curve, at $P = 11.37\,\mathrm{s}$ and with a pulsed fraction of 6%, has been identified with the neutron star rotation (Haberl & Zavlin 2002, Haberl et al. 2004a). The spin period of the source is the longest recorded so far for this group of objects. With a best fit blackbody temperature around 96 eV, RX

J0806.4-4123 lies among the hottest M7. The spectral fit is significantly improved by adding a shallow absorption line centered around 0.46 keV. From the energy of this feature, a rather high estimate for the magnetic field strength, $B_{\rm abs} = (6-9)\times 10^{13}$ G can be derived under the usual assumptions. The interstellar absorption towards the source is $N_{\rm H} = 4\times 10^{19}\,{\rm cm}^{-2}$ or $N_{\rm H} = 1.1\times 10^{20}\,{\rm cm}^{-2}$ depending on whether the low energy broad absorption line is included or not in the spectral fit. RX J0806.4-4123 is the M7 located at the lowest Galactic latitude ($b = -5°$). Its modest photoelectric absorption suggests small distances of the order of 240 pc (Posselt et al. 2007). No optical counterpart brighter than a non-constraining limit of $m_{\rm B} \sim 24$ is present in the error circle (Haberl & Zavlin 2002).

RX J0420.0-5022 The source is the X-ray faintest INS discovered in the ROSAT All-Sky Survey (Haberl et al. 1999). With a blackbody temperature of 45 eV, RX J0420.0-5022 is also the coolest of its group. It displays a broad absorption line at 0.33 keV (Haberl et al. 2004a), from which a magnetic field intensity of $B_{\rm abs} = (4-7)\times 10^{13}$ G is inferred. The source is located at relatively high Galactic latitude ($b = -44°$). The interstellar column density towards RX J0420.0-5022, on average about twice that of RX J0806.4-4123, is $N_{\rm H} = 1.0\times 10^{20}\,{\rm cm}^{-2}$ or $N_{\rm H} = 2.0\times 10^{20}\,{\rm cm}^{-2}$ – again depending on the inclusion or not of a Gaussian absorption line in the spectral model. XMM-Newton observations have revealed a pulsation period of 3.45 s, the shortest of all seven sources.

From a 2000 ESO-VLT observation, Haberl et al. (2004a) reported the possible existence of a $m_{\rm B} \sim 26.6$ object in the Chandra error circle of the source. This observation has been re-analyzed recently by Mignani et al. (2009), who only found marginal evidence for the detection of the object reported by Haberl et al.; furthermore, they updated its flux to $m_{\rm B} = 27.5 \pm 0.6$. The analysis of newer ESO-VLT imagings of the field of the neutron star, carried out in 2006 and 2007, failed to detect the 2000 optical candidate, showing instead evidence for a 3.9σ detection of an object of similar magnitude, $m_{\rm B} = 27.5 \pm 0.3$, located $\sim 0.5''$ north from the position of the 2000 object, but also within the updated Chandra error circle. Interestingly, the angular separation is consistent with the upper limit on the proper motion of the source reported by Motch et al. (2009), suggesting that both observations might have detected the actual optical counterpart of RX J0420.0-5022, which has moved. However, one can not exclude the rather high probability that one or both detections are mere artifacts of the noisy background. Indeed, the presence of a relatively bright star CD-50 1353 close to the INSs adds a lot of scattered optical light at the source position and makes deep imaging difficult. The distance estimate by Posselt et al. (2007), on the basis of interstellar absorption, is of the order of 345 pc.

2.2 Observations and data reduction

The proper motion campaign, having Christian Motch as PI of the observations, started in Chandra Cycle 3 (2002). During this year, first epoch images of the three targets were obtained, using the Advanced CCD Imaging Spectrometer (ACIS) detectors operating in imaging full-frame and timed exposure (TE) modes, with nominal aimpoints. With this configuration, the CCD chips collect data during a nominal frame time of 3.2 s, before

Table 2.1: Description of Chandra observations of three of the M7.

Target RX	Epoch	ObsID	Observation Date	Aimpoint Detector	t_{exp} (ks)	α_{NOM} (deg)	δ_{NOM} (deg)	Roll Angle (deg)
J1308.6+2127	1	2790	2002-05-21	ACIS-I	19.5	197.1962	+21.4502	226.57
	2	7610	2007-05-12	ACIS-I	20.2	197.1970	+21.4446	226.71
J0806.4−4123	1	2789	2002-02-23	ACIS-I	17.7	121.5981	−41.3799	322.44
	2	5540	2005-02-18	ACIS-I	19.7	121.6008	−41.3791	325.63
J0420.0−5022	1	2788	2002-11-11	ACIS-S	19.4	65.0250	−50.3790	18.65
	2	5541	2005-11-07	ACIS-S	19.7	65.0107	−50.3811	23.58

Note: Listed are the nominal coordinates α_{NOM}, δ_{NOM} and roll angle of the observations, as well as the exposure times t_{exp} filtered for background events. C. Motch is PI. All observations were taken in FAINT data mode, TE read mode and with no gratings (Appendix B.1.2).

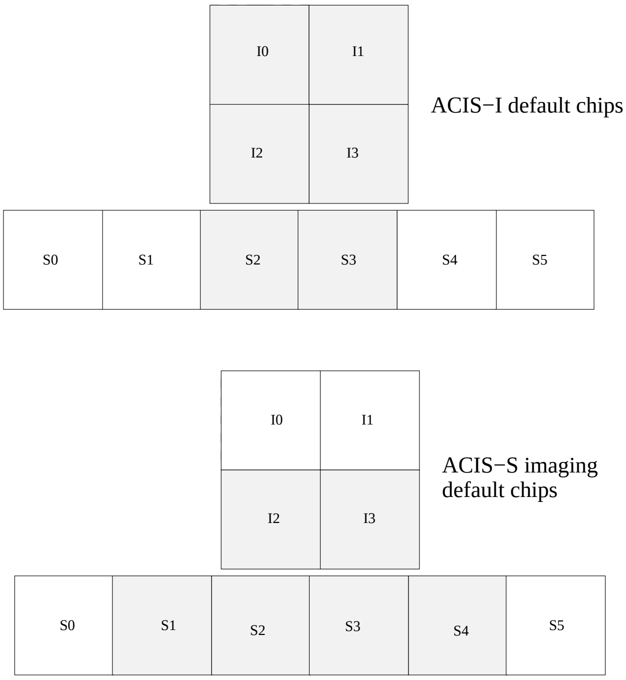

Figure 2.2: A schematic drawing of the ACIS focal plane (not to scale) showing the different imaging modes, ACIS-I (top) and ACIS-S (bottom; from the Chandra POG).

quickly (within ~ 41 ms) transfering the charge to the framestore region which is subsequently read out. The telemetry format selected was the "faint" one, which provides, for every photon that hits the detector, the event position in detector coordinates, its arrival time and amplitude, as well as the contents of a 3×3 island which are used to determine the event grade. Second epoch observations of the sources RX J0806.4-4123 and RX J0420.0-5022 took place after a three-year time interval had elapsed. The remaining target, RX J1308.6+2127 was re-observed five years after the first pointing (see the log of observations in Table 2.1). The observing strategy was to enforce the same acquisition mode, roll angle and aimpoints at both epochs so as to minimize the impact of a different orientation on the sky or camera settings on the final accuracy of the relative astrometry.

The ACIS detectors can be operated in any combination of the 10 CCDs, with a maximum number of 6 chips being simultaneously on. The most used combinations are the extended ACIS-I and ACIS-S imaging modes, using chips I0 – I3, S2 and S3, and chips S1 – S4, I2 and I3, respectively (Fig. 2.2; see also Appendix B.1.2). By construction, the ACIS detectors consist of two intrinsically different types of CCDs, depending on whether the X-ray photons hit the camera from the rear or front side (i.e. CCDs that are back or front-illuminated – BI, FI). The choice of imaging mode defines what type of CCD is placed at the aimpoint location of the focal plane; the nominal aimpoints being the FI chip I3 and BI chip S3, respectively, for ACIS-I and ACIS-S. Therefore, the choice of imaging mode depends critically on the properties of the target to be observed, since the effective area, quantum efficiency, event threshold, charge transfer inefficiency and energy resolution of the two types of CCDs considerably differ.

Our goal was to use the background of extragalactic sources, mainly AGN, to define an astrometric reference frame relative to which we could measure the displacement of the INS. Because of the enhanced soft X-ray sensitivity of ACIS-S compared to ACIS-I, the two X-ray brightest targets, RX J1308.6+2127 and RX J0806.4-4123, would have suffered from pile-up in ACIS-S and would thus have likely produced biased X-ray positions. Using ACIS-I for these two sources provided the best compromise between the need for observing enough background sources and the requirement of having the best position for the INS target. However, for the fainter and much softer X-ray source RX J0420.0-5022, ACIS-I would have collected too few counts. Accordingly, we chose to use ACIS-S at the expense of a smaller field-of-view (FoV).

Although the microchannel plate imaging detector on-board Chandra, the High Resolution Camera (HRC), is the scientific instrument designed to match the observatory point-spread function (PSF) most closely – with an outstanding spatial resolution of 0.5″, it would have had, in principle, a positive impact on our astrometric study – the choice of the ACIS detectors was motivated by their superior hard X-ray sensitivities relative to that of the HRC (important for the detection of background sources), as well as from the possibility of filtering X-ray events according to energy that otherwise would had possibly degraded the centering accuracy of the X-ray sources. Moreover, the fact that HRC pixels are determined by the electronic read-out was felt as being a risk for the long-term stability of the astrometry.

The Chandra X-ray tracer simulator MARX[3] was used for the evaluation of the exposure times needed in order to detect a suitable number ($N \gtrsim 10$) of well localized background reference sources for each INS field. With an exposure time of 20 ks, the simulations (carried out in 2001) suggested that an astrometric error of 0.07″ on the relative positioning of the two epochs could be expected.

In Table 2.2 we list the sky and equatorial coordinates, count rates and expected level of pile-up for the three INSs for both epochs, as observed with Chandra. The listed quantities are obtained by running the wavdetect detection task with default parameters (see Sect. 2.3.1 below); the observations were filtered in the 0.15 – 10 keV energy band.

2.2.1 Description of the reduction steps

Data reduction was performed in two steps with the Chandra Interactive Analysis of Observations software (CIAO; Fruscione et al. 2006). The 2002 and 2005 observations of RX J0806.4-4123 and RX J0420.0-5022 were analyzed using software version 3.3 while, for both epochs of observations of RX J1308.6+2127, versions 3.4 and 4.0 were applied. In all cases we used the most recently available calibration database (CALDB[4]) and followed standard reduction procedures for ACIS data[5], summarized below. Since the observations were taken, a major reprocessing of the Chandra data archive has been carried out by the

[3]Model of AXAF Response to X-rays, http://space.mit.edu/CXC/MARX; see Sect. 2.4.1
[4]http://cxc.harvard.edu/caldb
[5]http://cxc.harvard.edu/ciao/guides/acis_data.html

Table 2.2: Positions and counts of the three INSs.

Target RX	Epoch	X (pixel)	Y (pixel)	α (deg)	δ (deg)	Rate (10^{-2} s^{-1})	PSF (arcsec)	Pile-up Fraction
J1308.6+2127	1	4064.776 ± 0.016	4108.675 ± 0.016	197.2008958(23)	+21.4518804(22)	12.80 ± 0.26	0.200	0.10
	2	4072.366 ± 0.018	4149.783 ± 0.019	197.2005695(27)	+21.4519235(26)	10.11 ± 0.23	0.204	0.10
J0806.4−4123	1	4099.557 ± 0.023	4130.439 ± 0.022	121.597478(4)	−41.375254(3)	7.01 ± 0.20	0.200	0.06
	2	4114.823 ± 0.025	4125.659 ± 0.023	121.597462(4)	−41.375152(3)	5.72 ± 0.17	0.200	0.06
J0420.0−5022	1	4108.726 ± 0.029	4103.75 ± 0.03	65.008123(6)	−50.380059(4)	4.40 ± 0.15	0.197	0.03
	2	4108.720 ± 0.026	4103.738 ± 0.028	65.008124(6)	−50.380061(4)	4.27 ± 0.15	0.197	0.03

Note: Listed are the sky X, Y and equatorial α, δ coordinates of the three INSs for both epochs, together with detected count rates, PSF encircled energy radius size at the source position and expected level of pile-up. The energy band is 0.15 – 10 keV (results obtained by running the wavdetect detection task with default parameters).

Standard Data Processing (SDP[6]), the Reprocessing `III`[7]. We verified that the reprocessing does not affect our analysis since, relative to CIAO 3.3 (which is the oldest version of the software that we used), the latest CALDB improvements relevant to the analysis have already been applied by us.

The pipeline of the SDP runs in several stages or "levels", each of which is built on the results of the preceding one. For a given science observation, the SDP takes raw Chandra spacecraft telemetry and splits it along the observation boundaries (level-0). The output is then subjected to instrument-dependent corrections, such as the application of the aspect solution. To this point (level-1), nothing irreversible – like for instance, the rejection of photon events based on grades or bad pixel maps – has been done to the data. Accordingly, we manually reprocessed the observations starting from the level-1 stage.

Afterglow events and bad pixel map A first step in the reduction process is to flag X-ray detections in the level-1 event list that correspond to afterglow events. These are the subsequent release of charge that has been trapped in the detector due to the impact of a cosmic ray. Afterglows can be apparent up to a few dozen frame exposures following the cosmic ray event; if not removed, they can be mistaken for faint X-ray sources. Observations distributed by the pipeline prior to 2005 (SDP versions older than DS 7.4.0) used to have afterglow events flagged by the task acis_detect_afterglow, which was found to erroneously reject around 3 to 5% of real source counts from the event list. For this reason, a new and more precise method for identifying afterglows was developped, namely the script acis_run_hotpix. According to the Chandra X-ray Center (CXC) webpages, the new method finds afterglow events that would go unnoticed through the execution of acis_detect_afterglow, being also a more efficient tool to identify hot pixels or pixels with bad bias values. To be able to run this task, events flagged with the old tool must be reset. Since first epoch observations had been obtained in 2002, this correction was relevant for the analysis. We thus proceeded to reset the status bits corresponding to afterglows by means of the task dmtcalc and a pre-defined expression for this purpose, which is then processed line by line in the event list.

The next step is to flag hot pixels and afterglow events with the improved method by running the script acis_run_hotpix. In a nutshell, the script searchs for pixels where the bias value are too discrepant from average, as well as for locations where there is an unusually large or small number of events. It then proceeds in order to classify these pixels as being likely to be associated either with cosmic ray afterglows, hot pixels or astrophysical sources. Finally it creates a bad pixel map that points to the locations of these problematic pixels as well as of the ones in their immediate vicinity. In practice, the script calls subsequently the tasks acis_build_badpix, acis_find_hotpix and acis_classify_hotpix; a second passage through acis_build_badpix is needed in order to write the bad pixel map. In order to run the task, a level-1 event file, the original bad pixel map (as provided by the pipeline), the bias files for the observation, the mask file (which records the valid part of the detector used for the observation) and the parameter block file (which is used to determine the

[6] http://cxc.harvard.edu/ciao/data/sdp.html
[7] http://cxc.harvard.edu/ciao/repro_iii.html

observational parameters, such as which chips were active, the read mode and data mode used etc.).

Data processing and calibration After the creation of a bad pixel map, the following (and most important) step in the reduction procedure is to process the data with the latest CALDB calibrations, as well as to filter the detected X-ray photons by applying "good time intervals" (GTIs) and pixel flags. Using Chandra terminology, this process together with the position transformation to celestial coordinates correspond to taking the observation to the level-2 stage. To apply the calibration files, the task acis_process_events is used. By default, this task applies a correction for the charge transfer inefficiency (CTI; i.e. the loss of charge as it is shifted from one pixel to the next during read-out) as well as an adjustment for the time-dependent effective gain[8] that is drifting with time as a result of the increasing CTI. Presumably, these two corrections can together significantly improve the spectral resolution of the data. Although not strictly necessary for timing or imaging purposes, they do not have a negative effect in the analysis either. The task then randomizes the PHA channels, in order to avoid an aliasing effect in the binned spectra due to the conversion of PHA to PI: in the case of a sufficiently strong source in a small spatial region, the spectrum in energy will show a series of spikes and zeros[9]. Finally, by default, the task also randomizes the positions of events detected within a given pixel, which is done in order to remove the instrumental "gridded" appearance of the data as well as to avoid any possible aliasing effects associated with this spatial grid. This randomization process could in principle slightly degrade the source centering accuracy. We thus removed the pixel randomization by reprocessing the raw data according to available instructions[10] and analyzed these data in addition to the usual randomized sets.

In order to run acis_process_events, the level-1 event file, a bad pixel map and the aspect solution file of the observation – which describes the orientation of the telescope as a function of time and is used for the determination of the celestial position of every event – are required. Many different tasks are called by acis_process_events; refer to the CXC help pages for a full description.

Filtering and attitude errors After this step, the processed level-1 event file is subsequently filtered for bad grades (i.e. a number assigned to every event based on which pixels in its 3×3 island are above their threshold value) and GTIs. GTIs are the time periods when the mission time line parameters fell within acceptable ranges, excluding, for instance, periods of background flares etc. Usually there are GTIs for every active CCD detector. For the filtering process, we used the tool dmcopy, a very general task which copies subsets of a table or image. Some of its usage involves: selecting rows and columns from a table and making an output file consisting of the filtered table; binning tables to an image, i.e. selecting any n columns from a table, and making an n-dimensional binned image from them; and filtering images, selecting subsets (spatial, temporal, energy, etc.) of an image.

[8] The gain is used to compute the energy and pulse invariant (PI) of an event from the pulse height amplitude (PHA) value.

[9] See http://cxc.harvard.edu/ciao/why/acispharand.html; for details.

[10] http://cxc.harvard.edu/ciao/why/acispixrand.html

Following the standard reduction, we retained photon grades 0, 2, 3, 4 and 6 (using Chandra and ASCA terminology) corresponding to single, double and triple events. At this step, the event file is considered to be on the level-2 stage.

Finally, the last step in the reduction is to correct remaining attitude errors in the processed and filtered level-2 event file by using the aspect calculator available at the CXC webpages[11]. We found small offsets for the 2002 data, which were corrected accordingly.

2.3 Data analysis

In order to accurately determine the proper motion of the INSs using Chandra data, the general procedure for the analysis consists of measuring positions of a number of field X-ray background objects that are common to both epochs so as to be used as reference sources, as well as the position of the target at both epochs. Using the set of reference sources, a best-fit transformation between the two observations is derived and subsequently applied to the target in order to determine any detectable displacement. Of particular importance is to appropriately assess the uncertainties involved in each step of the analysis that, together with the observatory own capabilities and limitations, fully determine the final accuracy with which the proper motion can be measured. In this section, we thoroughly discuss each step of the analysis procedure.

2.3.1 Source detection

To set up the reference frame and then find a best-fit transformation between the two epochs, an immediate concern is to detect, as precisely as possible, a large number of homogeneously distributed sources on the sky. The background of extragalactic AGN, which is known to dominate the X-ray sky at intermediate to high galactic latitudes, is thus best suited for this purpose. Due to the fact that one of the targets, RX J0806.4-4123, is located at low galactic latitude, we expect that a fraction of the X-ray sources detected in its field consists of active coronae of Galactic late-type stars. These low luminosity X-ray sources ($L_X \lesssim 10^{31}\,\mathrm{erg\,s^{-1}}$) are mostly younger than $1 - 2\,\mathrm{Gyr}$ (Motch et al. 1997) and located at relatively short distances ($d \lesssim 1\,\mathrm{kpc}$). Stars younger than this age still share most of the motion of their parent molecular clouds and thus have a small random velocity dispersion of less than $\sigma_v \sim 20\,\mathrm{km\,s^{-1}}$ (Wielen 1977). Accordingly, the expected proper motion resulting from velocity dispersion and Galactic differential rotation is of the order of $22\,\mathrm{mas\,yr^{-1}}$ at $300\,\mathrm{pc}$ for RX J0806.4-4123. Averaged over the whole ACIS-I FoV, the effect of young star displacements on relative astrometry is therefore negligible compared to the overall error budget. We discuss further the nature of the X-ray objects used as reference sources for the astrometry in Sect. 2.4.1.

A suite of detection tools comprising different types of algorithms, is provided by CIAO[12]. In our analysis, we tested both the celldetect and wavdetect packages. The detection algorithm behind celldetect is that known as the "sliding cell", which has been

[11] http://cxc.harvard.edu/cal/ASPECT/fix_offset/fix_offset.cgi

[12] See the CIAO Detect Manual, http://cxc.harvard.edu/ciao/download/doc/detect_manual

used to analyze images from several past X-ray missions such as Einstein and ROSAT. The algorithm searches for sources by comparing counts in "detect cells" relative to those in "background cells", in order to identify locations where the signal-to-noise (S/N) ratio exceeds a given user-defined threshold. The detect cell in CIAO has a variable size, determined by the PSF of the image at the exact location of the cell and that is a function of the energy and off-axis angle. The background can be defined either locally around the detect cell or by means of a background map. By default, the task uses a detection scheme known as "recursive blocking" (due to a limitation on the allowed size of the data to be analyzed, currently set to 2048 × 2048 pixels): it first searches for sources in the inner allowed region; then, for larger data sets, the inner 4096×4096 pixel region (excluding the area that has already been analyzed) is blocked by 2 and searched for sources. The process progress successively until the whole image surface has been covered. The position of the detected source is then derived from the centroid of the X-ray events found in the detect cell. In addition, the major and minor axes of the events distribution are calculated, as well as the position angle of the major axis. celldetect is intended to provide good results for the detection of unresolved sources in a wide variety of data, such as oversampled or background-dominated images, as well as for data that cover a very large area compared to the size of the resolution element.

We run celldetect directly on the level-2 event lists, only filtering in energy. We limited the detection area to be within the central CCDs – those composing the 4×4 ACIS-I array (`ccd_id` = $0-3$), for the fields of targets RX J1308.6+2127 and RX J0806.4-4123, and the central two chips of the ACIS-S configuration (`ccd_id` = $6-7$), for the observations of RX J0420.0-5022. The parameter controlling the significance of the detection is the *threshold*, which is the S/N cutoff in units of Gaussian standard deviation. We systematically tested six different values for this parameter in interval 1.5 to 2.75. The background was set to be computed locally, which is the default usage. While using this option, the area of the background frame (centered on the same location as the candidate source) is roughly the same as the area of the detect cell. The variable size of the detect cell was set to match the instrument PSF at energy ~ 1.5 keV (again, the default). Finally, in order to avoid spurious detections, especially along the detector edges, exposures maps for the observation were supplied.

The detection method used by the wavdetect package correlates the X-ray image with wavelet functions of various spatial extents. The correlation value is compared in each pixel with the expected distribution of values (computed from the estimate of the background); if the value is discrepant within this distribution, the pixel is assumed to be associated with a source. The code comprises two different routines, wtransform and wrecon. The first performs the convolution of the image with the wavelet function for as many scales as selected by the user. The second task constructs a final source list and estimates various parameters for each source, such as the number of pixels and sum of counts within the source and background regions, the source significance, the estimated size of the PSF at the source location and its estimated 1σ semi-major and semi-minor axes.

In order to run wavdetect, we used full-resolution, unbinned images centered on the same CCD chips as listed for celldetect. Similarly, we filtered events in energy. Pixel scales of 1, 2 and 4 for the wavelet functions (which correspond to the radius of the "Mexican

Hat" function implemented in wtransform) were used. These values are well suited for the detection of unresolved sources at moderate off-axis angles. The final list of sources is then composed of the combination of detections at the different scales. The significance of source detection is given by the parameter *sigthresh*, which defines the expected number of spurious detections in any given image pixel. We tested five values between 10^{-8} and 5×10^{-5} implying between 0.01 and 52 spurious source per CCD chip in the worst case.

The final relative astrometric accuracy to which the neutron star displacement can be measured depends on the number of sources common to the two observations and on the quality of the determination of their positions (Sect. 2.3.2). Testing several different detection thresholds allows to find the best compromise between the number of sources and the mean positional errors, both rising with increasing detection sensitivity. The largest threshold value in wavdetect implies that a large number of false detections enters the source list. However, since we only considered sources detected at both epochs and located at a maximum distance of $1''$ to $3''$ for matching the two epochs (see the following sections), the actual probability that the source common to both observations is spurious is very low. Best positions are obtained in the energy range for which the S/N ratio of the reference sources is strongest. This range depends on the relative energy distribution of these sources and of the diffuse extragalactic and instrumental backgrounds. For the neutron star, measured in the same conditions as the reference sources, the choice of the energy range is much less critical since the object is brighter than any of the background sources. We decided to test energy bands 0.3 – 10 keV, 0.3 – 5 keV, 0.3 – 3 keV, 0.5 – 5 keV and 0.5 – 2 keV, for both celldetect and wavdetect runs.

According to Chapter 5 of the Chandra POG, a study based on over 1300 X-ray sources detected in the framework of the Chandra Orion Ultradeep Project (Getman et al. 2005), which were boresight-aligned and cross-correlated with the 2MASS catalogue, indicates that a systematic error, with 90% confidence value of $0.15''$ on X-ray positions which corresponds to a $\sim 0.07''$ radial 1σ residual error, is expected for relative astrometry with Chandra. Therefore, although the celldetect and wavdetect algorithms can in principle center a relatively bright X-ray source on the CCD chip with a theoretical accuracy only restricted by signal-to-noise ratio, the ultimate positioning precision is limited by other systematic effects of unknown origin, but probably related to pixel-to-pixel sensitivity changes, intra-pixel sensitivity variations, thermally-induced misalignements etc. We thus quadratically added a systematic error of $\sigma_{\rm sys} = 70$ mas to all ACIS source positions.

2.3.2 Matching reference frames

The absolute astrometric frame derived independently for each Chandra observation is already very accurate since the 90% confidence radius is estimated to be of $0.6''$ close to aimpoint (Chandra POG). However, reaching the ultimate precision on differential astrometry requires to correcting for the remaining relative random attitude errors affecting the observations at the two epochs.

We thus carried out a relative boresight correction by allowing the reconstructed equatorial positions of the sources in the second epoch to be slightly shifted in right ascension and declination and subjected to a small rotation around the aimpoint with respect to first epoch positions. We searched for translations of $\pm 1''$ in each direction with steps of $(d\alpha, d\delta) = 10$ mas and for a rotation of $\pm 0.1°$ with angular steps of $d\theta = 0.005°$. The best offset and rotation angles were estimated using a maximum likelihood scheme that, for a bivariate normal distribution, is equivalent to minimizing the quantity:

$$Q(d\alpha, d\delta, d\theta) = \sum_{i=1}^{N} \left(\frac{\Delta\alpha_i^2 + \Delta\delta_i^2}{\sigma^2_{\Delta\alpha_i} + \sigma^2_{\Delta\delta_i}} \right) \tag{2.1}$$

where $\Delta\alpha_i$ and $\Delta\delta_i$ are the distances in right ascension and declination between the positions of source i in the first epoch, (α_1, δ_1), and in the second epoch after transformation, (α'_2, δ'_2); N is the number of common sources:

$$\begin{cases} \Delta\alpha_i = (\alpha_{i,1} - \alpha'_{i,2}) \cos\delta_{i,1} \\ \Delta\delta_i = \delta_{i,1} - \delta'_{i,2} \end{cases} \quad \text{for } i = 1, 2, \ldots, N \tag{2.2}$$

The errors on the corresponding distances, $\sigma_{\Delta\alpha_i}$ and $\sigma_{\Delta\delta_i}$, are computed from the individual source uncertainties in right ascension and declination (returned by the centering algorithms) together with the systematic error $\sigma_{\rm sys}$.

The accuracy with which we can link the astrometric reference frames of the two epochs, $\sigma_{\rm fr}$, is given by the mean dispersion of the sources after the best-fit transformation parameters are applied to the coordinates of the second epoch:

$$\sigma^2_{\rm fr} = \frac{1}{N(N-1)} \sum_{i=1}^{N} \left(\Delta\alpha_i^2 + \Delta\delta_i^2 \right) \tag{2.3}$$

Therefore, an accurate determination is only achieved if a set of many well localized reference sources can be defined for matching the frames. The number of common sources between epochs is a function of several parameters, including the detection sensitivity and the maximum positional offset allowed between sources in the two epochs. In the analysis, we tested maximum offsets between $1''$ and $3''$. For any combination of parameters (energy band, detection sensitivity) we only actually performed the frame matching if at least 4 reference sources were available. For our pairs of observations, $\sigma_{\rm fr}$ is of the order of 100 mas and thus dominates the error budget.

Any displacement of the central source, the target INS, is then measured relative to the best-fit transformation found for the coordinates of the second epoch. The total error on the displacement is given by:

$$\sigma^2_{\Delta \rm INS} = \sigma^2_{\rm INS,1} + \sigma^2_{\rm INS,2} + \sigma^2_{\rm fr} + 2\sigma^2_{\rm sys} \tag{2.4}$$

where $\sigma_{\rm INS,1}$, $\sigma_{\rm INS,2}$ are the errors in the position of the INS as given by the detection algorithms in each epoch.

The process of matching the reference frames, finding the best-fit transformation and computing the INS motion was tested with sets of event lists for which pixel randomization was either applied or not, over source lists derived using both celldetect and wavdetect for a grid of different energy bands and detection thresholds. This totalized 110 independent analysis for each INS field, allowing us to assess the optimal configuration for each case, adding robustness to the final proper motion determinations.

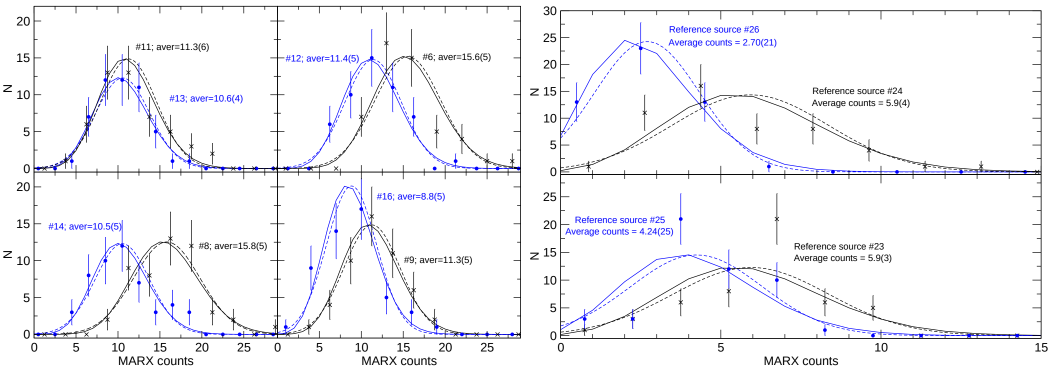

Figure 2.3: Count distributions of a typical sample of reference sources in ACIS-I drawn from a number of 50 MARX simulations. Solid and dashed lines are the expected Poisson probability distribution and its Gaussian limit for $N \gg 1$. The average counts are marked for each source referenced by its number on Table 2.3. *Left:* Sample of sources with counts between 10 and 15 for a total 20 ks exposure time. *Right:* Sample of sources with less than 5 counts for the same exposure time.

2.4 Checking the achievable accuracy

Before assessing the reality of the small displacement of an X-ray source on the sky, one needs to envisage all potential sources of errors. This is best done by measuring in X-rays the displacement of a source with known proper motion from observations at other wavelengths, e.g. radio or optical. Unfortunately, to our knowledge, the Chandra archive does not yet contain repeated ACIS observations of high proper motion INSs with properties such that they could be used as test data. The only possibilities left to test the error budget were then (*i*) to perform extensive simulations of moving targets and (*ii*) to use repeated observations of non-moving objects in order to test systematic errors. We examine these two options in the following subsections.

2.4.1 MARX Simulations

The goal of the simulations was twofold. First, they are used to evaluate the final accuracy at which the displacement of the INS can be detected in the real observations, for both ACIS-I and ACIS-S configurations. Second, to define the most efficient centering method and best suited set of parameters required to measuring proper motions with Chandra, such as optimal energy range, detection threshold and pixel randomization state.

We proceeded to simulate pairs of epochs that mimic, as far as instrumental and observing conditions are concerned, the actual Chandra observations, also reproducing the observed level of background noise, fluxes and spectral properties of the real sources in a given field. We used the Chandra ray tracer MARX version 4.2.1 and chose to simulate the fields of the INSs RX J0806.4-4123 (ACIS-I) and RX J0420.0-5022 (ACIS-S). Simulations of the field of RX J1308.6+2127, observed in ACIS-I mode as RX J0806.4-4123 and with roughly the same number of reference sources, would give similar results and were

Table 2.3: Background X-ray sources used as reference for ACIS-I simulations.

Ref.	α (deg)	δ (deg)	Counts (20 ks)	Off-axis (arcmin)	r (arcsec)	σ	m_R
1	121.62516(8)	−41.52852(9)	57 ± 10	9.00	0.728	1.7	13.36
2	121.63006(6)	−41.47582(6)	35 ± 6	5.93	0.382	1.3	14.96
3	121.67690(7)	−41.33937(4)	23 ± 5	4.30		...	
4	121.69754(6)	−41.39330(6)	20 ± 5	4.55	0.782	2.4	15.30
5	121.59210(9)	−41.46782(5)	18 ± 4	5.28		...	
6	121.53288(12)	−41.30647(4)	16 ± 4	5.29	1.425	3.1	20.27
7	121.52619(11)	−41.32490(4)	16 ± 4	4.62	2.954	7.0	16.31
8	121.53402(4)	−41.362472(21)	15 ± 4	3.07		...	
9	121.65854(11)	−41.54470(12)	14 ± 4	10.26		...	
10	121.48002(16)	−41.29328(10)	14 ± 4	7.43		...	
11	121.79077(14)	−41.33072(7)	13 ± 4	9.16		...	
12	121.54574(5)	−41.35207(4)	12 ± 3	2.89	1.335	6.0	14.06
13	121.58668(5)	−41.37178(3)	11 ± 3	0.71		...	
14	121.62138(4)	−41.38423(5)	11 ± 3	1.08		...	
15	121.54682(8)	−41.44811(7)	10 ± 3	4.70		...	
16	121.56252(9)	−41.45706(10)	10 ± 3	4.90		...	
17	121.60642(4)	−41.41079(6)	10 ± 3	1.89		...	
18	121.558100(28)	−41.38163(4)	7.9 ± 2.8	1.80		...	
19	121.71157(8)	−41.39028(6)	7 ± 3	5.15		...	
20	121.64004(11)	−41.45276(4)	7.2 ± 2.8	4.76	2.776	6.5	16.81
21	121.670173(10)	−41.39012(5)	6.9 ± 2.6	3.30	2.284	13.9	19.85
22	121.50367(9)	−41.33725(5)	6.8 ± 2.6	4.96	1.178	3.2	14.12
23	121.57058(3)	−41.36084(3)	5.0 ± 2.2	1.69	0.519	3.3	17.06
24	121.62575(12)	−41.439366(24)	4.8 ± 2.2	3.78	0.528	1.2	17.45
25	121.65436(6)	−41.42758(5)	3.8 ± 2.0	3.82		...	
26	121.54075(5)	−41.41136(4)	2.9 ± 1.7	3.20	0.747	3.3	16.02

Note: Equatorial coordinates, detected counts and off-axis angles as observed in the first epoch observation (2002); errors are 1σ. We also list the distance (in arcsec and in units of the standard deviation of the X-ray position) to the closest optical object as found in the USNO-B1.0 catalogue, as well as the object R magnitude.

Table 2.4: Background X-ray sources used as reference for ACIS-S simulations.

Ref.	α (deg)	δ (deg)	Counts (20 ks)	Off-axis (arcmin)	r (arcsec)	σ	$m_{\rm R}$
1	65.10923(5)	−50.386516(25)	51 ± 7	3.25	0.110	0.5	19.49
2	64.89999(7)	−50.43703(5)	45 ± 8	5.92	2.147	6.9	16.21
3	65.11099(5)	−50.42215(5)	33 ± 6	4.19	0.480	1.6	19.59
4	65.08910(5)	−50.35361(3)	32 ± 6	2.89	0.220	1.0	20.72
5	65.13178(10)	−50.37793(6)	23 ± 5	4.09		...	
6	65.03771(5)	−50.43048(5)	11 ± 3	3.13		...	
7	64.92772(10)	−50.4228(10)	10 ± 3	4.56		...	
8	64.89975(14)	−50.3620(10)	7.0 ± 2.8	4.90		...	
9	64.94999(7)	−50.35791(4)	6.8 ± 2.6	3.14		...	
10	65.02032(7)	−50.39973(3)	4.8 ± 2.2	1.26		...	
11	64.95730(4)	−50.32857(7)	4.4 ± 2.2	3.98		...	
12	65.03470(6)	−50.32266(4)	2.8 ± 1.7	3.40		...	

Note: Equatorial coordinates, detected counts and off-axis angles as observed in the first epoch observation (2002); errors are 1σ. We also list the distance (in arcsec and in units of the standard deviation of the X-ray position) to the closest optical object as found in the USNO-B1.0 catalogue, as well as the object R magnitude.

accordingly not performed.

A given simulation consists of an artificial event list that is the result of the composite contributions of a central target, reference sources and background noise to the total number of X-ray photons as they would be detected by the ACIS cameras, for a specific observing configuration and as a function of time. MARX simulates the probability of every emitted photon of being detected by ACIS by actually tracing its expected grazing incidence through the telescope mirror assembly. Among many other factors, this probability is strongly dependent on the emitted photon energy and on the angle of the emitting X-ray source to the telescope optical axis.

For each simulation, the core program creates an output directory consisting of binary vectors that store the properties of each "detected" photon: arrival time, energy, focal plane location, detected pulse height, etc. Post-processing tools can then be used to convert this native format to other formats, such as the usual FITS event list file that can be analyzed using the packages in CIAO as for a real Chandra observation. The start time of the simulation is provided as input in order to reproduce the appropriate quantum efficiency of the ACIS chips, which is worsening with time probably as a consequence of the increase of the level of molecular contamination on the optical blocking filters of the detectors (Chandra POG). MARX also takes as input the duration of the observation, the detector type at the aimpoint, the pointing nominal coordinates and roll angle, as well as the spatial extent and spectral energy distribution of the simulated source, its celestial coordinates and observed flux. For all simulations, we used the internal aspect dithering model built in MARX.

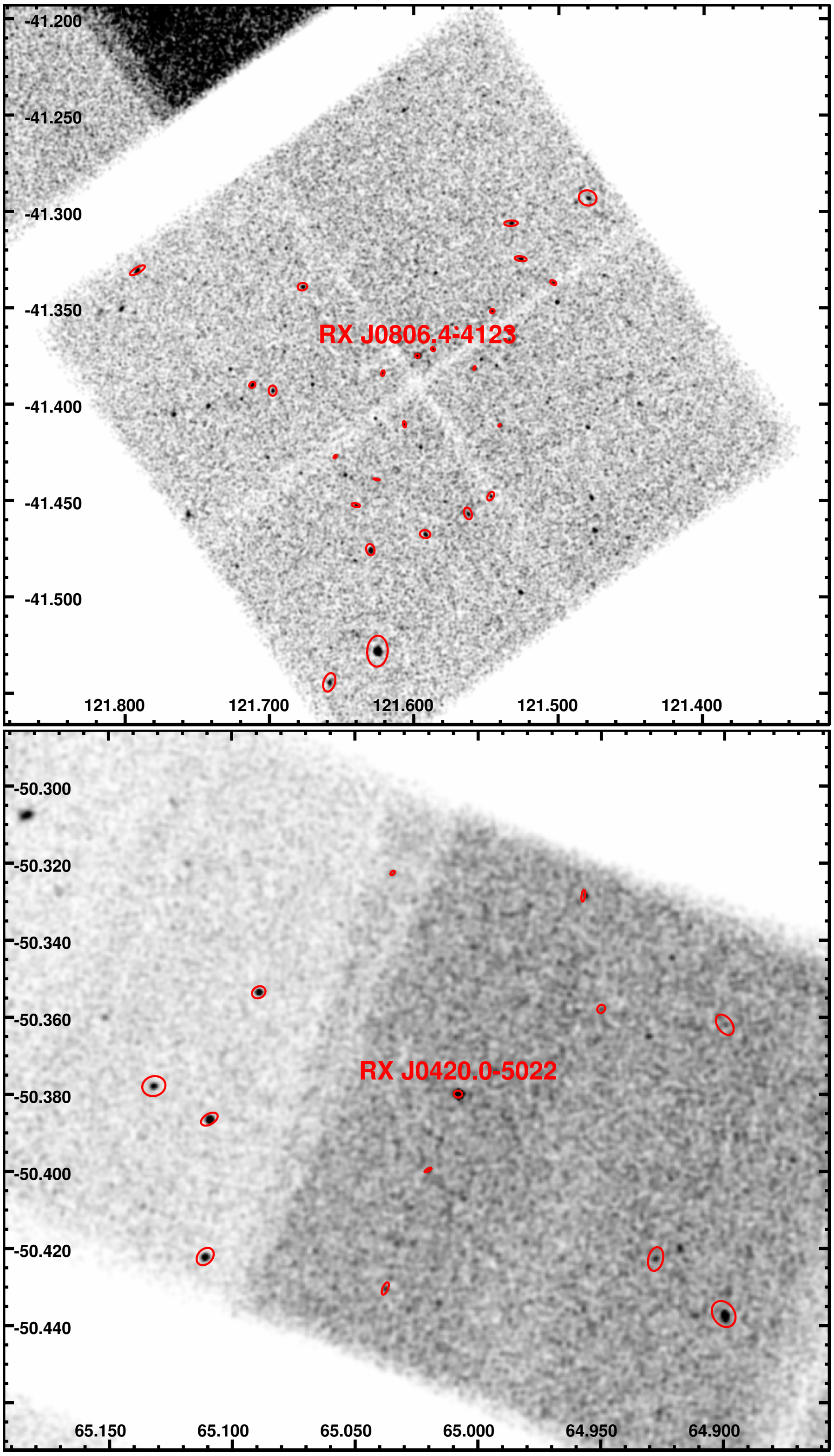

Figure 2.4: ACIS images of the fields of RX J0806.4-4123 and RX J0420.0-5022 with the positions of reference sources and central target highlighted by ellipses (which correspond to 3σ of their wavdetect errors). The images were smoothed using a Gaussian filter of 2 pixels in size and binned (the field in ACIS-S is also zoomed in by a factor of 2).

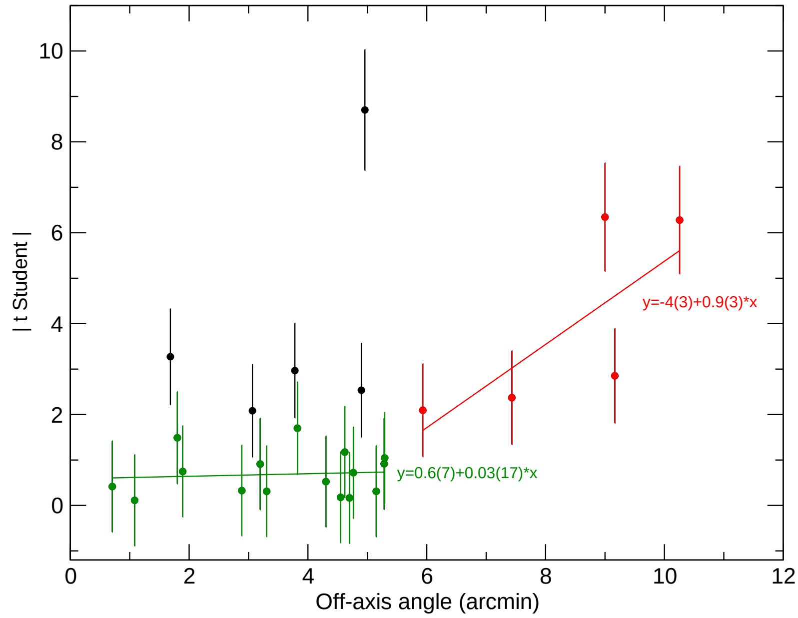

Figure 2.5: t-Student statistics as a function of off-axis angle for the 26 simulated reference sources in ACIS-I configuration. For sources in green, which show an acceptable value of t (see text), no correlation with off-axis angle is present while for sources in red, located at off-axis angles larger than $\sim 5.5'$, a correlation is clearly visible. The remaining sources with $t > 2$ are mostly situated close to the CCD gaps of the ACIS detectors.

Each source has to be simulated individually in a MARX run; the simulations are then merged into a single event list that keeps every photon's arrival time and properties as if they were emitting simultaneously. We made sure that every simulated source in a given epoch is independent from one to another by using a randomly generated numerical seed. By means of repeated simulations of a given reference source, we verified that their output count histogram is well in agreement with the expected Poisson distribution, no matter the brightness of the source (Fig. 2.3).

Since our goal was to reproduce as closely as possible the real observations, the simulated sources were in identical number and had the same positions and photon fluxes as those actually detected and that were common to both epochs up to a maximum distance of $1''$. Source parameters were determined in the 2002 and 2005 event files with wavdetect using the 0.5 – 5 keV energy band and a detection threshold of 10^{-6} for the field of RX J0806.4-4123 whereas, for ACIS-S, we used the 0.5 – 2 keV energy band and a threshold of 10^{-5}. These amount to respectively 26 and 12 reference sources, together with the central targets, to be simulated individually with MARX. Their positions across the ACIS chips can be seen in Fig. 2.4, where the images of the second epoch were reprojected to the tangential planes of the first epochs, in order to show the common sources. In Tables 2.3 and 2.4 the detected properties of the sources used to create the ACIS-I and ACIS-S simulations are listed.

The reference sources are located at maximum off-axis angles as large as $10'$ and $6'$ for the fields of RX J0806.4-4123 and RX J0420.0-5022, respectively, with average values of $4.5'$ and $3.7'$. Given the large distances to the aimpoint, the exposure maps and vignetting factors as a function of off-axis angle have to be taken into account while simulating the Chandra observations. Indeed, a simple statistical t-Student test conducted for the simulated field in ACIS-I configuration showed that a clear systematic correlation is present for sources located at large off-axis angles (Fig. 2.5). In this figure, all 16 sources with an acceptable value of $|t| = \frac{|\bar{\phi}-\phi_0|}{\sigma_{\bar{\phi}}} \leq t_{\rm cr} \equiv 2$ (for 49 degrees of freedom at 95% confidence level), where ϕ_0 is the source observed photon flux and $\bar{\phi}$ and $\sigma_{\bar{\phi}}$ are the average and mean standard deviation of 50 MARX simulations, are located not farther than an off-axis angle of $\sim 5.5'$. In order to take vignetting into account, we corrected the input photon fluxes of each X-ray reference source so as to reproduce the observed intensities as detected by celldetect and wavdetect. In Fig. 2.6 we compare the output counts of MARX sources (detected with wavdetect) to the counts of the real background reference sources.

As can be seen in Tables 2.3 and 2.4, the reference sources are too faint to allow significant constraining of their spectral energy distribution. We have looked for possible optical counterparts in the USNO-B1.0 catalogue and searched for finding charts in order to verify the assumption of an extragalactic origin. We list in the same Tables 2.3 and 2.4 the magnitudes of the optical objects lying within a maximum distance of $1''$ from the position of the X-ray source. Eight out of twenty-six (30%) of the reference sources in the field of RX J0806.4-4123 have optical objects lying within 4σ of their X-ray positions, showing a mean R magnitude of $m_{\rm R} \sim 16$. For the field of RX J0420.0-5022, this fraction is 25% and the mean magnitude is much fainter, $m_{\rm R} \sim 20$. These are well in agreement with what is expected for both fields, respectively located in the Galactic plane and at high galactic latitude. Finding charts of both fields can be seen in Appendix C, Figs. C.1 to C.4, for the field of RX J0806.4-4123, and C.5 to C.6, for the one of RX J0420.0-5022. As already mentioned, it is very likely that the sources with possible bright optical counterparts in the field of RX J0806.4-4123 consist of Galactic late-type stars instead of AGN; however, the assumption that the combined effect of their proper motion on the accuracy of the astrometry is small compared to the overall error budget is still valid.

Therefore, we assumed that the spectrum of the background sources is described by that typical of an AGN, i.e. an absorbed power-law of photon index $\Gamma = 1.7$, undergoing a hydrogen column density of $N_{\rm H} = 5.21 \times 10^{21}\,{\rm cm}^{-2}$ (for the field of RX J0806.4-4123) and $N_{\rm H} = 1.07 \times 10^{20}\,{\rm cm}^{-2}$ (for the field of RX J0420.0-5022). The total Galactic column densities were derived from the far infrared emission maps of Schlegel et al. (1998)[13], then applying the Predehl & Schmitt (1995) relation between optical and X-ray absorptions:

$$N_{\rm H} = (1.79 \pm 0.03) A_{\rm V} \times 10^{21}\,{\rm cm}^{-2} \tag{2.5}$$

The energy distribution of the neutron stars were taken as blackbodies with $kT = 96\,{\rm eV}$ and $kT = 44\,{\rm eV}$ absorbed by $N_{\rm H} = 4 \times 10^{19}\,{\rm cm}^{-2}$ and $N_{\rm H} = 1 \times 10^{20}\,{\rm cm}^{-2}$, for RX J0806.4-4123 and RX J0420.0-5022, respectively. Input count spectra were generated using the

[13] Also available from the NASA/IPAC Extragalactic Database, `http://nedwww.ipac.caltech.edu/forms/calculator.html`

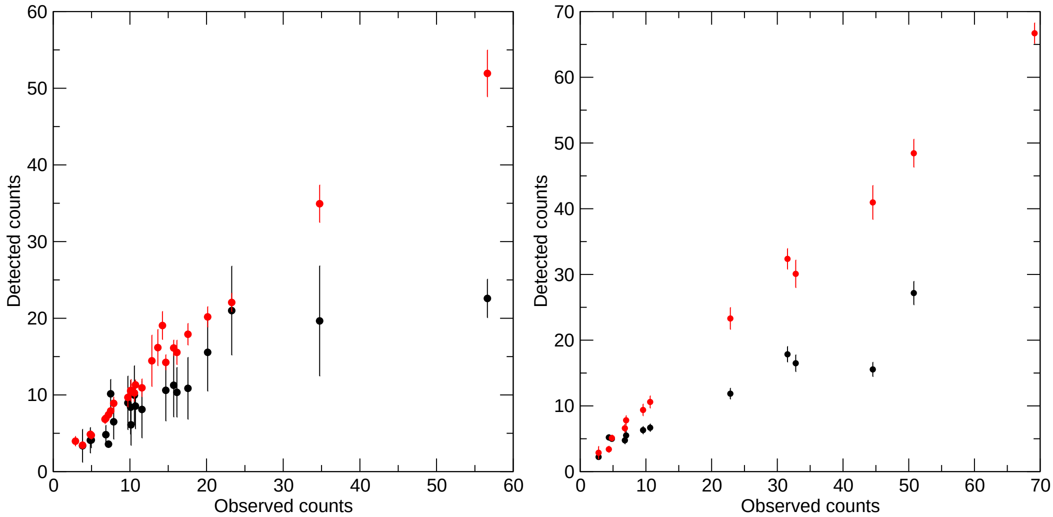

Figure 2.6: Detected *vs.* observed (in Chandra observations) counts for the simulated sources in ACIS-I (left) and ACIS-S (right) configurations. We show in black the average detected counts before taking into account the vignetting correction for each source. Symbols in red, after correction, show the good agreement between simulated and real sources for both ACIS configurations in our MARX simulations.

X-ray spectral fitting package XSPEC 12.2.1[14].

We created a diffuse background for each simulation using the observed deep blank fields provided by the Chandra calibration database[15], by re-projecting them to the tangent plane of the observations and, for each epoch simulation, by randomly picking background events so as to reproduce the level of background noise of the actual observation in the 0.5 – 5 keV energy band. Since the calibration blank fields have a number of events a factor of 10 to 25 times that needed for one of our epoch simulations, we ensure that, by randomizing the arrival times of the background events, each simulation has a different noise background. Finally, sources and background were merged into a single event file. The steps of creation of a simulated 2002 epoch for ACIS-I can be seen in Fig. 2.7.

In order to evaluate the effect of unknown observing conditions that may affect the final achievable precision, we allowed for slightly different aimpoint positions in the simulations and for systematic offsets of the reference frames between the two epochs. Table 2.5 lists the parameters of the 14 different settings used for the first and second epoch ACIS-I/S simulations. We applied three different target displacements, $d_t = 0.34'', 0.75'', 1.00''$, to the position of the central soft X-ray source representing the neutron star in the event file of the second epoch. We also simulated a pair of epochs, R14, for which the coordinates of the central target are not changed between epochs. A number of other parameters were tested as well. We changed the aimpoint coordinates of the simulations by fractions of a ACIS CCD pixel (size of 0.492″), $d_{ap} = 0.25, 0.50, 0.67$ pix, relative to the aimpoint coordinates

[14]See (Arnaud 1996; 2004); http://heasarc.gsfc.nasa.gov/docs/xanadu/xspec/
[15]http://cxc.harvard.edu/caldb/calibration/acis.html

Table 2.5: Simulation parameters.

Run	Epoch	d_{ap} (pixel)	$\Delta\alpha_{ap}$ (arcsec)	$\Delta\delta_{ap}$	d_t (arcsec)	$\Delta\alpha_t$ (arcsec)	$\Delta\delta_t$
R1	1	Nom.	0.000	0.000			
	2	Nom.	0.000	0.000	1.00	−0.707	−0.707
R2⋆	1	Nom.	0.000	0.000			
	2	Nom.	0.000	0.000	1.00	−0.707	−0.707
R3	1	0.25	−0.123	0.000			
	2	0.25	−0.123	0.000	1.00	−0.707	−0.707
R4	1	0.50	0.000	−0.246			
	2	0.50	0.000	−0.246	1.00	−0.707	−0.707
R5	1	0.67	0.232	0.232			
	2	0.67	0.232	0.232	1.00	−0.707	−0.707
R6	1	Nom.	0.000	0.000			
	2	Nom.	0.000	0.000	0.75	−0.375	−0.650
R7	1	0.25	−0.123	0.000			
	2	0.25	−0.123	0.000	0.75	−0.375	−0.650
R8	1	0.50	0.000	−0.246			
	2	0.50	0.000	−0.246	0.75	−0.375	−0.650
R9	1	0.67	0.232	0.232			
	2	0.67	0.232	0.232	0.75	−0.375	−0.650
R10	1	Nom.	0.000	0.000			
	2	Nom.	0.000	0.000	0.34	+0.232	+0.253
R11	1	0.25	−0.123	0.000			
	2	0.25	−0.123	0.000	0.34	+0.232	+0.253
R12	1	0.50	0.000	−0.246			
	2	0.50	0.000	−0.246	0.34	+0.232	+0.253
R13	1	0.67	0.232	0.232			
	2	0.67	0.232	0.232	0.34	+0.232	+0.253
R14	1	Nom.	0.000	0.000			
	2	Nom.	0.000	0.000	0.00	0.000	0.000

Note: For the simulation run marked with a star, all source positions in the second epoch were offset by a fraction of an arcsecond (see text).

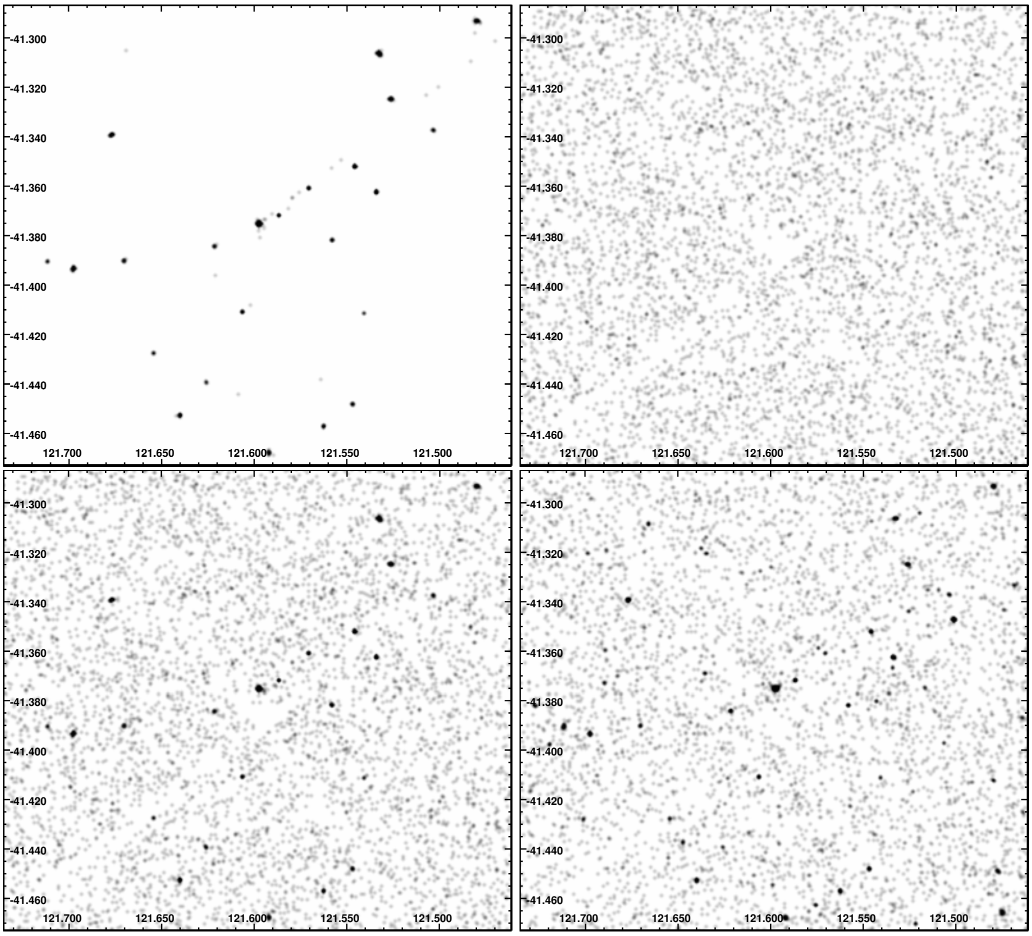

Figure 2.7: Steps of creation of a simulated event file (first epoch observation of the field of RX J0806.4-4123). *Top:* Simulated source and background event files. *Bottom:* Merged simulated event file and real Chandra observation. All event files were filtered in the 0.5 – 5 keV energy band. Images are zoomed around the aimpoint (central ACIS-I CCDs) and were smoothed using a Gaussian filter of size 2 pixels.

α_{NOM} and δ_{NOM} in Table 2.1, in order to produce slightly different distributions of the source PSF on the pixel grid. We note, however, that the slow Lissajous-shaped dithering applied to Chandra pointing during observations should smear out PSF effects to a large extent. A systematic offset of $0.29''$ ($\pm0.15''$ and $\pm0.25''$ in α and δ, respectively) was applied to the 2005 coordinate system of run R2 to test our ability to correct for small shifts in the astrometric frames. Additionally, the randomization in pixels – which is part of the standard processing in the Chandra pipeline – was disabled in an extra sample of simulations in order to investigate the impact of this effect on the final positional accuracy. All these artificial observations, in a total of 156 pairs of epochs, were eventually processed by the same pipeline as the real data and subjected to the source detection algorithms celldetect and wavdetect, resulting in 4620 independent matchings.

Table 2.6: Number of reference sources common to both epoch simulations, as a function of detection algorithm and randomization state.

Pixel Randomization	ACIS-I celldetect	ACIS-I wavdetect	ACIS-S celldetect	ACIS-S wavdetect
applied	8.27 ± 0.32	14.82 ± 0.23	6.15 ± 0.12	6.92 ± 0.12
not applied	7.80 ± 0.22	14.77 ± 0.17	6.44 ± 0.08	7.25 ± 0.07

Note: Results averaged over all energy bands and detection thresholds used. Errors are 1σ.

Table 2.7: Frame error as a function of detection algorithm, randomization state and energy band.

Pixel Randomization	ACIS-I celldetect	ACIS-I wavdetect	ACIS-S celldetect	ACIS-S wavdetect
applied	0.127(27)	0.123(26)	0.15(4)	0.17(4)
not applied	0.130(18)	0.119(15)	0.161(24)	0.17(3)
Energy Band (keV)	**ACIS-I celldetect**	**ACIS-I wavdetect**	**ACIS-S celldetect**	**ACIS-S wavdetect**
0.3 – 10	0.128(18)	0.117(15)	0.162(27)	0.180(28)
0.3 – 5	0.126(16)	0.119(17)	0.16(3)	0.17(3)
0.5 – 5	0.125(16)	0.120(17)	0.16(3)	0.17(3)
0.3 – 3	0.140(24)	0.129(18)	0.15(3)	0.17(3)
0.5 – 2	0.14(3)	0.133(17)	0.158(28)	0.183(29)

Note: Results are averaged over all configurations that provided more than 12 and 7 common sources for the fields of RX J0806.4-4123 and RX J0420.0-5022, respectively. Errors are 1σ and units are arcsec.

Results of simulations Probably as a consequence of the background and photon counting noises introduced in the simulations, none of the detection algorithms could recover all of the simulated reference sources, although generally wavdetect has proved to be a more efficient detecting tool. For ACIS-I simulations, the celldetect and wavdetect efficiencies were roughly 31% and 57%, averaging over all energy bands and detection thresholds used. Interestingly, for ACIS-S, the difference between the two packages was not as noticeable, with efficiencies around 52% and 59% for celldetect and wavdetect, respectively. No significant differences in the number of detected sources have been noticed between the sample of simulations with or without the randomization in pixel applied (Table 2.6).

We evaluated the relative merits of the two detection methods using as criterion the statistical error derived from the relative frame matching between the two epochs, $\sigma_{\rm fr}$, Eq. (2.3). Table 2.7 lists the distribution of these frame errors for ACIS-I and ACIS-S, first as a function of randomization state, averaging over all combinations of energy bands and detection thresholds for which the number of common sources was greater than 12

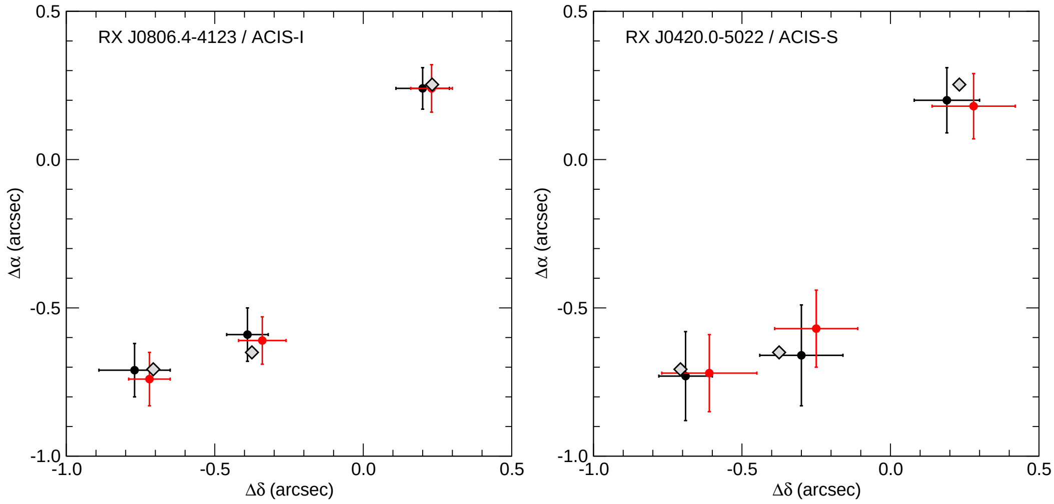

Figure 2.8: Mean displacements in α and δ, averaged over the selected simulations (see text), compared to their input values (diamonds). Error bars show the standard deviation of the measurement values. Black and red symbols denote celldetect and wavdetect, respectively.

(ACIS-I) and 7 (ACIS-S). Then, we give the results as a function of energy band, averaging over randomized and de-randomized simulations and applying the same restrictions for the number of reference sources. Neither of the two algorithms proves a clear-cut advantage, their performances remain statistically consistent with each other. In general, while for simulations of the field of RX J0806.4-4123 wavdetect provides smaller dispersions, the opposite is true for the field of RX J0420.0-5022. Removing the pixel randomization while keeping all other parameters identical does not significantly improve the source centering accuracy, a conclusion that was also obtained by Kaplan et al. (2009a), De Luca et al. (2009) for Chandra ACIS data.

Not unexpectedly, the energy band considered for source detection also affects to some extent the accuracy with which X-ray sources are centered. Wide bands allow more sources to be detected, but introduce a higher background. For ACIS-S simulations, the wider (0.3 – 10 keV) and narrower (0.5 – 2 keV) bands tend to yield slightly worse errors on positions. For ACIS-I, on the other hand, the two narrower bands (0.3 – 3 keV and 0.5 – 2 keV) are the ones presenting the largest frame errors. The small offsets in α and δ ($\pm 0.15''$ and $\pm 0.25''$) applied to the coordinate system of the second epoch of run R2 are also properly recovered with our matching method, again regardless of the detection algorithm and randomization state.

We finally checked the accuracy with which the small motion of the simulated neutron star could be sized after frame matching. We show in Fig. 2.8 the measured displacement of the neutron star compared to that entered in the simulation. We imposed the presence of at least 7 reference sources for ACIS-S and 12 for ACIS-I and discarded reductions yielding frame errors larger than the mean of all reductions (within 1σ). Randomized and de-randomized simulations are included. Error bars show the dispersion of the results from the selected reductions and simulations. Shifts as small as $0.34''$ are properly recovered with an accuracy of $0.18''$ and $0.11''$ for the ACIS-S and ACIS-I configurations respectively, using the wavdetect algorithm. Results are in Table 2.9.

2.4.2 Repeated fields

The MARX ray tracing suite relies on the characteristics of the telescope and cameras as measured before launch in the laboratory and later evolved to account for actual flight performances. However, a number of unknown effects might introduce additional errors on the final relative astrometry recoverable in real observations. We thus searched the Chandra archive for repeated observations of extragalactic targets taken under similar conditions as ours, in order to confirm that the relative positioning errors were indeed consistent with those estimated from simulations. Constraints were the existence of a rather bright unsaturated X-ray source with enough relatively faint reference objects around in pairs of ACIS images obtained with as far as possible similar roll angles and exposure times. Not surprisingly, very few observations matched these conditions since only programmes aimed at long or short-term monitoring are good candidates, the rest of the observations usually implying different instrumental configurations. We eventually found 3 pairs of ACIS-I and 3 pairs of ACIS-S observations suitable for the tests. We list in Table 2.8 the main properties of these fields. Images and tables listing the properties of the detected X-ray sources can be seen in Appendix C.

The pairs of observations were processed with exactly the same pipeline as that used for our astrometric programme. In four instances, the source whose position was monitored was the original AGN target. For the two blank field observations in ACIS-I mode, we had to select a relatively bright source located as close as possible to the aimpoint. As for our INS observations, we estimated the displacement of the target source using the combinations of detection thresholds and energy bands providing the lowest $\sigma_{\rm fr}$. We also compared the results obtained with these real observations to the ones of the simulated run R14 (Table 2.5), for which no displacement of the central target was applied.

Results of test fields In general, the results agree well with the simulations. Again, removing pixel randomization does not necessarily improve frame matching. The average values of the frame errors, $\sigma_{\rm fr} \sim 100$ mas, are usually smaller than those obtained by matching the simulated epochs due to the fact that only roughly half to 60% of the simulated background sources are recovered by the detection tools; in the fields of the extragalactic targets a factor of 3 more reference sources are available for matching the frames. Tables C.1 and C.2 in Appendix C can be consulted for a detailed listing of the mean number of common sources and frame errors as a function of randomization state, detection algorithm and energy band, obtained by matching the ensemble of epochs in the test fields.

We list in Table 2.10 the displacement of the central source as measured in the repeated fields and in simulation R14. As expected, none of the targets shows a significant motion on the sky since in all cases its significance remains below or around 1σ. The largest shift is seen on the pair of epochs of FIELD-142549+353248. We note however that the chosen

Table 2.8: Description of archival Chandra observations used as test fields.

Target	Epoch	ObsID	Observation Date	Aimpoint Detector	Data Mode	t_{exp} (ks)	α_{NOM} (deg)	δ_{NOM} (deg)	Roll Angle (deg)
LALA Cetus FIELD	1	4129	2003-06-13	ACIS-I	VFAINT	160.1	31.1837	−5.0882	121.58
(Blank field)	2	4402	2003-06-15	ACIS-I	VFAINT	14.2	31.1837	−5.0882	121.58
PKS 0312−770	1	1109	1999-09-08	ACIS-I	VFAINT	12.8	47.9998	−76.8605	63.86
(Seyfert 1 galaxy)	2	1110	1999-09-08	ACIS-I	VFAINT	12.6	48.1372	−76.8500	63.85
FIELD-142549+353248	1	3130	2002-04-16	ACIS-I	VFAINT	120.1	216.4076	+35.6000	163.43
(Blank field)	2	3482	2002-06-09	ACIS-I	VFAINT	58.5	216.4065	+35.5956	219.94
3C 33	1	6910	2005-11-08	ACIS-S	FAINT	19.9	17.2118	+13.3086	281.46
(Seyfert 2 galaxy)	2	7200	2005-11-12	ACIS-S	FAINT	19.9	17.2119	+13.3086	281.46
3C 325	1	4818	2005-04-17	ACIS-S	VFAINT	29.6	237.4793	+62.6960	145.23
(Quasar)	2	6267	2005-04-14	ACIS-S	VFAINT	28.7	237.4792	+62.6960	145.23
MG J0414+0534	1	3395	2001-11-09	ACIS-S	FAINT	28.4	63.6638	+5.5861	57.36
(Quasar)	2	3419	2002-01-08	ACIS-S	VFAINT	96.7	63.6637	+5.5860	295.24

Note: The sources used as central targets are the source located at 02:04:46.5 +05:04:04.4, PKS 0312-770, the source at 14:25:47.1 +35:39:54.8, 3C 33, 3C 325 and MG J0414+0534, respectively, for each pair of observations. Listed are the nominal coordinates α_{NOM}, δ_{NOM} and roll angle of the observations, as well as the exposure times t_{exp} filtered for background events. All observations were taken in TE read mode with no gratings (Appendix B.1.2).

Table 2.9: Measured displacements of the central target in the ACIS-I/S simulations.

Input	ACIS-I		ACIS-S	
d_t	celldetect	wavdetect	celldetect	wavdetect
1.00	1.05 ± 0.15	1.03 ± 0.11	1.00 ± 0.17	0.94 ± 0.21
0.75	0.71 ± 0.11	0.70 ± 0.11	0.72 ± 0.22	0.62 ± 0.19
0.34	0.31 ± 0.11	0.33 ± 0.11	0.28 ± 0.16	0.33 ± 0.18
Input	ACIS-I		ACIS-S	
$\Delta\alpha_t$	celldetect	wavdetect	celldetect	wavdetect
−0.707	−0.77 ± 0.12	−0.72 ± 0.07	−0.69 ± 0.09	−0.61 ± 0.16
−0.375	−0.39 ± 0.07	−0.34 ± 0.08	−0.30 ± 0.14	−0.25 ± 0.14
+0.232	+0.20 ± 0.09	+0.23 ± 0.07	+0.19 ± 0.11	+0.28 ± 0.14
Input	ACIS-I		ACIS-S	
$\Delta\delta_t$	celldetect	wavdetect	celldetect	wavdetect
−0.707	−0.71 ± 0.09	−0.74 ± 0.09	−0.73 ± 0.15	−0.72 ± 0.13
−0.650	−0.59 ± 0.09	−0.61 ± 0.08	−0.66 ± 0.17	−0.57 ± 0.13
+0.253	+0.24 ± 0.07	+0.24 ± 0.08	+0.20 ± 0.11	+0.18 ± 0.11

Note: Results are averaged over all configurations that provided more than 12 and 7 common sources for the fields of RX J0806.4-4123 and RX J0420.0-5022, respectively, additionally restricting configurations with $\sigma_{\rm fr}$ smaller than the average (within 1σ). Errors are 1σ and units are arcsec.

Table 2.10: Measured displacements of the central target in the repeated fields and in simulation R14.

Field	d_t		d_t Simulation R14	
	celldetect	wavdetect	celldetect	wavdetect
LALA Cetus FIELD	0.16 ± 0.27	0.11 ± 0.16		
PKS 0312-770	0.15 ± 0.10	0.12 ± 0.10	0.17 ± 0.14	0.12 ± 0.12
FIELD-142549+353248	0.40 ± 0.16	0.55 ± 0.16		
3C 33	0.20 ± 0.13	0.07 ± 0.11		
3C 325	0.08 ± 0.12	0.04 ± 0.09	0.18 ± 0.17	0.22 ± 0.19
MG J0414+0534	0.12 ± 0.10	0.08 ± 0.09		

Note: Results are averaged over all configurations with $\sigma_{\rm fr}$ smaller than the average (within 1σ). Errors are 1σ and units are arcsec.

Table 2.11: Number of reference sources common to both epoch observations of the three INSs, as a function of detection algorithm and randomization state.

Pixel	RX J0806.4-4123		RX J0420.0-5022		RX J1308.6+2127	
Randomiz.	celldetect	wavdetect	celldetect	wavdetect	celldetect	wavdetect
applied	5.7 ± 0.8	15.4 ± 1.3	6.8 ± 0.6	8.7 ± 0.4	11.6 ± 0.8	14.6 ± 0.9
not applied	6.9 ± 0.8	15.9 ± 1.3	7.0 ± 0.6	8.7 ± 0.4	11.3 ± 0.9	14.8 ± 0.8

Note: Results averaged over all energy bands and detection thresholds used. Errors are 1σ.

target for this field is the X-ray faintest among the tested central sources and additionally it is the one located at the largest off-axis angle, $\sim 3'$ (see Table C.5). In all other cases, the displacement of the bright source measured after matching the astrometric frames is smaller than 130 mas, on average. Although the final precision of the proper motion measurement depends on the quality and efficiency of the detection and centering method applied, no significant difference is seen between the values retrieved for the displacement of the central source either using wavdetect or celldetect source lists. Moreover, results obtained for simulated run R14 in ACIS-I/S configuration are fairly consistent with those of the test fields. Interestingly, small shifts in the coordinates of the aimpoint and large changes in the roll angle do not seem to impact the accuracy of the relative astrometry much.

2.5 Results

The simulations and test fields gave us high confidence in the possibility of measuring small displacements of unresolved X-ray sources with ACIS. In the following we report the analysis and results of the real Chandra observations of the three targeted M7. Similarly to the procedure conducted before, we first analyze the relative importance of the several tested sets of parameters to the overall astrometry. Then, we proceed to selecting the reductions that provide the most accurate matchings in order to determine any proper motion of the studied neutron star.

First of all, we investigated how the inclusion of reference sources showing different positional offsets between epochs affects the frame transformation. In general, the sources which exhibited significant offsets were either located at large off-axis angles or had a very small detection significance, suggesting a spurious detection. Several test runs performed on the data showed that smaller frame errors were obtained when positions between epochs were within $1''$. In order to avoid degrading the final frame accuracy, we only included in the frame transformation the reference sources showing offsets no larger than this maximum value, with no significant loss to the total number of common sources.

Altogether, the density of field sources around the two INSs observed with ACIS-I are comparable and considering the very similar effective exposure times can be directly estimated from Fig. 2.9, which shows the average number of sources detected per epoch and the number of common sources as a function of wavdetect detection threshold. For

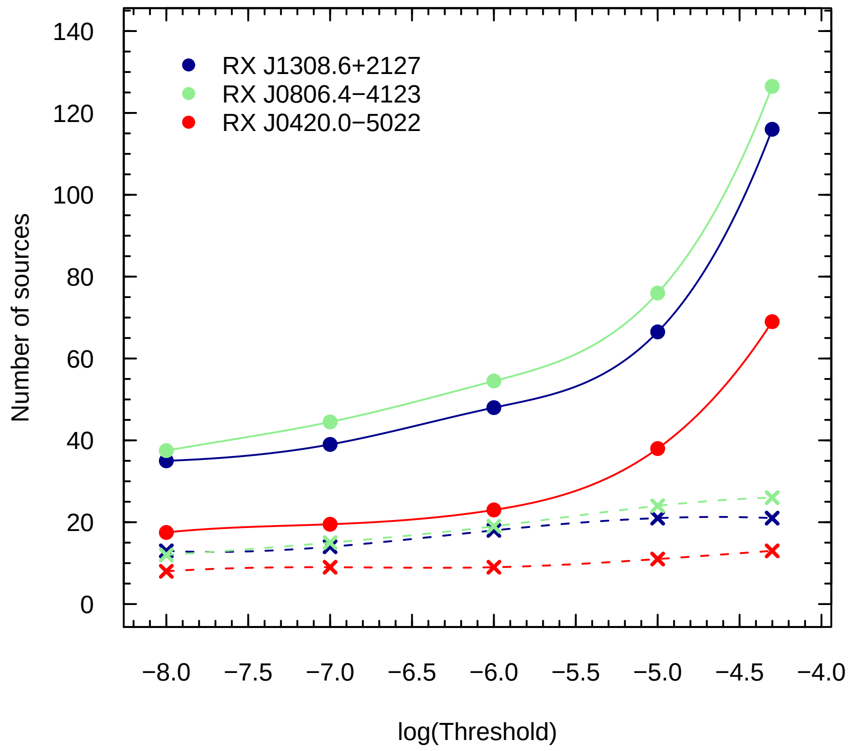

Figure 2.9: Number of sources as a function of wavdetect detection threshold. Filled circles show the mean number of sources per epoch for each INS field while crosses show the number of reference sources common to both epochs. Results for energy band 0.3 – 5 keV and randomized data.

illustrative purposes, data presented here are for the 0.3 – 5 keV energy band with pixel randomization applied. The slightly higher number of detections around RX J0806.4-4123 is likely due to the already mentioned contribution by additional stellar coronae to this low galactic latitude field. The number of ACIS-S detections is also very close to half that in ACIS-I, in accord with the ratio of the FoV used for the two configurations. Not unexpectedly, Fig. 2.9 shows that the number of detections dramatically rises with increasing sensitivity, reflecting the enhancement of the number of false sources. For RX J0806.4-4123 and RX J1308.6+2127 (ACIS-I), the number of sources detected in each field increases by a factor of ~ 1.4 when the threshold rises from 10^{-6} to 10^{-5}. In contrast, the number of sources common to the two observations, which therefore have a high probability of being real, increases much more slowly with detection threshold. A significant number of high-likelihood sources are not recovered from one observation to the next. At very low thresholds of 10^{-7} or 10^{-8}, for which the number of spurious detections should be neg-

Table 2.12: Frame error as a function of detection algorithm, randomization state and energy band for the Chandra observations of the three INSs.

Pixel Randomiz.	RX J0806.4-4123 celldetect	RX J0806.4-4123 wavdetect	RX J0420.0-5022 celldetect	RX J0420.0-5022 wavdetect	RX J1308.6+2127 celldetect	RX J1308.6+2127 wavdetect
applied	0.124(9)	0.094(15)	0.187(19)	0.188(25)	0.143(13)	0.122(9)
not applied	0.141(23)	0.116(15)	0.20(3)	0.179(22)	0.129(21)	0.100(10)
Energy Band (keV)	**RX J0806.4-4123 celldetect**	**RX J0806.4-4123 wavdetect**	**RX J0420.0-5022 celldetect**	**RX J0420.0-5022 wavdetect**	**RX J1308.6+2127 celldetect**	**RX J1308.6+2127 wavdetect**
0.3 – 10	0.136(3)	0.094(9)	0.20(4)	0.198(10)	0.141(23)	0.108(14)
0.3 – 5	0.129(20)	0.101(17)	0.194(24)	0.169(17)	0.129(10)	0.109(18)
0.5 – 5	0.132(12)	0.101(57)	0.187(21)	0.178(13)	0.126(12)	0.109(9)
0.3 – 3	0.23(5)	0.126(15)	0.201(26)	0.167(18)	0.153(20)	0.121(24)
0.5 – 2	0.25(7)	0.13(11)	0.24(4)	0.210(20)	0.139(6)	0.117(12)

Note: Results are averaged over all configurations that provided more than 12 and 7 common sources for the fields observed in ACIS-I and ACIS-S, respectively. Errors are 1σ and units are arcsec.

ligible, only one third of all sources are detected at both epochs. Selecting the brightest sources only, half of them are still not recovered from one observation to the other. This strongly suggests that a large fraction of extragalactic sources, mostly AGN, are significantly variable on a timescale of several years.

We list in Tables 2.11 and 2.12 the average number of common reference sources and frame error on the transformation resulting by matching the two epochs of observations of the INSs. Qualitatively, the figures are well in agreement with those obtained before, i.e. wavdetect has proved to be a more efficient detection tool relative to celldetect especially for the ACIS-I observations of RX J0806.4-4123; the results either removing or not the randomization in pixel are consistent with each other within errors; the process of filtering in energy slightly affects the accuracy at which sources are centered in the same way as in the respective ACIS-I/S simulations. Interestingly, the final precision of the astrometry obtained with celldetect is systematically worse than that obtained with wavdetect, although the results are generally statistically consistent with each other. This is also generally true for the simulations and test fields, with the exception of the results obtained for the simulations in ACIS-S mode.

These results are illustrated in Fig. 2.10, where we plot the frame accuracy $\sigma_{\rm fr}$ as a function of the number of background reference sources available for frame matching. The different plots show the relative influence of the tested parameters on the final precision at which the proper motion can be measured. From these plots, it is clear that the results obtained for ACIS-I are more accurate than those derived using only the two central CCDs in ACIS-S, which is a natural consequence of the larger FoV. It is also clear that wavdetect systematically provides more accurate sets of source positions for performing frame matching compared to celldetect. On the other hand, the two bottom plots of Fig. 2.10

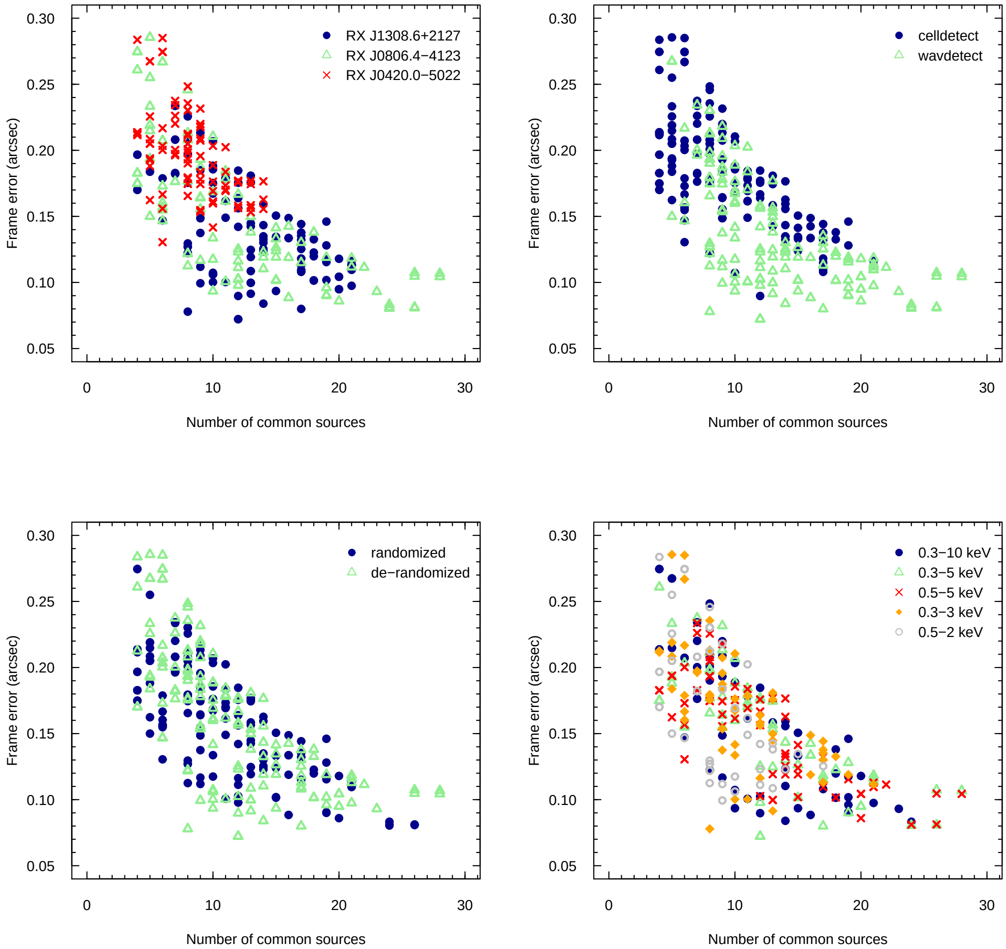

Figure 2.10: Frame error as a function of number of common sources for epoch matching in the observations of the three INSs. On the top left epoch matching is discriminated by observing configuration mode (sources RX J1308.6+2127 and RX J0806.4-4123 in ACIS-I *vs.* source RX J0420.0-5022 in ACIS-S). On the top right the influence of the detection and centering algorithm to the frame errors is seen. The processes of removing the pixel randomization (bottom left) and filtering in energy (bottom right) have a minor impact on the final achieved precision, which further depends on the configuration mode and slightly varies from field to field.

show that the influence of the pixel randomization and energy filtering is more complex and results vary from field to field; no energy band or randomization state clearly shows an advantage relative to the others for the whole analyzed sample of observations. We note, however, that the restricted 0.3 – 5 keV, 0.3 – 3 keV or 0.5 – 5 keV bands usually yield the smallest errors. This behaviour is consistent with the increasing ACIS background above 5 keV and lower number of photons in the narrower 0.5 – 2 keV band and is similar to that found in simulations.

Table 2.13: Best-fit values for epoch matching and results for displacement of the three INSs.

Result	RX J0806.4-4123		RX J0420.0-5022		RX J1308.6+2127	
	celldetect	wavdetect	celldetect	wavdetect	celldetect	wavdetect
$d\alpha$	+0.187(25)	+0.18(5)	−0.10(5)	+0.11(11)	+0.11(4)	+0.07(5)
$d\delta$	−0.32(7)	−0.38(3)	+0.00(10)	+0.19(8)	+0.13(6)	+0.20(4)
$d\theta$	−0.033(13)	−0.017(11)	+0.022(21)	−0.017(26)	+0.017(19)	+0.016(8)
d_{t}	0.20(13)	0.15(10)	0.24(19)	0.17(19)	0.95(13)	1.09(11)
μ_{t}	$\lesssim 87\ (2\sigma)$		$\lesssim 113\ (2\sigma)$		214 ± 14	

Note: Results are averaged over all configurations that provided more than 12 and 7 common sources for the fields observed in ACIS-I and ACIS-S, respectively, and with σ_{fr} smaller than the average (within 1σ). Errors are 1σ. Units are arcsec except for the rotational angle $d\theta$, in degrees, and the proper motion determination μ_{t}, in mas yr^{-1}.

In order to be less sensitive to a particular configuration of reference sources and obtain more conservative errors, we averaged results obtained for the combinations of detection thresholds and energy bands which yielded the lowest frame matching errors[16], with no distinction regarding pixel randomization state. The best matche of the astrometric reference frames (i.e. offsets in right ascension and declination and rotations around the aimpoint – $d\alpha$, $d\delta$, $d\theta$ – c.f. Sect. 2.3.2) were obtained with the parameters listed in Table 2.13. Finally, we list the displacements of the three M7 and their associated errors measured between the two epochs and corrected for the best-fit values for the transformation listed in the same table.

The positions of RX J0806.4-4123 and RX J0420.0-5022 in 2002 and 2005 are consistent within one Gaussian standard deviation (see Fig. C.10 in Appendix C). Considering the best frame transformation for each field, the 2σ upper limits on the proper motions of RX J0806.4-4123 and RX J0420.0-5022 are 87 mas yr^{-1} and 113 mas yr^{-1}, respectively. In contrast, a very significant displacement, with a statistical significance of $\sim 9\sigma$ on average, is detected for RX J1308.6+2127, corresponding to a total proper motion of $\mu = 214 \pm 14$ mas yr^{-1} for the best frame transformation. The magnitude and direction of the displacement with respect to the background reference sources does not depend significantly on the randomization step being applied or not in the processing of the individual photons, nor on the number of sources considered to perform the transformation. Expressed in J2000 equatorial and in galactic coordinates, the proper motion vector of RX J1308.6+2127 is:

$$
\begin{array}{rclcrcl}
\mu_\alpha \cos(\delta) & = & -199 \pm 10\,\mathrm{mas\,yr^{-1}} & ; & \mu_\delta & = & 75 \pm 10\,\mathrm{mas\,yr^{-1}} \\
\mu_l \cos(l) & = & -123 \pm 17\,\mathrm{mas\,yr^{-1}} & ; & \mu_b & = & 174 \pm 14\,\mathrm{mas\,yr^{-1}}
\end{array}
$$

The source is therefore moving towards higher galactic latitudes as would be expected for a neutron star born in the Galactic plane. Such a large neutron star transverse motion

[16] As for the simulations and test fields, we selected matche that provided at least 12 and 7 common sources for ACIS-I/S and with frame errors within 1σ of their means in Table 2.12.

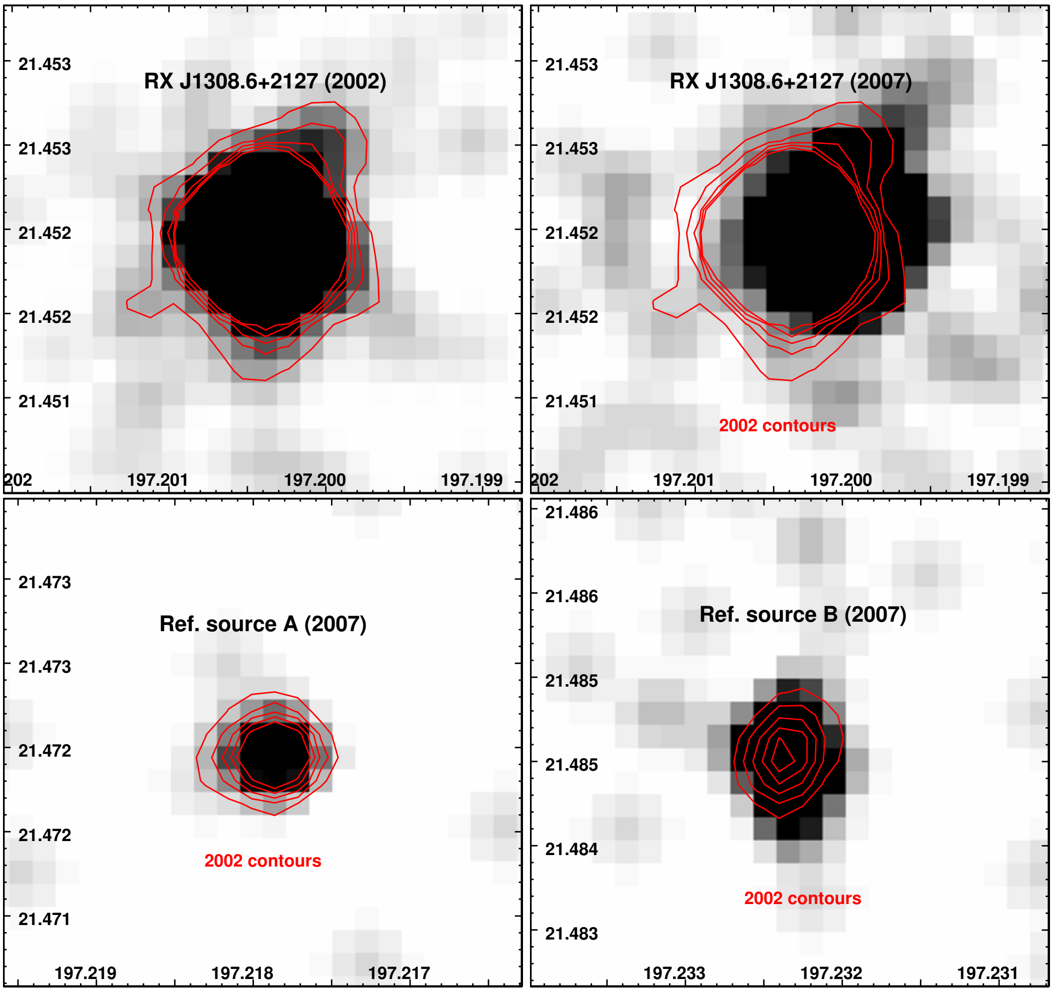

Figure 2.11: Proper motion of RX J1308.6+2127 as measured in a five-year time span. The first epoch contours are superposed on the 2002 and 2007 images of RX J1308.6+2127 (top pictures). For comparison, the bottom two pictures display 2007 images of two reference sources exhibiting no displacement relative to their first epoch contours. Images are zoomed by a factor of 32 and were smoothed using a Gaussian filter of size 2 pixels.

can clearly be noticed in the pictures of Fig. 2.11, where we show the 2002 and 2007 images of the source overlayed to the first epoch contours. For comparison, the 2007 images of reference sources showing no displacement at all after five years are also shown. RX J1308.6+2127 is thus the INS displaying the second largest proper motion among the M7, just after the X-ray brightest RX J1856.5-3754.

We note that the proper motions results reported here are fully consistent with those published in Motch et al. (2007b), Motch et al. (2008) and Motch et al. (2009).

2.5.1 Possible age and birth places of RX J1308.6+2127

The accuracy with which Chandra is able to measure proper motion vectors does not exactly compare with what can be achieved for radio pulsars or in the optical using ground-based telescopes or the HST. Nevertheless, the present determination turns out to be quite useful to estimate the possible origin of the neutron star and its likely kinematic age.

Several distance estimates are proposed for RX J1308.6+2127 in the literature. By assuming that the optical emission of the M7 arises from neutron star atmospheres which have similar compositions and emitting areas, Kaplan et al. (2002b) derived a distance of 670 pc scaling from the preliminar parallactic distance determination of RX J1856.5-3754, $d = 140$ pc. The revised value of 160 pc for RX J1856.5-3754 (see discussion in Sect. 2.1.1) increases RX J1308.6+2127 estimate to ~ 760 pc. In spite of being a rather crude estimate, the distance predicted for RX J0720.4-3125 under the same assumption is in fair agreement with that derived from the HST parallax by Kaplan et al. (2007). Based on detailed X-ray light curve and spectral modelling, Schwope et al. (2005) derived distances in range 76 to 380 pc for RX J1308.6+2127. The lower limit resulted from a model that assumed small, isothermal hot spots on the cool stellar surface undetected in X-rays. While this model explained the source spectral energy distribution and the X-ray timing variability, it was regarded as unlikely due to the unknown heating mechanism of the spots. The more realistic surface temperature distribution model based on calculations by Geppert et al. (2004) resulted in a comparable description of the data but a much larger distance estimate.

The growth of the integrated interstellar absorption in the line-of-sight (LOS) has been used by Posselt et al. (2007) to constrain the distance of several of the M7 and nearby pulsars. This method applied to neutron stars having astrometric parallaxes yields consistent values. However, the local ISM absorption models, which rest on the measurement of the Na I line equivalent width in hot or fast rotating stars, has a too sparse coverage at high galactic latitude to be used effectively and has to be replaced by a less accurate analytical description. In addition, the exact value of the photoelectric absorption derived from X-ray modelling somewhat depends on the number and position of the low-energy shallow absorption lines. Fitting the XMM-Newton spectra of RX J1308.6+2127 with two low-energy lines gives $N_{\mathrm{H}} \sim (1.2 - 1.8) \times 10^{20}\,\mathrm{cm}^{-2}$ (Schwope et al. 2007). This column density value suggests a distance of at least ~ 500 pc (Posselt et al. 2007), which would be incompatible with the very short estimate of 76 pc proposed by Schwope et al. (2005). The best distance estimate of RX J1308.6+2127 is thus probably in the range of 400 to 800 pc.

We computed the past trajectories of the neutron star over the last 4 Myr assuming a $\pm 2\sigma$ range in μ_α and μ_δ, present distances from 50 to 1200 pc and radial velocities in the interval of $\pm 700\,\mathrm{km\,s^{-1}}$. We corrected the observed proper motion vector for the displacement of the Sun with respect to the Local Standard of Rest (LSR). Considering the high velocity, low age and proximity of the neutron star and the relatively short time during which we follow it, we neglected effects due to the Galactic gravitational potential and differential Galactic rotation. For most trajectories, these effects should be less than 1% (Bienaymé et al. 2006).

A displacement towards higher galactic latitude does not necessarily imply that RX J1308.6+2127 escapes from the Galactic plane since at $b \sim 80^\circ$ the unknown radial velocity

Table 2.14: Possible birth places of RX J1308.6+2127.

OB Assoc.	Distance (pc)	Age Range (Myr)	d_0 (pc)	$v_{\|\|}$ (km s^{-1})
UpperSco	145	0.55 ± 0.25	260 ± 50	-430 ± 180
SctOB2 A	510	0.90 ± 0.15	535 ± 53	-550 ± 95
SctOB2 B	1170	1.38 ± 0.26	800 ± 90	-520 ± 110

Note: We list the distances of the OB associations and corresponding neutron star flight times, current distances d_0 and radial velocity $v_{||}$ ranges.

dominates the component perpendicular to the Galactic plane. Any radial velocity towards the Earth in excess of a few tens of km s^{-1} would imply that RX J1308.6+2127 was born at a large distance from the Galactic plane and the vast majority of the trajectories escaping from the plane require receding radial velocities.

We first investigated whether some backward trajectories would cross any of the known nearby OB associations. For that purpose we compiled a merged list from the catalogues in Humphreys (1978), Ruprecht et al. (1981) and de Zeeuw et al. (1999), keeping for each association the most accurate information available, mainly the boundaries and mean distances determined by Hipparcos for the nearest groups.

The number of past flight paths crossing any given OB association is low, less than $\sim 2\%$. This reflects the small volume of the targeted associations compared to that sampled in total, which is necessarily large owing to the substantial uncertainties on the proper motion vector, current distance and, more importantly, on the unknown radial velocity. In addition, only a few nearby OB associations are counted in the $l \sim 0° - 20°$ range of galactic longitude from where RX J1308.6+2127 seems to originate. The times at which backward trajectories cross any given group of massive stars show a well defined peaked distribution with a small tail extending to the oldest ages considered in our study (4 Myr), caused by few very low radial velocity trajectories. Hereafter, current distances, d_0, and radial velocities, $v_{||}$, will refer to their mean over all trajectories within one FWHM of the peak of the age distribution.

Our analysis shows that only three OB associations (Table 2.14) could have given birth to RX J1308.6+2127, if it is assumed that the current distance to the neutron star is less than 900 pc. Because of its proximity ($d = 145$ pc), the Upper Scorpius OB association ($l = -17°, 0°; b = 10°, 30°$) exhibits a significant motion which has to be taken into account when computing intersection times. The Upper Scorpius moving group is part of the general Sco OB2 association. Its past position was computed using group proper motion and radial velocity derived from Hipparcos and listed in de Zeeuw et al. (1999). According to Reichen et al. (1990), the Scutum OB2 association is likely to be the superposition on the LOS of two disctinct groups, one located at 510 pc and another at 1.17 kpc. Intersections with more remote ($d > 1.5$ kpc) OB associations – such as Sgr OB1, Sct OB3, Sgr OB7, Ser OB2, Sgr OB6, Ser OB1, Sgr OB4, Sgr OB5 – all imply unrealistic present distances to the source larger than $d_0 = 900$ pc, with average crossing times of the order of 1.5 to

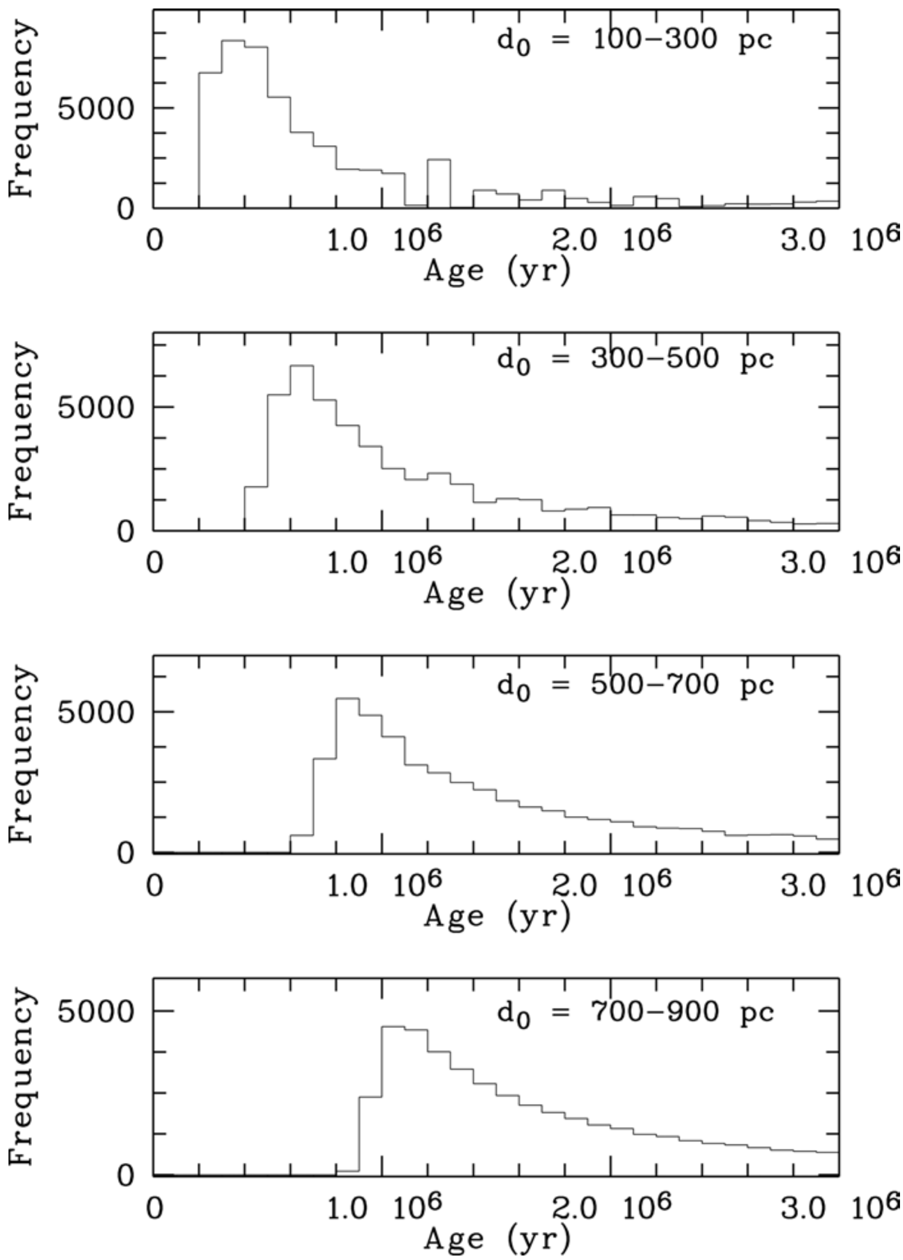

Figure 2.12: Histograms of the crossing times of the Galactic plane for various assumed present distances to source RX J1308.6+2127.

2.2 Myr.

However, a significant number of early-type stars are found far from identified OB associations. The relative fraction of these field stars is not very well constrained and depends on the accuracy of the photometric distances used and on the definition of the chosen boundaries for the associations. According to Garmany (1994), the frequency depends on spectral type, with the fraction of early-type field stars varying from $\sim 40\%$, for stars hotter than B2, to 25%, for O stars only. The majority of field objects are runaway stars identified from their high velocities (Blaauw 1961, Stone 1991) while the rest cannot be related to any group and might therefore be true field stars born outside clusters. Some of the runaway stars can convincingly be associated with the birth of radio pulsars (Hoogerwerf et al. 2001) and were thus ejected from their parent associations in the supernova explosion in a massive binary. Alternatively, the existence of many binary runaway stars (Gies & Bolton 1986) brings support to the dynamical ejection scenario in which early gravitational interaction with one or more cluster stars is responsible for the jump in velocity (Poveda et al. 1967).

In a second step, we thus relaxed the condition of a birth place close to a catalogued OB association and only imposed an origin in the supernova explosion of a field star, assumed to be originally located in the Galactic plane. Fig. 2.12 shows the histograms of the ages at which the backward trajectories intercept the Galactic plane, for different ranges of assumed present distances to the source. In a similar manner as for trajectories impacting OB associations, for a given range of current distances, the age histogram of all trajectories crossing the Galactic plane displays a clear peak with a reduced tail extending to longer times. Although ages older than 2 Myr appear possible for some parameters, the most probable ages peak at values increasing from 0.4 ± 0.2 Myr for $d_0 = 100 - 400$ pc to 1.3 ± 0.3 Myr for $d_0 = 0.8 - 1$ kpc[17]. For the most probable "intermediate" present distance range of 400 to 800 pc, the age distribution peaks at 0.96 ± 0.30 Myr. Galactic longitudes at birth span a sector from approximately $l = -4°$ to $l = +24°$. Old birth dates correspond to large present distances and more remote birth places ranging from 130 pc ($d_0 = 100 - 400$ pc) to 1.6 kpc ($d_0 = 0.8 - 1.2$ kpc). We note that the random position of the progenitor star with respect to the Galactic plane smears to a small extent the travel times computed above. The scale height of O to B5 stars belonging to the local Galactic disk is $\sim 40 - 60$ pc (see Elias et al. 2006; and references therein). Taking this effect into account adds a scatter of $\sim 10^5$ yr to the ages shown in Fig. 2.12.

The main parameter determining the age of RX J1308.6+2127– and which is therefore its most important source of uncertainty – is its present distance d_0. A best guess in range 400 to 800 pc leaves as most likely birth place candidate the OB association Sct OB2 A and an age of 0.90 ± 0.15 Myr. If the early-type star from which RX J1308.6+2127 originates was a field object in the Galactic plane, then comparable ages of 0.96 ± 0.30 Myr appear as most probable.

2.6 Discussion

The proper motion of RX J1308.6+2127 is the second largest among the M7 (Table 2.15). Although the source distance is not well constrained, the present proper motion study and other observational evidence hint that this neutron star is more remote than other high proper motion members of the group; in particular, the nearest RX J1856.5-3754. Therefore, the tangential speed of RX J1308.6+2127 is likely to be considerable, with an estimated value within $v_\perp \sim 400 - 800\,\mathrm{km\,s^{-1}}$. The parameter range of radial velocity con-

[17]The interval of ages quoted here corresponds to the FWHM of the peak of the histogram.

Table 2.15: Proper motions and transverse velocities of the M7.

Source RX	μ (mas yr^{-1})	d (pc)	$v_\perp$ (km s^{-1})	Ref.
J1856.5−3754	333 ± 1	161^{+18}_{-14}	254	(a, b)
J0720.4−3125	107.8 ± 1.2	361^{+172}_{-88}	184	(c)
J1605.3+3249	155 ± 3	~ 390	286	(d)
J1308.6+2127	214 ± 14	$400 - 800$	$410 - 810$	(e)
J2143.0+0654	?	~ 430	?	
J0806.4−4123	< 87	~ 235	$\lesssim 97$	(e)
J0420.0−5022	< 113	~ 345	$\lesssim 185$	(e)

Note: Upper limits are at the 2σ confidence level. *Ref.* [(a)]Kaplan et al. (2002b), [(b)]van Kerkwijk & Kaplan (2007), [(c)]Kaplan et al. (2007), [(d)]Zane et al. (2006), [(e)]Motch et al. (2009).

strained by the backward trajectories is rather large as well, of the order of 550 km s^{-1}, and depends very weakly on the assumed present-day distance. Hence, RX J1308.6+2127 might be crossing the Galaxy with a spatial velocity as high as 1000 km s^{-1}. Although large, such a value is not unsound, as far as neutron stars are concerned. In particular, the transverse velocity of the hyperfast radio pulsar B1508+55, with $v_\perp = 1083^{+103}_{-90}$ km s^{-1}, has been determined in a completely model-independent way, through the direct measurement of both the pulsar parallax and proper motion (Chatterjee et al. 2005). Among the high speed pulsars in the statistical study conducted by Hobbs et al. (2005) are the sources B2011+38 and B2224+64, with two-dimensional speeds around 1600 km s^{-1}. Despite distance uncertainties in the assumed electron scattering model of the ISM implying that transverse speeds inferior to 1000 km s^{-1} cannot be ruled out, the bow-shock nebula detected around pulsar B2224+64, known as the Guitar Nebula, provides evidence that this neutron star is travelling with a speed in excess of 800 km s^{-1} (Cordes et al. 1993, Chatterjee & Cordes 2004). The likely high velocity of RX J1308.6+2127 precludes accretion of matter from the tenuous ISM that is present at the great distance above the Galactic plane where the source is currently located (see Appendix A.2). Undoubtedly, this INS is thus another example of a young cooling neutron star among the M7.

The astrometric study conducted for RX J0806.4-4123 and RX J0420.0-5022 yielded significant constraints on the tangential velocities of these two neutron stars. Assuming the distance estimates from Posselt et al. (2007), one can infer that the sources' transverse speeds lie among the lowest ones, with upper limits of $v_\perp \lesssim 97(d/235\,\text{pc})$ km s^{-1} and $v_\perp = 185(d/345\,\text{pc})$ km s^{-1}, respectively. The value derived for RX J0420.0-5022 is already as low as that inferred for source RX J0720.4-3125, the lowest among all sources for which a measurement exists. Interestingly, the low transverse velocity of source RX J0806.4-4123 and its location in the gas rich environment of the Galactic plane could imply that a fraction of its X-ray luminosity is powered by accretion from the ISM. This possibility is however rather unlikely since the known neutron star spin period and its magnetic field estimate, $P = 11$ s and $B \sim (6-9) \times 10^{13}$ G, would imply that the source could not yet

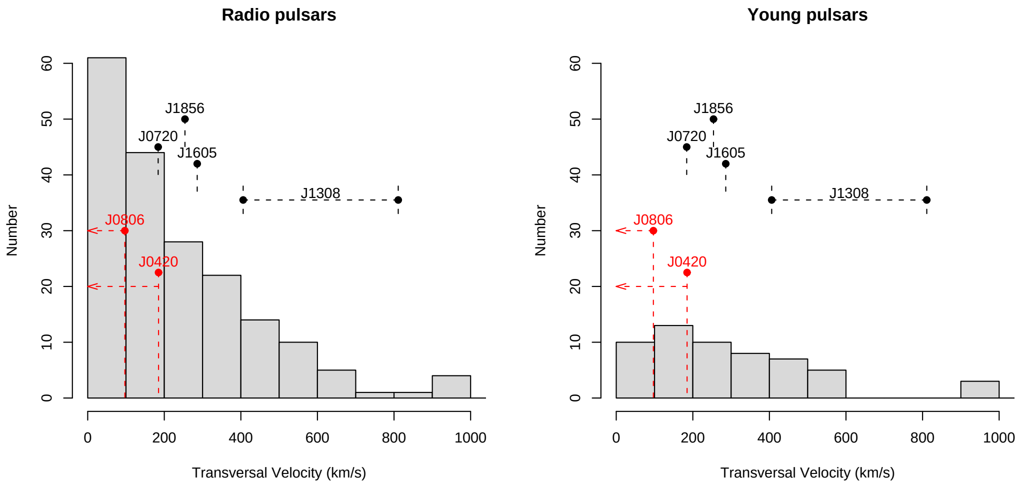

Figure 2.13: Tranverse velocities of some of the M7 compared to the distribution seen in the population of non-recycled radio pulsars from the ATNF catalogue. Also shown is the young population of radio pulsars (age $\lesssim 3$ Myr).

be in the accretor phase (see e.g. Treves et al. 2000). Assuming Bondi-Hoyle accretion, a spatial velocity of $100\,\mathrm{km\,s^{-1}}$, a local medium density of $10\,\mathrm{cm^{-3}}$ and a canonical neutron star mass and radius of $1.4\,M_\odot$ and 10 km, it is mostly the effects of the still fast neutron star rotation[18] that would make accretion impossible at this stage of the neutron star's life. The source would rather be in the ejector phase (c.f. formulae in Appendix A.2). Indeed, RX J0806.4-4123 would have to slow down to a spin period of the order of an hour for accretion to set in, even under these favoured circumstances. Moreover, the source X-ray spectrum and flux stability, rather similar to those of other known cooling members of the group, are at variance with what would be expected for an accreting neutron star.

The present work adds three new measurements or upper limits and doubles the size of the sample of ROSAT-discovered INSs for which information on proper motion exists, leaving the seventh member, RX J2143.0+0654, for further studies. It is now possible to better compare the distribution in transverse velocities of the M7 with that of radio pulsars. We plot in Fig. 2.13 the distribution of transverse velocities of non-recycled pulsars from the ATNF catalogue. The positions of the six INSs are also indicated for comparison. The M7 exhibit two-dimensional velocity distributions consistent with those of radio pulsars. A simple Kolmogorov-Smirnov test gives a probability greater than 50% that the distribution of the M7 tangential velocities is identical to that of the young (age $\lesssim 3$ Myr) radio pulsars. RX J1308.6+2127 fills in the large velocity tail of the radio pulsar distribution thus strengthening the similarity between the two populations. Within the limits enforced by small number statistics, it seems that the different birth conditions leading to the large magnetic fields and long spin periods of the M7 are not related to a specific kick

[18]For these parameters and with $B = 7.5\times10^{13}$ G, the size of the neutron star magnetosphere (i.e. the Alfven radius) would however be smaller than the accretion radius.

mechanism. This extends the apparent lack of dependence of radio pulsar properties on kick velocity (see e.g. Wang et al. 2006a) towards larger magnetic field intensity and spin period.

RX J1308.6+2127 is the fifth brightest INS in the ROSAT PSPC band and might be the first discovered to be born outside of the Gould Belt, either in one of the Sct OB associations or from a field OB star. This INS could thus mark the approximate flux boundary beyond which the production of other more distant OB associations or field stars becomes noticeable. Although higher, we note that the 0.1 – 2.4 keV PSPC count rate of 0.29 s^{-1} is roughly consistent with the expected rate predicted by the population synthesis model of isolated cooling neutron stars of Posselt et al. (2008), ~ 0.1 s^{-1}.

Assuming that the distance to RX J1308.6+2127 is indeed smaller than 800 pc yields ages of less than $t_{\mathrm{kin}} = 0.80$ Myr (for a birth in Upper Sco), 1.05 Myr (for a birth in Sct OB2 A) or 1.26 Myr for a birth from a field early-type star. In contrast, the characteristic age derived from spin-down, $\tau_{\mathrm{ch}} = 1.5$ Myr, is somewhat longer. Similar and even greater disagreements between kinematic travel times and spin-down ages are found for the two other M7 for which the period derivative has been measured (see Sect. 1.3.1.1). In the case of RX J0720.4-3125, the flight time from the most likely parent OB associations is in the range of 0.5 to 1 Myr against a characteristic age of 1.9 Myr (Kaplan et al. 2007). van Kerkwijk & Kaplan (2008) reported the determination of the spin-down of RX J1856.5-3754 with again a huge discrepancy between the kinematic age of 0.4 Myr, consistent with the estimated cooling age of ~ 0.5 Myr, and the much longer spin-down age of 4 Myr.

Several mechanisms have been put forward to explain this discrepancy (see e.g. Kaplan & van Kerkwijk 2005a;b). Among these are a long birth period of the order of several seconds and an early additional braking due to interaction with a fall-back disk. Another mechanism envisaged is magnetic field decay. Originally proposed by Heyl & Kulkarni (1998), it has recently been investigated in greater detail by Aguilera et al. (2008). First, field decay provides through Joule heating an additional source of energy which accounts for a slower decrease of temperature with time. Second, the characteristic times derived from $\dot{P}$ then strongly overestimate the true age of the neutron star. Both effects converge to reconcile the relatively high polar temperatures observed in RX J0720.4-3125 and RX J1308.6+2127 with kinematic ages of up to 1 Myr while explaining the discrepancy between travel times and spin-down ages. In addition, the strongly mass dependent cooling efficiency makes the age temperature relation even more complex. If both mass and kinematic ages were known with enough accuracy, it could become possible, in principle, to estimate the strength of the magnetic field at birth and, in the case of the M7, find out whether these objects have evolved from a magnetar population (age ~ 10^6 yr) or, if middle-aged, were born with lower fields in the range of 10^{13} – 10^{14} G (Aguilera et al. 2008). The magnetic field of RX J1308.6+2127 ($B_{\mathrm{dip}} \sim 4 \times 10^{13}$ G; Schwope et al. 2005) ranks among the lowest of the M7 (Haberl 2007). Decay from a typical magnetar field (B few 10^{14} G) would require an interval of time of the order of $t_{\mathrm{ohm}} \sim 1$ Myr. A large present distance to the source could thus bring some support to a magnetar origin for RX J1308.6+2127. However, the estimated relative birthrate of the M7 and magnetars seems to exclude that the entire group evolved from former magnetars (Popov et al. 2006b).

CHAPTER 3

Searching for thermally emitting isolated neutron stars

Contents

3.1 Introduction

Neutron stars should represent a non-negligible fraction of the stellar content of the Galaxy, with a total number estimated to be more than 10^8, as inferred from constraints on the nucleosynthetic yields produced in core-collapse supernovae and from the known present rate of these events in nearby spiral galaxies. More than 40 years after the discovery of PSR B1919+21, the first observational manifestation of a neutron star as realised by Hewish et al. (1968), radio pulsars still dominate neutron star statistics in spite of the observed sample being rather incomplete: while current estimates of the number of active radio pulsars are several times 10^5, only around 1800 objects are currently known (Sect. 1.2). Yet, if one neutron star is born in the Galaxy every 30 to 100 years, then for every active radio pulsar there must be ~ 1000 radio-quiet neutron stars. Most of these objects are expected to be old – therefore, to have exhausted their internal resources of particle production and acceleration – and, moreover, are expected to be in isolation (Lorimer 2005); in principle, without a close companion, these old radio-quiet neutron stars could only be detectable through radiative processes if accretion from the interstellar medium (ISM) occured on the stellar surface (Ostriker et al. 1970).

Young isolated neutron stars, on the other hand, are expected to be strong X-ray and γ-ray sources, the high energy emission being due to the rotation of the neutron star (non-thermal mechanisms) or to an internal heat reservoir which follows formation (cooling) or which is provided through magnetic field decay[1]. Some high energy pulsars and isolated neutron stars (INSs) are also detected in radio wavelengths while others are not. The lack of radio emission may be due to either unfavourable viewing geometries or to physical mechanisms that, for example, inhibit pair creation in the pulsar magnetosphere, thus quenching persistent coherent radio emission. Searches and surveys at other wavelength regions of the electromagnetic spectrum are thus needed in order to unveil INSs that are undetectable in the radio regime.

In the pre-ROSAT era, the evidence found by several authors (e.g. Helfand & Tademaru 1977, Vivekanand & Narayan 1981, Chevalier & Emmering 1986, Narayan & Ostriker 1990) that the population of pulsars could be described by two individual subclasses of fast and slow rotators – with different (magnetic field and spin period) evolutionary histories and, most important here, kinematically distinct in their scale heights and mean spatial velocities – was essential since it provided a significant number of neutron stars ($\sim$55% of the total population) that were slow enough, $v \sim 60\,\mathrm{km\,s^{-1}}$, to be detected through Bondi-Hoyle accretion by ROSAT[2]. Early estimates of the detectable number of "re-heated" old neutron stars were thus high, $10^2 - 10^3$ (Sect. 1.2.2). This number decreased dramatically after more recent and precise measurements of the proper motion of radio pulsars showed that such a bimodal velocity distribution was not required, and observations could be well described by a single component with mean $v \sim 400\,\mathrm{km\,s^{-1}}$ (Lyne & Lorimer 1994, Lorimer et al. 1997, Cordes & Chernoff 1998, Hobbs et al. 2005). The adoption of a new scale distance (Taylor & Cordes 1993, Cordes & Lazio 2002) as well as the realisation that previous velocities were systematically low by a factor of 2 (Harrison & Lyne 1993) also contributed to limit the expected number of slow moving objects in the Galaxy. Moreover, due to the Earth's location within the Galactic plane, the observed velocity distribution is still likely to be biased towards lower velocities. Since neutron star progenitors, the massive OB stars, inhabit the plane as do we, higher velocity pulsars escape our detection volume faster than lower velocity ones. This observational bias is aggravated by pulsar searches that focus more heavily on the target-rich environment of the Galactic plane and which are the main providers of new pulsars detected in the radio regime.

In fact, the average high neutron star velocity, although crucial due to the Bondi-Hoyle accretion rate dependency that goes with v^{-3}, is only one of the several factors that act together in order to inhibit spherical accretion from the ISM – or at least decrease it to a rate that the produced X-ray luminosity is well below the sensitivity of current observatories, which we discuss further (Sect. 3.6). Despite the early (pre-ROSAT) optimistic expectations, no accreting INS is known to date.

Radio-quiet INSs are extremely elusive and difficult to detect. Among the known neutron stars lacking radio emission, seven thermally emitting X-ray sources have been discovered by ROSAT and these are not accreting from the ISM as was originally thought;

[1]See Sect. 1.2.2, 1.4.1 for the current observational picture of INSs at high energies and Appendix A.1 for a basic account of neutron star cooling theory.

[2]See Introduction in Sect. 1.2.2. For an overview of the Bondi-Hoyle theory, see Appendix A.2.

rather, the X-ray emission comes from the still hot surface of a middle-aged ($10^5 - 10^6$ yr) neutron star with no significant magnetospheric emission (Sect. 1.3). Although invaluable for individual investigations, the seven sources are too diverse in detail for the properties of the population as a whole to be assessed. For instance, while the brightest among the seven INSs, RX J1856.5-3754 shows a featureless thermal spectrum, evidence for broad absorption lines has been found in the spectra of the other sources. The second X-ray brightest INS, RX J0720.4-3125, is the only one which has shown long-term spectral variations, the physical origin of which is not definitely understood (Sect. 1.3.3). In this respect, it is striking that the "Magnificent Seven" (M7) appear to represent about half of all young (aged less than 3 Myr) INSs known within ~ 1 kpc (Popov et al. 2003). They could thus be the tip of an iceberg of a large hidden population of stellar remnants which may be, at least locally, as numerous as radio pulsars.

For several years, considerable efforts discover new INSs. This is a difficult and time-consuming task due to the need of cross-correlating X-ray sources that often have poorly determined sky positions with a large number of catalogued objects at other wavelengths, as well as to appropriately deal with the level of sample contamination by other classes of X-ray emitters. By cross-correlating the ROSAT All-Sky Survey Bright Source Catalogue (RASS BSC; Voges et al. 1999) with optical (USNO-A2.0; Monet 1998), infrared (IRAS PSC; Helou & Walker 1988) and radio (NVSS; Condon et al. 1998) source catalogues, Rutledge et al. (2003) searched for candidate INSs by excluding X-ray sources with plausible counterparts. Out of 15,205 ROSAT sources above a limiting flux of $\sim 5.4 \times 10^{-13}$ erg s^{-1} cm^{-2} (sky coverage of $\sim 92\%$ at the $0.1-2.4$ keV energy band), the method selected 32 candidates among which were two of the M7; 17 sources belonged to other classes of X-ray emitters or were considered spurious detections while 13 sources remained with undetermined classification. Chandra follow-up observations of 8 candidates excluded the possibility of INS identifications on the basis of either X-ray variability or alternative identifications with late-type stars, cataclysmic variables (CV) or active galactic nuclei (AGN). Assuming isotropy, the Rutledge et al. study implied a 90% confidence level upper limit of 67 INSs to be present in the RASS, which was in clear contrast to the expectations prior to launch. Due to the rather low mean positional accuracy of the ROSAT sources at faint fluxes, with 1σ error circles around $13''$, and intrinsic properties of the cross-correlation method which was applied, Rutledge et al. estimated that only around 20% of the INSs in the Galaxy could be identified through their selection procedure; the high number of false correlations of optical objects with the ROSAT sources in the populated Galactic plane being the major barrier that hampers efficient INS identification.

A more recent investigation of the RASS used the optically deeper Data Release 4 (DR4; Adelman-McCarthy et al. 2006) of the Sloan Digital Sky Survey (SDSS) in order to select potential INS candidates (Agüeros et al. 2006). This search proved to be an order of magnitude more selective than previous ones and more efficiently excluded typical classes of "contaminating" X-ray sources, i.e. quasars, galaxies, bright stars and clusters of galaxies. This was achieved using the spectral information on the possible optical counterparts of the ROSAT sources, available in the SDSS database for optical objects that are bright enough. Considering the standard X-ray-to-optical flux ratios of typical classes of X-ray emitters, this was often the case. Moreover, by applying a deeper (compared to the USNO-

A2.0) optical limit of $g < 22$, Agüeros et al. could extend the search to the RASS Faint Source Catalog (FSC) to a total of 22, 700 X-ray sources covered by the SDSS DR4 footprint ($\sim 6670\,\mathrm{deg}^2$), down to a limiting flux of few times $10^{-13}\,\mathrm{erg\,s^{-1}\,cm^{-2}}$. The method allowed the selection of 11 candidates, 9 of which were previously unknown. However, no identification with an INS has been confirmed since.

In order to avoid the rather high level of source confusion caused by the large RASS PSPC positional uncertainties, Chieregato et al. (2005) looked for "blank fields" – i.e. fields of X-ray sources lacking plausible counterparts in other wavelengths – by cross-correlating data from the much better spatial resolution instrument that operated in ROSAT, the High Resolution Imager (HRI), with optical (GSC2; McLean et al. 2000), infrared (2MASS Second Data Release; Kleinmann et al. 1994 and IRAS PSC) and radio (FIRST; White et al. 1997) catalogues. The resulting database, the Brera Multiscale Wavelet ROSAT HRI source catalogue (Panzera et al. 2003), contained $\sim 30,000$ entries to a limiting count rate of $\sim 10^{-4}\,\mathrm{s^{-1}}$ (corresponding to an unabsorbed flux of $\sim 3.8 \times 10^{-15}\,\mathrm{erg\,s^{-1}\,cm^{-2}}$); the sky coverage was $732\,\mathrm{deg}^2$. Among these, four candidates with no optical counterparts brighter than magnitudes 19 to 23 were selected for follow-up observations on the basis of source brightness, distance from possible counterparts at other wavelengths, point-like shape and a good estimate of the X-ray flux. However, no new INS was identified.

A long-term project aiming at surveying X-ray sources from the RASS BSC that show a high probability of having large X-ray-to-optical flux ratios was initiated in 2005 and is now close to completion (Fox 2004, Rutledge et al. 2008, Letcavage et al. 2009, Shevchuk et al. 2009). The programme applies the X-ray and UV imaging capabilities of NASA's Swift γ-Ray Burst Mission (Gehrels et al. 2004) in order to derive $< 5''$ positions for the 18, 811 RASS BSC sources, for a total observing time of 500 s each. It is expected that the improvement by a factor of 10 to 30 in positional accuracy of the BSC sources will enable optical identification or set deep limits in nearly every case. The first X-ray source that resulted from these survey efforts is 1RXS J141256.0+792204, nicknamed *Calvera*, an object that shows an extremely high X-ray-to-optical flux ratio of $F_X/F_V \gtrsim 8700$ (Rutledge et al. 2008), indicating a compact nature. However, the source does not seem to conform to any class or group of compact objects or INSs known at present, a point to which we come back later in Sect. 3.6.

Based on preliminary analysis of the Swift-RASS BSC survey, it is estimated that fewer than ~ 48 INSs are present in the ROSAT data, at 90% confidence level and assuming all-sky isotropy (Shevchuk et al. 2009). From this point of view and in spite of its role in the discovery of the nearby M7, at present the RASS BSC does not seem to be a promising provider of new cooling neutron star candidates. These would rather have to be sought at fainter fluxes; consequently, they will consist of the products of more distant OB associations beyond the Solar vicinity and the Gould Belt. The large effective area and field-of-view (FoV) of the XMM-Newton Observatory as well as its good positional accuracy at soft X-ray energies make it ideal for serendipitous science and to look for faint INSs.

We report in the present chapter the search for new candidate isolated neutron stars using the 2XMMp catalogue, a preliminary version of the serendipitous catalogue of X-ray sources drawn from XMM-Newton observations, the results of follow-up optical investigations on a sample of selected candidates and the discovery of a new thermally emitting

INS, the first similar to the M7 since RX J2143.0+0654, discovered some eight years ago (Zampieri et al. 2001). The chapter is structured as follows: in Sect. 3.2 we describe the methodology which was applied to select the 2XMMp sources and restrict the number of INS candidates; in Sect. 3.3 the optical data obtained on a subsample of our candidates are described together with their analysis and results; Sect. 3.4 is devoted to the analysis of the X-ray emission of these candidates. The discovery of a new thermally emitting INS 2XMM J104608.7-594306, the X-ray brightest among our sample, and the discussion of its nature as, in particular, a cooling or an accreting neutron star are presented in Sect. 3.5. Finally, the discussion is in Sect.s 3.6. These results were published in Pires et al. (2009b;a).

We refer the reader to Appendix B.1.1 for details about the XMM-Newton Observatory and EPIC instruments, as well as to Appendix B.3.1 for a description on XMM-Newton data processing and catalogue creation. Appendices B.2.1 and B.2.2 provide references for the optical facilities used in this work.

3.2 Selection of candidates

We searched for new thermally emitting INSs similar to the M7 in the pre-release of the XMM-Newton serendipitous source catalogue, 2XMMp[3] (Appendix B.3.1). This version of the catalogue, released in July 2006, contains source detections drawn from 2400 individual XMM-Newton EPIC observations made between 2000 and 2006. It contains more than 120,000 unique X-ray sources with a median flux of 2.4×10^{-14} erg s^{-1} cm^{-2} (in the total energy band 0.2 – 12 keV; below 1 keV the average flux is 6.5×10^{-13} erg s^{-1} cm^{-2}). Approximately 95% of the catalogued objects are point sources. Positional accuracy is generally $< 2''$ (68% confidence radius) and the total sky area covered is ~ 285 deg^2. The sky distribution of the X-ray sources above a EPIC pn count rate of 0.01 s^{-1} (total of $\sim 7.2 \times 10^4$ objects) can be seen in Fig. 3.1.

Being a serendipitous catalogue, the 2XMMp was not compiled from a set of homogenous observations. The sky distribution is wide, although the percentage of sky coverage is very low, $\sim 0.7\%$. Approximately 25% of the sources are in the Galactic plane, with $|b| \leq 20°$. Integration times cover a broad range, as evident in the histogram of Fig. 3.2; the used observing modes and optical blocking filters are also diverse, as are the astrophysical content of the observed targets. The observations are processed by the Survey Science Centre (SSC) using the XMM-Newton Science Analysis Software (SAS[4]) in order to generate high level science products from the raw Observation Data Files (ODF). The processing

[3]The 2XMMp includes approximately 65% of the fields and 75% of the sky area covered by the final version of the catalogue, 2XMM, released by the Survey Science Centre (SSC) in August 2007. As a member institute of the SSC, the Strasbourg Observatory hosts a part of the XMM-Newton pipeline and has privileged access to most of the recent satellite data for survey purposes. By the time we initiated our search for INS candidates, in October 2006, we had available an unreleased version of the catalogue that can be considered intermediate between the 2XMMp and the 2XMM; as such, we actually worked with nearly 50% more sources than the version released three months earlier that year. In the following description of our selection procedure, we give the number of sources relative to this intermediate "working" catalogue, which may differ in absolute numbers from the actual 2XMMp. This difference, however, does not impact the figures reported here, as far as e.g. mean flux or source positional accuracy are concerned.

[4]http://xmm.esac.esa.int/sas

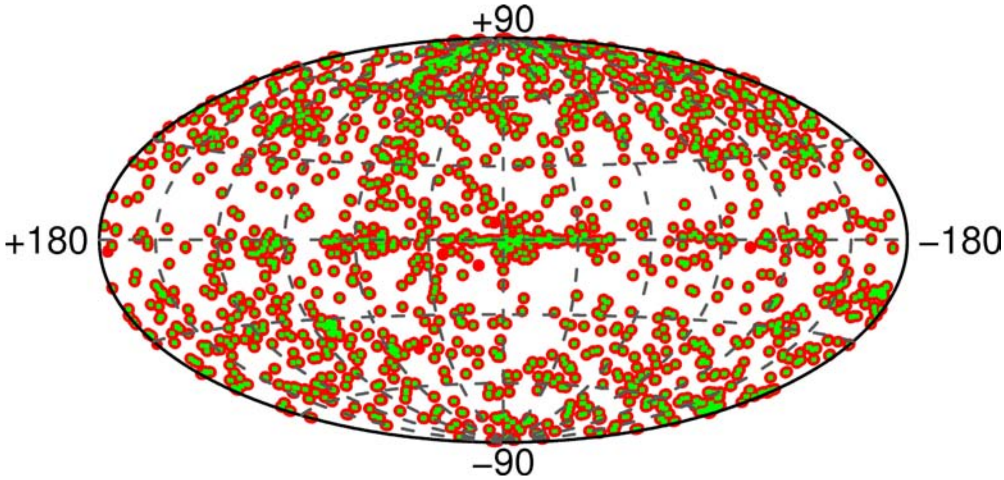

Figure 3.1: Hammer-Aitoff projection in Galactic coordinates of the more than $\sim 72,000$ sources present in the 2XMMp catalogue above a EPIC pn count rate of 0.01 s^{-1} (red circles). We show as green dots the sources with no correlations with the optical USNO-A2.0 catalogue. Because of the resolution of this plot we see the distribution of XMM-Newton pointings rather than the individual sources.

pipeline is briefly summarized in Appendix B.3.1; a full detailed description can be found in Watson et al. (2009).

Despite the small percentage of sky coverage, the EPIC instruments provide much better positional accuracy at soft energies and faint fluxes relative to ROSAT, making the XMM-Newton catalogue a powerful tool to look for unidentified INSs. In the near future, the ROSAT successor eROSITA (Appendix B.1.3) mission should perform the first imaging all-sky survey up to 10 keV with unprecedented spectral and angular resolution, and which could potentially increase the number of identifiable cooling INSs by up to one order of magnitude (Posselt et al. 2008).

3.2.1 Main selection criteria

The EPIC pn camera on-board XMM-Newton detects X-ray photons in the total energy band of the satellite with good spectral and angular resolutions; the detector efficiency is extremely high and homogeneous and the instrument is reasonably stable on timescales of years, in contrast to EPIC MOS[5]. For these reasons, we only considered detections in the EPIC pn camera at a limiting count rate of 0.01 s^{-1} (0.2 – 12 keV), corresponding to a total number of $\sim 7.2 \times 10^4$ X-ray sources above a flux of 6×10^{-14} erg s^{-1} cm^{-2} (assuming an absorbed power-law spectrum with photon index $\Gamma = 1.7$ and $N_H = 3 \times 10^{20}$ cm^{-2}).

We then required X-ray sources that had been well detected and were point-like by selecting the 2XMMp objects with a reported large value of detection likelihood, PN_DET_ML > 8, and a low probability for extension, EP_EXTENT_ML < 4, both

[5]See the EPIC calibration webpages, http://xmm2.esac.esa.int/external/xmm_sw_cal/calib/index.shtml

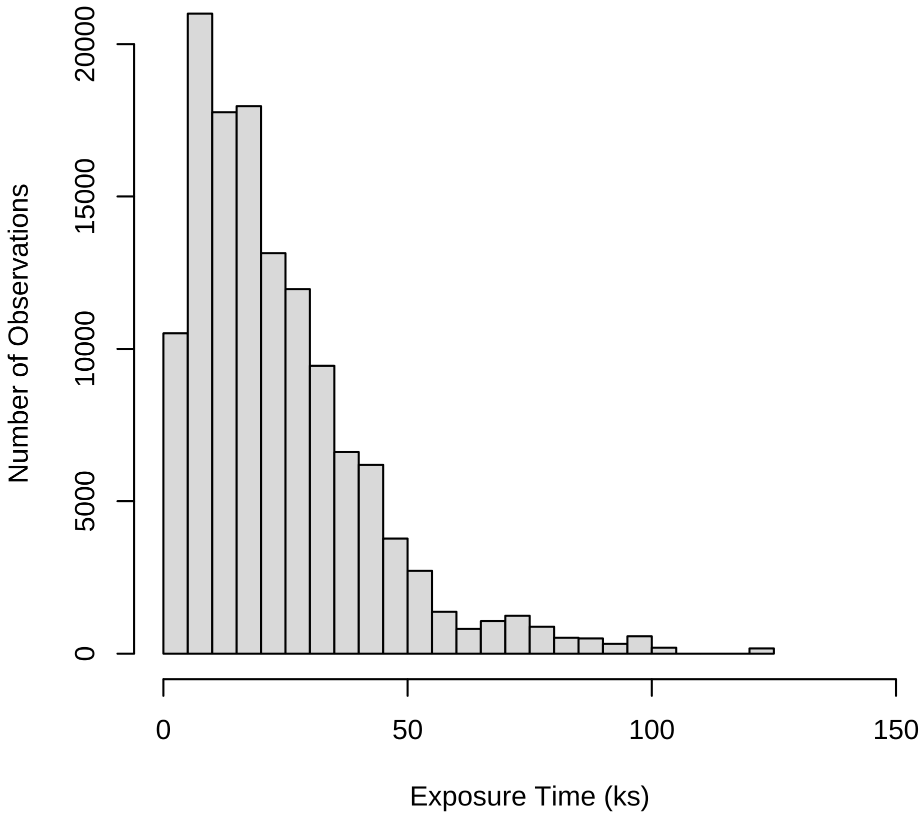

Figure 3.2: Distribution of exposure times of the 2XMMp sources, filtered for periods of high background activity.

parameters computed by the catalogue pipeline with the SAS task emldetect. This task computes source parameters by means of a maximum likelihood fitting routine that adjusts the instrumental point spread function (PSF), convolved with a source extent model (a beta-model profile), into the source photons detected in the five pre-defined energy bands of the catalogue (see Table B.3 in Appendix B.3.1). Free fitting parameters are the source position, extent and count rate. The first two are constrained to be the same in all energy bands while count rates are obtained for the best-fit value for each camera and energy band. Detection and extent likelihoods are derived together with the total source count rate and hardness ratios (HR).

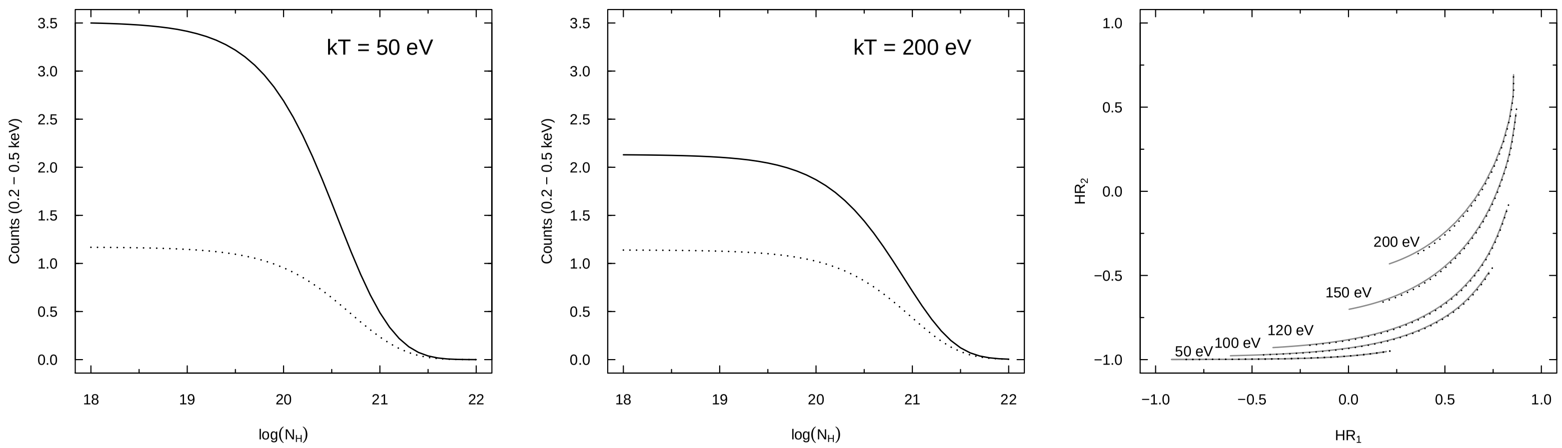

Figure 3.3: Counts and hardness ratios (HR) as a function of blackbody temperature and column density. Solid lines represent counts and HR for a blackbody source observed with the thin filter, while dotted lines denote the same source but observed with the thick filter, as a function of the photoelectric column density $N_{\rm H}$. Although the difference in counts for a given energy band (here we show $kT = 50, 200\,{\rm eV}$ and $0.2-0.5\,{\rm keV}$) can be significant, the impact on the $\rm HR_1 \times HR_2$ diagram is not significant.

The hardness ratio HR is defined as

$$\mathrm{HR}_i = \frac{C_{i+1} - C_i}{C_{i+1} + C_i} \qquad i = 1, \ldots, 4 \tag{3.1}$$

where C_i and C_{i+1} are source counts into two contiguous energy bands of the 5 (Table B.3); by construction, it can range between -1 and $+1$. Source count rates and, therefore, HR are instrument-dependent and vary as a function of the filter used for the observation. This is especially true for the ratio between the two softest energy bands, HR_1, since soft X-ray photons are more severely affected by the intervening photoelectric absorption in the line-of-sight.

As part of the pipeline, several quality flags are set to the catalogued sources. This is done during data processing by a number of automated procedures as well as by means of visual screening in order to assure the final quality and to keep track of software issues or intrinsic problems with the data. The automatic flags, numbered from 1 to 9, are set by the SAS task dpssflag over the available information provided by emldetect on each detected source. In particular, the task's goal is to warn the user of objects located in problematic areas (e.g. near a bright source, within extended emission, in defective pixels, rows or columns of the CCD chips, etc), or that had a low coverage on the detector. Five columns in the catalogue – one for each camera, one for the ensemble of the EPIC detectors plus a summary for the source detection – summarize the results of the automatic flags and classify each detection as being "good", "likely spurious" or with "some parameters that may have been affected". In addition to the quality of each detection, the pipeline automatically flags source variability by means of a modified χ^2 test, appropriate for Poissonian data, carried out in the binned time series of sources that are sufficiently bright. This is performed by the task ekstest. According to the 2XMMp User Guide, in some cases the automatic detection flags 2 to 7 were not set properly due to a bug in dpssflag. Moreover, possible overestimation of the χ^2 statistics was verified to erroneously flag constant sources as being variable (see `http://xmmssc-www.star.le.ac.uk/dev/Catalogue/2XMMp/UserGuide_2xmmp.html#ProblFlag`, for details). We therefore decided to not use any of the source quality or variability flags provided by the catalogue in the selection and screening process for our INS candidates.

Based on the most obvious properties of INSs (i.e. lack of strong emission at other wavelengths and thermal X-ray spectral energy distribution), we then required for the remaining $\sim 4.6 \times 10^4$ entries the two main selection criteria:

(i) no correlations (within 3σ) with the USNO-A2.0 optical catalogue;

(ii) a soft energy distribution.

Applying the first criterion led to the rejection of more than 2.1×10^4 X-ray sources having a positive match with USNO-A2.0 entries (Monet 1998). We note that this major cut (around 45% of the sources are rejected) does not reflect any significant change in the overall sky distribution of sources; this can be visualized in Fig. 3.1, where the remaining 2XMMp objects that have no correlations with the USNO-A2.0 catalogue are plotted in green, which can then be compared to the original distribution of 2XMMp sources (red

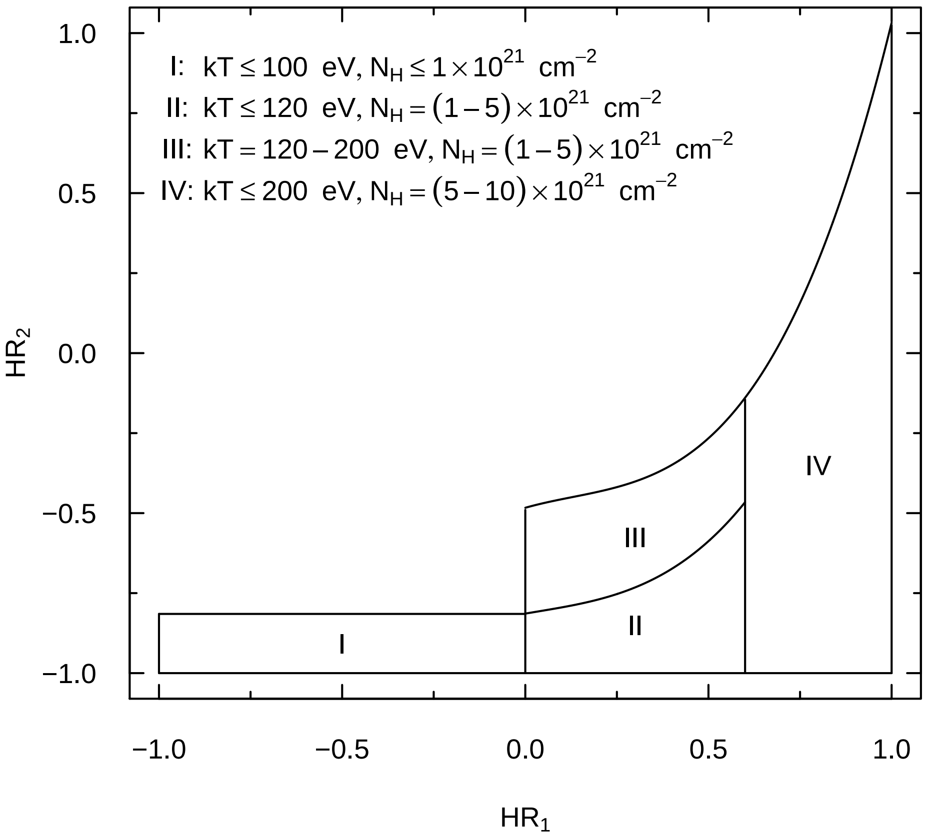

Figure 3.4: Boundaries of the 4 different selection regions considered in the $HR_1 \times HR_2$ diagram.

circles). This is important because the expected spatial distribution of (young) isolated neutron stars at distances beyond the Solar vicinity is highly anisotropic and, as it would be natural for sources evolved from massive stars, is strongly concentrated in the Galactic plane (see e.g. Posselt et al. 2008). Therefore, we do not want our selection procedure or cross-correlation method to avoid any particular region of the sky as was the case with previous INS searches (e.g. Rutledge et al. 2003), since the XMM-Newton coverage is already significantly lower than RASS. Moreover, thanks to the very good positional accuracy of the XMM-Newton sources relative to previous X-ray imaging missions, the expected level of source confusion is very low, since the average number of optical sources in the USNO-A2.0 catalogue in a 3σ error circle of a 2XMMp source, although higher in the regions of the Galactic plane, is usually < 1. At such source densities, the probability of chance association is $\ll 0.1\%$.

In order to select sources in agreement with requirement (*ii*), we used the X-ray spectral

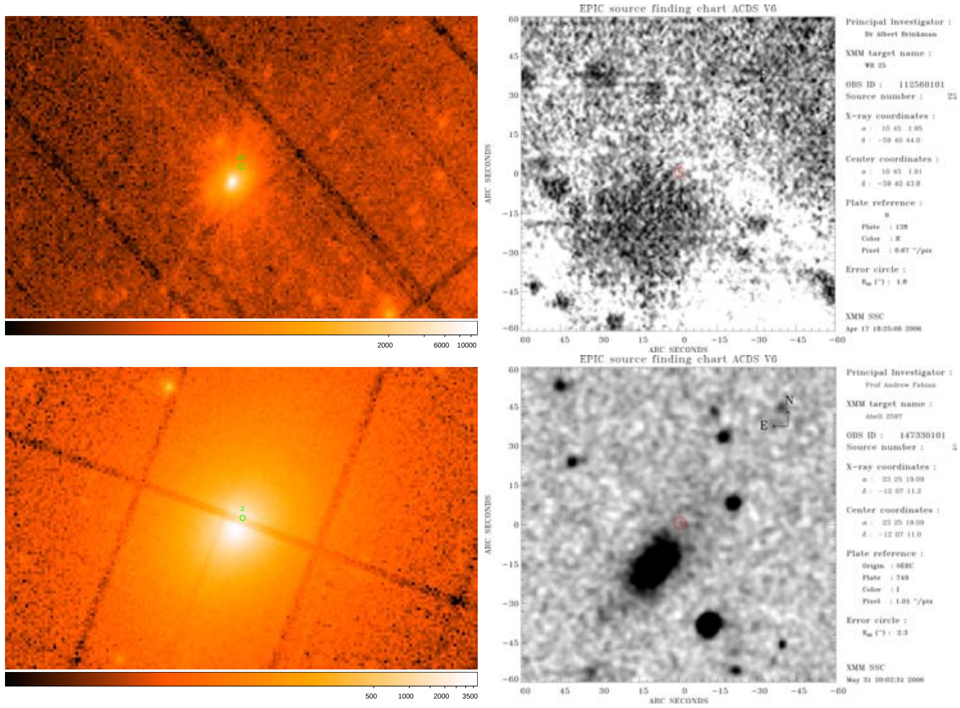

Figure 3.5: X-ray images and optical finding charts of false detections in wings of nearby bright objects (WR25; top) or in diffuse emission (cluster of galaxies Abell 2597, bottom row) as examples spurious objects among the 2XMMp sources selected for visual screening.

fitting package XSPEC 12.3[6] (Arnaud 1996; 2004) to generate input source spectra of blackbodies of temperatures between 50 eV and 200 eV, seen through interstellar column densities in the range $N_{\rm H} = 10^{19}-10^{22}\,{\rm cm}^{-2}$. Spectra were convolved with the instrumental (on-axis) response matrix and auxiliary files of the EPIC pn detector[7] for the three different optical blocking filters. We then defined the loci occupied by these blackbody templates in hardness ratio diagrams in order to extract the 2XMMp sources with a compatible (within 1σ) spectral energy distribution, as a function of photoelectric absorption.

Although the effective areas of the thin, medium and thick filters at energies below 1 keV can differ by a factor of up to 3, we verified that their influence in the HR diagrams is minor. In Fig. 3.3 we show examples to illustrate the effect of the different filters in the templates sources: first, we plot counts as a function of column density and then the hardness ratio diagram $\mathrm{HR}_1 \times \mathrm{HR}_2$ taking into account the whole considered parameter space of blackbody temperatures and $N_{\rm H}$. Only the thin and thick filters are shown since these represent the two opposite extremes, as far as the number of detected photons and HR are concerned. Not unexpectedly, the decrease of detected soft counts when observing with the thick filter (and corresponding "hardening" of the source) relative to the thin one is significant for a given temperature (we show the cases of the softest and the hardest

[6] http://heasarc.gsfc.nasa.gov/docs/xanadu/xspec

[7] http://xmm2.esac.esa.int/external/xmm_sw_cal/calib/epic_files.shtml

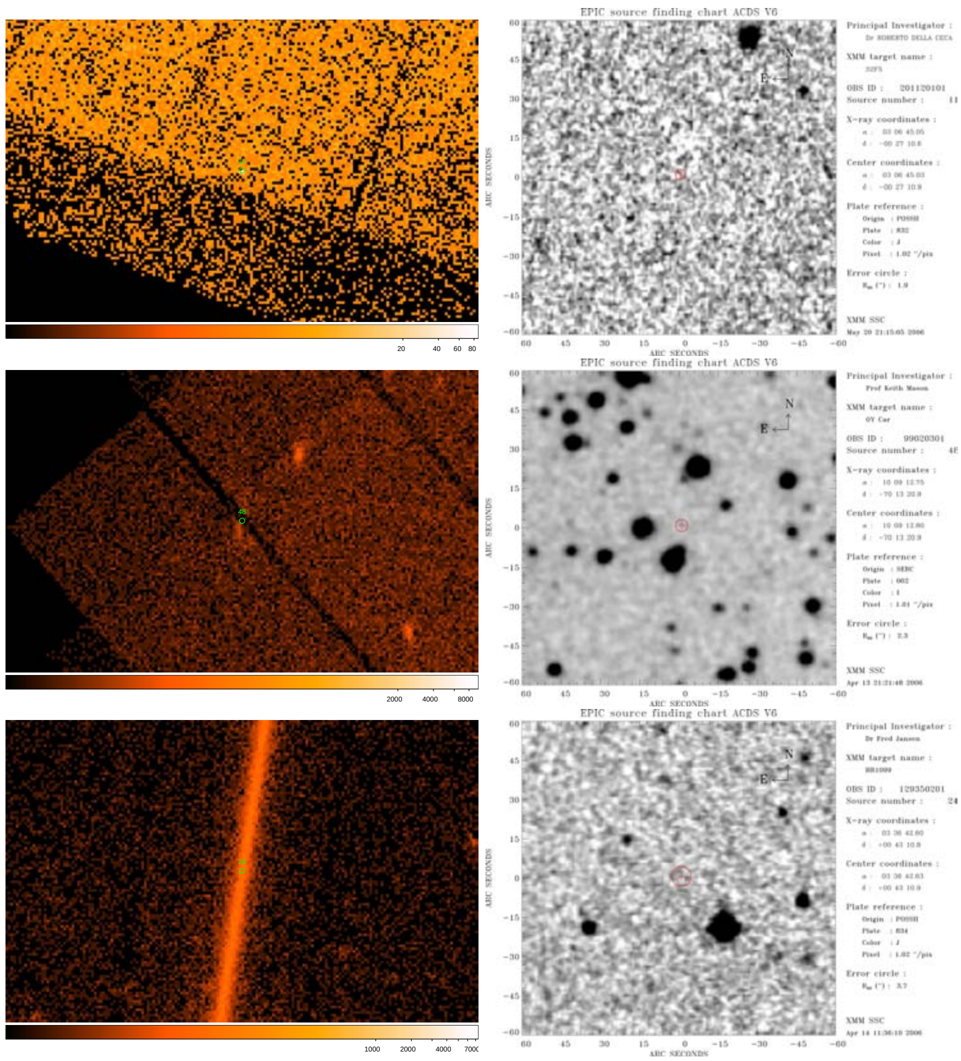

Figure 3.6: X-ray and optical finding charts of false detections (edge, gap, OOT event) as examples of spurious objects among the 2XMMp sources selected for visual screening.

temperatures that have been considered as well as the energy band of the satellite that is most affected by interstellar absorption, $0.2-0.5$ keV). However, the effect on the $HR_1 \times HR_2$ is hardly noticeable while defining the loci of these very sources, rather independently of the blackbody temperature considered.

The X-ray column densities of the catalogue sources were then verified to be less than or equal to the total Galactic value (Schlegel et al. 1998) in order to discard intrinsically absorbed objects. Sources with very large positional uncertainties ($r_{90} > 4''$, where r_{90} is the source 90% confidence level error circle) or which were too far from the optical axis (at off-axis angles $\theta > 11'$) were also discarded. After applying these selections, we ended up with ~ 1000 sources. Of these, a total additional number of 461 X-ray sources with matches in one or more of the optical/IR catalogues USNO-B1.0 (Monet et al. 2003),

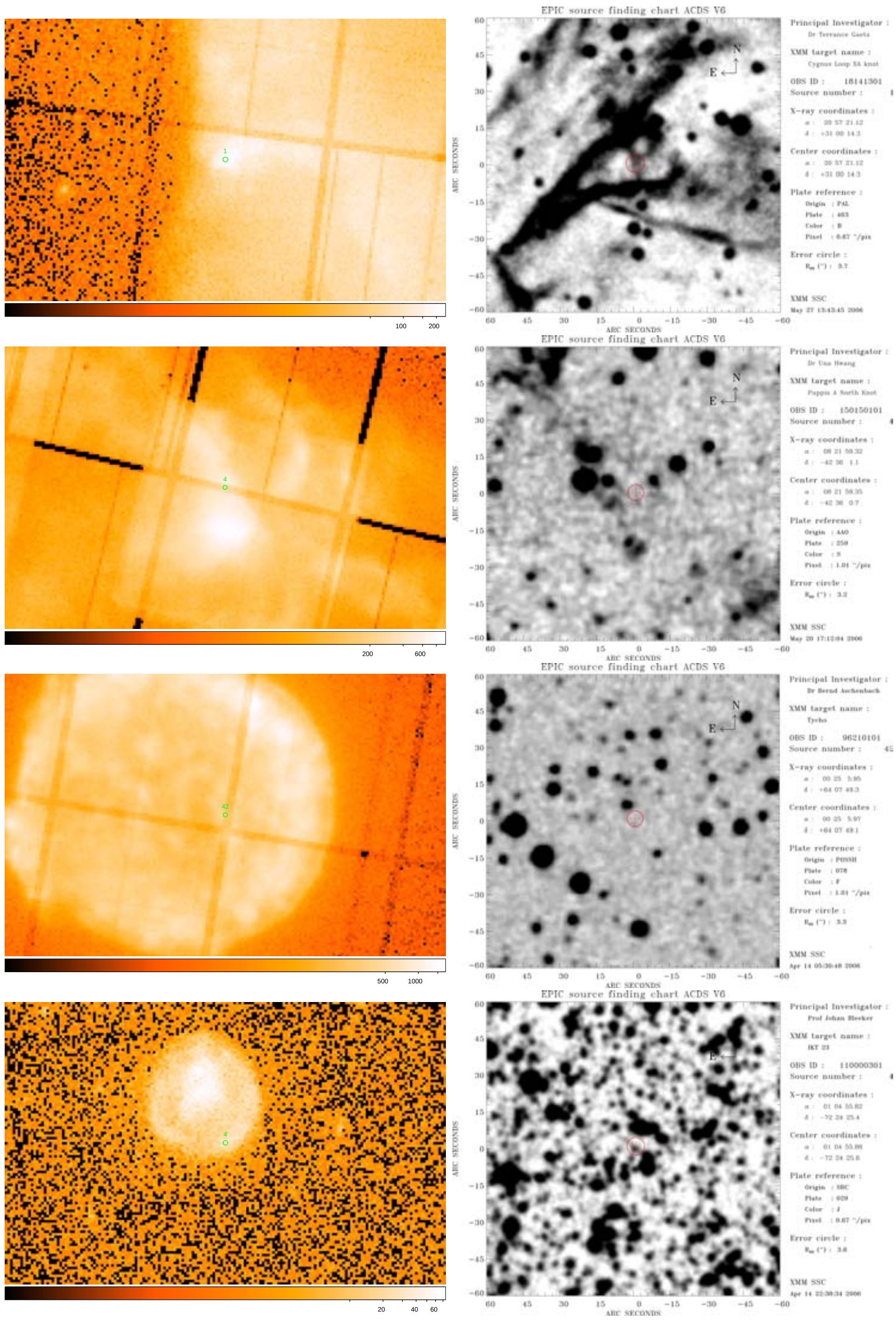

Figure 3.7: X-ray and optical finding charts of false detections (bright knots in the diffuse emission of SNR) as examples of spurious objects among the 2XMMp sources selected for visual screening. We show Cygnus Loop, Puppis, Tycho and a SNR in the SMC.

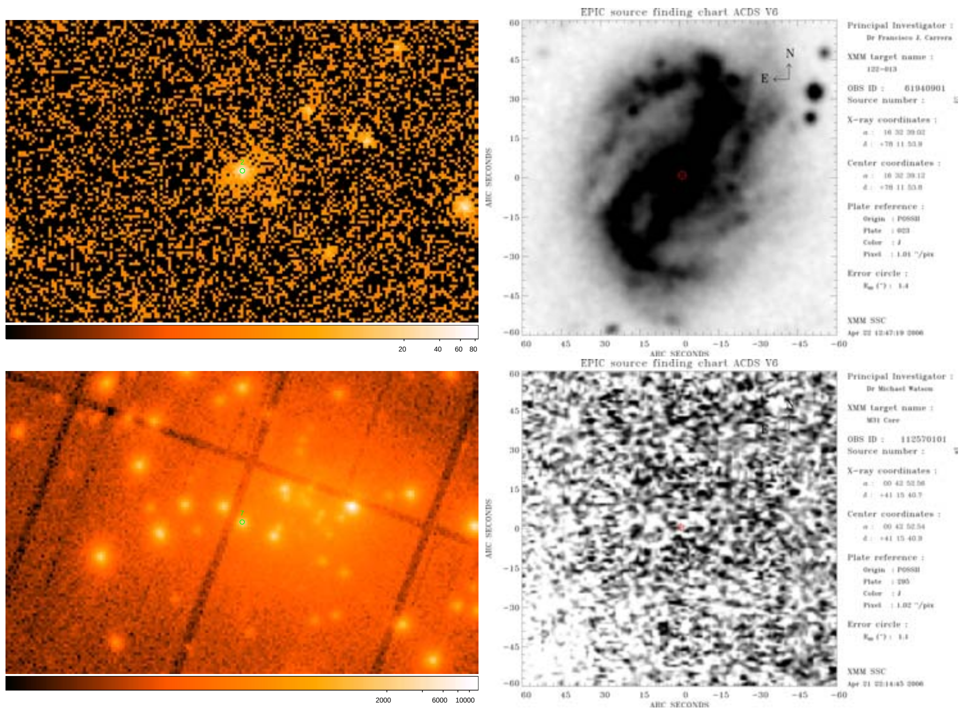

Figure 3.8: X-ray and optical finding charts of extragalactic X-ray sources as examples of discarded objects among the 2XMMp sources selected for visual screening. We show above the nucleus of galaxy NGC 6217 and an X-ray source in M31.

SDSS DR4 (Adelman-McCarthy et al. 2006), GSC2 (McLean et al. 2000), APM (McMahon et al. 2000) and 2MASS (Cutri et al. 2003) was discarded as well. We note that our main sources of information on the possible astronomical content of the X-ray source error circles were the cross-correlations computed by the Astronomical Catalogue Data Subsystem (ACDS). This module of the XMM-Newton reduction pipeline provides lists of archival entries in over 170 archival catalogues having a position consistent within 3σ with that of the 2XMMp source.

3.2.2 Visual screening

So as to more easily classify the 561 remaining sources which fulfilled the above selection criteria, we considered 4 different regions in the $\mathrm{HR}_1 \times \mathrm{HR}_2$ diagram, based on temperature and column density (see Fig. 3.4). We note that, although this diagram represents our main means of selecting INS candidates, we required soft emission in the $\mathrm{HR}_3 \times \mathrm{HR}_4$ diagram as well so as to avoid X-ray sources with significant emission above 2 keV. For each source in these regions, we visually checked the X-ray and optical images[8] and searched for possible identifications in astronomical catalogues and databases like NED[9] and Simbad[10]. Source

[8] Finding charts from SDSS or created from digitized optical plates.
[9] http://nedwww.ipac.caltech.edu
[10] http://simbad.u-strasbg.fr/simbad

Table 3.1: Results of visual screening of the selected 2XMMp sources per selection region.

	I	II	III	IV
Known INSs	16	0	1	1
INS candidates	1	5	24	2
Solar system objects	2	0	0	0
Extragalactic X-ray sources	12	31	39	6
Bright knots in SNRs	9	59	18	51
Diffuse emission in clusters of galaxies	2	6	9	0
Spurious out-of-time events / edge	10	70	58	8
Spurious in wing of bright object	2	15	18	6
Sources in CCD gap	3	13	46	5
Other	2	3	8	0
Total	59	202	221	79

Note: The number of classified sources are sorted per region of the $HR_1 \times HR_2$ diagram (Fig. 3.4). "Other" relates to high proper motion stars and quiescent neutron stars in globular clusters (see text).

selection and screening processes used the facilities provided by the XCat-DB[11] (Motch et al. 2007a), a data base hosting the 2XMM catalogue and its associated pipeline products, including the archival cross-correlations.

Many of the sources turned out to be false detections in extended diffuse emission mostly of supernova remnants (SNRs) or due to out-of-time (OOT) events. In Fig. 3.6 we show examples of X-ray images and the respective blank optical finding charts of such spurious detections: a faint dubious detection on edge of the detector FoV, in the gap between the CCD chips and an OOT event; one can also see spurious detections in the wings of a bright object or in the diffuse X-ray emission of bright galaxies or clusters of galaxies (Fig. 3.5). In Fig. 3.7 we show some examples of bright knots in the diffuse emission of SNRs: Cygnus Loop, Puppis, Tycho and a SNR in the Small Magellanic Cloud (SMC). The high number of spurious detections among our selected sources reflects the fact that we did not use the source quality flag information in the early steps of the selection process.

X-ray sources located in the direction of nearby galaxies (sometimes with an optical or infrared counterpart visible in the finding charts) were classified as "extragalactic" and thus were no longer regarded as potential INS candidates. Some illustrative examples can be seen in Fig. 3.8. Finally, because the spectral properties of some faint X-ray sources are not well determined in short exposures, the last step in our procedure was to check if any source with no evident classification (and thus a potential INS candidate) was spectrally harder in other (longer) XMM-Newton exposures. A total of 8 sources were discarded on this basis.

[11] http://amwdb.u-strasbg.fr/2xmmi/home

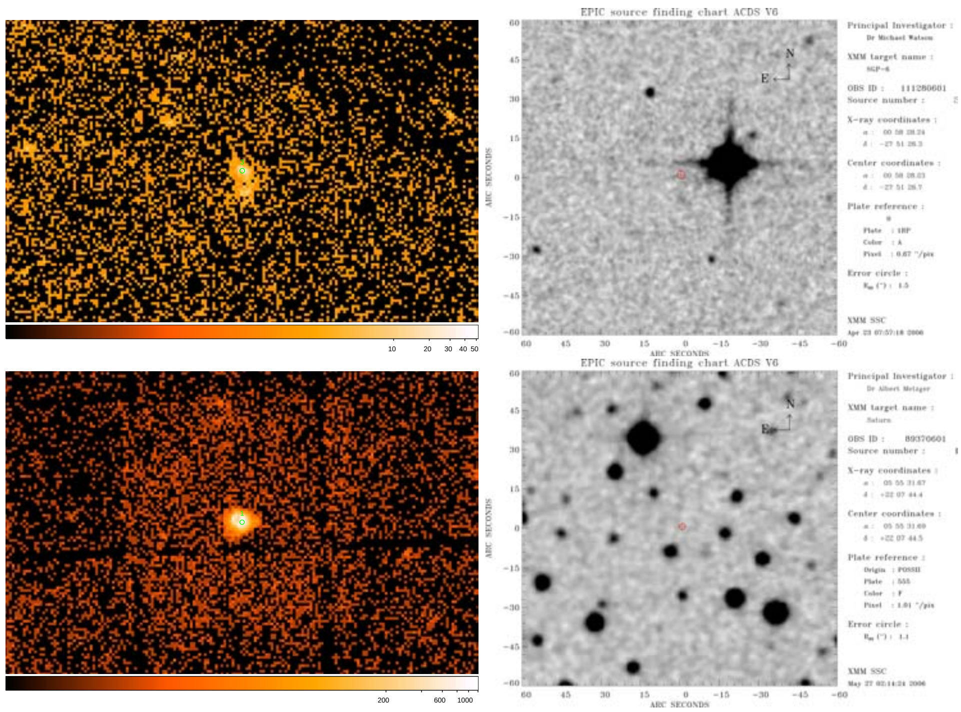

Figure 3.9: X-ray and optical finding charts of a high proper motion star and of Saturn, X-ray sources that entered our selection region I, as examples of miscellaneous objects selected by our procedure.

3.2.2.1 Results of visual screening

In Table 3.1 we list the results of the final screening of sources, sorted by selection regions. The numbers refer to detections that might have entered more than once or refer to more selection regions and not to unique sources[12]. It is worth noting that the known M7 or, more precisely, the pn observations of the M7 included in the compilation of the 2XMMp, were among the final list of INS candidates, providing a confirmation of the correctness of our procedure in selecting thermally emitting neutron stars. The cases of the M7 RX J0720.4-3125 and RX J0806.4-4123, both selected in selection region I, are shown in Fig. 3.10. As examples of previously unknown INS candidates selected through our procedure, we show in the same figure the X-ray image and optical finding chart of the X-ray brightest source among the final list of INS candidates, source 2XMM J104608.7-594306, and the case of another candidate, source 2XMM J214026.1-233222. These sources are much fainter than the nearby ROSAT-discovered M7. In the remainder of this section we report our results in detail for each one of the four selection regions of Fig. 3.4, also giving the numbers of INS candidates extracted by our procedure.

[12]In other words, a soft source which was observed several times by XMM-Newton, e.g. one of the M7, can enter the same selection region more than once, provided that its spectral properties are compatible. Similarly, one INS candidate can show HR that are consistent with more than one selection region, and in this case it is counted accordingly.

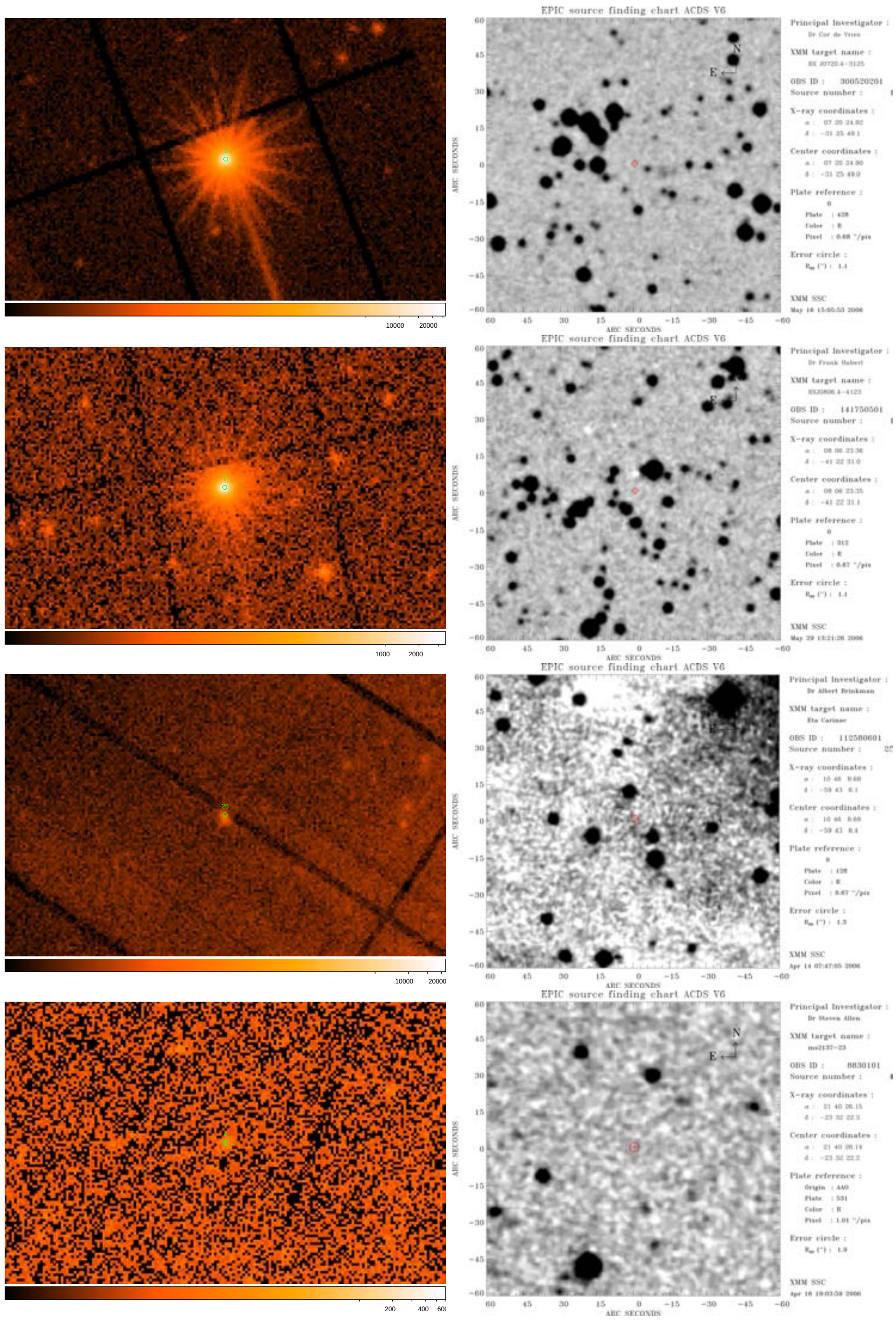

Figure 3.10: X-ray and optical finding charts of two of the M7 selected by our procedure, as well as of two much fainter INS candidates, source 2XMM J104608.7-594306 and source 2XMM J214026.1-233222. We show the M7 RX J0720.4-3125 and RX J0806.4-4123.

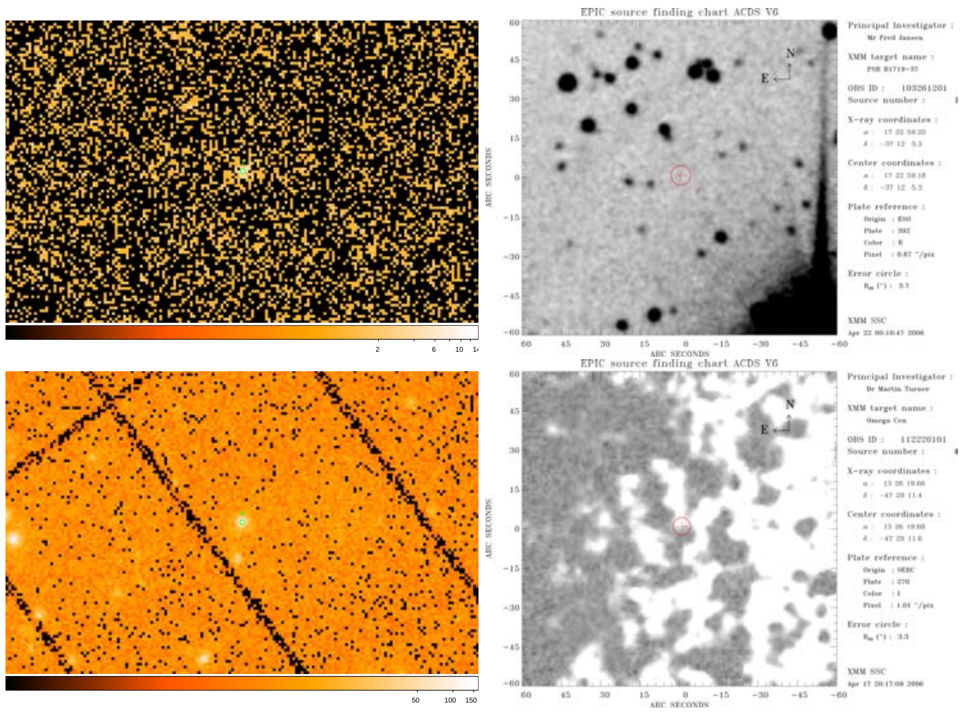

Figure 3.11: X-ray and optical finding charts of pulsar PSR 1722-3712 and of a quiescent neutron star in globular cluster ω Cen, X-ray sources that entered our selection region III, as illustrative examples of neutron stars selected by our procedure.

Selection region I Altogether, we found 59 very soft and low-absorbed sources with X-ray emission consistent with blackbodies of temperatures $kT \leq 100\,\mathrm{eV}$ and column densities $N_{\mathrm{H}} \leq 1 \times 10^{21}\,\mathrm{cm}^{-2}$ (region I in Fig. 3.4). In this region we retrieved the totality (16) of pn observations of the M7 carried out until 2006. Two observations of Saturn (Fig. 3.9) and a number of bright knots in the extended diffuse emission of Galactic SNRs (of the supernova SN 1006 and of the relatively old and nearby Cygnus Loop) also are included in this region. Interestingly, we noted that there were some cases (included as "other" in Table 3.1) in which the X-ray source had no optical candidate (Fig. 3.9) but was nonetheless related to (optically bright) high proper motion (HPM) stars. For these cases, we checked that the position of the X-ray source was compatible with the position of the HPM star at the time of the X-ray observation. Region I provided 1 INS candidate.

Selection region II There were 202 more absorbed and slightly hotter sources, consistent with blackbodies of $kT \leq 120\,\mathrm{eV}$ and $N_{\mathrm{H}} = (1-5) \times 10^{21}\,\mathrm{cm}^{-2}$ (region II). This selection region provided 4 INS candidates (in addition to the one that had also been selected in region I). Most of the sources consisted of bright knots in SNRs – the Galactic remnants of Puppis, RCW 86 and SN 1006 as well as SNRs in galaxies M33, M31, M51 and the Small Magellanic Cloud – and of spurious detections (mostly of bright objects on the edge of the CCDs or sources located in the CCD gaps) and of OOT events.

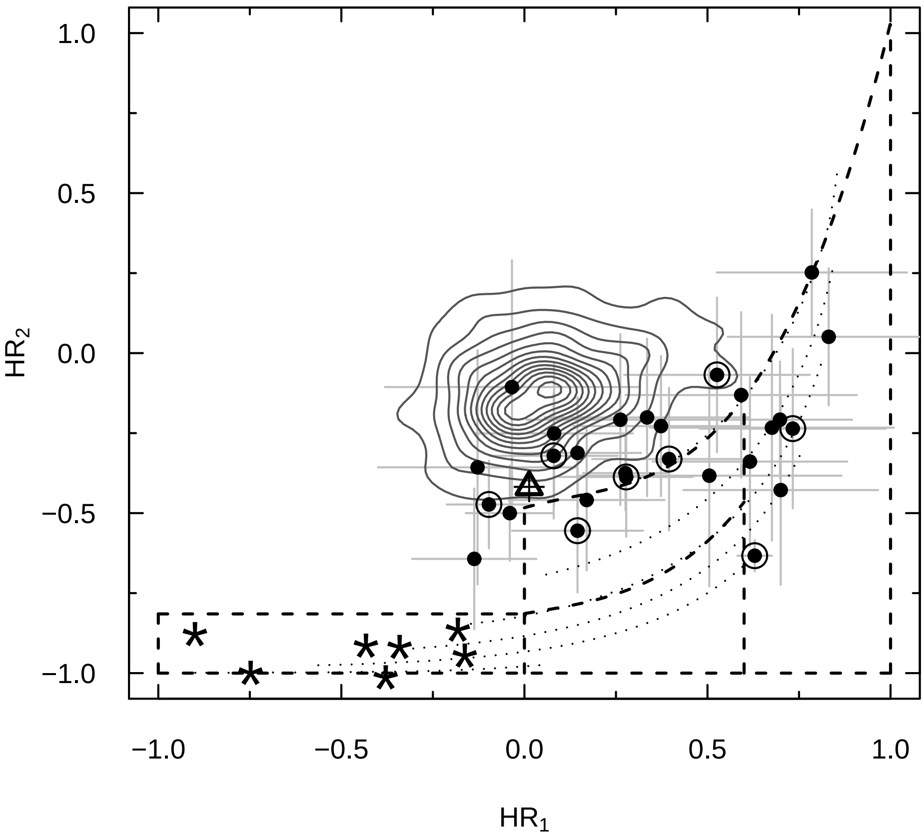

Figure 3.12: Positions of the final list of INS candidates in the $HR_1 \times HR_2$ diagram (filled circles with error bars). The known ROSAT-discovered INSs (asterisks) occupy the lowest (less absorbed) part of the diagram. Dotted lines denote soft absorbed blackbodies of different temperatures (50 eV, 80 eV, 100 eV, 120 eV, 150 eV and 200 eV, from bottom to top) seen through hydrogen column densities in the range 10^{19} to 10^{22} cm^{-2}. The selection regions are delimited by dashed lines. Contours show the HR distribution of quasars from SDSS DR3 (see text). The candidates selected for follow-up optical observations are highlighted by open circles. The open triangle is a newly discovered intermediate-mass black hole (Farrell et al. 2009).

Selection region III A total of 221 sources were found in region III ($kT = 120 - 200$ eV and $N_H = (1-5) \times 10^{21}$ cm^{-2}). Relative to region II, a smaller fraction of the total number of selected sources consisted of spurious detections in SNRs, which in this region were mostly extragalactic. Also relative to region I and II, a larger number of extragalactic X-ray sources were found. Region III also provided the largest number of INS candidates (22, in addition to 2 repeated entries of selection regions I and II). Interestingly, in this region we detected the X-ray emission of pulsar PSR J1722-3712 and the quiescent neutron stars in two low-mass X-ray binaries (LMXBs), XMMU J164143.8+362758 and CXOU J132619.7-472910, in the globular clusters M13 and ω Cen (Fig 3.11) We note, however, that the inclusion of these two sources in the sample selected for visual screening only derives from the fact that optical catalogues like the USNO-A2.0 ignore the overcrowded sky regions of globular clusters. These two neutron stars in LMXBs were included as "other" in Table 3.1 while the pulsar was included as "known INSs".

Selection region IV We found 79 highly absorbed sources, with X-ray emission consistent with $kT \leq 200$ eV and $N_\mathrm{H} = (5 - 10) \times 10^{21}$ cm^{-2} (region IV). The detections mainly consisted of knots in the Galactic SNRs Puppis, RCW 86, RCW 89 and Tycho as well as in some extragalactic SNRs in the Small and Large Magellanic Clouds. This region provided no new INS candidate – the objects in Table 3.1 correspond to INS candidates that already had been selected in region II and to the pulsar found in region III. The results sorted by selection region can be seen in the histograms of Fig. 3.13.

Thus, out of 7.2×10^4 serendipitous EPIC pn sources above 0.01 s^{-1}, fewer than 30 candidates met all the selection criteria; these are thus intrinsically soft sources not associated with any catalogued optical or infrared object and not likely to be spurious. A list containing the equatorial coordinates, EPIC pn count rates and hardness ratios of the sample of 27 INS candidates can be found in Table 3.2. In Fig. 3.12 we show the positions of the final list of unique INS candidates in the hardness ratio diagram $\mathrm{HR}_1 \times \mathrm{HR}_2$. The lowest left part of the diagram is occupied by the soft, low-absorbed M7 while our candidates, undergoing higher photoelectric absorptions, move upwards, along with the blackbody lines of hotter temperatures. Contour lines in the same diagram show the hardness ratio distribution of quasars from the SDSS DR3 (Schneider et al. 2005) that have counterparts in the 2XMMi catalogue with a maximum likelihood of detection greater than 20 (total of 796 sources; the list of correlated sources was extracted using the XCat-DB). Their location is above our selection region III. We can see already that several of our INS candidates have hardness ratios compatible with those of the SDSS quasars. We also show in this figure the location of a newly discovered intermediate-mass black hole (Farrell et al. 2009; see Sect. 3.6).

We list in Table 3.3 the equatorial coordinates and count rates of a subsample of the candidates, which were the object of follow-up observations in the optical during 2007, 2008 and 2009. The choice of sources for follow-up was made by selecting the X-ray brightest INS candidates that were visible from the southern hemisphere. We are currently establishing collaborations in order to observe the sample of INS candidates visible from the northern hemisphere. The positions are those derived by the catalogue pipeline with the SAS task emldetect. The 90% confidence level error circle on the position is given by:

$$r_{90} = 2.15\sqrt{\sigma^2 + \sigma_\mathrm{syst}^2} \tag{3.2}$$

where σ is the nominal error as given by emldetect. The systematic error σ_syst on the detection position is provided by the 2XMMp catalogue and is computed during pipeline processing by the SAS task eposcorr. The task correlates the X-ray positions from an

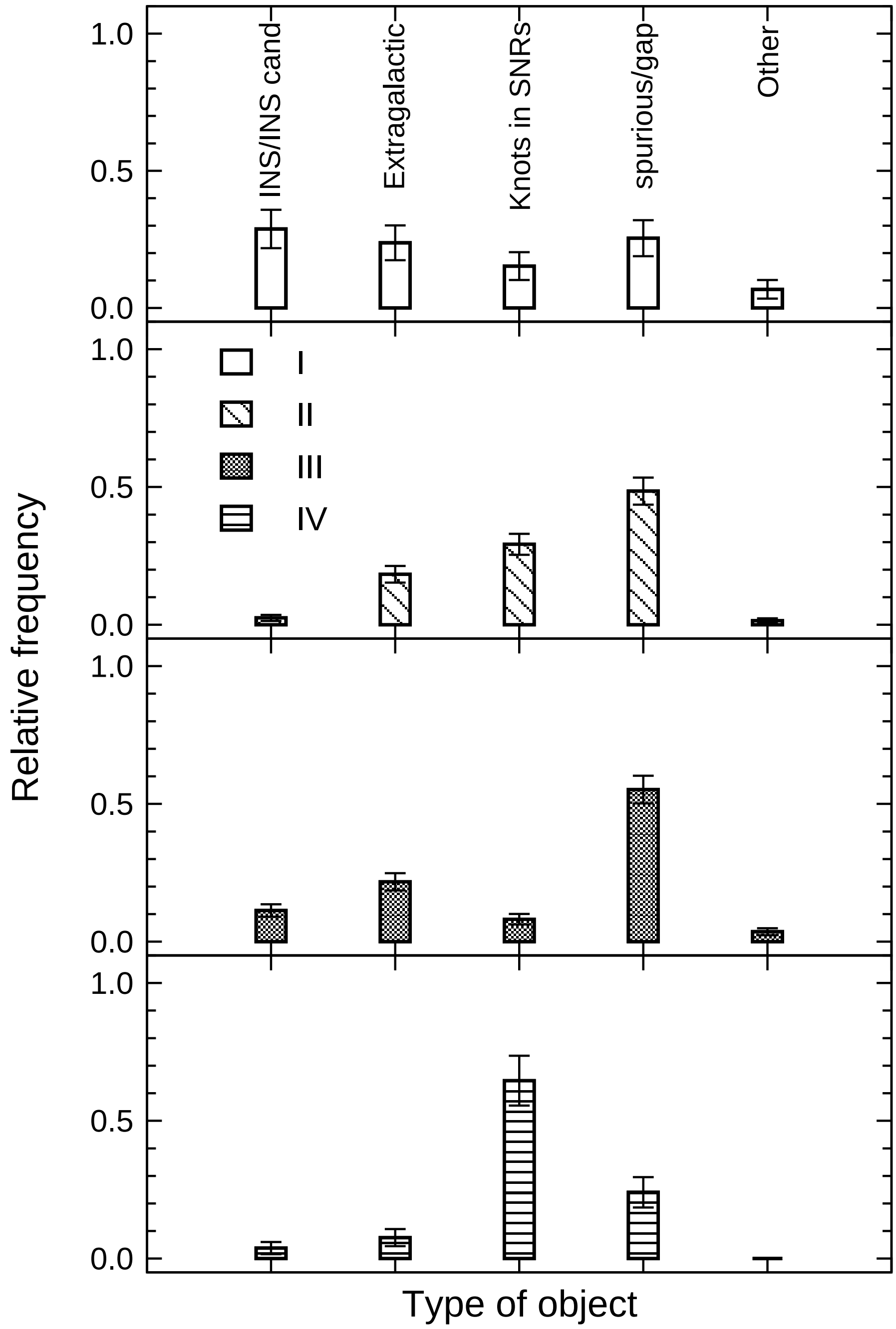

Figure 3.13: Histograms showing the relative frequency of the 2XMMp sources that fulfilled the selection criteria applied in order to find new INS candidates and that were subjected to visual screening. The four plots show the same histograms in the different selection regions (see Fig. 3.4).

Table 3.2: Final list of INS candidates, selected from among more than 70, 000 2XMMp sources.

Source indetification 2XMM	α (J2000)	δ (J2000)	pn CR s^{-1}	r_{90} (arcsec)	b (degrees)	Selection Region	HR_1	HR_2
J022424.8-034319	02 24 25.1	−03 43 20.3	0.0135(25)	3.71	−57.74	I	−0.14 ± 0.17	−0.64 ± 0.22
J104608.7-594306	10 46 08.7	−59 43 06.1	0.060(4)	1.33	−0.60	II	+0.63 ± 0.05	−0.63 ± 0.05
J022718.8-051104	02 27 19.1	−05 11 03.8	0.016(5)	3.97	−58.33	II	+0.7 ± 0.3	−0.2 ± 0.4
J004046.0-272412	00 40 47.0	−27 23 26.2	0.015(4)	3.23	−87.62	II	+0.70 ± 0.27	−0.4 ± 0.3
J041430.5-553941	04 14 30.7	−55 39 42.5	0.0100(26)	3.26	−43.95	II	+0.62 ± 0.27	−0.34 ± 0.26
J125948.8+163935	12 59 48.8	+16 39 37.9	0.049(10)	2.40	+79.35	III	+0.17 ± 0.21	−0.46 ± 0.22
J121017.0-464609	12 10 17.1	−46 46 11.2	0.027(6)	2.61	+15.52	III	+0.53 ± 0.25	−0.07 ± 0.24
J010642.3+005032	01 06 42.4	+00 50 31.3	0.020(5)	3.75	−61.79	III	+0.73 ± 0.25	−0.24 ± 0.25
J043553.2-102649	04 35 53.2	−10 26 50.0	0.019(3)	2.69	−34.80	III	+0.15 ± 0.18	−0.56 ± 0.19
J031459.9-291816	03 14 59.9	−29 18 15.5	0.018(4)	2.40	−58.42	III	+0.40 ± 0.21	−0.33 ± 0.22
J214026.1-233222	21 40 26.2	−23 32 22.3	0.0181(20)	1.91	−46.95	III	−0.10 ± 0.12	−0.47 ± 0.14
J000509.3+001113	00 05 09.4	+00 11 13.0	0.016(3)	2.46	−60.51	III	+0.83 ± 0.28	+0.05 ± 0.21

Continued on next page...

Note: Equatorial coordinates α and δ, Galactic latitude b, positional error (90% confidence level) r_{90}, hardness ratios and count rates of the final list of 27 INS candidates. Count rates are in the total energy band of the EPIC pn camera (0.2 – 12 keV).

Table 3.2: Final list of INS candidates, selected from among more than 70, 000 2XMMp sources. (continued)

Source indetification 2XMM	α (J2000)	δ (J2000)	pn CR s^{-1}	r_{90} (arcsec)	b (degrees)	Selection Region	HR_1	HR_2
J221733.7-163242	22 17 33.9	−16 32 43.3	0.014(4)	3.99	−52.92	III	−0.13 ± 0.27	−0.36 ± 0.37
J125904.5-040503	12 59 04.6	−04 05 02.3	0.0129(21)	1.93	+58.73	III	+0.08 ± 0.18	−0.32 ± 0.20
J103947.5+205740	10 39 47.6	+20 57 39.9	0.013(3)	2.79	+59.41	III	+0.26 ± 0.26	−0.21 ± 0.27
J125045.7-233349	12 50 45.7	−23 33 47.7	0.0122(21)	3.31	+39.31	III	+0.28 ± 0.18	−0.39 ± 0.19
J015709.1+373740	01 57 09.1	+37 37 40.7	0.0120(14)	1.78	−23.43	III	+0.28 ± 0.12	−0.38 ± 0.12
J134123.8+002205	13 41 23.8	+00 22 05.7	0.0118(18)	2.20	+60.67	III	+0.15 ± 0.17	−0.31 ± 0.17
J052932.1-391815	05 29 32.0	−39 18 14.8	0.012(3)	3.86	−31.99	III	+0.51 ± 0.36	−0.38 ± 0.35
J163237.9+703503	16 32 38.2	+70 35 03.1	0.012(4)	3.05	+36.76	III	−0.03 ± 0.35	−0.11 ± 0.40
J083738.6+254507	08 37 38.6	+25 45 07.7	0.0110(26)	3.24	+33.81	III	+0.34 ± 0.28	−0.20 ± 0.25
J120518.8+352235	12 05 18.9	+35 22 35.9	0.0109(22)	2.85	+77.16	III	+0.37 ± 0.24	−0.23 ± 0.22
J041450.7-553948	04 14 50.7	−55 39 46.6	0.0107(22)	3.48	−43.90	III	+0.08 ± 0.22	−0.25 ± 0.22
J123124.2+152428	12 31 24.3	+15 24 27.3	0.0107(22)	2.86	+77.39	III	+0.79 ± 0.26	+0.25 ± 0.20
J061344.7-240151	06 13 44.8	−24 01 51.7	0.0103(27)	3.26	−18.59	III	+0.59 ± 0.32	−0.13 ± 0.26
J125802.2-293701	12 58 02.3	−29 37 01.3	0.0103(20)	2.71	+33.23	III	+0.70 ± 0.20	−0.21 ± 0.18
J054739.8-320039	05 47 39.8	−32 00 39.2	0.0100(12)	2.13	−26.68	III	−0.04 ± 0.12	−0.50 ± 0.15

Note: Equatorial coordinates α and δ, Galactic latitude b, positional error (90% confidence level) r_{90}, hardness ratios and count rates of the final list of 27 INS candidates. Count rates are in the total energy band of the EPIC pn camera (0.2 – 12 keV).

Table 3.3: Overall properties of the INS candidates selected for optical follow-up.

Source identification 2XMM	α (J2000)	δ (J2000)	b (degrees)	$N_{\rm H}^{\rm Gal}$ (cm^{-2})	r_{90} (arcsec)	pn CR (s^{-1})	Selection Region	Optical Data
J104608.7-594306	10 46 08.7	−59 43 06.1	−0.60	1.35×10^{22}	1.33	0.060(4)	II, III, IV	⋆, ◇
J121017.0-464609	12 10 17.1	−46 46 11.2	+15.52	8.70×10^{20}	2.60	0.027(6)	III	⋆
J010642.3+005032	01 06 42.4	+00 50 31.3	−61.79	3.18×10^{20}	3.80	0.020(5)	III	⋆
J043553.2-102649	04 35 53.2	−10 26 50.0	−34.80	5.80×10^{20}	2.70	0.019(3)	III	‡
J031459.9-291816	03 14 59.9	−29 18 15.5	−58.42	1.32×10^{20}	2.41	0.018(4)	III	‡
J214026.1-233222	21 40 26.2	−23 32 22.3	−46.95	3.51×10^{20}	1.90	0.0181(20)	III	†
J125904.5-040503	12 59 04.6	−04 05 02.3	+58.73	1.81×10^{20}	1.90	0.0129(21)	III	†
J125045.7-233349	12 50 45.7	−23 33 47.7	+39.31	7.37×10^{20}	3.30	0.0122(21)	III	†

Note: Equatorial coordinates α and δ, Galactic latitude b, total Galactic extinction $N_{\rm H}^{\rm Gal}$ (Dickey & Lockman 1990), positional error (90% confidence level) r_{90} and count rates of the INS candidates selected for optical follow-up. Count rates are in the total energy band of the EPIC pn camera (0.2 – 12 keV). Optical data were obtained during different observing periods: ⋆ESO-VLT P79 (pre-imaging), †SOAR 2007A, ‡SOAR 2007B, ◇SOAR 2008A.

observation with the USNO-B1.0 catalogue, minimizing positional offsets through translations and rotations of the coordinates of the EPIC sources that have optical objects within 15″ of their positions.

3.3 Optical follow-up

We are presently conducting an optical campaign with the purpose of investigating the nature of the X-ray brightest INS candidates of our sample. The immediate goal is to find a possible alternative identification – essentially faint polar-type cataclysmic variables (CVs), late-type stars or active galactic nuclei (AGN) – for the selected sources, through the analysis of the spectra and the colour indices of the optical objects that may be present in the X-ray error circles.

The 8 INS candidates in Table 3.3 were observed using the 8.2 m ESO Very Large Telescope (ESO-VLT) and the 4.1 m Southern Astrophysical Research Telescope (SOAR) facilities in Chile during 2007, 2008 and 2009. Table 3.4 shows the log of all the observations that we have obtained and analysed so far. We note that the exposure times, seeing and airmasses listed in Table 3.4 are averaged per filter. Hereafter, we adopt the convention "XMM J*hhmm*" to designate the 8 X-ray sources discussed in this work.

3.3.1 Observations and data reduction

We obtained deep imaging of the fields of our candidates under photometric conditions and dark sky for a total ~ 12.4 h observing time (see the log of observations in Table 3.4). Only pre-imaging data were obtained with the ESO-VLT during period P79 while ~ 90% of the proposed observing time was executed by SOAR in three different observing periods (2007A,B and 2008A). Dedicated observing time on one INS candidate, XMM J1046, was obtained in P82 with ESO-VLT during the present year (2009). The Focal Reducer low/dispersion Spectrograph (FORS; Appenzeller et al. 1998) and SOAR Optical Imager (SOI; Schwarz et al. 2004) were used.

The FORS detector consists of a mosaic of two 2k × 4k MIT CCDs (15 μm). In P79 we used FORS2, the camera mounted on UT1 (Antu Unit Telescope) that is optimized for the red band, while the 2009 observations of P82 were conducted with FORS1 in UT2 (Kueyen Unit Telescope). FORS1 is most sensitive in the blue range (see Appendix B.2.1 for a brief description and references). The detector provides imaging at a pixel scale of 0.25″ pixel^{-1} using standard read-out mode and a 2 × 2 binning (6.8′ × 6.8′ FoV). With this configuration the gain and the read-out noise in FORS2 are 1.25 e$^-$ ADU^{-1} and 2.7 e$^-$ while, in FORS1, these values are 2.2 e$^-$ ADU^{-1} and 4.2 e$^-$.

The SOI instrument uses a mosaic of two E2V 2k × 4k CCDs (15 μm) and it is optimized for the blue and UV bands. It has a field-of-view of 5.3′ × 5.3′ and a pixel scale of 0.15″ pixel^{-1} using a 2 × 2 binning. It was used in slow read-out mode, minimizing the read-out noise to 3.1 e$^-$ with a gain of 0.4 e$^-$ ADU^{-1} (see Appendix B.2.2 for a brief description and references).

Dithering patterns with offsets of 2″ and 5″ were chosen for the SOAR and the ESO-VLT observations, respectively. Seeing during the several nights of observation varied between 0.5″ and 1.2″ FWHM, with mean values of 0.67″ and 0.88″ for the ESO-VLT and SOAR nights.

3.3.1.1 Reduction of the ESO-VLT optical data

A data reduction pipeline[13] is provided by the European Southern Observatory for each of the VLT instruments at work in Paranal with the aim of monitoring instrument performance and to produce master calibration products and reduced science observations. The pipeline recipes, as well as front-end applications to launch them, are made public to the observers and user community in order to enable a more personalised processing of the data from each instrument.

The pre-imaging data of period P79, which had the purpose of investigating the X-ray error circles of a handful of our INS candidates (sources XMM J1046, XMM J1210 and XMM J0106) in order to select potential optical candidate counterparts for either spectroscopy or deep imaging, were analysed using these already bias and flat-field corrected frames provided by the ESO-VLT pipeline. The two exposures in each filter – the sources were observed in the B_BESS (λ_0 = 4290 Å, FWHM = 880 Å) and R_SPECIAL (λ_0 = 6550 Å, FWHM=1650 Å) broad-band filters – were combined using an algorithm to remove cosmic rays and bad pixels based on CCD statistics (ccdclip in IRAF[14] task imcombine; see below).

The 2009 observations of XMM J1046 (three exposures taken with the V_HIGH filter, whose central wavelength is λ_0 = 5550 Å and FWHM = 1232 Å) were analysed in two steps. Firstly, we applied IRAF (Tody 1986) to process raw frames; secondly, EsoRex[15] and ESO-VLT recipes were used in order to recreate the instrument pipeline. For both softwares, standard procedures were adopted and carried out for each FORS CCD chip, Marlene and Norma, independently. Very briefly (below we give more details while describing the IRAF reduction steps for SOAR data), we subtracted the overscan pedestal count level from the observations, also removing second-order bias and residual noise by means of a master combined bias frame, flat-fielded the images with master sky and dome flats and finally combined the scientific exposures in order to remove cosmic rays, bad/hot pixels and increase the signal-to-noise (S/N) ratio of the data. We verified that both (IRAF/EsoRex) reductions yielded very similar results in the analysis, which was also true when compared to the results obtained with the pipeline reduced scientific frames distributed by ESO-VLT. Therefore, we only discuss hereafter the results of analysis conducted on the scientific images distributed by the ESO pipeline.

The transformation of the instrumental magnitudes to the standard photometric system was done using the zero-points, extinction coefficients and colour terms for each filter as provided by the ESO-VLT calibration webpages[16]. While for period P79 we used averaged values for the observing period, the deeper images of source XMM J1046 in period P82 were calibrated with the coefficients obtained on the night of the observation.

[13] http://www.eso.org/sci/data-processing/software/pipelines/index.html
[14] http://iraf.noao.edu
[15] http://www.eso.org/sci/data-processing/software/cpl/esorex.html
[16] http://www.eso.org/observing/dfo/quality

Table 3.4: Description of the optical observations obtained for the eight X-ray brightest INS candidates in Table 3.3.

Target	Night	Telescope	Exposures	Exp. Time (s)	Total Exp. Time (s)	FWHM (arcsec)	Airmass
XMM J1046	2007-02-22	ESO-VLT	$2 \times$ B, $2 \times$ R	150, 150	300, 300	0.81, 0.68	1.27, 1.26
XMM J1210	2007-02-25	ESO-VLT	$2 \times$ B, $2 \times$ R	150, 150	300, 300	0.83, 0.70	1.16, 1.15
XMM J1250	2007-05-09	SOAR	$1 \times$ U, $7 \times$ B, $3 \times$ R	500, 200, 200	7000, 1400, 600	0.90, 0.74, 0.80	1.10, 1.03, 1.01
XMM J1259	2007-07-10	SOAR	$4 \times$ U, $4 \times$ B, $4 \times$ R	500, 200, 200	2000, 800, 800	0.75, 0.68, 0.62	1.02, 1.01, 1.01
XMM J2140	2007-07-11	SOAR	$4 \times$ U, $4 \times$ B, $3 \times$ R	500, 200, 200	2000, 800, 600	1.11, 0.95, 0.80	1.19, 1.23, 1.25
XMM J0106	2007-07-21	ESO-VLT	$2 \times$ B, $2 \times$ R	150, 150	300, 300	0.62, 0.58	1.16, 1.15
XMM J0314	2008-01-29	SOAR	$4 \times$ U, $5 \times$ B, $4 \times$ R	500, 200, 200	2000, 1000, 800	0.85, 0.82, 0.72	1.18, 1.22, 1.24
XMM J0435	2008-01-30	SOAR	$4 \times$ U, $4 \times$ B, $4 \times$ R	500, 200, 200	2000, 800, 800	1.14, 1.16, 1.10	1.10, 1.11, 1.12
XMM J1046	2008-02-08	SOAR	$6 \times$ V, $6 \times$ Hα	1120, 1575	6720, 9450	0.94, 1.04	1.23, 1.20
XMM J1046	2009-02-21	ESO-VLT	$3 \times$ V	1100	3300	0.50	1.22

Note: The exposure times, seeing and airmasses are averages per filter.

3.3.1.2 Reduction of the SOAR optical data

The SOAR observations carried out during 2007 in periods A and B had the same simple observing strategy: we obtained for each INS candidate field two series of UBR double exposures (i.e. $2 \times$ U, $2 \times$ B, $2 \times$ R, $2 \times$ U, $2 \times$ B, $2 \times$ R) together with a short exposure of a standard star field observed in the same filters as the scientific targets. The INS candidates observed by SOAR were XMM J0435 and XMM J0314 in period 2007B and XMM J2140, XMM J1259 and XMM J1250 in period 2007A. We used Bessel filters with central wavelengths and FWHM of $\lambda_0 = 3624\,\text{Å}$, FWHM $= 784\,\text{Å}$ for U, $\lambda_0 = 4326\,\text{Å}$, FWHM $= 1269\,\text{Å}$ for B and $\lambda_0 = 6289\,\text{Å}$, FWHM $= 1922\,\text{Å}$ for R[17]. The observations of source XMM J1046 in period 2008A consisted of six exposures in the broad-band Bessel V ($\lambda_0 = 5332\,\text{Å}$ and FWHM $= 1073\,\text{Å}$) and Hα ($\lambda_0 = 6571\,\text{Å}$ and FWHM=93 Å) filters. We had the coordinates of the X-ray source positioned on the CCD on the right of the gap defined by the two chips of the SOI mosaic and at a distance of $30''$ from its edge, next applying $2''$ translations in right ascension and declination relative to this position.

Data reduction followed very standard procedures and it was conducted within the IRAF package ccdred[18]. We first determined the bias level in each frame by defining an overscan region for each CCD chip and fitting the count values in this region as a function of line number (data were averaged over all columns in the overscan region). We inspected the illuminated area of the detector in the flat-field images in order to define the overscan regions for each chip. Next, we combined the zero-count bias frames using the task zerocombine in order to create a master bias frame. The task performs a simple average of the pixel values in the bias images, rejecting pixels with the highest and lowest count values. By running the task ccdproc, we then processed all frames in order to remove the overscan level and subtract the averaged bias counts. The data were also trimmed in this first pass through ccdproc so as to keep only the useful parts of the CCD chips. We next produced master sky and dome flats using the task flatcombine, which combines images averaging pixel values that were not rejected by the crreject algorithm. This algorithm computes the average of the pixel values, excluding the highest and lowest pixels, and then computes the expected standard deviation $\sigma_{\rm ccd}$ using the known chip gain g in electrons per ADU, read-out noise ϱ in electrons and sensitivity noise s given as a fraction, according to:

$$\sigma_{\rm ccd} = \sqrt{\left(\frac{\varrho}{g}\right)^2 + \frac{\mathscr{I}}{g} + \left(s\mathscr{I}\right)^2} \tag{3.3}$$

where $\mathscr{I}$ is the true pixel value approximated by the average in ADUs; a value $s = 0$ (the default) was used due to uncertainties in the pixel sensitivities. Pixel with values above $3\sigma_{\rm ccd}$ of the average are then excluded and the process is iterated until no further pixels are rejected. A multiplicative scaling of the pixel counts by the inverse of the mode of the processed data values is applied to each pixel prior to averaging. The rejection algorithm at work in ccdclip is rather identical to the one just described for crreject; the only difference being that in ccdclip pixels below or above $\pm 3\sigma_{\rm ccd}$ of the average are rejected. The

[17] http://www.ctio.noao.edu/~points/SOIFILTERS/filters/maintext.html
[18] http://iraf.noao.edu/docs/photom.html

frames are then processed again with ccdproc in order to flatten the images and eliminate the instrumental signature from the data by dividing the scientific frames by the master flat images created with flatcombine. When both dome and sky flats were available, the processing was done to first approximation with the master dome flat by running ccdproc and switching the option flatcor to TRUE and subsequently with the master sky flat, which performs the final illumination correction in a third pass through ccdproc with the parameter illumcor switched to TRUE. There were cases however where only sky flats were available but they were sufficient to flatten the images.

3.3.1.3 Photometry of standard stars

In order to calibrate the SOAR images, we selected photometric standard star fields from Landolt (1992) that were located at reasonably close right ascensions and declinations as the scientific targets as well as choosing fields that were suitable for colour transformation, with a very blue/UV object that is usually a white dwarf. Fields RU 149, Mark A and PG1323-085 were selected to calibrate the observations of sources XMM J0435, XMM J0314, XMM J2140, XMM J1259 and XMM J1250. The deeper observations of XMM J1046 were calibrated with the standards PG1047+003 and SA 104. For each field (as appropriate depending on the requested observations of the science target) we obtained 10 s (U or V), 15 s (Hα) and 5 s (B or R) single exposures. The airmasses at which the observations of standard stars were carried out were similar to those of the science targets.

The instrumental magnitudes in the standard star fields were measured through aperture photometry with the IRAF task phot within the daophot package. We chose the aperture size based on the seeing of the observations, setting the radius to roughly three times the FWHM in pixels. While using phot, one has to specify specific data parameters in the task, such as the size of the point spread function (PSF) and the range in ADUs in which the chip response is linear. The read-out noise and gain are also provided in order to obtain realistic error estimates. A centroid algorithm based on the intensity weighted means in detector coordinates x and y is used in order to center the star profiles. The size of the centering box was usually set to twice the FWHM of the observation. The sky count level is determined by means of an annulus centered on the star position in which the modal background value is computed. Typically, we used a width of 5 pixels for the annulus, whose inner radius was set larger than the aperture size used for photometry. The output instrumental magnitudes m already take into account the exposure time of the observation, according to:

$$m = m_0 - 2.5 \log \mathscr{C} + 2.5 \log t \tag{3.4}$$

where m_0 is an arbitrary constant (the zero-point of the magnitude scale), $\mathscr{C}$ is the total number of counts excluding sky in the aperture and t is the integration time. The aperture correction was only accounted for while transforming the instrumental magnitudes of the science targets to the standard system (see Sect. 3.3.2.2).

3.3.1.4 Shutter correction in SOAR images

We had to perform a shutter calibration on the SOAR[19] images so as to obtain more accurate photometry. This correction is needed since short observations taken by cameras with mechanical shutters can give measurably different effective exposure times depending on the object position on the detector. This is only a consequence that no device is ideal; i.e. no shutter instantly opens (or closes) the camera aperture to expose the CCD to light, although they can be very fast. As a result, the detector is not exposed homogenously to the incoming radiation and this can introduce a significant systematic error in the computed magnitudes of objects observed with short integration times, such as the observations of standard stars.

In order to calibrate the shutter, we considered a number of repeated exposures of fields of standard stars that had been taken with different exposure times ($1-5$ s, $5-10$ s, ...) and which were distributed to us as part of the SOAR calibration data. We note that a series of illuminated dome screen exposures, taken at different exposure times, would be more appropriated for this purpose (e.g. Zissell 2000). However, we had not specifically asked for frames aiming at performing this calibration and used instead what we had available. We computed the instrumental magnitudes of stars in these fields, which were spread across the CCD, as a function of *nominal* exposure time and then found the shutter correction to be applied that minimized the difference between the measured magnitudes of the stars in the images, on average. The correction value found, $t_{\mathrm{sh}} = 0.07$ s, was therefore added to the effective exposures of all frames, standard stars and scientific targets included.

3.3.1.5 Fit to the standard system

As only one exposure was taken in each filter (at a given airmass) it was not possible to determine the extinction coefficients E_λ; mean values for the periods were adopted instead. On the other hand, the zero-point magnitudes Z_λ and colour coefficients C_λ were determined from our observations of the standard stars in each night. The fit to the standard system was performed relative to the $U-B$ (for the U magnitudes) and $B-R$ (for the B and R magnitudes) colours, according to:

$$m_{\mathrm{U}} = U + Z_{\mathrm{U}} + E_{\mathrm{U}}X_{\mathrm{U}} + C_{\mathrm{U}}(U-B) \tag{3.5}$$

$$m_{\mathrm{B}} = B + Z_{\mathrm{B}} + E_{\mathrm{B}}X_{\mathrm{B}} + C_{\mathrm{B}}(B-R) \tag{3.6}$$

$$m_{\mathrm{R}} = R + Z_{\mathrm{R}} + E_{\mathrm{R}}X_{\mathrm{R}} + C_{\mathrm{R}}(B-R) \tag{3.7}$$

where X_λ are the effective airmasses at the observing site as computed by the task setairmass. The m_{V} SOAR instrumental magnitudes of period 2008A were transformed adopting a null colour coefficient and the mean value of the extinction coefficient for the period, according to:

[19] The ESO-VLT observations already take into account the shutter correction.

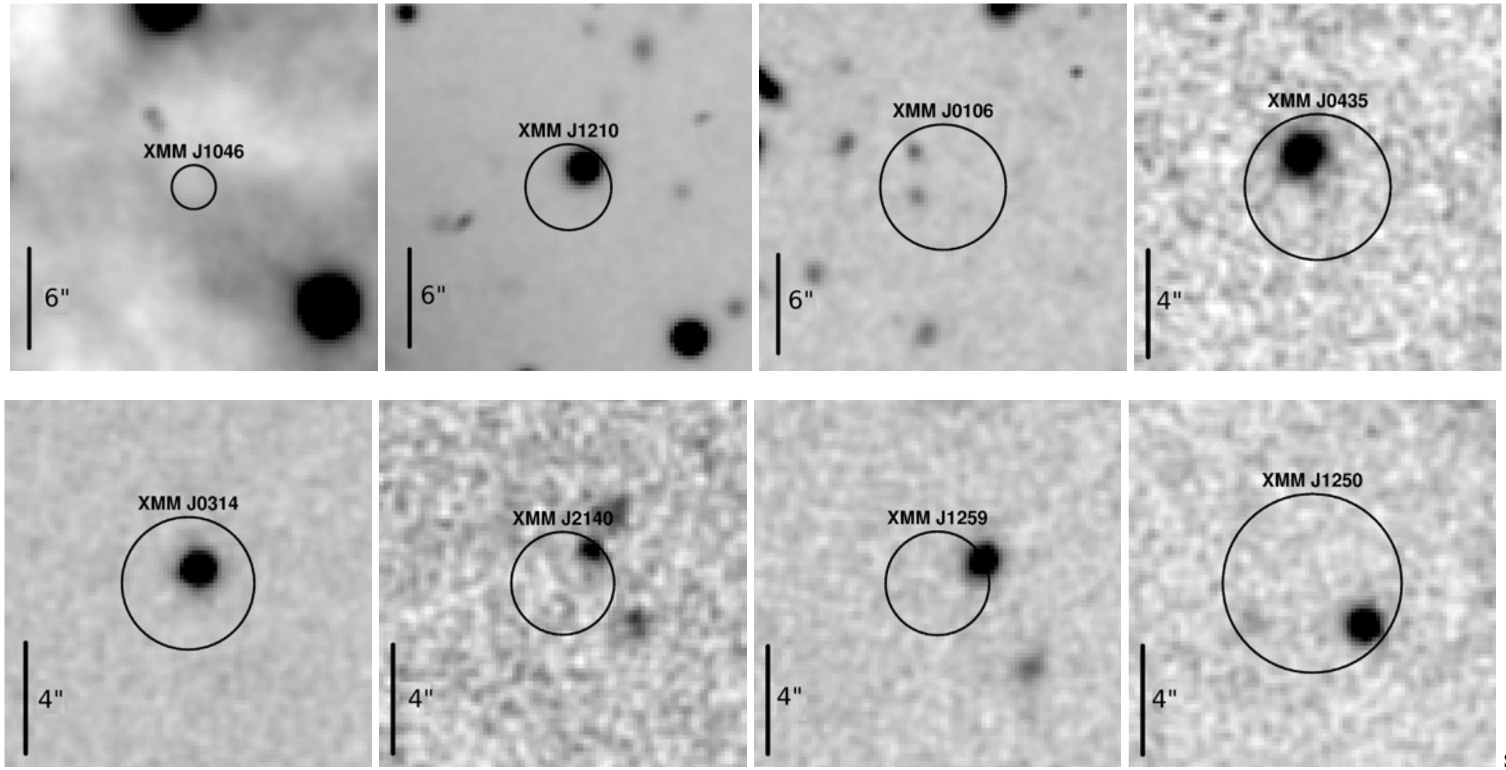

s

Figure 3.14: R images of the fields of observed INS candidates. Candidates XMM J1046, XMM J1210 and XMM J0106 were observed with the ESO-VLT in period P79 while candidates XMM J0435, XMM J0314, XMM J2140, XMM J1259 and XMM J1250 were observed using the SOAR telescope. In these images, north and east point upwards and to the left, respectively.

$$m_{\mathrm{V}} = V + Z_{\mathrm{V}} + E_{\mathrm{V}} X_{\mathrm{V}} \tag{3.8}$$

We compared the R magnitudes of non-saturated GSC2 stars present in the fields with our ESO-VLT and SOAR results and concluded that the agreement is good with a mean dispersion of ~ 0.03 mag.

3.3.2 Data analysis and results

3.3.2.1 Astrometry

The astrometric calibration of the stacked science frames was performed using the USNO-B1.0, 2MASS and GSC2 catalogues and the GAIA 4.2-1 software[20]. For a given image, we obtained reference positions for the optical objects by querying these catalogues – sometimes filtering in magnitude or in magnitude errors and deleting problematic objects like saturated stars or extended sources – in order to obtain the most precise reference table of celestial positions. A two-dimensional Gaussian function fit to the objects' intensity profiles was then performed so as to determine the pixel coordinates of the objects in the image. Next, an astrometrical solution was computed by fitting the pixel to the celestial coordinates. We repeated this method with different catalogues or by applying filtering to the reference positions until the fit errors were minimal. In general, our astrometric errors are of $\sim 0.15''$ or better.

3.3.2.2 Photometry

Two different approaches were adopted to measure magnitudes: standard PSF fitting, as implemented in the daophot (Stetson 1987) package for the IRAF environment and, for the fields of candidates located at high galactic latitudes ($|b| > 20°$, see Table 3.3), variable elliptic apertures and background maps using SExtractor 2.5.0[21].

PSF fitting using a two-dimensional Gaussian function was adopted whenever there were a fair number of isolated[22] and bright non-saturated stars available, allowing a good determination of the modelled PSF to apply to all detected sources on the image (including faint and overlapping stars). When this was not the case, we adopted SExtractor instead. This software is most commonly used to reduce galaxy survey data but it also performs well in moderately crowded stellar fields. As many extragalactic objects were likely to be present in our high galactic latitude fields, its usage is convenient since it is possible to derive, for instance, information on how elongated an object is; additionally, making use of a neural network, SExtrator classifies any given object as stellar or non-stellar. However, this classification is less reliable for faint fluxes. Its main advantage is that flux measurements of extended objects tend to be more accurate when compared to those obtained using fixed aperture photometry, since elliptical apertures with variable sizes (based on the object intensity) are used instead. Another advantage is that a global background map is created,

[20] http://star-www.dur.ac.uk/~pdraper/gaia/gaia.html
[21] http://terapix.iap.fr/rubrique.php?id_rubrique=91
[22] We note, however, that none of the fields are severely crowded, not even the one located at $b \sim 0°$.

which better accounts for local spatial variations of brightness due e.g. to nebular emission or caused by scattered light from bright objects. We briefly describe in the following the procedures adopted in order to perform both the PSF fitting with daophot and the photometry and catalogue creation with SExtractor.

PSF fitting First, we determined the PSF fitting radius taking into account the size in pixels of the brightest non-saturated star in the images for which we wanted to perfom photometry. This parameter, psfrad, was passed to the daopars parameter file within daophot as other data-specific parameters were passed to datapars, such as the detector gain, read-out noise, FWHM and maximum count value before saturation. We then used the task daofind in order to automatically find the optical objects in the image. This task convolves a Gaussian of width set equal to the observation FWHM with the image, and then looks for intensity peaks greater than some threshold in the smoothed image. It then only keeps the objects that are within certain roundness and sharpness criteria in order to reject non-stellar objects such as cosmic rays, background galaxies and bad columns. To run the task, we estimated the sky background level on the images and computed the expected 1σ error. If $\mathscr{B}$ is the typical sky value in ADUs, g the conversion factor between photons and ADU and ϱ the read-out noise, then the expected sky standard deviation $\sigma_{\rm sky}$ is, similar to Eq. (3.3), given by :

$$\sigma_{\rm sky} = \sqrt{\left(\frac{\varrho}{g}\right)^2 + \frac{\mathscr{B}}{g}} \tag{3.9}$$

We note, however, that since we combined frames, the used values of the gain and read-out noise above are not the nominal ones but rather $g' = Ng$ and $\varrho' = \sqrt{N}\varrho$, for a

Table 3.5: Results of the optical follow-up investigations.

Cand XMM	r (arcsec)	R	$U-B$	$B-R$	LR	$P_{\rm chance}$ (%)	e	$\log(f_{\rm X}/f_{\rm R})$
J1210	1.55	20.13(3)	?	1.35(3)	8.4	2.8	0.037	0.18
J0106	2.75	24.51(9)	?	$\gtrsim 2.0$	1.2	22.4	0.178	1.93
	1.68	24.58(9)	?	$\gtrsim 1.9$	1.2	22.4	0.162	1.96
J0435	1.20	22.15(4)	−0.51(8)	0.93(7)	15.2	2.3	0.068	0.77
J0314	0.67	21.37(3)	−0.13(7)	1.43(4)	32.1	1.7	0.022	0.41
J2140	1.26	23.78(9)	−1.08(16)	1.06(15)	6.0	6.4	0.156	1.40
J1259	1.34	21.64(4)	−1.08(4)	0.76(5)	25.5	1.0	0.098	0.61
J1250	1.80	22.19(4)	−0.71(4)	0.74(4)	8.4	4.1	0.029	0.57

Note: Distance r (relative to the X-ray position), likelihood ratios LR, probability of chance association $P_{\rm chance}$, ellipticity e and logarithmic X-ray-to-optical flux ratio $\log(f_{\rm X}/f_{\rm R})$ refer to the objects found on the R images. The X-ray flux is computed in the 0.15 – 3 keV energy band assuming an absorbed power-law model.

number of N stacked images. The minimum count data value, the parameter datamin, was then adopted as being roughly the sky value minus $\sim 3\sigma_{\rm sky}$. The threshold for detection was considered between $3\sigma_{\rm sky}$ and $5\sigma_{\rm sky}$. We then performed aperture photometry in the objects that had been found by daofind using the task phot (see Sect. 3.3.1.3); this is necessary in order to derive magnitudes and sky counts that are used later as starting points during actual PSF fitting. Unlike what had been done for the standard stars, no centering is performed at this stage since photometry is carried out using the pixel coordinates x, y of the objects found by daofind. The sky counts are derived in an annulus around the object positions as for the standard stars although the aperture size was usually set smaller than what had been used before. The next step consisted in defining the PSF model by selecting the brightest non-saturated and isolated stars present in the image, which was done with the task psf. The actual PSF fitting was then performed with allstar. Finally, we computed the aperture corrections with mkapfile in order to compensate for the intensity loss due to the different aperture sizes used by phot in the science frames and standard star fields.

SExtractor SExtractor is used for the automated detection and photometry of sources in FITS image files. The analysis of an image consists first of the determination of a background model and estimation of a number of global statistics in the image. The construction of the background map is perhaps the most important step in the analysis, since the sky counts are used both for source detection and photometry. Concisely, it is computed through a combination of clipping and mode estimation similar to the algorithm employed in daophot and described before: the local background histogram is clipped interatively until convergence at $\pm 3\sigma$ around its median counts. The resulting background map is thus simply a two-dimensional cubic spline interpolation of the grid set up by the sky count determination. The software next works in a series of different steps. The image is background subtracted, filtered and subjected to detection algorithms. The detection process consists of separating astronomical objects from the sky background model by means of detection thresholds and segmentation algorithms if the field is crowded. Detections are next de-blended and cleaned in order to perform photometry and object classification. The final step is to build a catalogue of the objects present in the image, which can be in ASCII or FITS format. With SExtractor, we created catalogues gathering position, intensity and shape information on every optical object present in our high galactic latitude frames. Source detection was carried out by convolving a Gaussian filter having the mean image FWHM. The resulting list of sources in each field was then correlated to keep the optical objects which were detected in all filters. In the following subsections we use the information extracted from these optical catalogues to discuss the nature of our sample of INS candidates and field objects.

3.3.2.3 X-ray/optical associations

We found at least one optical object inside the X-ray error circles (90% confidence level) of all INS candidates but one, the X-ray brightest source XMM J1046 (see Fig. 3.14). In this case no optical object brighter than the limiting magnitude of our present data is present within $\sim 4.3''$ ($\gtrsim 5\sigma$) from the position of the X-ray source (see discussion in 3.3.2.5).

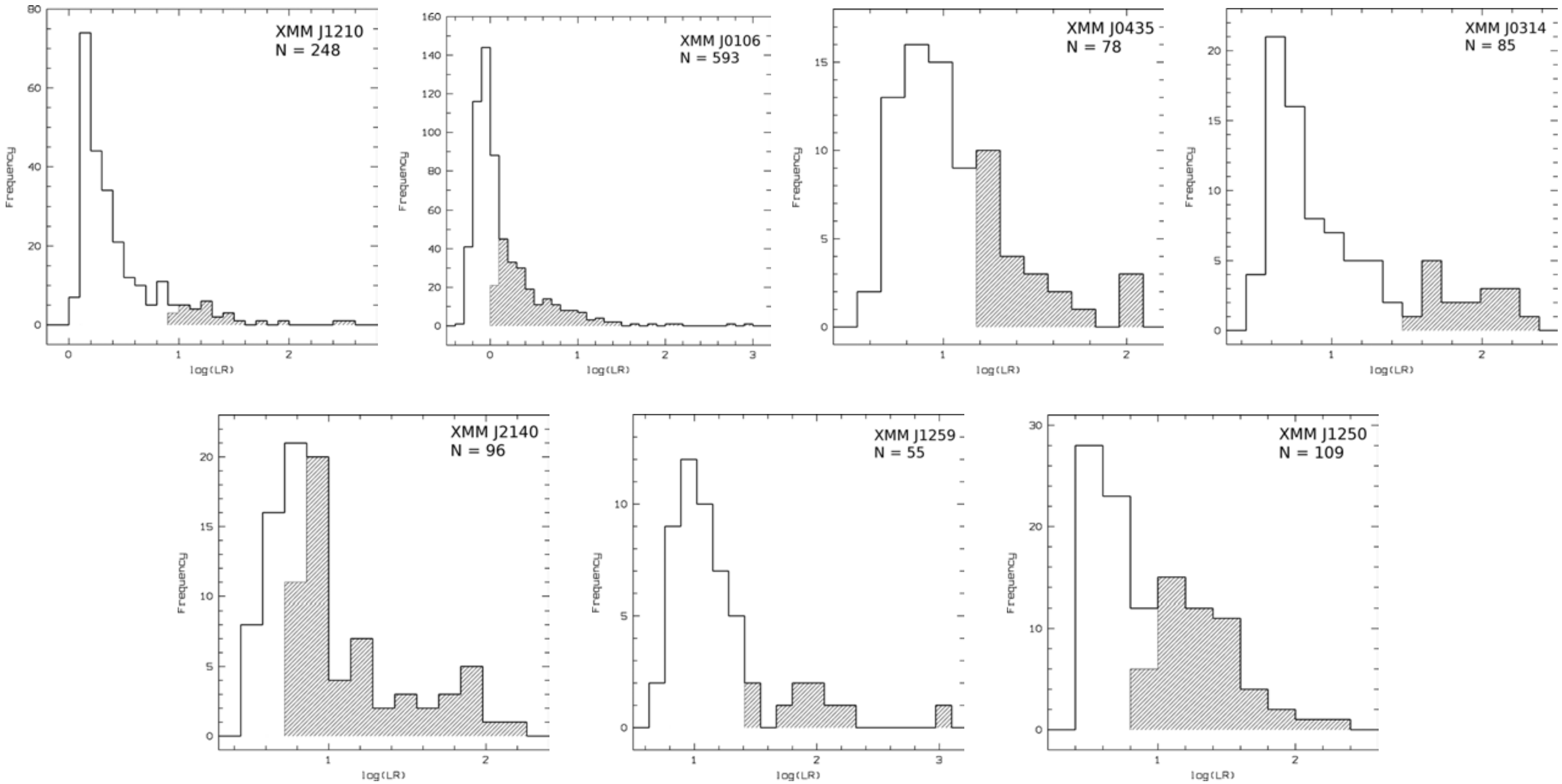

Figure 3.15: Histograms showing the *LR* distribution of X-ray/optical associations in the fields of candidates for which possible optical counterparts were found. Each histogram is computed from 1000 Monte Carlo simulations. The number of matche is given in the right upper corners. Hatched bars show simulated X-ray/optical associations which have a *LR* greater than or equal to that found for the X-ray source.

Table 3.5 lists the R magnitudes and $B-R$ and $U-B$ (only for SOAR data) colours of the possible optical counterparts of the remaining seven sources, as well as their positional offsets relative to the X-ray coordinates and the implied logarithmic X-ray-to-optical flux ratios, uncorrected for absorption. The candidate counterparts were well detected in all (UBR or BR) filters, with the exception of the two optical objects possibly associated with XMM J0106, only detected in the R image. Among the possible counterparts, these were also the faintest ones ($R\sim 24.5$).

To estimate the reliability of each X-ray/optical association, we defined a likelihood ratio (*LR*) based on the probabilities that, given the positions, an optical object is the true counterpart of the X-ray source or is just a random object that happens to lie angularly close to its position. The *LR* takes into account the magnitude of the optical object, the angular distance to the X-ray source (and its significance) and the local density of similar objects on the sky. Following de Ruiter et al. (1977), the *LR* can be described by the ratio between a Rayleigh (true counterpart) and a Poisson (random object) probability density distributions, i.e.:

$$dP_{\rm (Ra)} = xe^{-\frac{x^2}{2}}dx \tag{3.10}$$

$$dP_{\rm (Po)} = 2\lambda xe^{-\lambda x^2}dx \tag{3.11}$$

where λ is defined as $\lambda=\pi\sigma^2\rho$, σ is the error in the X-ray and optical position and ρ is the surface density of brighter or equally bright objects on the image. The dimensionless variable $x=r/\sigma$ is the significance of the position offset (r). The *LR* is then defined as:

$$LR = \frac{dP_{\rm (Ra)}}{dP_{\rm (Po)}} = \frac{1}{2\lambda}\exp\left[\frac{x^2}{2}\Big(2\lambda-1\Big)\right] \tag{3.12}$$

We list in Table 3.5 the *LR* quantities for every possible X-ray/optical association, which ranges from ~ 1 to 32. Although objects with large *LR* are more likely to constitute a true association, the computation of actual probabilities of identification requires a calibration of *LR* taking into account the *a priori* probability that any X-ray source has a counterpart in the optical sample considered (see e.g. Pineau et al. 2008).

LR strongly depends on the local density of optical objects; the chance of a spurious association rising with the number of objects of similar or brighter magnitudes. In order to derive the *LR* distribution of spurious associations and therefore estimate the chance probability of X-ray/optical associations in our data, we performed Monte Carlo simulations randomly changing the position of the X-ray source across the optical fields. For a given simulated X-ray source, we then computed the *LR* value given by Equation (3.12) for each optical object (if any) lying inside r_{90}. The overall distribution of positive matches (among 1000 simulations) can be seen in the histograms of Fig. 3.15. As expected, the distribution of *LR* is highly asymmetrical, strongly peaking at low values and then monotonically extending towards high *LR*. The hatched bars in Fig. 3.15 highlight the number of simulated random X-ray/optical associations with $LR_i \geq LR_{\rm X}$, where LR_i and $LR_{\rm X}$ are the likelihood ratios of simulated and actual X-ray/optical association of the given field.

In general, the simulations show that the probability of a chance association is low for the optical objects found inside r_{90} on the real data (Table 3.5). Out of 1000 simulations, we usually found that less than 3% of the cases had an X-ray/optical association with a likelihood ratio greater than or equal to the real one. The two exceptions were the associations found for source XMM J0106, with $P_{\rm chance} \sim 22\%$ and, to a lesser degree, for source XMM J2140, with $P_{\rm chance} \sim 6\%$. These are the two X-ray sources with the faintest optical candidates and the only ones with $\log(f_{\rm X}/f_{\rm R}) > 1$. However, while the two candidate counterparts for XMM J0106 were detected only in the R band, the one for XMM J2140 was well detected in the U, B and R filters, and it shows very blue colours. We argue in the following that, based on the results obtained here and together with the analysis of their colours and X-ray-to-optical flux ratios (Sect. 3.3.2.4), the optical objects found inside the X-ray error circles of all INS candidates are very likely to be their true optical counterparts, with, again, the exception of source XMM J0106.

3.3.2.4 Identification with other classes of X-ray emitters

As mentioned before, some populations of astrophysical objects are expected to pollute our sample of INS candidates. In order to identify these among the sources having optical candidates, we compared their positions in the colour-colour $g'-r' \times u'-b'$ diagram with those of the major classes of X-ray emitters (Fig. 3.16). The magnitudes in the Sloan photometric system were computed using the Johnson-Morgan-Cousins transformation equations in Fukugita et al. (1996). In this diagram the spectroscopically identified population of quasars (Richards et al. 2001) and cataclysmic variables (Dillon et al. 2008; and references therein) from the SDSS, as well as late-type stars (Bilir et al. 2005), are plotted as contours. Only the five INS candidates observed with SOAR are shown, since we do not have U magnitudes for the two candidates observed with the ESO-VLT (sources XMM J1210 and XMM J0106). We note, however, that the $B-R$ colours of the optical candidates of these sources are among the "reddest" of our sample (Table 3.5).

The $u'-g'$ and $g'-r'$ colours of the optical candidates of the SOAR targets are clearly consistent with those of AGN and CVs. Among the five sources, the proposed counterpart of XMM J0314 is the only one that is somewhat more isolated from the bulk of these two populations of X-ray emitters, although some quasars at still low redshifts from Richards et al. do show similar colours. None of the optical sources exhibits colours typical of late-type stars. The strong blue/UV excess, with $u'-g' < 0$, shown by the proposed counterparts of sources XMM J1259 and XMM J2140 is remarkable. The colours of the optical objects in the error circles of XMM J1250 and XMM J0435 are more intermediate but still consistent with those of AGN and CVs.

Interestingly, when compared to other uncatalogued field objects present in our SOAR frames and *detected in all filters*, the colours and even the UV excess exhibited by our sample of optical candidates do not stand out from the overall field population (Fig. 3.17). For further comparison, we also plot as density contours SDSS objects present in five regions of the sky located at similar column densities as the SOAR fields. More precisely, we gathered SDSS entries in a SOAR field-of-view centered at equatorial coordinates $(\alpha, \delta) = (180^\circ, +60^\circ)$, $(210^\circ, +15^\circ)$, $(215^\circ, +50^\circ)$, $(310^\circ, -1^\circ)$, $(240^\circ, +20^\circ)$, requiring r'

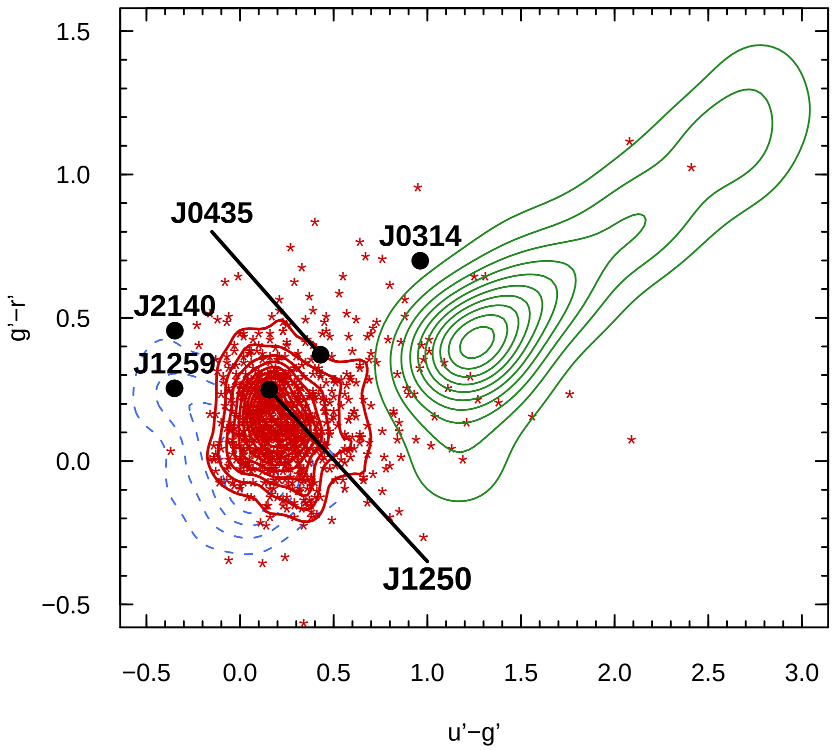

Figure 3.16: Colour-colour $g' - r' \times u' - g'$ diagram comparing the locations of different astrophysical populations of X-ray emitters. Red stars (and contours) show the position of identified QSOs at redshifts lower than 3. Hashed blue and solid green contours are CVs and late-type stars from the SDSS, respectively (see text). The five INS candidates observed with SOAR are represented by plain black circles with labels.

magnitudes between 21 and 24, which is the range covered by our SOAR field objects, and u', g' and r' errors smaller than 0.5. Overall, the plot shows that the SOAR and SDSS objects constitute the same population of "blue field objects" located at high Galactic latitudes, with colours not particularly distinguishable from those of the sample of soft X-ray counterparts. Apart from these blue objects, a smaller fraction of the SOAR field population occupies the same location in the colour diagram as the one of quasars identified at more remote redshifts ($z > 3$; see open triangles in Fig. 3.17). Most ($\gtrsim 99\%$) of the SOAR objects do not have a correlation with the 2XMMi and none with the FIRST (radio) catalogues. According to Mateos et al. (2008), the expected density of soft (0.5 – 2 keV) X-ray sources at high galactic latitudes $|b| > 20°$, with fluxes greater than $f_X > 10^{-14}$ erg s^{-1} cm^{-2} is ~ 100 deg^{-2}, corresponding to ~ 0.75 sources in a typical SOAR FoV – which is roughly in agreement with our results. In summary, the SOAR field objects do not seem to be active

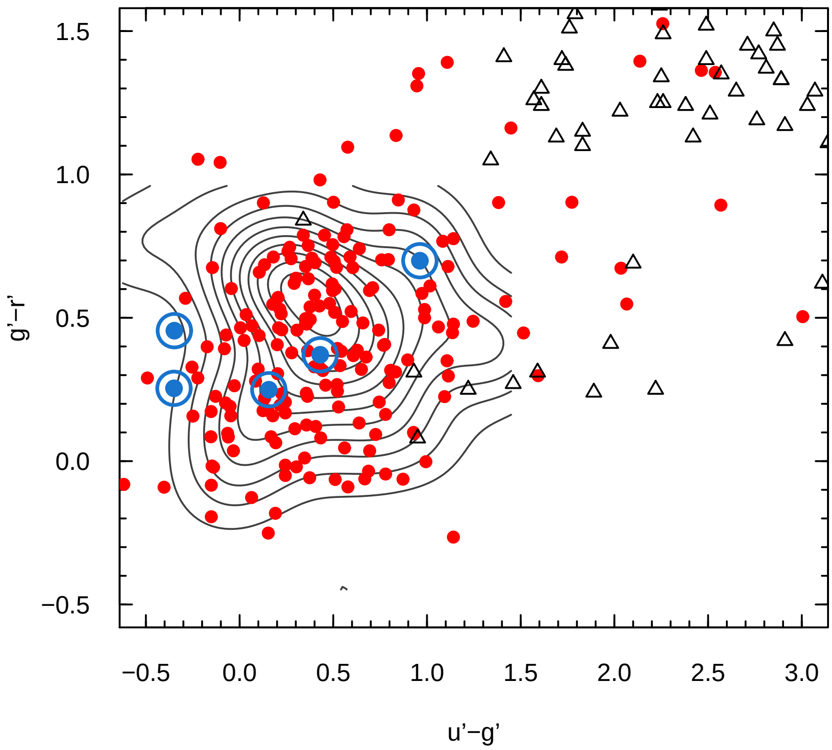

Figure 3.17: Colour-colour $g' - r' \times u' - g'$ diagram showing the colours of field objects detected in the three (U, B and R) filters of our SOAR observations (plain red circles). The population of SDSS objects located at a similar column densities is shown for comparison as a density contour. Open triangles are identified quasars located at redshifts greater than 3. Optical candidates of the soft X-ray sources are shown as large blue circles.

in X-rays or radio wavelengths, despite their blue colours being similar to those of the INS candidates.

We analysed the extent distribution of field objects and optical counterparts using the ellipticity derived by SExtractor. The goal was to verify the possibility of separating stars/AGN from galaxies by measuring their point spread functions. Defining ellipticity as usual ($e = 1 - b/a$, where a and b are the semi-major and semi-minor axis lengths, respectively) we found that most ($\gtrsim 60\%$) of the SOAR field objects are not elongated ($e \lesssim 0.2$, see distribution in the histograms of Fig. 3.18). The counterparts of the INS candidates are also rather point-like, with mean ellipticity ~ 0.08 – the most elongated being source XMM J2140 and the two objects possibly associated with XMM J0106 (see values in Table 3.5).

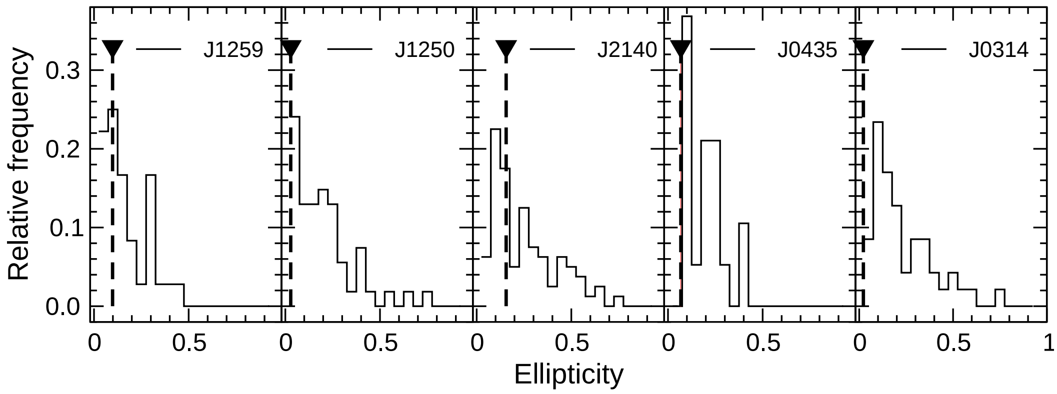

Figure 3.18: Histograms showing the ellipticity distribution of field objects in the SOAR frames. The ellipticity values for the possible optical counterparts of the INS candidates are shown as arrows.

3.3.2.5 Optical upper limits for XMM J1046

The only INS candidate of our sample that remains without an optical candidate is source XMM J1046. The short ESO-VLT exposure obtained in 2007 revealed no counterparts brighter than $R \sim 25$. The location of XMM J1046 towards the Carina star forming region explains the presence of many bright stars and of relatively intense diffuse emission in its optical field. The R filter, which includes the strong Hα line, is thus particularly affected by background intensity variations, impacting the quality of the photometry. In the light of this, we obtained additional deep SOAR exposures in 2008 as well as with the ESO-VLT in 2009 in the V filter. The V band excludes some of the strongest lines found in HII regions (Balmer emission as well as [NII] and [SII] emission lines) and is thus best suited for a deep upper limit on the optical emission of XMM J1046. However, the V filter is still somewhat contaminated by the nebular [OIII] emission.

The deeper observations have also failed detecting the optical counterpart of XMM J1046: as can be seen in the optical images of Fig. 3.19, no object lies within $\sim 4.3''$ ($\gtrsim 5\sigma$) of the position of the source,

$$\alpha = 10:46:08.72 \quad , \quad \delta = -59:43:06.4$$

as derived running the SAS task emldetect on the best XMM-Newton observation 311990101 (Sect. 3.4). The 90% confidence level error circle on the position, r_{90} = 1.33 arcsec, is computed using Eq. (3.2). Similarly, we used the CIAO task wavdetect to determine the position and the 90% confidence level error circle using the Chandra data, which is fully consistent with the XMM-Newton results ($\alpha = 10:46:08.7$, $\delta = -59:43:06.7$, $r_{90} = 1.96$ arcsec).

To test the detection limit specifically in the region covered by the error circle of the

Table 3.6: Upper limits on the optical counterpart of XMM J1046.

Telescope	Filter	Total Exp. (s)	m_{syn} (mag)	σ_{det}	m_{det} (mag)	$\log(F_X/F_\lambda)$
ESO-VLT	B	300	26.0	2.4	26.2(5)	$\gtrsim 2.2$
SOAR	V	6720	25.5	2.5	25.9(4)	$\gtrsim 3.1$
ESO-VLT	R	300	24.2	2.4	25.5(5)	$\gtrsim 3.2$
ESO-VLT	V	3300	27.0	2.0	27.6(5)	$\gtrsim 3.7$

Note: m_{syn} denote the magnitude of the faintest simulated star detected at a signal-to-noise ratio σ_{det}. m_{det} is the measured magnitude.

X-ray source, small[23] sections of the B, V and R images were analysed so as to minimize the contributions of nearby bright stars and of nebular emission. The frames were binned by a factor of 2 in order to increase the S/N ratio. Images of synthetic stars (created using the PSF model derived from the data with the IRAF task addstar) of progressively fainter magnitudes were added at the position of the X-ray source (see Fig. 3.20). The composite images were then subjected to automatic detection and to magnitude measurement using daophot. In this process, the synthetic star was no longer detected or was rejected (while trying to fit the PSF model) when the S/N ratio was worse than $S/N \sim 2 - 2.5$. We then defined the limiting magnitude as the magnitude of the faintest synthetic star still succesfully measured at these confidence levels. We give in Table 3.6 the magnitudes of the faintest simulated star (m_{syn}) detected at a S/N ratio σ_{det}, along with the measured magnitude (m_{det}). The discrepancy between the simulated and detected values of the R magnitude is due to a somewhat poorly defined PSF model in the wavelength range most affected by background intensity variations.

Taking the limiting magnitudes as upper limits on the brightness of the optical counterpart of XMM J1046, Table 3.6 also lists the implied X-ray-to-optical flux ratios corrected for photoelectric absorption and interstellar extinction. The observed optical fluxes were simply calculated according to:

$$f_\lambda = 10^{\left[-0.4(m_\lambda - m_\lambda^0)\right]}\Delta\lambda \tag{3.13}$$

using the magnitude scale zero-points m_λ^0 and filter widths $\Delta\lambda$ as in Bessell (2005). In order to compute the unabsorbed fluxes we adopted the best blackbody fit parameters of the source (see Sect. 3.4) and derived $A_V = 1.96$ using the Predehl & Schmitt (1995) relation between the X-ray absorption and optical extinction, Eq. (2.5). For the other bands, we adopted the A_λ/A_V extinction relations of Cardelli et al. (1989) and corrected the optical fluxes for the reddening.

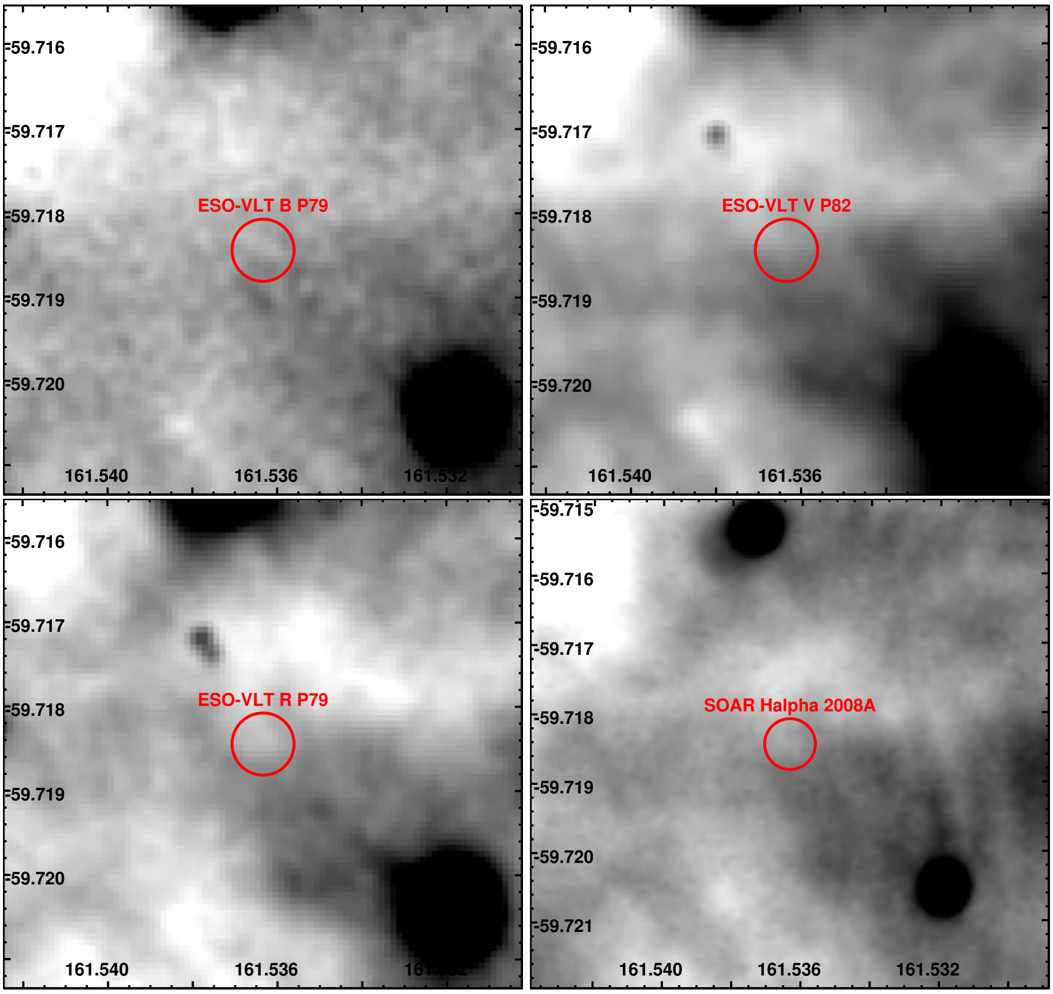

Figure 3.19: Images of the field of source XMM J1046in the B, V, R and Hα filters. The 90% confidence level error circle on the position of the source is of size 1.33″. The images were smoothed using a Gaussian filter of 2 pixels in size and zoomed by factors of 8, for the ESO-VLT observations, and 4, for the SOAR one.

3.3.2.6 Possible Balmer-dominated nebula arround XMM J1046

The Hα SOAR observations had the purpose of investigating the presence of a possible structure near the position of the X-ray source, which would be further evidence for the identification of candidate XMM J1046 with an INS. Indeed, the dense environment of the Carina Nebula and the possibly lowly ionised very local medium surrounding XMM J1046 favour the formation of a bow-shock or of a photoionised nebula that could be well detectable in the optical, due to the interaction of the rapidly moving neutron star with its gaseous surroundings. The fraction of neutral hydrogen in the Nebula depends on the

[23] 54″ × 46″, 128″ × 100″ and 70″ × 70″ respectively for the R, B and V images.

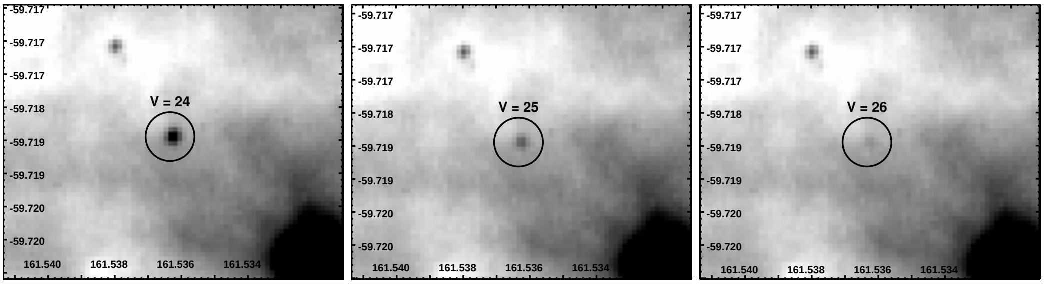

Figure 3.20: Images of the synthetic stars added to the position of source XMM J1046, in order to derive an upper limit for the optical counterpart. We show the illustrative example of the V ESO-VLT image of period P82, for simulated magnitudes in the range $V = 24 - 26$.

distance from sources of ionising radiation, mostly OB stars present in the young clusters Tr16 (where Eta Carinae is) and Tr14, and on the clumpiness of the local medium. XMM J1046 lies in a region of low diffuse background relative to other parts of the Nebula, as can be seen in Fig. 3.21. The source could thus be located behind an ionisation front and most of the local ISM could still be neutral.

A Balmer dominated nebula has been seen around a number of radio pulsars (e.g. Gaensler & Slane 2006) and one of the M7, RX J1856.5-3754 (van Kerkwijk & Kulkarni 2001). Two possible scenarios are invoked to explain the presence of such a nebula: bow-shocks (e.g. Chatterjee & Cordes 2002) and photoionisation by X-rays (Blaes et al. 1995). The shape and emissivity of the nebula can give valuable information on the INS velocity, direction of motion and rotational energy losses, allowing one to constrain its age, evolutionary state and possible links to other classes of INSs. They may also provide evidence about the existence and location of a former generation of massive stars which may have triggered the current starburst in the Carina Nebula. We give below the expected flux of such a Balmer-dominated nebula around XMM J1046 for both scenarios, assuming a total observing time of 3 h with the ESO-VLT FORS camera.

Photoionised nebula For the purpose of an illustrative calculation, we consider angular (projected) separations of the apex of the cometary-shaped nebula relatively to the neutron star position (stand-off radius R_0) in the range of $0.5 - 5$ arcsec. Using XSTAR[24], simulations give an observed Hα flux (taking into account the interstellar extinction) of $\sim 10^{-17} - 10^{-16}$ erg s^{-1} cm^{-2} arcsec^{-2}, assuming a local density of 50 cm^{-3}. This software assumes a spherical gas shell surrounding a central source of ionizing radiation, which absorbs some of the emitted energy and re-radiates it in other parts of the electromagnetic spectrum. Therefore, XSTAR computes the effects of the absorbing energy on the gas and the resulting spectrum of the re-radiated light. The user supplies the shape and strength of the incident continuum, the elemental abundances in the gas, its density or pressure and its thickness; the code returns the ionization balance and temperature, opacity, and emitted line and continuum fluxes. The resulting flux range that we obtained with XSTAR is

[24] http://heasarc.gsfc.nasa.gov/docs/software/xstar/xstar.html

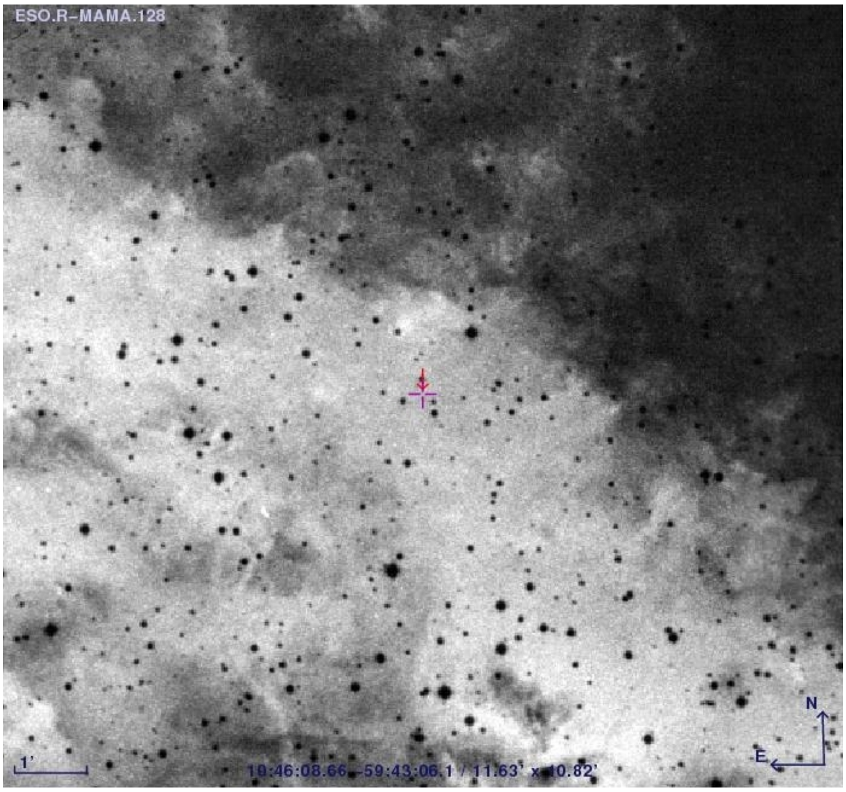

Figure 3.21: ESO-MAMA wide-field R band image of the area around XMM J1046, in the direction of the Carina Nebula. The young OB associations TR16 and TR14, as well as Eta Carinae, are located NW of the source toward the bright diffuse emission. XMM J1046 apparently lies behind an ionization front in a region of low background, which could favour the detection of a possible Hα signature around the position of the presumed fast-moving neutron star.

consistent with the expectations of Blaes et al. for a similar neutron star luminosity and medium density, and with that measured for the M7 RX J1856.5-3754.

Bow-shock nebula Alternatively, for the bow-shock scenario and assuming the same angular separations as before, a neutron star velocity in the range 10 to 100 km s^{-1} and with a spin-down luminosity of $\dot{E} = 5 \times 10^{34}$ erg s^{-1} would imply Hα fluxes again in the same range, $10^{-17} - 10^{-16}$ erg s^{-1} cm^{-2}, applying the stand-off radius R_0 formula (e.g. Chatterjee & Cordes 2002):

$$R_0 = \left(\frac{\dot{E}}{4\pi\rho_{\rm ISM} v_{\rm ns}^2} \right) \tag{3.14}$$

for a star moving with velocity $v_{\rm ns}$ through an uniform medium of density $\rho_{\rm ISM}$. In this scenario, the Balmer dominated nebula is produced when the neutron star moves supersonically through the ambient ISM, creating a shocked layer in which ram-pressure balance is established between the relativistic neutron star wind, $\dot{E}/c$, and the medium. The flux in the

Balmer line could thus be large enough that it would be possible to measure the geometry of the nebula.

Unfortunately, the SOAR Hα images (Fig. 3.19) are spoiled by heavy fringing that cannot be corrected by the flat-field exposures, and the seeing of the observations ranked among the worst we obtained in our optical campaign. Although some structure can be seen near the position of the X-ray source, it is not particularly distinguishable from other similar structures visible elsewhere on the image.

3.4 X-ray analysis

In the present section we discuss the X-ray analysis of the sample of INS candidates that were investigated in the optical. Since the X-ray brightest as well as most promising INS candidate among the sample of eight sources is XMM J1046, we provide more details on the analysis of its data and dedicate more time to discussing its nature than the other sources (Sect. 3.4.1 and 3.5). The X-ray analysis of the other candidates, which are nearly one order of magnitude fainter than XMM J1046, is reported in Sect. 3.4.2.

3.4.1 XMM J1046

3.4.1.1 Observations and data reduction

Thanks to the fact that source XMM J1046 is at an angular distance of only $\sim 8.5'$ from the well studied binary system Eta Carinae, it was serendipitously observed by the EPIC pn and MOS detectors on board XMM-Newton on many different occasions. As part of an observational campaign to study the star forming region of the Carina Nebula, XMM J1046 was also serendipitously observed once in a more recent Chandra observation (September 2008). Although this X-ray mission observed Eta Carinae many times, XMM J1046 was not detected before given the smaller FoV of the ACIS instruments relative to the EPIC cameras.

We analysed 16 XMM-Newton public archival observations, spanning from July 2000 to February 2006, in which XMM J1046 was visible. The event files were processed applying standard procedures with SAS 7.1.0. The MOS and pn observations were reduced using emchain and epchain, respectively, applying default corrections. These SAS tasks generate event list products – which correspond to the Chandra level-2 stage (Sect. 2.2.1) – from the ODFs for each EPIC camera; actuallly they consist of scripts that make use of other SAS tasks. For the case of epchain, first the task atthkgen is called in order to create the observation attitude history file that is used later in the processing by attcalc. Then the main subchain calls the tasks epframes, badpixfind, badpix and epreject so as to process the ODFs in order to create raw event lists, find bad pixels, correct the energy scale in specific pixels, flag low energy detector noise and soft flare events. The task epevents then process the raw event list files, flagging trailing events, performing pattern recognition, gain and CTI corrections and computing linearized detector coordinates in order to create the calibrated events lists. Finally, attcalc calculates the X and Y sky coordinates of the detected events. The processing chain is similar for the MOS cameras.

Table 3.7: Description of the set of X-ray observations that serendipitously detected source XMM J1046.

OBSID	Observation Date	Detector	Filter	t_{exp} (ks)	θ (arcmin)	t_{eff} (ks)	Counts	Rate ($10^{-2}\,\mathrm{s}^{-1}$)	Near Gap?
112580601	2000-07-26	pn	thick	27.7	9.7	15.0	558	3.73 ± 0.18	yes
		M1	thick	33.2	8.7	17.8	244	1.37 ± 0.10	no
		M2	thick	30.1	9.1	15.7	198	1.26 ± 0.10	yes
112580701	2000-07-27	pn	thick	8.0	9.7	4.3	161	3.7 ± 0.3	yes
		M1	thick	10.9	8.7	5.9	88	1.50 ± 0.19	no
		M2	thick	7.9	9.1	4.1	41	1.00 ± 0.18	yes
112560101	2001-06-25	pn	thick	21.5	15.8	6.7	291	4.4 ± 0.3	yes
112560201	2001-06-28	pn	thick	20.5	15.9	6.3	200	3.2 ± 0.3	yes
145740101	2003-01-25	M1	thick	6.9	8.3	4.6	78	1.68 ± 0.22	yes
145740201	2003-01-27	M1	thick	6.9	8.3	4.6	73	1.59 ± 0.21	yes
		M2	thick	6.9	8.0	4.8	69	1.44 ± 0.20	yes
145740301	2003-01-27	M1	thick	6.8	8.3	4.5	59	1.30 ± 0.20	yes
		M2	thick	6.8	8.0	4.7	68	1.44 ± 0.19	yes
145740501	2003-01-29	M2	thick	6.9	7.9	4.8	67	1.41 ± 0.19	yes

Continue on next page…

Note: The exposure times (t_{exp}), filtered for background flares, and the effective exposures (t_{eff}) on XMM J1046, accounting for vignetting, are reported; θ is the source off-axis angle. Net source photons and the on-axis count rates are in the $0.15-3$ keV (XMM-Newton) and $0.5-3$ keV (Chandra) energy bands.

Table 3.7: Description of the set of X-ray observations that serendipitously detected source XMM J1046 (continued)

OBSID	Observation Date	Detector	Filter	t_{exp} (ks)	θ (arcmin)	t_{eff} (ks)	Counts	Rate (10^{-2} s^{-1})	Near Gap?
160160101	2003-06-08	M1	thick	16.5	8.5	8.8	127	1.44 ± 0.15	yes
		M2	thick	15.5	8.2	8.6	114	1.33 ± 0.15	no
160160901	2003-06-13	M1	thick	31.1	8.5	16.6	207	1.25 ± 0.10	no
		M2	thick	31.1	8.3	17.1	217	1.27 ± 0.10	no
145780101	2003-07-22	M1	thick	8.4	9.4	4.6	76	1.66 ± 0.21	no
160560101	2003-08-02	M2	medium	11.8	9.1	6.3	121	1.93 ± 0.19	no
160560201	2003-08-09	M1	thick	12.2	8.6	6.8	105	1.54 ± 0.17	no
		M2	medium	12.1	9.1	6.4	96	1.50 ± 0.18	no
160560301	2003-08-18	M1	thick	18.5	8.6	10.8	155	1.42 ± 0.13	no
		M2	medium	18.5	9.4	10.0	160	1.60 ± 0.14	no
206010101	2004-12-07	pn	medium	19.3	17.3	5.8	366	6.3 ± 0.4	no
311990101	2006-01-31	pn	thick	24.3	7.7	15.9	837	5.27 ± 0.26	no
		M2	thick	65.3	8.2	44.2	731	1.65 ± 0.15	no
9488	2008-09-05	ACIS-I	OBF	60.0	6.7	57.0	567	0.95 ± 0.04	no

Note: The exposure times (t_{exp}), filtered for background flares, and the effective exposures (t_{eff}) on XMM J1046, accounting for vignetting, are reported; θ is the source off-axis angle. Net source photons and the on-axis count rates are in the 0.15 – 3 keV (XMM-Newton) and 0.5 – 3 keV (Chandra) energy bands.

The event lists were filtered for intervals of high background activity as well as to retain the pre-defined patterns corresponding to single, double, triple and quadruple pixel events for the MOS observations, and single and double pixel events for the pn observations, as these have the best energy calibration. Source and background events were extracted using circular regions of radii 25″ (centered on the position of the X-ray source) and 50″, respectively. Background regions were defined on an area free of sources in the same CCD and roughly at the same distance from the readout node as the source region. We restricted our analysis to the 0.15 – 3 keV energy range. Whenever possible for a given observation, data from all EPIC cameras were analysed simultaneously to better constrain the spectral parameters.

The Chandra observation was analysed using CIAO 4.0.1 and CALDB 3.4.5. We processed the event files with the task acis_process_events, also applying default corrections (see Sect. 2.2.1 in Chapter 2). Since the observation was taken in VFAINT mode, we cleaned the ACIS background while processing the event file. We checked for the presence of known processing offsets using the aspect calculator tool available on the CIAO web pages. Finally, we selected events corresponding to grades 0, 2, 3, 4 and 6 (in ASCA terminology) and applied the good time intervals, also filtering for periods of background flares. For the spectral analysis, we used the 0.5 – 3 keV energy band due to the molecular contamination that degrades the quantum efficiency of the ACIS front-illuminated chips, at energies below 0.5 keV[25]. Source and background regions were extracted applying similar criteria as for XMM-Newton data. In Table 3.7 we list, for each observation, the effective exposure times, off-axis angles, the number of extracted source photons for the spectral analysis and the source count rate, corrected for vignetting, in the given energy bands.

3.4.1.2 Spectral analysis

EPIC and Chandra images do not reveal any particular background enhancement close to the X-ray source. However, the Chandra data, which benefit from a lower instrumental background, do show some weak diffuse extended emission (a filamentary structure roughly consistent with some large-scale nebulosity seen in the optical[26]). The brightest part is located 5′ to 7′ south-east of the X-ray source. This filament is not detected on the XMM-Newton images, although it is seen marginally in the FoV of the EPIC cameras. None of the background regions used in the spectral analysis overlaps with this diffuse X-ray emission. Therefore, it is expected that the noise for the EPIC data is dominated by the (position independent) instrumental background. The noticeable vignetting and spreading of the PSF prevailing at the large off-axis angles where the source lies in many XMM-Newton observations both contribute to the difficulty in measuring the spectrum of XMM J1046 in these cases.

Spectra were binned requiring a different minimum number of counts per energy bin, depending on the total number of source counts. Spectra extracted from the shortest exposures have at least 5 counts per bin. Using XSPEC 12.4, we tested different models (blackbody, power-law, bremsstrahlung, Raymond-Smith, . . .), allowing the fit parameters

[25] http://cxc.harvard.edu/proposer/POG

[26] ESO MAMA-R digitized plate. This filament is not in the FoV of our ESO-VLT/SOAR images.

Table 3.8: X-ray spectral analysis of INS candidate XMM J1046.

		Absorbed blackbody fit						Constant $N_{\rm H}$			
OBSID	Detector	$N_{\rm H}$ (10^{21} cm^{-2})	kT (eV)	$f_{\rm X,14}$ (erg s^{-1} cm^{-2})	C	d.o.f.	Goodness (%)	kT (eV)	C	d.o.f.	Goodness (%)
112580601	M1	$3.7^{+1.4}_{-1.1}$	132^{+16}_{-17}	10.4(8)	19	21	43.7	134(5)	19	20	40.6
112580701	M1	$3.8^{+2.2}_{-2.1}$	124^{+35}_{-23}	$11.6^{+1.5}_{-1.4}$	15	21	11.2	128^{+9}_{-8}	15	20	12.6
160160101	M2	$5.6^{+3}_{-2.3}$	103^{+26}_{-21}	$9.9^{+1.1}_{-1.0}$	19	13	81.6	125^{+7}_{-6}	20	12	87.2
160160901	M1 / M2	$3.1^{+0.8}_{-1.0}$	132^{+17}_{-12}	10.3(6)	25	32	13.1	126(4)	25	31	16.0
145780101	M1	$2.7^{+2.2}_{-2.0}$	124^{+43}_{-26}	$12.9^{+1.7}_{-1.6}$	15	24	3.6	114^{+8}_{-7}	16	23	4.0
160560101	M2	$5.9^{+2.6}_{-4}$	96^{+45}_{-23}	11.5(1.2)	34	37	25.0	121^{+7}_{-6}	35	36	25.7
160560201	M1 / M2	$1.4^{+1.1}_{-0.9}$	160^{+28}_{-23}	11.6(9)	53	42	79.5	122(5)	56	41	88.8
160560301	M1 / M2	$6.0^{+2.3}_{-1.1}$	92^{+9}_{-14}	$10.5^{+0.7}_{-0.8}$	33	30	44.9	115^{+4}_{-3}	37	32	65.9
206010101	pn	$4.0^{+1.2}_{-1.0}$	106^{+14}_{-12}	9.0(6)	35	26	86.7	112(4)	35	25	89.1
311990101	pn / M2	$3.9^{+0.7}_{-0.5}$	122(8)	10.1(3)	62	65	38.1	127(2)	63	64	43.0
9488	ACIS-I	$6.3^{+0.7}_{-1.2}$	103^{+9}_{-8}	7.8(3)	13	20	12.9	125^{+4}_{-3}	18	18	37.7

Note: Only the set of 10 best XMM-Newton observations (see text) and the Chandra one are shown. The best fit parameters listed are for an absorbed blackbody model for which all parameters were allowed to vary freely (middle column). The right column shows the blackbody temperatures obtained when the column density is held constant at the mean value, $N_{\rm H} = 3.5 \times 10^{21}$ cm^{-2}. Errors are 1σ. The observed flux $f_{\rm X,14}$ refers to ranges 0.15 – 3 keV and 0.5 – 3 keV for XMM-Newton and Chandra data, respectively, in units of 10^{-14} erg s^{-1} cm^{-2}. The "goodness-of-fit" is derived from 1000 Monte Carlo simulated spectra.

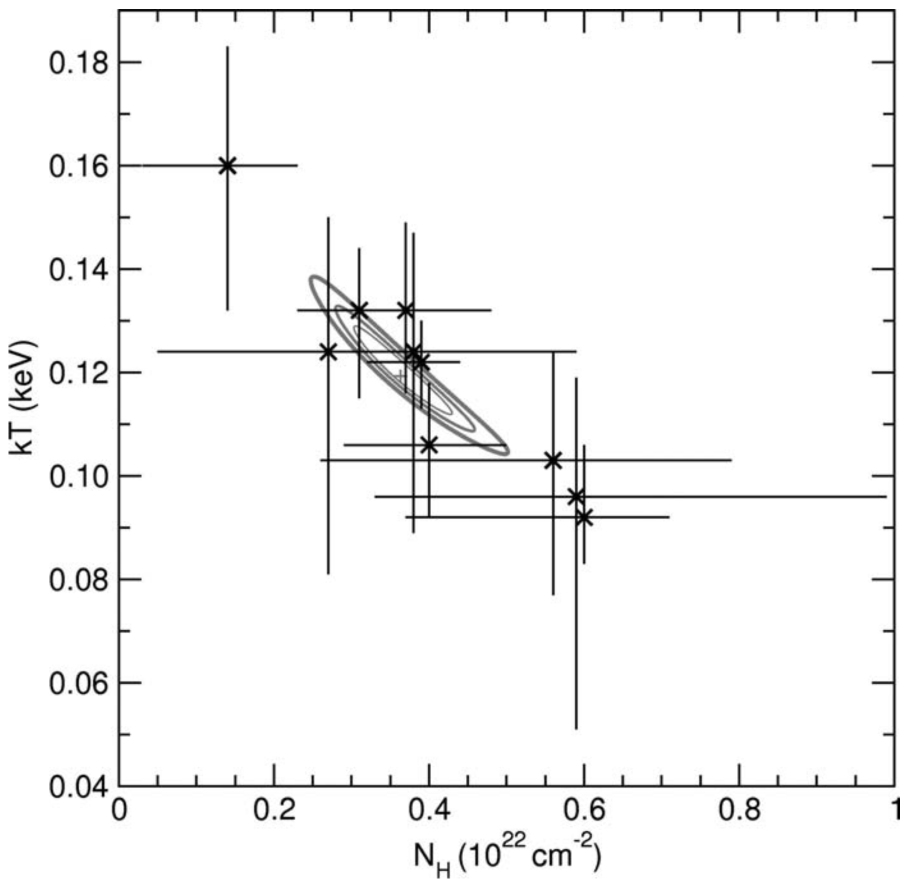

Figure 3.22: Contour plot corresponding to the overall X-ray fit of source XMM J1046, using the 10 best XMM-Newton observations ($kT = 122^{+10}_{-8}$ eV and $N_\mathrm{H} = 3.6^{+0.6}_{-0.7} \times 10^{21}$ cm^{-2}; errors are 3σ). The $kT - N_\mathrm{H}$ parameter space is shown for 1σ, 2σ and 3σ confidence levels. The individual best fits of Table 3.8 are shown as crosses with 1σ error bars.

to vary freely. Due to the low number of counts, we applied the maximum likelihood C statistic (Cash 1979) in order to derive the best fit parameters and their uncertainties. The quality of each fit ("goodness") is estimated by means of Monte Carlo simulated spectra, drawn from the best fit model, and the distribution of corresponding C fit statistics. If most (> 50%) of the simulated spectra have a smaller fit statistic than the current model, then it is unlikely that the observed data were drawn from the model.

The spectrum of XMM J1046 is always best fitted by a single absorbed soft blackbody; other models (in particular, power-law, optically thin thermal plasmas and magnetized neutron star hydrogen atmospheres; Pavlov et al. 1995, Zavlin et al. 1996) invariably result in worse fits and there is no evidence for an additional (hard) component. In general, the X-ray emission of radio pulsars results from the sum of thermal and non-thermal components (see Kaspi et al. 2004; for a review). A power-law component usually dominates the X-ray emission of young pulsars (age $\lesssim 10^5$ yr) while old pulsars (age $\gtrsim$ few Myr) exhibit a weak thermal component, probably originating from small heated polar caps, in addition

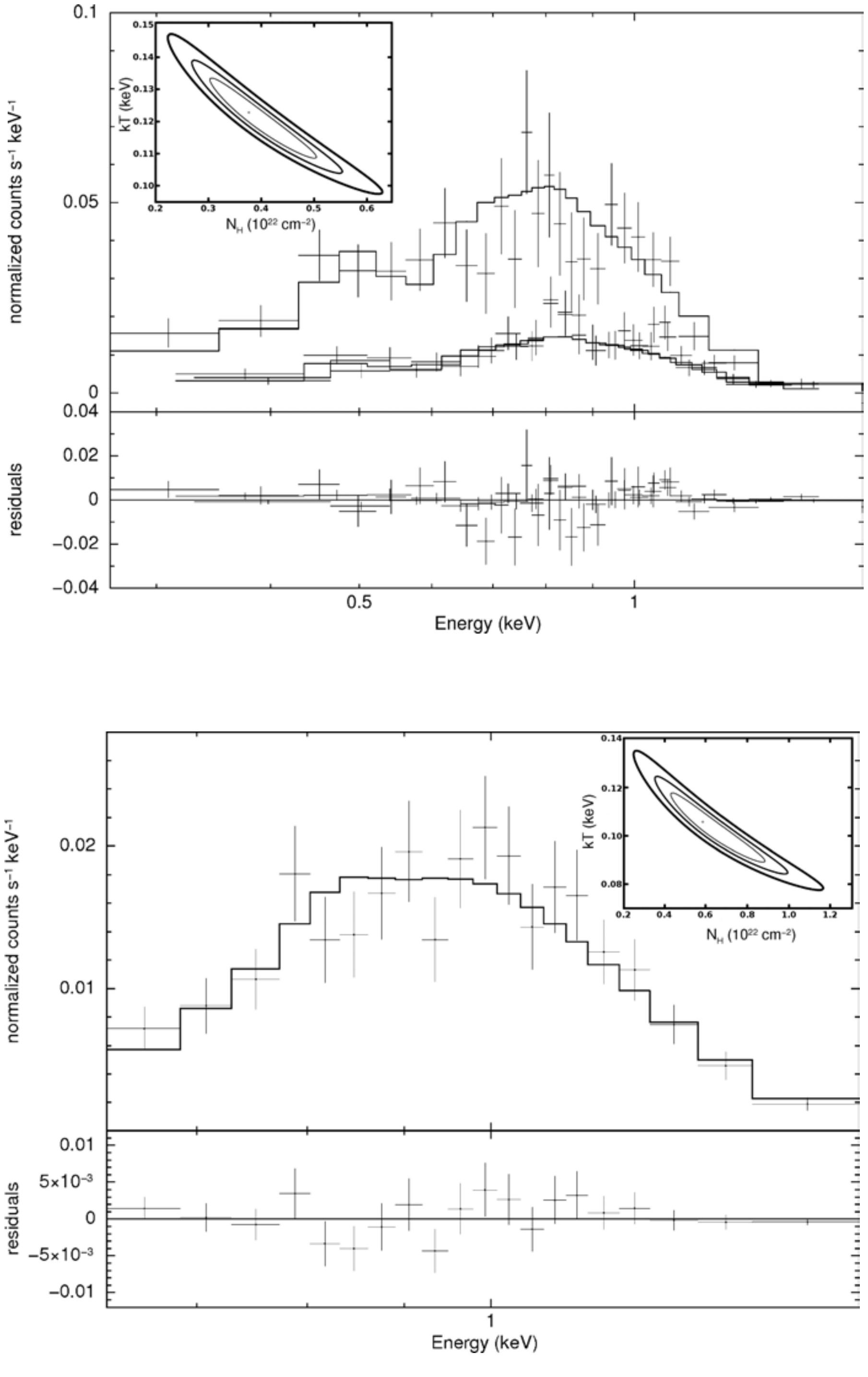

Figure 3.23: X-ray spectra and best fits of source XMM J1046 as observed with XMM-Newton (top, OBSID 311990101, pn and MOS2 cameras; the two lower data points consist of two subsequent MOS2 exposures) and Chandra (bottom, ACIS-I). The contour plots in the insets show the $kT - N_{\mathrm{H}}$ parameter space for 1σ, 2σ and 3σ confidence levels.

to a dominating power-law. On the other hand, the X-ray emission of the middle-aged pulsars (age $\sim$ few 10^5 yr) known as the "Three Musketeers" is clearly dominated by soft blackbody components superposed on a high energy tail with photon indices 1.7 to 2.1 (De Luca et al. 2005). The addition to the blackbody model of a power-law component with similar photon indices does not improve the fit of XMM J1046. Any power-law component contributes at most 4% (3σ confidence level, 0.5 – 10 keV range) to the source luminosity. Therefore, a power-law flux as low, relative to the thermal component, as that of the Three Musketeers (0.3 – 1.7%) would not be detectable in XMM J1046 with the available data and presently cannot be excluded. However, an X-ray spectrum dominated by a non-thermal component is clearly ruled out.

The M7 show rather stable spectral and timing properties. In particular, the X-ray brightest source RX J1856.5-3754 shows very constant flux and spectral properties over several years. Its X-ray spectrum is remarkably well reproduced by a blackbody with no significant deviations (e.g. Burwitz et al. 2003). Recently, Kaplan & van Kerkwijk (2009) found no evidence for spectral variability above the $\sim 2\%$ level in the XMM-Newton data of source RX J2143.0+0654. On the other hand, the second brightest source RX J0720.4-3125 is the only one among the M7 that has been shown to undergo long-term variation in its spectral parameters, at more or less constant flux (Sect. 1.3.3). In the light of this, we looked for evidence for long-term variations in the spectral parameters of source XMM J1046.

Considering the 16 XMM-Newton observations, single absorbed blackbodies have temperatures and column densities[27] ranging from 76^{+18}_{-11} to 160^{+28}_{-23} eV and from $\left(1.4^{+1.1}_{-0.9}\right)\times 10^{21}$ to $\left(8.5^{+2.6}_{-2.8}\right)\times 10^{21}$ cm^{-2}; errors are 1σ. In some cases, the small number of counts prevents a well constrained fit. In order to check the significance of the variations of the spectral parameters of XMM J1046, we performed a χ^2 test on the 16 XMM-Newton observations, assuming that they do not change in time and have values equal to their respective weighted means $kT = 113 \pm 11$ eV and $N_{\rm H} = (3.6 \pm 0.9) \times 10^{21}$ cm^{-2} (hereafter, reported errors on the weighted means are 3σ, unless otherwise noted). We found that kT and $N_{\rm H}$ are consistent with being the same in all observations at an acceptable but low confidence level for the temperature ($\chi^2_{kT} \sim 26$ and $\chi^2_{N_{\rm H}} \sim 19$ for 15 degrees of freedom, respectively; the probabilities of obtaining a larger χ^2 are $\sim 4\%$ and $\sim 19\%$). However, we note that among the data sets with the largest values of χ^2 there are some observations for which the source elongated PSF overlaps the CCD gaps of the EPIC instruments. The correction for the missing part of the energy-dependent PSF might not be well calibrated, in particular at large off-axis angles (XMM J1046 is located at $\sim 9'$, on average, but its off-axis angle can be as large as $\sim 17'$, see Table 3.7). This would require the inclusion of an additional systematic error which would have the effect of lowering the χ^2 values. On the other hand, if we only consider the 10 observations for which the source is not located close to a gap[28], we find that the temperature and column density are steady over the six-year time interval at rather high confidence levels: $kT = 117 \pm 14$ eV (23%) and $N_{\rm H} = (3.5 \pm 1.1) \times 10^{21}$ cm^{-2} (44%), see Table 3.8.

[27] The errors in $N_{\rm H}$ reported in Pires & Motch (2008; Table 2) should be multiplied by a factor of 10.
[28] Observations flagged with "no" in Table 3.7.

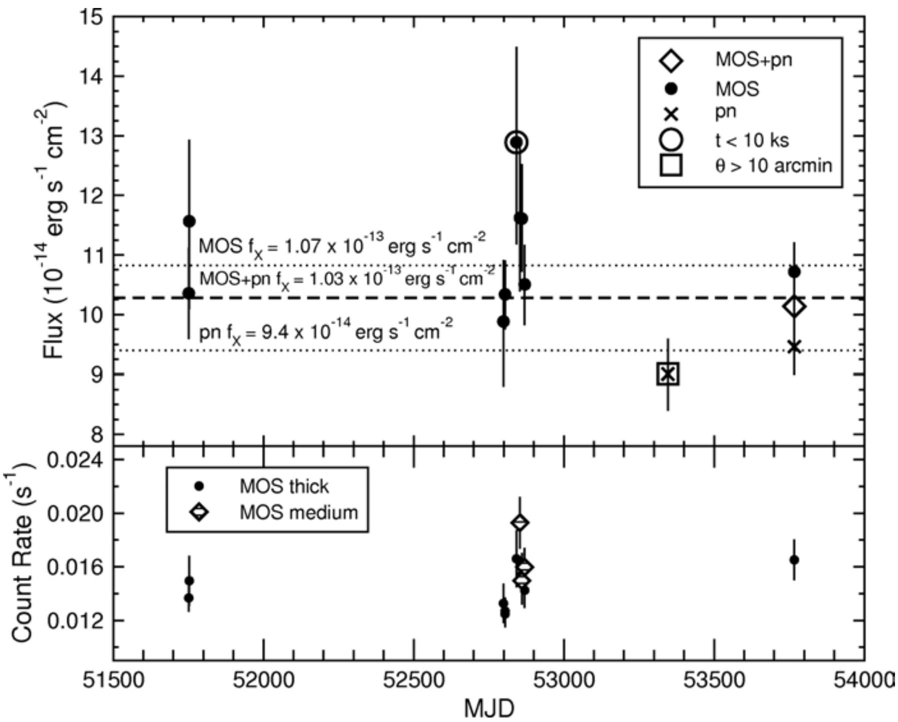

Figure 3.24: *Top:* Long-term evolution of the observed flux (0.15 – 3 keV) of the INS candidate XMM J1046. Only the set of 10 XMM-Newton observations not close to a gap is shown. Errors are 1σ confidence level. The flux is stable in both pn and MOS detectors over the six-year time interval although there is a $\sim 13 - 20\%$ discrepancy between the measured fluxes in these instruments. Observations with short exposure times and for which the source is located at a large off-axis angle are highlighted. *Bottom:* MOS on-axis count rates, discriminated by filter, for the same set of observations.

Alternatively, if the column density is held constant at the mean value $N_{\rm H} = 3.5 \times 10^{21}\,{\rm cm}^{-2}$, the computed range in kT is narrower, $111 - 132$ eV, and the parameters are better constrained (1σ errors correspond to $\sim 5\%$ of the best values against $\sim 20\%$ when $N_{\rm H}$ is free to vary, see Table 3.8 for the individual fits). In this case, the variations in kT are statistically significant (99.26%). We note, however, that the sample of analysed observations is highly heterogeneous and thus subject to systematic uncertainties. In particular, the different observing conditions – distance to the optical axis, observing modes and cameras – as well as calibration uncertainties at energies below 0.5 keV especially for the MOS cameras[29], do not allow one to draw definite conclusions on the source intrinsic spectral variability. Hereafter, we adopt the weighted mean blackbody temperature and column density of the 10 best XMM-Newton observations for the purpose of further discussion of the source properties. In Fig. 3.22 the individual best fits are plotted together with the $N_{\rm H} \times kT$ contours obtained fitting all data with one single blackbody model.

A slightly more absorbed blackbody fit is found for the Chandra observation (Ta-

[29] http://xmm2.esac.esa.int/docs/documents/CAL-TN-0018.pdf

ble 3.8). We note, however, that the response of the front-illuminated ACIS chips is not best suited to derive the spectral parameters of a source as soft as XMM J1046. This, and the fact that only photons with energies above 0.5 keV were considered, act together to cast some doubts on the column density derived in the blackbody fit. In Fig. 3.23 we show the spectral fits of the two data sets with the best S/N ratio among the analysed data.

The weighted mean of the 0.15 – 3 keV observed flux is $f_X = (9.7 \pm 0.5) \times 10^{-14}$ erg s^{-1} cm^{-2}, considering the 16 XMM-Newton observations; the computed range is $(7.7 \pm 0.7) \times 10^{-14}$ to $\left(12.9^{+1.7}_{-1.6}\right) \times 10^{-14}$ erg s^{-1} cm^{-2} (1σ). Although a constant flux is not statistically acceptable ($\chi^2 = 43$ for 15 degrees of freedom), a long-term variability is excluded once the fluxes in the EPIC cameras are considered separately: the averaged flux in the pn camera is systematically fainter than that measured in the MOS cameras but both are consistent with a constant flux (at confidence levels of ~ 19% and ~ 92%, respectively). The same ~ 13 – 20% discrepancy between the two instruments is seen in the three observations where both cameras were simultaneously on. According to recent cross-calibration studies (Mateos et al. 2009), the MOS cameras register 7 – 9% higher flux than pn below 4.5 keV – the discrepancy between the cameras is even larger (of ~ 12 – 13%) at higher energies, according to the work just cited – and this excess increases with off-axis angle. The larger discrepancy can thus be explained by the large off-axis angle of XMM J1046 in the set of analysed observations. The probabilities that temperature and column density are constant also increase when the cameras are considered individually (a consequence of the larger errors), but there is no systematic relation as for the flux (i.e. the weighted mean values are roughly the same).

Once again, accounting only for the set of 10 observations not close to a gap, the overall picture further argues against significant flux variations: the MOS and pn fluxes can be considered to be constant either when the cameras are analysed together or separately (Fig. 3.24). The weighted means and respective confidence levels for the two cameras are $f_{X,pn} = (9.4 \pm 1.1) \times 10^{-14}$ erg s^{-1} cm^{-2} (44%) and $f_{X,MOS} = (1.07 \pm 0.08) \times 10^{-13}$ erg s^{-1} cm^{-2} (78%). Despite the discrepancy between the two instruments, the fluxes are compatible within errors. We adopt here the mean value of the flux as measured by the two cameras, which is also consistent with the value inferred when the cameras are analysed together, $f_X = (1.03 \pm 0.06) \times 10^{-13}$ erg s^{-1} cm^{-2}. A direct comparison of the source count rate, corrected for vignetting, for the MOS cameras is also shown in Fig. 3.24.

3.4.1.3 Timing analysis

One of the most intriguing and discernible features of the M7 is that, when compared to radio pulsars, the neutron star spin periods are longer and distributed in a much narrower range. Six of the sources show sinusoidal X-ray pulsations with pulsed fractions between ~ 1% and 18%. The detection of pulsations in the X-ray emission of source XMM J1046 would represent further evidence of its nature. However, despite the large number of archival observations that detected the source, only one (OBSID 311990101, pn) is really suitable to conduct timing analysis – the others being either too short and having few source counts or, for the MOS observations, taken in full frame mode which has a too poor frame resolution (2.6 s) for timing purposes. Similarly, the Chandra data was carried out

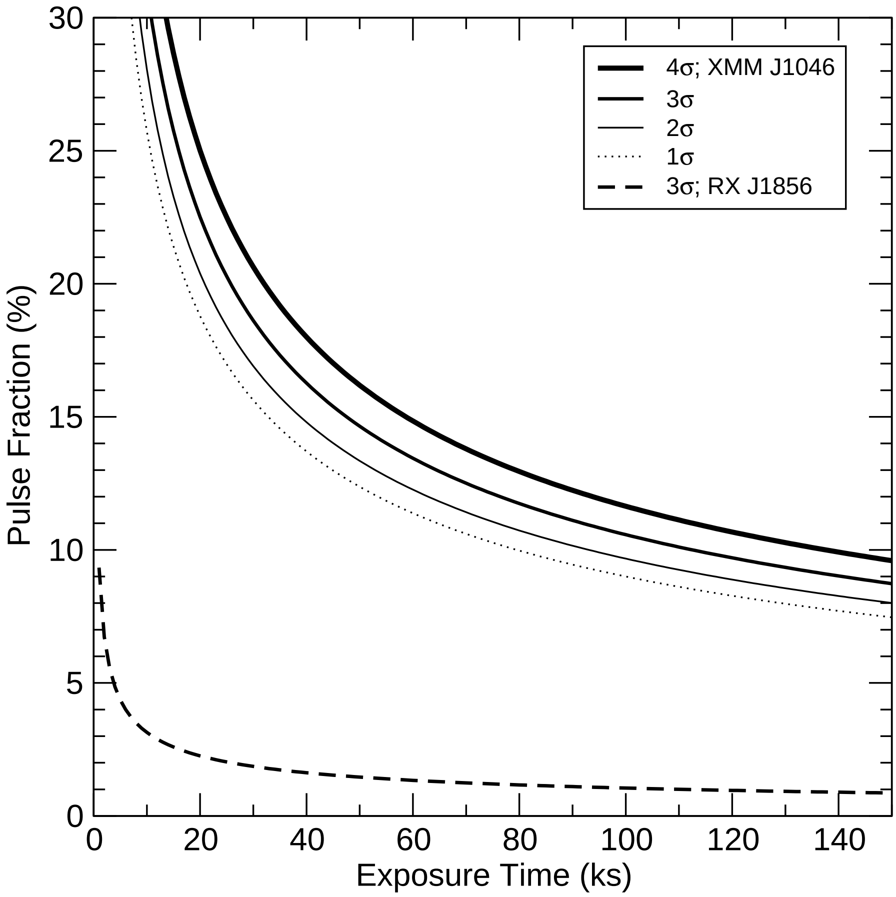

Figure 3.25: Pulsed fraction as a function of observing exposure time for source XMM J1046. The similar curve for the brightest of the M7 – and also the one with the smoothest pulse fraction of ~ 1.3% – is also shown for comparison.

with a 3.4 s time resolution imaging configuration.

With the aim to search for pulsations, we converted the photon arrival times of the pn observation from the local satellite to the Solar system barycentric frame using the SAS task barycen. Source photons were extracted in a smaller elliptical region (relative to the extracted region for the spectral analysis) in order to avoid background events. For the same reason and, since XMM J1046 does not show counts above ~ 1.5 keV, we only considered the 0.15 – 2 keV energy range. We next searched for pulsations using a Z_n^2 (Rayleigh) test (Buccheri et al. 1983), which is appropriate for smooth pulsations like the ones present in the X-ray emission of thermally emitting INSs (in particular, three out of six of the M7 show pulsed fractions, p_f, smaller than 10%). It consists of computing a phase from the photon arrival times t, according to:

$$\phi_{ij} = \text{fractional part of } (\nu_i \Delta t_j) \qquad j = 1, \ldots, N \tag{3.15}$$

with N the total number of counts extracted from the source and ν_i the trial frequency;

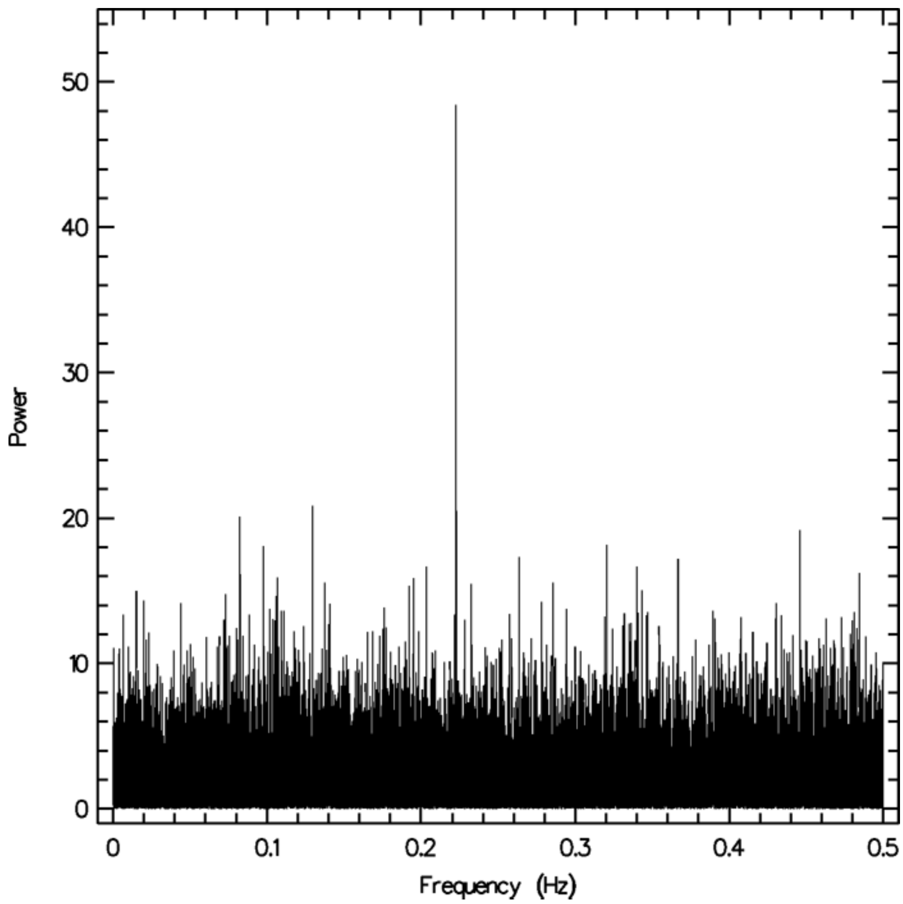

Figure 3.26: Timing analysis of a simulated light curve of XMM J1046 for a exposure time of 120 ks in a EPIC pn observation. A shallow sinusoidal signal with $P = 4.5$ s and $p_f = 15\%$ was added to the expected count rate of 0.06 s^{-1} of the source (observed on-axis with the thin filter). The pulsation is detected at very high confidence level or, inversely, witha chance probability of $\sim 10^{-6}$. The searched range in frequency totals 1 Hz in this simulation.

$\Delta t_j = t_j - t_0$, where t_0 is the reference epoch. The statistical variable Z_n^2 is then defined:

$$Z_n^2 = \frac{2}{N} \sum_{k=1}^{n} \left[\left(\sum_{j=1}^{N} \cos\left(2k\pi\phi_{ij}\right) \right)^2 + \left(\sum_{j=1}^{N} \sin\left(2k\pi\phi_{ij}\right) \right)^2 \right] \tag{3.16}$$

with n the number of harmonics (we used $n = 2$). Z_n^2 has a probability density function equal to that of a χ^2 with $2n$ degrees of freedom. Therefore, the N phase values can be Fourier analysed in a range of frequencies ν_i by means of the Z_n^2 statistics. In the absence of pulsations, the expected value of Z_n^2 is low. On the other hand, when a periodic signal is present on the data, a peak is produced in the power spectrum (Z_n^2 statistics as a function of frequency range) due to the contribution of the number of sigmas above the average to the value of the Z_n^2 statistics.

However, no pulsations are found to a non-constraining 30% upper limit (3σ), in the

0.073 – 100 s period range; the dimness of the source would require a longer exposure in order to significantly constrain the upper limit on pulsations. Indeed, simulations show that observing times larger than what is available with present serendipitous data are needed in order to significantly constrain pulsations on the X-ray emission of XMM J1046. As can be seen in Fig. 3.25, the source count rate is the critical parameter in order to detect pulsations and source XMM J1046 is two orders of magnitude fainter than the M7. In particular, assuming that the source has a spin period of $P = 4.5$ s and the intensity variations are modulated by a sinusoidal component with $p_f = 15\%$, the periodicity could be recovered very significantly (with a chance probability of 10^{-6}) if the source is observed by the EPIC pn camera for 100 – 120 ks (Fig. 3.26). With an observing time in this range, we infer that a neutron star spin period of the order of seconds can be detected at a 4σ confidence level for pulsed fractions as low as $p_f = 10\%$. These simulations were carried out using the XRONOS[30] timing analysis software package in order to add and analyse a sinusoidal signal in the light curve of the source, by means of the tools fakelc and addsine. The source was assumed to be observed on-axis and with the thin filter by the EPIC pn camera on-board XMM-Newton.

3.4.2 Other candidates

Each one of the other INS candidates was serendipitously observed only once by the XMM-Newton detectors. The event files were reprocessed using SAS 8.0.0 applying standard procedure as for the source XMM J1046. For the spectral analysis, the low S/N ratio spectra were only fitted assuming an absorbed blackbody or power-law using XSPEC 12.4. Being roughly one order of magnitude fainter than XMM J1046, the low number of counts prevents well constrained spectral fits; in particular, it does not permit a strong constraint on the value of the column density. Blackbody fits show rather high temperatures, typically $kT \gtrsim 200$ eV, and column densities ranging from 0 to 4.2×10^{21} cm^{-2}, at 68% confidence level. Although apparently in disagreement with our selection criteria ($kT \leq 200$ eV), the significant errors in HR explain the inclusion of these X-ray sources among the selected sources. We thus decided to hold $N_{\rm H}$ fixed at the Galactic value (Dickey & Lockman 1990; Table 3.3) in order to obtain better constrained spectral fits. The results of the blackbody and power-law fits for these sources can be seen in Table 3.9 (errors are 1σ). Again, the quality of each fit ("goodness") corresponds to the fraction of simulations yielding a better fit statistic than the actual data, with high values implying bad fits.

Whereas the relatively large number of counts collected for XMM J1046 safely allows one to exclude a power-law shape for its X-ray spectrum, the much lower S/N spectra of the seven sources studied here is equally well described by either a hot blackbody or by a soft power-law energy distribution, with spectral indexes usually larger than 2.

[30] http://heasarc.gsfc.nasa.gov/docs/xanadu/xronos/xronos.html

Table 3.9: X-ray spectral analysis of the other seven INS candidates (excluding XMM J1046).

Candidate	OBSID	t_{exp} (ks)	d.o.f	kT (eV)	$f_{\mathrm{X},14}$ (erg s^{-1} cm^{-2})	C	Goodness (%)	Γ	$f_{\mathrm{X},14}$ (erg s^{-1} cm^{-2})	C	Goodness (%)
XMM J1210	204710101	2.1	22	253^{+53}_{-40}	$3.6^{+0.8}_{-0.7}$	14	4.6	2.0(4)	$4.6^{+1.0}_{-0.9}$	17	9.9
XMM J0106	150870201	1.7	5	247^{+116}_{-60}	$2.6^{+0.9}_{-0.7}$	5	18.4	1.5(8)	$4.6^{+1.4}_{-1.3}$	5	19.8
XMM J0435	307001301	7.3	24	200^{+29}_{-24}	$2.00^{+0.3}_{-0.29}$	22	26.8	2.4(4)	2.8(4)	21	22.7
XMM J0314	201750901	11.6	17	229^{+58}_{-44}	1.7(3)	24	76.7	2.1(4)	2.5(5)	21	60.0
XMM J2140	008830101	10.5	15	144^{+14}_{-12}	$2.00^{+0.22}_{-0.24}$	17	58.5	$2.94^{+0.24}_{-0.23}$	$2.59^{+0.3}_{-0.25}$	9	6.8
XMM J1259	203020101	9.8	26	176^{+21}_{-18}	$2.15^{+0.26}_{-0.25}$	44	96.7	$2.43^{+0.23}_{-0.22}$	3.1(3)	35	79.4
XMM J1250	303561001	7.8	11	186^{+34}_{-27}	$1.30^{+0.26}_{-0.24}$	6	6.7	2.6(4)	1.7(3)	6	7.0

Note: Exposure times t_{exp} are filtered for background flares. The best fit parameters listed are for absorbed blackbody (middle column) and power-law models (right column) for which the column density is held fixed to the Galactic value (Table 3.3); errors are 1σ. The observed flux $f_{\mathrm{X},14}$ refers to range 0.15 – 3 keV in units of 10^{-14} erg s^{-1} cm^{-2}. The "goodness-of-fit" is derived from a number of 1000 Monte Carlo simulated spectra.

3.5 A newly discovered isolated neutron star

After correcting for photoelectric absorption and interstellar extinction, the spectral parameters derived for XMM J1046, together with the lack of optical counterpart candidate, imply $\log(F_{\rm X}/F_{\rm V}) \gtrsim 3.7^{+0.3}_{-0.1}$. For an assumed $N_{\rm H} = (3.5 \pm 1.1) \times 10^{21}\,{\rm cm}^{-2}$, $A_V \sim 1.96(6)$ (Eq. (2.5)) and the unabsorbed X-ray flux[31] is $F_{\rm X} \sim \left(1.4^{+2.4}_{-0.8}\right) \times 10^{-12}\,{\rm erg\,s^{-1}\,cm^{-2}}$ in the 0.1 – 12 keV energy band. The high value of the X-ray-to-optical flux ratio pratically rules out any other possibility than an INS. For instance, late-type (M, G, K) stars and AGN show logarithmic X-ray-to-optical flux ratios $\lesssim -1$ and within -1 and 1 (e.g. Barcons et al. 2007; and references therein) respectively, while CV systems and BL Lac objects, which are among the most extreme classes of objects, have $\log(F_{\rm X}/F_{\rm V}) \lesssim 2$ (e.g. Schwope et al. 1999). Obscured T-Tauri stars would exhibit much more absorbed X-ray spectra. We also note that the high total Galactic extinction in the direction of XMM J1046 ($E(B-V) \sim 12$; Schlegel et al. 1998) rules out a background AGN. Moreover, the Parkes-MIT-NRAO Multibeam Survey of the southern hemisphere shows no radio source located at $\lesssim 6'$ from the position of XMM J1046 to a flux limit of ~ 32 mJy (Wright et al. 1994). The Parkes Multibeam Pulsar Survey has a sensitivity of about 0.14 mJy for a canonical pulsar (Lyne 2008, Manchester et al. 2005) and also failed to detect the source – the nearest entry in the ATNF Pulsar Catalogue is AXP 1E 1048.1-5937, at ~ 32′ from XMM J1046, and the young radio pulsar PSR J1052-5954, at ~ 50′.

This very high X-ray-to-optical flux ratio, together with its thermal, soft energy distribution, makes XMM J1046 a very likely newly discovered INS, with overall properties similar to the M7. Deep radio searches and dedicated X-ray and optical observations should be carried out in order to confirm its nature and to determine to which subgroup of INSs it may belong. For comparison, the identification of the M7 RX J2143.0+0654 with an INS was first proposed on the basis of a ~ 500 net counts ROSAT PSPC spectrum and of follow-up optical observations yielding $\log(F_{\rm X}/F_{\rm V}) \gtrsim 3$ (Zampieri et al. 2001); the nature of the source was then confirmed by a dedicated XMM-Newton observation (Zane et al. 2005). XMM J1046, together with Calvera, are thus the first examples since RX J2143.0+0654 of a presumably radio-quiet and X-ray dim INS, located at a significantly greater distance than the M7. We note however that, unlike for XMM J1046, the interpretation of Calvera as a cooling neutron star similar to the M7 is challenging (Sect. 3.6).

Most probably, all cooling INSs contained in the ROSAT Bright Source Catalogue have already been identified (Popov et al. 2000b, Rutledge et al. 2003), so that new sources must be looked for at lower fluxes. The search for "blank field" sources in the entire ROSAT All-Sky Survey and in HRI pointings (Sect.3.1) produced candidates with X-ray-to-optical flux ratios of ~ 10 to 100. However, most of the INS candidates discovered in the ROSAT data at faint fluxes are located at high galactic latitudes while it is expected that both accreting and cooling INSs at greater distances should be more abundant close to the Galactic plane.

Detailed population synthesis calculations (Posselt et al. 2008) show that, in general, cooling INSs at lower soft X-ray fluxes are also expected to be hotter than the M7 (an

[31] In this work we adopted the notation $F_{\rm X}$ and $F_{\rm V}$ to denote the unabsorbed fluxes while $f_{\rm X}$ is used for the observed flux.

observational bias due to the higher photoelectric absorptions) and still at small angular distance from their birth star forming regions. Recently, Muno et al. (2008) used ~ 1000 XMM-Newton and Chandra archival observations covering significant part of the sky close to the Galactic plane ($|b| \leq 5^{\circ}$) to present constraints on the number of magnetar candidates. The search was sensitive to sources with luminosities $L_{\rm X} \geq 3\times10^{33}$ erg s^{-1} and pulsed fractions $p_f \geq 15\%$, at distances within a few kiloparsecs (see their Fig. 6). Interestingly, their results can also be used to constrain the number of cooling INSs, since no new pulsating neutron star candidate was found in a spin period range of ~ 5 to 20 s. Rescaling luminosity down to the typical values inferred for the M7 ($L_{\rm X} \geq 3 \times 10^{31}$ erg s^{-1}) we obtain that the search presented by Muno et al. is sensitive to such objects up to a few hundred parsecs. Taking into account the expected distribution of cooling INSs on the sky (Popov et al. 2005, Posselt et al. 2008), we obtain as a rough estimate that the limits by Muno et al. can be translated into $\lesssim 1000$ detectable cooling neutron stars up to a few hundred parsecs. In comparison with other limits this does not provide new important constraints.

The spatial location of XMM J1046, close to the center of the Carina Nebula, and the derived value of the source column density suggest that it may be physically associated with this giant HII region. The Carina Nebula harbours a large number of massive stars and has ongoing active star formation (see e.g. Smith & Brooks 2007; and references therein). The source column density is a factor of ~ 10 higher than those typical of the M7 and is consistent with the one towards Eta Carinae ($N_{\rm H} \sim 3\times10^{21}$ cm^{-2}, Leutenegger et al. 2003). Eta Carinae's distance, measured with high accuracy through the expansion parallax of its circumstellar nebula, is 2.3 kpc (Smith 2006). The distance to XMM J1046 is then likely to be comparable.

If the star surface is an isotropic blackbody emitter, then

$$\frac{R_\infty}{d} \sim 3.05 \left(\frac{F_{\rm X}}{10^{-12}\,{\rm erg\,s^{-1}\,cm^{-2}}}\right)^{1/2} \left(\frac{kT}{100\,{\rm eV}}\right)^{-2} {\rm km\,kpc^{-1}} \tag{3.17}$$

which gives a radiation radius – as seen by an observer at infinity; c.f. Eq. (1.3) – of $R_\infty \sim$ 6.1 km for XMM J1046, assuming that it is at the same distance as Eta Carinae. Although smaller than the canonical neutron star radius, such a value is in agreement with what is measured for the M7: their redshifted radiation radii, as derived from X-ray blackbody fits and distance estimates, are in the range of, roughly, 2 to 7 km.

As it is characteristic of the sources among the M7 with detected optical counterparts, the extrapolation of the best X-ray blackbody fit to longer wavelengths falls well below the measured optical/UV fluxes – the so-called optical excess (Sect. 1.3.2). The slope of the Rayleigh-Jeans tail is a measure of the optical temperature, which is often associated with cooler parts of the neutron star surface. Phenomenological models, consisting of two blackbodies of different temperatures and sizes of emission radii, each describing the optical/UV and X-ray energy distributions independently as if they are provenient from different regions of the neutron star surface, are then invoked in order to properly fit the overall flux distribution (Sect. 1.3.2). The presence of small hot regions on the surface, which would be responsible for the X-ray flux, is understood in terms of the anisotropic heat transport that occurs in the crust of cooling neutron stars endowed with a strong toroidal magnetic field component (Pérez-Azorín et al. 2006, Page et al. 2007). Recent investigations of neutron star thermal evolution which account for these effects (Aguilera et al. 2008) confirm that cooling isolated neutron stars can easily have polar caps with high temperatures and small radii. Moreover, it is well known that larger emission radii (and lower temperatures) are inferred when the thermal radiation is described by more realistic and phisically motivated models that appeal to e.g. a geometrically thin hydrogen atmosphere on top of the condensed neutron star surface (for instance, Motch et al. 2003, Zane et al. 2004, Ho et al. 2007; see also Sect. 1.3.2).

Alternatively, the rich star forming environment of the Carina Nebula brings the intriguing possibility that XMM J1046 could be a much older neutron star accreting from the ISM, probably born outside the nebula and whose orbit is presently intersecting the HII region. We note that, in this case, position and velocity are not expected to be correlated. The gas mass in the Carina Nebula is $\sim 10^6\,\mathrm{M}_\odot$ (Smith & Brooks 2007) which, for a typical HII region size of ~ 100 pc, implies an average density of $\sim 10\,\mathrm{cm}^{-3}$. In fact, as reported by Mizutani et al. (2002), two distinct electron density components are detected in a 30 pc area centered on the Carina I and II HII regions: a high-density ($n_\mathrm{e} \sim 100 - 350\,\mathrm{cm}^{-3}$) component and an extended low-density ($n_\mathrm{e} \lesssim 100\,\mathrm{cm}^{-3}$) component detectable over the entire mapped region. If XMM J1046 is moving inside the nebula, the corresponding increase in the column density is $\sim 1.5 \times 10^{20}\,\mathrm{cm}^{-2}\,\mathrm{pc}^{-1}$, assuming a typical density of $\sim 50\,\mathrm{cm}^{-3}$. This means that the source could be up to 10 pc inside the nebula and N_H would still be compatible with the measured value and with the one derived for Eta Carinae.

At 2.3 kpc, the luminosity of XMM J1046 is $L_\mathrm{X} \sim \left(9^{+15}_{-5}\right) \times 10^{32}\,\mathrm{erg\,s}^{-1}$. Although the estimated emission radius of XMM J1046 is comparable to those of the M7, the higher blackbody temperature is responsible for the factor of nearly 10 higher X-ray luminosity. If XMM J1046 is in the accretion phase, mass entrainment should then proceed at a rate (c.f. Appendix A.2):

$$\dot{M} = L_\mathrm{X}/\eta c^2 \sim 5 \times 10^{12}\ \mathrm{g\,s}^{-1} \tag{3.18}$$

where $\eta \sim 0.2$ is the efficiency. The Bondi-Hoyle accretion rate for a star moving through the ISM with particle density n is:

$$\dot{M} = 10^{11} n v_{10}^{-3} \mathrm{g\,s}^{-1} \tag{3.19}$$

where v_{10} is the velocity of the neutron star relative to the ISM in units of $10\,\mathrm{km\,s}^{-1}$. For $n \sim 10 - 100\,\mathrm{cm}^{-3}$, as appears likely inside the nebula, Bondi-Hoyle accretion can produce the required luminosity but the star should move very slowly through the gas, $v \sim 10\,\mathrm{km\,s}^{-1}$. Radio pulsars are known to have very high spatial velocity (typically $v \sim 400\,\mathrm{km\,s}^{-1}$; e.g. Hobbs et al. 2005, Faucher-Giguère & Kaspi 2006; Sect. 1.3.1.2, 3.1), thus the chance to have an object so slow is very small. Morevover, several mechanisms are known to inhibit accretion such as the presence of the magnetic field of the neutron star (Toropina et al. 2003, Ikhsanov 2007) and that of an infalling material which is weakly magnetized (Perna et al. 2003) or heated by the emergent X-rays (e.g. Blaes et al. 1995). In any case, it is believed that accretion should proceed at a rate well below the Bondi-Hoyle one, thus affecting the actual number of sources that can be observed by current X-ray missions.

Interestingly, and in agreement with the results of simulations by Posselt et al. (2008), a higher temperature and greater distance than those of the M7 are also observed in the only RRAT (J1819-1458, McLaughlin et al. 2007, Rea et al. 2009, McLaughlin et al. 2009, Lyne et al. 2009) detected up to now in X-rays. The XMM-Newton spectrum of RRAT rat is well fitted by a blackbody with $kT \sim 140$ eV and a broad absorption feature at ~ 1 keV – similar to those of the M7, which are usually interpreted as evidence for magnetic fields in range $10^{13} - 10^{14}$ G. Its DM (dispersion measure) distance is ~ 3.6 kpc and the observed flux is $f_X \sim 1.5 \times 10^{-13}$ erg s^{-1} cm^{-2} (0.3 – 5 keV). The M7 and this RRAT also share similar spin periods and period derivatives. On the other hand, radio emission is not detected in any of the M7 to a rather sensitive limiting flux of $\sim$ few 10 μJy for pulsed emission and 20 mJy for single dispersed pulses (Kondratiev et al. 2008; 2009). In order to better understand the relations between these two classes of INSs, further, deeper pointings in X-rays and in radio are required to firmly assess the nature of this and other RRAT sources.

3.6 Discussion

At energies below 2 keV, the X-ray spectra of quasars and Seyfert I galaxies usually show an excess relative to the extrapolation of the high energy (2 – 10 keV) power-law. It is generally believed that this "soft excess" is produced by the scattering of thermal optical/UV photons from the accretion disk surrounding the central black hole to soft X-ray energies, by a population of ambient hot electrons (e.g. Atlee & Mathur 2009; and references therein). Over a limited energy range – in particular, that covered by the sensitivity of the ROSAT instruments, 0.1 – 2.4 keV – the energy distribution of the soft excess is roughly described by a power-law of spectral index $\gtrsim 2$ (e.g. Boller et al. 1996, Grupe et al. 1998, Page et al. 2004b). This is in agreement with the results obtained in Sect. 3.4, for the INS candidates with optical counterparts (Table 3.9). Moreover, X-ray emitting quasars cluster in a region of the $\mathrm{HR}_1 \times \mathrm{HR}_2$ diagram that is above selection region III (contours in Fig. 3.12), the location where we expect to find sources with emission compatible with the hottest blackbodies that entered our selection. At faint fluxes, the 2XMMp sources show rather large HR errors, reflecting the fact that the low number of detected photons prevents a precise determination of the source spectral energy distribution. As it is evident from Fig. 3.12, several of the INS candidates share hardness ratios common to both (Galactic and extragalactic) populations. For these reasons, our search procedure is sensitive to optically faint AGN, especially those showing soft X-ray excess.

Magnetic CVs exhibit a low temperature component detectable in soft X-rays or at UV wavelengths, depending on whether the source is in a high or low accretion state (e.g. Ramsay & Cropper 2004, Ramsay et al. 2004). This emission is due to the reprocessing of hard X-ray photons (of several tens of keV) produced in a shock of the accretion flow into the photosphere of the white dwarf. In principle, faint polars showing a particularly large soft X-ray excess and with uncatalogued optical counterparts can be present in our sample of INS candidates as well.

Active coronae of late-type stars manifest themselves as soft X-ray emission with luminosities generally below 10^{31} erg s^{-1}. This population dominates soft X-ray samples at low Galactic latitudes (Motch et al. 1997). It is well known, however, that the high latitude X-ray sky at flux levels of 10^{-14} erg s^{-1} cm^{-2} is dominated by AGN (e.g. Maccacaro et al. 1982, Barcons et al. 2007, Mateos et al. 2008); the stellar content, although more important in soft X-ray-selected samples such as ours, should be less than 10%. In the optical, none of the INS candidates shows colours typical of M, G, K stars (Fig. 3.16). It is expected that late-type stars have $\log(f_X/f_R) < -1$ (e.g. Maccacaro et al. 1982, Stocke et al. 1991) which is clearly not the case for any of our INS candidates, all with $\log(f_X/f_R) > 0$. Therefore, we do not expect any of the investigated X-ray sources to be identified with late-type stars.

Based on the X-ray/optical colour and *LR* associations discussed in Sect. 3.3.2.3, the objects found inside the error circles of the INS candidates are very likely to constitute their true optical counterparts, all with a very low ($\lesssim 5\%$) probability of chance association, with the exception of XMM J0106. The strong UV excess exhibited by several of the sources (XMM J1259, XMM J2140, and XMM J1250) is clearly consistent with those of AGN and CVs (Fig. 3.16). However, optical colours alone would not be sufficient to distinguish these X-ray sources from the population of (X-ray and radio-quiet) blue objects located at high galactic latitudes. In spite of the more average colours of the optical candidates for sources XMM J1210, XMM J0435 and XMM J0314, their high X-ray-to-optical flux ratios leave no doubt that they are likely of extragalactic origin. According to Barcons et al. (2007), the fraction of X-ray sources with $\log(f_X/f_R) > 1$, where obscured AGN are expected, although larger in hard X-ray-selected samples, is of just a few percent in soft ones. As mentioned in Sect. 3.3.2.3, two out of seven of our candidates show $\log(f_X/f_R) > 1$, XMM J0106 and XMM J2140. These are the sources with the most elongated optical candidates as well. In particular, the two optical objects found in the error circle of source XMM J0106 correspond to the most dubious of the X-ray/optical associations. They have been detected only in the R filter, preventing colour estimation, whereas the optical candidate of source XMM J2140 has been well detected in the U, B and R filters. XMM J0106 was detected in a very short exposure and therefore its HR errors are more poorly determined; however, the two possible optical counterparts define an already very high $\log(f_X/f_R) \sim 2$, characteristic of the most extreme classes of X-ray emitters as AM Her systems and BL Lac objects (Schwope et al. 1999), and it is worthy of further investigation.

XMM J1046 is very likely a newly discovered thermally emitting INS. Its spatial location in the Galactic plane and the derived value of the column density suggest that it may be physically associated with the Carina Nebula, a giant HII region harbouring a large number of massive stars and with ongoing active star formation (see e.g. Smith & Brooks 2007; and references therein). Interestingly, Hamaguchi et al. (2009) suggested that the presence of this likely neutron star in the Carina Nebula implies that the region might have experienced at least two major episodes of massive star formation. Therefore, the newly discovered INS can help to shed light on the star forming history, as well as on how massive stars form and affect their environment.

Several attempts to identify new thermally emitting INSs have been carried out in the years that followed the discovery of the seven sources, usually by cross-correlating ROSAT data with optical, radio and IR catalogues (Sect. 3.1). However, these searches are hampered by the large ROSAT positional errors at faint fluxes, especially in the populated regions of the Galactic plane. For these regions, many spurious (low significance) candidate optical/IR counterparts enter the X-ray error circle of a given ROSAT source. This makes the probability of erroneously assigning an identification significant, thus excluding the source as a potential INS candidate. The final effect is that the Galactic plane is largely "avoided" by the usual cross-correlation algorithms (see e.g. Rutledge et al. 2003; Fig. 1), and proposed INS candidates are usually located at high galactic latitudes.

A long-term project that investigates INS candidates selected from the ROSAT Bright Source Catalogue (Voges et al. 1999), making use of follow-up investigations with the Swift satellite, is presently being conducted by Rutledge et al. (2008), Letcavage et al. (2009). Follow-up X-ray and optical observations of one candidate with no evident counterpart led to the discovery of Calvera, a likely compact object with a very large $F_X/F_V \gtrsim 8700$ (Rutledge et al. 2008). Not an exception, Calvera is located at high b. For an interpretation as a cooling object similar to the M7, the high galactic latitude of Calvera, $b = 37°$, would imply a remote distance of $d = 8.4$ kpc and a vertical velocity in excess of $\sim 5100\,\mathrm{km\,s^{-1}}$ to explain its current position well above the plane, considering standard cooling time, thermal emission and a likely origin in the Galactic plane (Rutledge et al. 2008). Alternatively, the source could be a nearby $(80 - 260\,\mathrm{pc})$ millisecond pulsar with properties similar to those of the population in the globular cluster of 47 Tuc. However, Hessels et al. (2007) found no radio emission at frequencies 400 MHz or 1.4 GHz, down to the limits of $L_{400} \sim 0.3(d/250\,\mathrm{pc})^2\,\mathrm{mJy\,kpc^2}$ and $L_{1400} \sim 0.03(d/250\,\mathrm{pc})^2\,\mathrm{mJy\,kpc^2}$. Therefore, if the source is indeed a radio pulsar, it is beamed away from Earth. Recent Chandra observations of Calvera failed to detect periodicities in the X-ray emission with pulsed fractions higher than 8% and with periods longer than $P \sim 0.8$ s (Shevchuk et al. 2009) and do not solve the puzzle of the source identification.

According to the detailed population synthesis calculations of Posselt et al. (2008), it is expected that, in general, new unidentified cooling INSs at faint soft X-ray fluxes are to be found in the Galactic plane, at small angular distances from their birth star forming regions – in particular, of the rich OB associations located beyond the Gould Belt, such as Carina, Vela, and Cygnus-Cepheus. At the flux limit applied in our search, the expected number of cooling neutron stars having the same properties as those exhibited by XMM J1046 – i.e. a slightly hotter source located at a greater distance relative to the M7 – is of only $\sim 50 - 80$ on the whole sky[32], which translates into less than one source to be present in the 2XMMp catalogue. The fact that we found one source exhibiting these unique characteristics corroborates the Posselt et al. (2008) conclusions that a search for new cooling INSs should not be blind, i.e. one has to look preferentially in the most promising regions of the sky – i.e. near more remote OB associations.

This work confirms the use of the XMM-Newton catalogue of sources as an efficient tool to identify new thermally emitting INSs and other interesting classes of soft X-ray sources. In particular, it was analysing serendipitous data from the 2XMM catalogue that Farrell et al. (2009) discovered a source that has been identified with a black hole with a mass of more than $500\,M_\odot$. This discovery is the best detection to date of a new class of

[32]The range shown here for the expected number of sources is derived from Posselt et al. (2008) adopting the dotted and hashed curves of their Fig. 5 as lower and upper limits, respectively. See Posselt et al. (2008) for details on the assumed parameters. EPIC pn counts were converted to ROSAT PSPC counts using WebPIMMS (http://heasarc.gsfc.nasa.gov/Tools/w3pimms.html).

astrophysical objects that has long been searched for, the intermediate-mass black holes, a missing link between lighter stellar-mass and heavier supermassive black holes. We verified that this soft X-ray source, which was serendipitously observed in 2004, was among the sample of $\sim 72,000$ EPIC pn sources investigated by us with the 2XMMp. However, it did not make through our selection criteria due to its slighly harder hardness ratios, $HR_1 = +0.01 \pm 0.04$ and $HR_2 = -0.42 \pm 0.05$, typical of the extragalactic sources that lie above our selection region III. Although the HR values are similar to those of many of our own sources selected in this region, the black hole is much brighter in X-rays and therefore has much more accurate HR errors relative to the faint INS candidates (see the open triangle in Fig. 3.12, with error bars that do not overlap selection region III, unlike the INS candidates). Moreover, it is important to note that the source would be rejected in the visual screening process anyway; since it lies in the outskirts of the optical galaxy ESO 243-49 (see finding charts in Fig. C.11), the black hole would be classified as “extragalactic source” and would not be regarded as a potential INS candidate.

CHAPTER 4

Population synthesis

Contents

4.1 Introduction

Population (or evolutionary) synthesis is a fundamental tool in astrophysics used in order to compare observational results, e.g. from surveys, with theoretical expectations for a given population. The method usually consists of modelling individual objects from birth up to the present time by convolving their formation history with numerous physical aspects that affect both their evolution and eventual detectability by our observing facilities. Tracking such evolutionary paths provides an overview of how these sources are expected to develop, a process we cannot observe having only "snapshots" of sources that possess very long evolutionary timescales. Moreover, since astronomical measurements are highly affected by selection effects and observational biases, population synthesis is valuable in recovering the properties of a population as a whole, offering a more complete interpretation of the behaviour of the astrophysical sources and the radiative processes that eventually lead (or not) to a detection at the Earth. If a significant number of objects are known, as is the case for radio pulsars, it allows the testing of many of the population's physical (and theoretically unknown) properties. Very often, however, the number of poorly constrained physical parameters is so large that very different models might be consistent with a given set of observational data. A comprehensive overview of its use in astrophysics can be found in Popov & Prokhorov (2007).

Some works that can be cited concerning radio pulsar statistics are those of Stollman (1987), Emmering & Chevalier (1989), Bhattacharya et al. (1992), Hartman et al. (1997), Arzoumanian et al. (2002) and Gonthier et al. (2004). Recent examples that apply the evolutionary method are the work of Faucher-Giguère & Kaspi (2006), conducted for the population of radio pulsars, the study carried out by Story et al. (2007) with the population of disk millisecond radio and γ-ray pulsars, the investigation of Ferrario & Wickramasinghe (2006) of the magnetic fossil field hypothesis in the context of radio pulsars and magnetars and the work of Kiel et al. (2008), Kiel & Hurley (2009), which aims at modelling pulsar evolution within binary systems along with isolated objects from the Galactic plane. Population synthesis has also been applied in order to investigate how a given population affects its environment. As an example, Voss et al. (2009) developed a detailed population synthesis code to follow the evolution of massive stars in order to investigate the ejection of ^{26}Al and ^{60}Fe into the interstellar medium (ISM) surrounding OB associations and star forming regions.

Worth mentioning is the application of population synthesis as a tool to predict the number or type of astrophysical sources – which possibly have never been observed – that could be detected in order to justify the need for a new scientific instrument. This allows the scientific community to evaluate the impact that a proposed mission or observatory could have on the development of different fields. In the particular case of thermally emitting isolated neutron stars (INSs), population syntheses conducted in the early 90s predicted that a large number of old neutron stars accreting from the ISM would be detected by ROSAT (Sect. 1.2.2). The absence of such a population in the ROSAT All-Sky Survey data made it clear that the unrealistic overprediction was due to several simplifications in the models, forcing theoreticians to reassess the validity of accretion theories (Sect. 3.6). This reflects the other side of such a tool when too few observable quantities are known beforehand. Of course, astrophysical sources and their evolution in the Galaxy are highly complicated: the large number of hypotheses and simplifying assumptions used always leave room for caution about the absolute predictive power of a given model.

The population of cooling nearby INSs from the Gould Belt has been extensively modelled by Popov et al. (2000a; 2003; 2005) (Sect. 1.5). Posselt et al. (2008) improved many of the features of their population synthesis model, mainly by providing a new description of the ISM distribution and that of the massive progenitors. Interestingly, they used the spatial distribution of the synthetic population in order to define search strategies to identify new cooling INSs. So far, these authors have only made predictions for the ROSAT All-Sky Survey. The ten years of operation of Chandra and XMM-Newton, with their outstanding sensitivity, angular resolution as well as broader spectral range relative to ROSAT, have provided a wealth of information on the X-ray sky that can now be used in order to constrain new models of thermally emitting neutron stars. Moreover, the advent of a new X-ray surveying mission, the ROSAT successor eROSITA (which is expected to be launched in 2012; see Appendix B.1.3), similarly demands new figures on the thermal INSs that might be observed in the future.

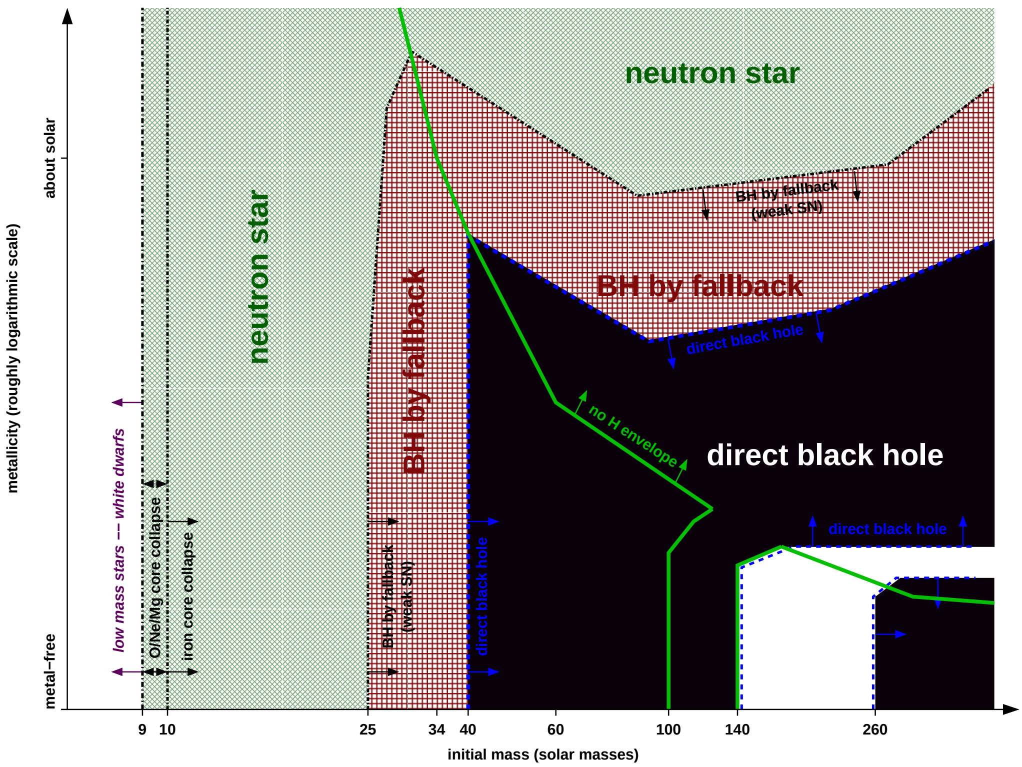

Figure 4.1: Remnants of massive stars as a function of initial metallicity and initial mass (from Heger et al. 2003).

A crucial question that any neutron star population study has to try to address from now on is the apparent discrepancy between the expected number of neutron stars in the Galaxy as inferred from estimates of the number of past core-collapse supernovae in the Milky Way and from the sum of the respective birthrates estimated for the different groups of INSs: radio pulsars, RRATs, radio-quiet thermally emitting INSs (XDINS) and magnetars (Sect. 1.5; Keane & Kramer 2008). If the birthrates of some particular object, such as the poorly constrained XDINS and RRATs, are not overestimated – or conversely, if the rate of core-collapse supernovae in the Galaxy is not incorrect – then different viewing conditions and/or evolutionary trends between the groups must be invoked. For example, XDINS could be RRATS in which the radio transient behaviour is not detected due to a narrow emission cone that beams away from the Earth; alternatively, XDINS could be the descendents of old magnetars. In other words, in order to avoid superpopulating the Galaxy with otherwise unrelated neutron stars, the several groups might consist of different observational manifestations of a single object in a somewhat more self-consistent way.

The expected number of cooling thermally emitting INSs to be detected by current or future X-ray missions is strongly model-dependent. It relies on the parametrization of properties inherited at birth (kick velocity, mass distribution and magnetic field of the compact remnant) to that of the cooling history and emission mechanism of the neutron star. Together with realistic descriptions of the Galactic gravitational potential, the ISM distribution and the detector characteristics, these ingredients determine the neutron star thermal and dynamic evolution and detectability. Similarily, from the observational point of view, selection biases and the area effectively covered by the survey (considering the surface excluded when correlating X-ray sources with other wavelengths) have to be taken into account in order to derive reliable observational upper limits on the number of sources at a given flux. Overall, even the simplest models have a level of complexity that is evident from the number of assumed hypotheses – many of them involving significant theoretical and observational uncertainties. Our objective is to develop a model for this Galactic population having the least number of uncertain assumptions, even at the expense of having a less sophisticated description of the real population. Monte Carlo simulations and observations in particular with XMM-Newton are expected to make it statistically robust so as to constrain important properties of this population of unique Galactic remnants, especially beyond the Solar vicinity.

In this chapter, we first review our current understanding of neutron star formation and evolution in the Galaxy, a topic that resides at the very core of what we aim to simulate, as well as the theoretical and observational uncertainties involved in such an effort (Sect. 4.2). In Sect. 4.3 we then proceed to the discussion of the ingredients in our own population synthesis code, stressing the already implemented steps and pointing to future improvements we wish to consider. We next describe the simulation procedure and preliminary results with XMM-Newton in Sect. 4.4 and 4.5. Perspectives for future work are in Sect. 4.6.

4.2 General picture

In the following we provide an overview of some of the most important stages in the life of a neutron star, as well as of the main physical properties that determine its further evolution and detectability on Earth. We also point out how these properties have usually been modelled in population syntheses, of either radio pulsars or other groups of isolated neutron stars, so as to evaluate our current understanding on the subject and what are the main sources of uncertainty involved.

4.2.1 Pre-supernova conditions

Neutron stars are the remnants of the gravitational collapse of the iron core of a massive star in a supernova event[1]. From a theoretical point of view, the range in progenitor mass

[1]In theory, neutron stars might also result from the collapse of accreting white dwarves in close binary systems when the white dwarf mass approaches the Chandrasekhar limit (e.g. Nomoto & Kondo 1991). This so-called *accretion-induced collapse* would, for instance, explain the range of low magnetic field intensities in MSPs – with typical values of white dwarves – without the need for invoking field decay mechanisms (Ferrario & Wickramasinghe 2008b; see also Sect. 1.4.1). It is not however clear what is the exact fraction of white dwarves in interacting systems that would give origin to accretion-induced neutron stars since it is

that gives origin to a neutron star is not clear since it depends, among other uncertainties, on the poorly constrained mass loss history, chemical composition and metallicity of the star, as well as on the effects of rotation during the main sequence phase and of fall-back accretion right after the supernova event. At present, there is no general consensus on the exact details of how massive stars evolve and eventually end their lives. The overall scenario is however rather well established: for sufficiently massive progenitors (but with low metallicity compositions), a black hole forms promptly. In a mild supernova explosion, however, the inner layers of the star lack the momentum to eject all the matter exterior to the newly formed neutron star in the stellar core; in this case, matter falls back onto the collapsed remnant which may then become a black hole by accretion of this fall-back material (e.g. MacFadyen et al. 2001). Very massive (metal-rich) stars are also expected to form neutron stars due to huge mass losses during the main sequence phase.

Taking the calculations of Heger et al. (2003) as an illustrative example for solar metallicity, one can see in Fig. 4.1 that progenitor masses in range $\sim 10-25\,M_\odot$ and $60-250\,M_\odot$ give origin to neutron stars and that these ranges are strongly dependent on the stellar composition. These authors have computed the evolution of non-rotating stars with masses in range $9-300\,M_\odot$ from birth in the main sequence to death in an iron core-collapse or pair-instability supernova, including semi-empirical effects of mass loss. Increasing observational evidence (e.g. Gaensler et al. 2005, Muno et al. 2006) seems to indicate that neutron star progenitors can be as massive as $\gtrsim 40\,M_\odot$.

In spite of the exact range of progenitor masses, one thing is clear: neutron stars are mostly born in the star forming regions of the Galactic plane where massive stars are located; therefore, population syntheses simulate the progenitor spatial distribution taking this fact into account in a more or less realistic way, either with a large scale description by means of an assumed radial distribution and scale height or linking the simulated progenitor population with exact locations of observed massive stars and OB associations (e.g. Posselt et al. 2008). This last approach is however limited to the very local Solar vicinity if optical catalogues of OB stars are considered, due to extinction by intervening dust (e.g. Bronfman et al. 2000). Strictly speaking, however, a fraction of neutron stars originates from field stars as well as from runaway stars outside associations in general (see Sect. 2.5.1 for a discussion). In these cases, the birth location is expected to be somewhat less concentrated in the Galactic disk. Bromley et al. (2009) simulated the spatial and kinematic properties of these objects and found that they have a flattened spatial distribution, with higher velocity stars at galactic latitudes less than 30°; however, around 80% of the simulated stars are within $|b| < 15°$.

4.2.2 Properties of the newly born neutron star

Among the uncertainties involved in the modelling of the newly born neutron star are the *type of remnant*, its *mass*, *rotation rate*, *spatial velocity* and inherited *magnetic field*. However, any population synthesis model relies on assumptions concerning these very neutron star properties. In the case of radio pulsars, while the mass of the remnant is usually not

believed that before the Chandrasekhar limit is attained the strongly degenerate matter in the white dwarf core ignites giving origin to a Type Ia supernova (e.g. Canal & Gutiérrez 1997, Gutiérrez et al. 2005).

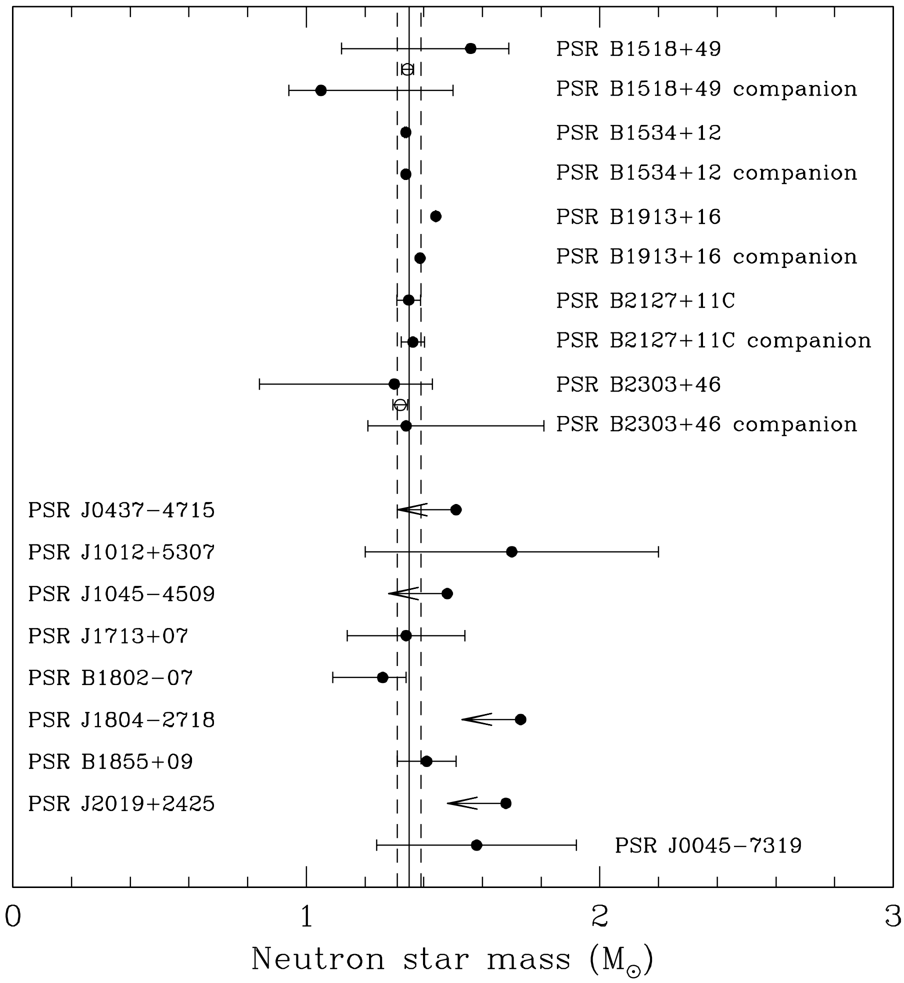

Figure 4.2: Neutron star masses from observations of radio pulsar systems (from Thorsett & Chakrabarty 1999). Five double neutron star systems are shown at the top of the diagram. A more recent update of this plot can be seen in Fig. A.1 in Appendix A.1.

crucial for the radio emission model[2], the spin period and magnetic field strength at birth are (as well as in the way which they evolve). For XDINS and magnetars, on the other hand, the remnant mass could determine the cooling history and the magnetic field inherited at birth under the fossil field hypothesis. The workaround consists of inferring distributions from observations whenever possible, in spite of these being subjected to various selection effects and the observed sample of sources being already evolved, which thus requires the

[2]In fact, in population syntheses of radio pulsars the neutron star mass is taken into account under the assumption of magneto-rotational braking; however, all synthetic pulsars are generally assumed to have the same momentum of inertia $I = 10^{45}$ g cm^{-2}, which is that of a rotating neutron star of mass 1.4 M$\odot$ and radius 10 km.

assumption of some temporal evolution of these parameters. In many cases, population syntheses are then used to justify *a posteriori* the choice of more or less arbitrary distributions; however, this fact also reaffirms the usefulness of the method in constraining unknown properties of the studied population. We discuss in the following the theoretical and observational aspects of these neutron star properties.

Mass spectrum Binary motion is at the core of observational determinations of neutron star masses. After the discovery of the first binary radio pulsar (Hulse & Taylor 1975), it became clear that the measurement of relativistic orbital effects allowed extremely precise mass estimates (Thorsett & Chakrabarty 1999). However, in order to obtain unbiased determinations, it is important that the neutron star has not undergone phases of mass accretion, which is usually satisfied in the case of the younger pulsarss in these systems. These neutron stars have measured masses in a narrow range, $\sim 1.2 - 1.4\,\mathrm{M}_\odot$, as is visualized in the classical plot of Thorsett & Chakrabarty (Fig. 4.2).

In spite of the inherent uncertainties in the physics of supernova explosion and the neutron star equation of state (EoS; Sect. A.1.2), theoretical calculations have been pursued to determine the mass of the compact remnant. Such estimates are further subjected to uncertainties regarding the poorly constrained effects of fall-back, mass loss, rotation and binarity. Nonetheless, e.g. Zhang et al. (2008; and references therein) have computed ranges for black hole and neutron star masses following the stellar evolution of non-rotating progenitors of both Population I and III (stars with solar metallicity or cosmic abundance, respectively) with masses $9 - 100\,\mathrm{M}_\odot$, taking into account the effects of stellar wind and fall-back. The range in neutron star mass obtained is $1.24 - 1.72\,\mathrm{M}_\odot$, considering solar metallicity and $M_{\rm NS}^{\rm max} = 2\,\mathrm{M}_\odot$; around $75 - 90\%$ of the remnants are neutron stars. Although dependent on the neutron star EoS, maximum mass $M_{\rm NS}^{\rm max}$ and the exact explosion mechanism and energetics, this represents a broader mass range relative to what is measured in neutron star binary systems. Rotation is expected to increase the remnant mass for a given main sequence star since it leads to a larger helium core during the main sequence phase (Zhang et al. 2008).

Spatial velocity Another neutron star property inherited at birth is its spatial velocity. If the neutron star is in a binary and if enough material is ejected during the supernova event (more than about half of the total binary mass, Hills 1983), then the system is disrupted and the neutron star acquires a high speed. For isolated objects, it is generally believed that asymmetric neutrino emission occuring in the core-collapse process is responsible for the kick imparted to a newly born neutron star, although the physical mechanisms giving origin to such an asymmetry are a matter of debate (Sect. 1.3.1.2).

The observed velocity distribution of radio pulsars, which is based on accurate proper motion and parallax determinations whenever possible, have a much higher mean than their parent population of massive stars, with typical velocities relative to the ISM of $v \sim 400\,\mathrm{km\,s^{-1}}$ against $v \sim 10\,\mathrm{km\,s^{-1}}$. Velocities in excess of $1000\,\mathrm{km\,s^{-1}}$ have been observed (Sect. 2.6). The main source of uncertainty in determining three-dimensional pulsar speeds resides in the model of Galactic distribution of free electrons (Taylor & Cordes

1993, Cordes & Lazio 2002), which is applied in order to estimate distances from the dispersion measure (DM) of the radio pulse (Sect. 1.2.1). In recent years, the use of interferometry and radio array telescopes such as the VLBI, VLBA and VLA (e.g. Chatterjee et al. 2001, Brisken et al. 2002; 2003, Dodson et al. 2003) have greatly contributed in providing accurate parallax measurements (and thus unbiased distance determinations) for many radio pulsars. Although more recent pulsar population statistics argue in favour of simple exponential (Faucher-Giguère & Kaspi 2006) or Maxwellian (Hobbs et al. 2005) velocity distributions, in the past double-peaked distributions have been proposed, the most recent examples being Arzoumanian et al. (2002) and Brisken et al. (2003). Such bi-modal velocity distributions do not seem to be *required* by present data. However, as has been noted by many authors, the exact shape of the birth velocity distribution is still poorly constrained by observations; a variety of functions can be shown to be consistent with the observed sample (e.g. Lorimer et al. 1997, Hobbs et al. 2005, Faucher-Giguère & Kaspi 2006).

Rotation rate Initial spin periods may be determined from the observation of pulsars with independent age estimates (for instance, if the pulsar is associated with a supernova remnant of known age) by assuming a temporal evolution, which is usually the magnetic dipole braking model (Sect. 1.4.1.1). For pulsars with an independent age estimate and assumed or measured braking index, initial spin periods are in the range 50 to 150 ms (see e.g. Faucher-Giguère & Kaspi 2006; Table 7). However, while the initial spin period estimated for example, for the Crab, 19 ms, favours the general idea that neutron stars are born rotating significantly faster than is currently observed, other observations tend to suggest that the usual claim $P_0 \ll P$ is not valid – for instance, the case of the central compact object (CCO) in the Kes79 supernova remnant that might have been born spinning near its current period of 105 ms (e.g. Gotthelf et al. 2005). In addition, several population studies have supported the idea that the birth spin period distribution may extend to considerably larger values. As a recent example based on PMPS data, Vranesevic et al. (2004) estimated that perhaps as many as 40% of the pulsars may be born with periods in the range $0.1-0.5$ s.

From the theoretical side, Heger et al. (2005) attempted to simulate the evolution of rotating magnetized progenitor stars with masses in the range 12 to 35 M$\odot$, under the assumption that the instabilities generated in the magnetized differentially rotating radiative zones of the star affect the transport of angular momentum through a dynamo mechanism. The bottom line of such a model is that, if this mechanism is in operation, the star would transfer more angular momentum to the stellar wind during its life, which would result in a slower rotating core at the moment of the supernova. They concluded that, without invoking any braking during or after the supernova explosion, pulsars originating from stars with $10-15$ M$\odot$ have rotation rates around $10-20$ ms. These figures are however under debate since the calculations of Zahn et al. (2007) called into question the formation of a dynamo mechanism under these circumstances and its efficiency as a powerful process of angular momentum transport.

Magnetic field The magnetic field of a neutron star is a complex entity resulting from electron currents in both the stellar core and crust. The theory behind its formation, structure and evolution is far from being completely established.

It is natural to suppose that the magnetic field of the newly born neutron star depends significantly on the pre-supernova conditions. Only by means of magnetic flux conservation, a neutron star is expected to possess a field strength consistent with what is inferred for the bulk of radio pulsars, $B \sim 10^{11} - 10^{12}$ G. This is a simple order-of-magnitude estimate obtained when a stellar radius of 10^6 km is collapsed into no much more than 10 km, consequently scaling up both the rotational frequency (by conservation of angular momentum) and the magnetic field of the progenitor star (e.g. Glendenning 1996). During the collapse, however, a purely poloidal field is unlikely to be generated (Thompson & Duncan 1993): any poloidal component in the crust will be wrapped due to differential rotation, giving origin to strong toroidal components (e.g. Kluźniak & Ruderman 1998). While the electron currents in the core are expected to support the large scale, long living ($\gtrsim 10^8$ yr) dipolar field responsible for the rotational evolution, poloidal and toroidal magnetic fields in the crust may decay over a shorter time, $10^6 - 10^7$ yr. Such a decay might significantly affect the neutron star cooling history and be responsible for the anisotropic surface temperature distribution seen in thermally emitting INSs.

Magnetic field estimates in the observed INS population (excluding recycled millisecond pulsars) lie in a broad range, $B \sim 10^{10} - 10^{15}$ G. On the observational side, the situation is even more uncertain than the estimation of initial spin periods described before: while the present neutron star rotation rates can actually be measured, magnetic fields are only *indirectly inferred* for the objects we observe, for example under magnetic dipole braking or cyclotron absorption line assumptions. These observational and theoretical uncertainties make the modelling in population studies of initial magnetic field strengths, evolution and their effects on both cooling and rotation subject to several particular choices. For instance, while it is reasonable to invoke a spin-down law under the assumption that any rotating magnetic dipole loses angular momentum, the time evolution of the neutron star magnetic field is, at present, somewhat more speculative. Whether the field stays more or less constant during the neutron star's lifetime or significantly decays, providing an extra source of energy that could power some observational "anomalous" manifestations of the pulsar, is a matter of constant debate and a subject for theoretical speculation. In which way the magnetic field decays and the relative contributions of each component to, for instance, neutron star heating are also open issues, which we discuss further in Sect. 4.2.3.

Theoretical investigations show that the magnetic field may pass through a variety of evolutionary phases which directly depend on its strength and topology as well as on the neutron star temperature, rotation rate and other properties (Geppert 2009). In particular, MHD instabilities in the proto-neutron star phase may reduce an original 10^{15} G dipolar field to standard pulsar field strengths of $\sim 10^{12}$ G, depending on the neutron star spin period and the inclination angle between the magnetic and rotational axes at the time these instabilities arise. This would define a turning point in the neutron star's early life where either a magnetar or a canonical radio pulsar could be formed. Depending on the power of fall-back accretion and on the time that the buried magnetic field takes to diffuse again to the surface (which depends on the electron conductivity of the crust), the neutron star could manifest itself either as a radio pulsar or a radio-quiet neutron star. After the crustal relaxation time, the magnetic field evolution could proceed inconspicuously since electric conductivity is very high and the magnetic field is not affected by external influences. However, several factors – depending mainly on the varying neutron star composition with density – may act together to make the so-called magnetization parameter[3], $\omega_B\tau$, locally and/or temporarily exceed unity, with dramatic consequences for the field structure and magnitude.

4.2.3 Neutron star evolution

After the neutron star is born, it dynamically evolves in the Galactic potential while radiating at the expense of its thermal, rotational and magnetic energy. The radiated emission is produced through various mechanisms, with photon energies that cover the entire electromagnetic spectrum from radio to γ-rays. The spin-down luminosity is responsible for both the coherent pulsed emission of radio pulsars as well as for the particle acceleration and related (radio and high energy) radiative processes that occur in the pulsar magnetosphere. The internal heat reservoir that remains after formation is responsible for the thermal photons arising from the neutron star's surface. Therefore, the neutron star's properties inherited at birth discussed before, as well as the way they evolve, completely determine its emission mechanisms as they are perceived at Earth[4].

We discuss in the following how neutron stars are expected to evolve both energetically and dynamically, until their energy resources are eventually exhausted. We also comment on how these issues have usually been modelled in population syntheses of INSs. Generally speaking, for most objects (i.e. typical radio pulsars), magneto-rotational and thermal evolution proceed almost independently. For neutron stars with larger magnetic fields, $\gtrsim 10^{13}$ G, these are likely connected and affect each other due to the possible heating by magnetic field decay and magneto-rotational energy dissipation. Neutron stars may show up as active radio pulsars for a total time of roughly 10^7 to 10^8 yr, which depends on the pulsar's B and P. Until at most $\sim 10^7$ yr, the neutron star's surface might still be hot enough that its thermal emission can be detected, which may also be a side effect resulting from pulsar activity (see e.g. Sect. 1.4.1 for surface heating in the context of MSPs).

Thermal evolution The cooling history of the neutron star depends on many properties of its interior: the central density (and hence the neutron star mass and radius), composition (the presence of nucleonic or exotic matter at high densities), equation of state, baryon superfluidity in the inner core, the core heat capacity, the electron conductivity in the crust, the neutrino reactions at work and their emissivities, the magnetic field in the crust and envelope etc (for an overview we refer to Appendix A.1). Unfortunately, most of these properties are rather uncertain and, in addition, are intrinsically correlated to one another.

Generally speaking, in population studies of thermally emitting INSs, one can make a choice of a given EoS and stick to it, under the assumption that the underlying physics

[3] $\omega_B = eB/m_e^* c$ is the Larmor frequency, B is the magnetic field strength, m_e^* the effective electron mass (which depends on the density and composition); τ is the electron relaxation time between collisions (Geppert 2009).

[4] Evidently, other effects such as beaming conditions, the distribution of the ISM, the distance to the source and instrument sensitivity are also crucial for detectability.

is the same for all neutron stars, only considering a range of neutron star masses (and possibly magnetic fields, see below). Alternatively, inner neutron star compositions, and therefore different EoS, can be tested via the modelling of the group of INSs with known or estimated current ages and surface temperatures, as the example study of Popov et al. (2006a) has shown[5].

Until very recently, the effects of the magnetic field in the neutron star cooling history have been somewhat neglected since, for most of the known INSs (radio pulsars with $B_{\rm dip} \sim 10^{11} - 10^{12}$ G), their effect is indeed expected to be insignificant. However, an increasing number of INSs are now known to be endowed with rather high magnetic fields in comparison with radio pulsar standards: $B \gtrsim 10^{13}$ G. These are the groups of high magnetic field radio pulsars (HBPSRs) and XDINS, with estimated fields in range the 10^{13} to 10^{14} G; one of the RRATs (J1819-1458) has similarly inferred properties which strikingly resemble those of the XDINS (Sect. 1.4.1, 1.4.2, 3.5). In addition, there are the magnetars, with $B \gtrsim 10^{14} - 10^{15}$ G. The majority of these sources – some exceptions are among the HBPSRs – have had thermal emission in their X-ray spectra reported, to a higher or lesser degree relative to other non-thermal components. Therefore, it is clear that most of the neutron stars whose thermal emission can potentially be used in order to constrain cooling curves actually have high magnetic field intensities. Exceptions are made for the well known cases of the "Three Musketeers", middle-aged pulsars that show thermal components in their spectra but have rather ordinary magnetic fields, of a few times 10^{12} G; see Sect. 3.4.1.2 for details on their spectral properties. In any case, for the sake of consistency, the effect of high magnetic fields on cooling has then to be assessed.

The effects of crustal confined magnetic fields in the neutron star surface temperature have been investigated in recent years by Geppert et al. (2004; 2006), Pérez-Azorín et al. (2006), Pons et al. (2007b), Aguilera et al. (2007; 2008). In particular, Pérez-Azorín et al. have succeeded in explaining simultaneously the observed X-ray spectrum, optical excess, pulsed fraction, absorption feature and long-term spectral variation of the M7 RX J0720.4-3125 invoking a free precessing magnetized neutron star with a condensed iron surface (Sect. 1.3.3). In Aguilera et al. (2008) the neutron star cooling was investigated combining the effect of strong non-radial fields with an additional source of heating due to Ohmic dissipation of the magnetic field in the crust. They showed that during the neutrino cooling era and the early stages of the photon cooling era the thermal evolution is coupled to the magnetic field evolution and both cooling and magnetic field diffusion proceed on a similar timescale of $\sim 10^6$ yr. In particular, they found that the observed temperatures of the M7 could be explained either if they are old ($\sim 10^6$ yr) magnetars or if they are middle-aged and their magnetic field has not changed considerably relative to the current value. Lowly magnetized stars are expected to reach low temperatures more quickly and therefore are more difficult to detect through their thermal emission.

[5]Strictly speaking, however, Popov et al. tested several different assumptions concerning heat transport in the crust and the physical processes in the core, for a given EoS and a range of neutron star masses. The idea nonetheless is the same.

Magneto-rotational evolution The magneto-rotational evolution includes the neutron star spin-down and the possible magnetic field decay. In population syntheses of radio pulsars, the losses of rotational energy are generally assumed to be dominated by magnetic dipole braking (Sect. 1.4.1). Several simplifications (of a perfect dipole rotating in vacuum, constant magnetic field, same braking index and momentum of inertia for all pulsars etc) are made since the physics of realistic pulsar spin-down in plasmas is still poorly understood, in spite of being actively researched (e.g. Spitkovsky 2006). Moreover, the constant magnetic field assumption during the neutron star's life as an active radio pulsar seems to be in general a good approximation for the bulk of observed sources (see discussion in e.g. Faucher-Giguère & Kaspi 2006).

On the other hand, magnetic field decay for neutron stars with initial fields in excess of 10^{13} G is expected to occur over shorter timescales and, as discussed before, can play an important role as an additional source of heating. However, to our knowledge, the magnetic field decay or its effects on the surface temperature and source luminosity have not been modelled in population synthesis studies of thermally emitting INSs in a self-consistent way. In Ferrario & Wickramasinghe (2008a), for instance, no explicit magnetic field decay law is invoked; the X-ray luminosity of magnetars depends on the initial magnetic field strength and is parametrized as an exponentially decaying function of time. For the population of old INSs accreting from the ISM, magnetic field decay could in principle be an important ingredient since accretion does not take place if the size of the magnetosphere (determined by the Alfvèn radius and the magnetic field intensity) is larger than the corotation radius of the pulsar. Moreover, accretion is not expected to occur if the energy density of the relativistic momentum outflow produced by the rotating magnetosphere of the neutron star is too large compared to the gravitational energy density of the incoming material (Sect. A.2; see also Treves et al. 2000). In Popov et al. (2000b), the population of old accreting INSs was also modelled assuming spin-down under constant magnetic field, for two values of the magnetic dipole moment.

Dynamic evolution Given the initial kick velocities, a neutron star trajectory has to be integrated into the Galactic gravitational potential for as long as relevant to the studied population. In the case of XDINS, one is interested in following a given neutron star orbit for at most $\sim 10^7$ yr, which corresponds roughly to its lifetime as a (detectable) thermally emitting source. In this case, the use of a very accurate description of the Galactic potential is not necessary given the small integration time compared to the epicyclic period of a Galactic object, which is of the order of 10^8 yr.

In general, the Galactic gravitational potential considered in population syntheses accounts for the joined contributions of the bulge, disk and halo, although other components or secondary effects can be included as well, such as the contribution of the central black hole and bar and the force components caused by spiral wave perturbations in the potential of the disk. Simple functional forms for the mass profile and gravitational potential of each component must then be supplied. Those are parametrized in order to adequately describe the observed rotational velocity curve of the Milky Way as well as to reproduce as closely as possible the local volume density near the Sun (e.g. Binney & Tremaine 1987). All components must satisfy Poisson's equation:

$$\nabla^2\Phi_i = 4\pi G\rho_i \qquad \text{for } i = 1, 2, \dots, N \text{ components} \tag{4.1}$$

where Φ_i and ρ_i are the potential and density profile of component i. The large scale force from the overall mass distribution acting in each individual object can then be computed and the equations of motion solved:

$$\ddot{\mathbf{x}} = -\nabla\Phi \tag{4.2}$$

where $\Phi = \sum_{i=1}^{N} \Phi_i$ is the model total gravitational potential.

4.2.4 Emissivity and detectability

Despite more than four decades of study, the emission mechanism and the beaming geometry of radio pulsars remain poorly understood. Population syntheses have therefore been applied in order to test the various possible phenomenological models that have been put forward to explain the observed sample. For instance, Faucher-Giguère & Kaspi (2006) tested both a model where the radio luminosity is related to the pulsar period and period derivative, under the assumption that it is the spin-down that powers the radio luminosity (Lyne et al. 1975), and one in which it is, conversely, independent of any pulsar observable (Lyne et al. 1998). Regarding the modelling of the highly beamed emission of radio pulsars, it has become common usage to adopt the relation of Tauris & Manchester (1998) between the fraction of pulsars that are beamed towards the Earth and the pulsar spin period.

On the other hand, it is well known that the X-ray spectra of thermal sources such as the M7 are better described by simple blackbodies, at least phenomenologically. Despite such a description being unrealistic compared to physically motivated models that take into account the reprocessing of the thermal energy by the neutron star atmosphere (e.g. Zavlin 2009), it suffices quite well for the purpose of population synthesis. This is especially true when one is interested, as it is often the case, in modelling the X-ray emission of these objects to predict the number of sources that might be detected by a mission instrument or survey, as well as to constrain birthrates and other neutron star parameters, rather than constraining the thermal emission mechanism. However, an important source of uncertainty is the size of the emission region since these sources are not isotropic blackbody emitters. The radiation radii of the M7 derived from blackbody fits range between $R_\infty \sim 2-7$ km, which translate into even smaller sizes of the emission radius, assuming a canonical value for the gravitational redshift.

The nearest source, RX J1856.5-3754, has an accurately measured parallactic distance and its emission from optical to X-rays is the best studied case among the M7. Accounting for the X-ray emission only, RX J1856.5-3754 shows a redshifted blackbody temperature of $T_X^\infty = 7.2 \times 10^5$ K and a radiation radius of $R_X^\infty = 6$ km at a distance of $d = 161$ pc. Its spectral parameters are much closer to what is expected for a cooling neutron star when one considers the broadband emission and a realistic atmosphere model: $T_\infty \sim 4.3 \times 10^5$ K and $R_\infty = 19$ km; the size of the emission radius is $R_{\rm em} \sim 16$ km for a gravitational redshift of $z_g = 0.22$ (see Ho et al. 2007; for details). Hence, the actual source bolometric luminosity corresponds to 10% of the value that could have been derived for RX J1856.5-3754 if the source emitted isotropically with the blackbody fit temperature. Popov et al. (2005) attempted to account for the reduced emissivity by assuming that the blackbody emission arises from $\sim 1/3$ of the whole surface, as for the case of RX J1856.5-3754.

Another crucial factor for the detectability of thermally emitting INSs is the distribution of matter in the ISM. Soft X-rays are severely absorbed by heavy elements on their way to the Earth. This is accounted for in population syntheses by assuming a model for the spatial distribution of intervening matter; relative abundances and cross-sections have also to be considered in order to modify the emitted spectrum to what would actually be observed.

Once the spectral form of the emitted flux, the total photon cross-section in the line-of-sight and the source distance are known, the count rate S in a given detector and energy band $\varepsilon_1 - \varepsilon_2$ can be computed according to:

$$S = \int_{\nu_1}^{\nu_2} \frac{f_\nu}{\varepsilon_\nu} A_\nu \exp\Big[-\sigma_\nu N_{\rm H}(r = d_\star, l, b)\Big] d\nu \tag{4.3}$$

where f_ν is the flux detected at a distance $r = d_\star$ (which is geometrically diluted), $\varepsilon_\nu = h\nu$ is the photon energy, A_ν is the detector effective area and finally σ_ν is the ISM total cross-section. The detected flux can be rewritten in terms of the redshifted flux F_ν^∞ that leaves the gravitational potential of the neutron star:

$$f_\nu = \left(\frac{R_\infty}{d_\star}\right)^2 F_\nu^\infty \tag{4.4}$$

The hydrogen column density to the source $N_{\rm H}$ is computed by integrating the number density n of the interstellar matter in the line-of-sight:

$$N_{\rm H} = \int_0^{d_\star} n(r, l, b) dr \tag{4.5}$$

where r, l and b are the galactic coordinates of the source.

4.3 Ingredients of the model

In order to simulate the evolutionary tracks of X-ray thermally emitting INSs, we developed a model in which neutron stars are created from a progenitor population of massive stars distributed in the spiral arms of the Galactic disk; after receiving a kick velocity, their evolution in the Galactic potential is followed while they cool down emitting soft X-rays. The expected source count rates are then computed in the EPIC pn detector on-board XMM-Newton. In the following we discuss the ingredients of our model in detail.

4.3.1 Galactic model

We defined a Galactic model for the Milky Way simulating its spiral arm structure, Galactic potential and ISM distribution. At this stage of the population synthesis procedure, it is convenient to define a Galactocentric system of coordinates. The origin is defined to be the Galactic center (GC). The X, Y and Z axes are defined parallel to $(l, b) = (90°, 0°)$,

Table 4.1: Spiral arm parameters.

Name	Arm Number	κ (rad)	R_s (kpc)	ϕ_0 (rad)
Norma	1	4.25	3.48	1.57
Carina-Sagitarius	2	4.25	3.48	4.71
Perseus	3	4.89	4.90	4.09
Crux-Scutum	4	4.89	4.90	0.95

Note: Numerical values taken from Faucher-Giguère & Kaspi (2006).

$(180°, 0°)$ and $(0°, 90°)$, respectively, forming a right-handed Cartesian frame. In a further stage we perform a transformation of coordinates from this reference frame to the conventional galactic system. As usual,

$$\mathbf{x} = (X, Y, Z) \qquad R = \sqrt{X^2 + Y^2} \qquad \phi = \arctan(Y/X) \tag{4.6}$$

The distance of the Sun to the Galactic center is adopted as $R_0 = 8.5\,\mathrm{kpc}$, basically for a matter of consistency with other ingredients of the model that also adopt this value. We note that recent observations of Keplerian orbits of stars around the Galactic central supermassive black hole have shown that the Sun is rather located at a distance of $R_0 = 8.0 \pm 0.6\,\mathrm{kpc}$ from the GC (Ghez et al. 2008). However, the adopted value is still compatible with this determination within the errors. Furthermore, Ghez et al. show that, if the central black hole is assumed to be at rest with respect to the Galaxy, the derived value for the distance of the Sun to the Galactic center is $R_0 = 8.4 \pm 0.4\,\mathrm{kpc}$.

Spiral arm structure Historically, the morphology of spiral galaxies has always been perceived through the observation of its young stellar population and their associated optically bright star forming regions. The observed morphology can evidently change with the wavelength of observation, which reflects the dynamical behaviour of the different disk components. In our own Galaxy, the exact spiral arm structure is difficult to determine since the Sun is located in the Galactic disk, between the Perseus and Sagittarius arms.

In order to determine the exact number of arms and each arm's pitch angle and initial Galactocentric radius, one has to fit the distribution of observed "tracers" of the spiral arm structure, namely, well localized HII regions and giant molecular clouds. Recently, Hou et al. (2009) found that three or four logarithmic spiral arms are required in order to connect most data available on these tracers; the best fits resulted from models where the logarithmic arm structure has varying pitch angles. The most up-to-date picture of the Milky Way, as it would be seen face-on, is reported in Churchwell et al. (2009). In order to constrain such a picture, data from the Spitzer Space Telescope as well as from radio HI and CO surveys of the Galactic plane were used, including data from the new spiral arm discovered on the far side of the Galactic center (Dame & Thaddeus 2008). This picture shows the Milky Way to be a barred, grand-design two-armed spiral with at least two secondary arms, the Sagittarius and Norma arms.

Similarly to Faucher-Giguère & Kaspi (2006), we modelled the spiral structure of the Milky Way invoking four logarithmic arms with parameters as in Wainscoat et al. (1992), which are themselves derived from data on HII regions investigated by Georgelin & Georgelin (1976). Analytically, the arms are modelled according to the formula:

$$\phi(R) = \kappa \ln(R/R_s) + \phi_s \tag{4.7}$$

where κ is a winding constant, R_s is the inner radius and ϕ_s the angle at that inner radius for each one of the four spiral arms. The values of these parameters are in Table 4.1.

Gravitational potential We considered for the gravitational potential[6] of the Milky Way the contributions of the disk, bulge and halo. We also took into account spiral wave perturbations on the exponential disk. We describe each component below.

A. Bulge

The observed luminosity distribution of elliptical galaxies and bulges is usually described by the empirical de Vaucouleurs $r^{1/4}$ law (de Vaucouleurs 1948), where r is the projected radius on the plane of the sky. Hernquist (1990) developed a simple analytical description of a density profile and its related potential which closely mimics this behaviour. We therefore modelled the bulge using a Hernquist density distribution function:

$$\rho_\mathrm{b}(R) = \frac{\varrho_\mathrm{b}}{(R/R_\mathrm{b})(1+R/R_\mathrm{b})^3} \quad ; \quad \Phi_\mathrm{b}(R) = -\frac{M_\mathrm{b}}{R+R_\mathrm{b}} \tag{4.8}$$

where M_b and R_b are the bulge mass and scale length, respectively; Φ_b is the gravitational potential corresponding to the density profile ρ_b, c.f. Eq. (4.1). The parameter ϱ_b is written in terms of the bulge mass and characteristic scale length according to:

$$\varrho_\mathrm{b} \equiv \frac{M_\mathrm{b}}{2\pi R_\mathrm{b}^3} \tag{4.9}$$

We used the parameters M_b and R_b as in Widrow & Dubinski (2005) (see Table 4.2).

B. Disk

The disk is assumed to be axisymmetric with radially and vertically varying density. We assume that the surface density profile of the disk is exponential in the radial direction with scale radius R_d and the vertical structure is given by $\cosh^{-2}(Z/Z_\mathrm{d})$, where Z_d is the vertical scale height. An implicit assumption in the formulation is that the velocity dispersions are small so that the epicyclic approximation is valid in the treatment of disk star orbits (thin-disk limit). The density profile is thus:

$$\rho_\mathrm{d}(R,Z) = \varrho_\mathrm{d} \exp\left(-\frac{R}{R_\mathrm{d}}\right) \cosh^{-2}\left(\frac{Z}{Z_\mathrm{d}}\right) \tag{4.10}$$

[6] We acknowledge discussions with Christian Boily for the inclusion of the gravitational potential in our population synthesis model. The orbital integration code was also kindly provided by him.

where $\varrho_{\rm d}$ is written in terms of the scale lengths and the disk mass $M_{\rm d}$:

$$\varrho_{\rm d} \equiv \frac{M_{\rm d}}{4\pi Z_{\rm d} R_{\rm d}^2} \tag{4.11}$$

The analytical form of the potential is derived solving Eq. (4.1) for the density profile in Eq. (4.10); it can be found in e.g. Earn (1996). The parameters $M_{\rm d}$, $R_{\rm d}$ and $Z_{\rm d}$ for the disk component were taken from Ruphy et al. (1996) and are listed in Table 4.2.

C. Halo

While the Hernquist potential aims at reproducing the observed surface brightness of an elliptical galaxy or ellipsoidal mass distribution and their dependency on the projected radius, the dynamics of a galaxy may hardly be explained by its luminous component only. This requires the introduction of a dark halo, although its shape, structure and nature cannot be determined uniquely and usually make use of detailed N-body simulations of structure formation in order to find realistic and physically motivated models. In particular, the unknown effect of numerical convergence and resolution on the asymptotic behaviour of the density profile make it unclear whether the obtained results depend on the software used both to simulate the system and to identify bound structures. In spite of these difficulties, it is generally accepted that relaxed systems exhibit a density profile that is well described by a double power law with an outer asymptotic slope of 3 and inner values in the range of 1.0 to 1.5 (e.g. Cardone et al. 2005; and references therein).

Following the formulation of Cardone et al. (2005) which is a particular case of the general model proposed by Zhao (1996), we used as the density profile for the halo and its derived potential:

$$\rho_{\rm h}(R) = \varrho_{\rm h} \exp\left\{ -\frac{2}{\gamma}\left[\left(\frac{R}{R_{\rm h}}\right)^{\gamma} - 1\right]\right\} \quad ; \quad \Phi(R) = -\frac{GM_{\rm h}}{R_{\rm h}}\mathscr{F}(R/R_{\rm h} = 1, \gamma) \tag{4.12}$$

where γ is the slope of the inner core, $R_{\rm h}$ is the scale radius at which the width of the transition region between the two power-laws equals the value of the isothermal sphere (see Cardone et al. 2005 for the analytical derivation). The function $\mathscr{F}(x, y)$, $x \equiv R/R_{\rm h}$, is given by:

$$\mathscr{F}(x,\gamma) = \frac{\Gamma(3/\gamma) - \Gamma(3/\gamma, 2x^{\gamma}/\gamma)}{x\Gamma(3/\gamma)} + \left(\frac{2}{\gamma}\right)^{1/\gamma} \frac{\Gamma(2/\gamma) + \Gamma(2/\gamma, 2x^{\gamma}/\gamma)}{\Gamma(3/\gamma)} \tag{4.13}$$

The $\varrho_{\rm h}$ parameter is defined in terms of the halo total mass and scale length:

$$\varrho_{\rm h} \equiv \frac{M_{\rm h}}{4\pi R_{\rm h}^3}\left(\frac{2}{\gamma}\right)^{3/\gamma} \frac{\gamma}{\Gamma(3/\gamma)\exp(2/\gamma)} \tag{4.14}$$

The parameters of the halo component γ, $M_{\rm h}$ and $R_{\rm h}$ were taken from Cardone et al. (2005) (see Table 4.2).

Table 4.2: Galactic potentials parameters.

Parameter	Description	Value	Unit	Ref.
				Bulge component
$M_{\rm b}$	Bulge total mass	0.52	10^{10} M⊙	(a)
$R_{\rm b}$	Bulge scale length	1.0	kpc	(b)
				Disk component
$M_{\rm d}$	Disk total mass	5.1	10^{10} M⊙	(c)
$R_{\rm d}$	Disk radial scale length	3.0	kpc	(c)
$Z_{\rm d}$	Disk vertical scale length	0.25	kpc	(c)
				Halo component
$M_{\rm h}$	Halo total mass	20.0	10^{10} M⊙	(d)
$R_{\rm h}$	Halo scale length	2.71	kpc	(d)
γ	Slope of the inner core	0.17	...	(d)
				Spiral wave perturbations
α_σ	Constant	5.0	10^{-10} cm^3 g^{-1} s^{-2}	(e)
$\varphi_{\rm s}$	Pitch angle	20	degrees	(e)
$\beta_{\rm s}$	Contrast parameter	0.5	...	(e)
$\upsilon_{\rm s}$	Phase	5.23	rad	(e)

Note: See text for details. *Ref.:* (a)Binney & Tremaine 1987, (b)Widrow & Dubinski 2005, (c)Ruphy et al. 1996, (d)Cardone et al. 2005, (e)Patsis et al. 1991.

D. Spiral wave perturbations

In order to reproduce the density enhancement in the spiral arm regions, we introduced spiral wave perturbations on the disk potential, following Patsis et al. (1991). This is of the form:

$$\Phi(R) = \alpha_\sigma \zeta(Z) H(R) g(R,\phi) \tag{4.15}$$

where α_σ is a constant that normalizes the velocity dispersion; the function $\zeta(Z)$ describes the vertical dependence of the perturbed spiral potential while $H(R)$ and $g(R,\phi)$ give its radial drop-off and angular variation, respectively, with ϕ the azimuthal angle:

$$H(R) = \frac{R}{R_{\rm d}} \tanh\left[\left(\frac{R}{R_{\rm d}}\right)^3\right] \exp\left(-\frac{R}{R_{\rm d}}\right) \tag{4.16}$$

$$g(R,\phi) = \cos\left[2\frac{\ln(R)}{\tan(\varphi_{\rm s})} - 2(\phi + \upsilon_{\rm s})\right] + \beta_{\rm s}\cos\left[4\frac{\ln(R)}{\tan(\varphi_{\rm s})} - 4(\phi + \upsilon_{\rm s})\right] \tag{4.17}$$

where φ_s is the pitch angle, β_s is a parameter that controls the intensity of the secondary arms relative to primary ones and υ_s is a angular phase introduced in order to locate the Sun before the Orion spiral arm. The parameter values were taken from Patsis et al. (1991) and are listed in Table 4.2.

Interstellar medium distribution The soft X-rays emitted by cooling neutron stars are severely absorbed mostly by the oxygen and iron atoms present in the interstellar material. In particular, at the energy pass-band of the ROSAT satellite, 0.1 –2.4 keV, the absorption cross-section of the ISM changes by more than three orders of magnitude. As a result, the observed spectral energy distribution of a given source at low energies is highly affected by the amount of material in the line-of-sight, its assumed relative abundances and the photoelectric absorption processes that the X-ray photons undergo on their way to the Earth.

The hydrogen column density in the line-of-sight, $N_{\rm H}$ c.f. Eq. (4.5), quantifies the amount of intervening material towards a source. However, the ISM distribution $n(r, l, b)$ is far from being a static and homogenous layer of absorbing material. Rather, it is a result of the integrated dynamical effects of stellar activity and supernova explosions, which are responsible for sweeping the surrounding medium, creating bubbles and cavities of underdense and warmer material. Moreover, the ISM is full of structures on all spatial scales, with the presence of dense rims and molecular clouds, and is highly concentrated in the Galactic plane.

In Posselt et al. (2008) the very local ($d \lesssim 230$ pc) ISM distribution is modelled in detail taking into account the observational results of Lallement et al. (2003). These authors mapped the interstellar extinction in the Solar neighbourhood through measurements of the equivalent width of the NaI doublet at 5890 Å towards targets with accurately determined Hipparcos distances. The NaI absorption is regarded as a good tracer of the total amount of the neutral interstellar gas and it can be converted into hydrogen column density by means of the relation in e.g. Ferlet et al. (1985). However, at more remote distances, the Posselt et al. model has to invoke either an average analytical description or much coarser extinction measurements such as those of e.g. Hakkila et al. (1997).

Similarly to what was done in Zane et al. (1995), Popov et al. (2000b; 2005), we applied an analytical description of the ISM which is based on layers of hydrogen in both atomic and molecular form, as parametrized by Dickey & Lockman (1990) and de Boer (1991). The total hydrogen density is hence:

$$n = n_{\rm HI} + 2n_{\rm H_2} \tag{4.18}$$

where $n_{\rm HI}$ and $n_{\rm H_2}$ are the atomic and molecular hydrogen densities, respectively. The molecular component can be modelled according to:

$$n_{\rm H_2} = \eta_{\rm H_2} \exp\left(- \frac{Z^2}{2\sigma^2_{\rm H_2}} \right) \tag{4.19}$$

where the central density $\eta_{\rm H_2}$ and the Gaussian standard deviation $\sigma_{\rm H_2}$ are given by de Boer (1991). Observational data from Lyα and 21 cm absorption measurements show that the

Table 4.3: Parameters for the description of the ISM distribution.

Parameter	Description	Value	Unit	Ref.
				H_2 component
η_{H_2}	Central density	0.6	cm^{-3}	(a)
σ_{H_2}	Gaussian standard deviation	0.07	kpc	(a)
				HI component
η_1	Central density	0.395	cm^{-3}	(b)
σ_1	Gaussian standard deviation	0.090	kpc	(b)
η_2	Central density	0.107	cm^{-3}	(b)
σ_2	Gaussian standard deviation	0.225	kpc	(b)
η_3	Exponential central density	0.064	cm^{-3}	(b)
h_3	Vertical scale length	0.403	kpc	(b)

Note: See text for details. *Ref.:* [(a)]de Boer 1991, [(b)]Dickey & Lockman 1990.

ISM distribution within 3.4 kpc $\lesssim R \lesssim$ 8.5 kpc is rather constant in radius while its vertical dependency can be described by the sum of two Gaussians and an exponential distribution with suitably parametrized standard deviations and scale height (Dickey & Lockman 1990), i.e.:

$$n_{\mathrm{HI}} = \eta_1 \exp\left(-\frac{Z^2}{2\sigma_1^2}\right) + \eta_2 \exp\left(-\frac{Z^2}{2\sigma_2^2}\right) + \eta_3 \exp\left(-\frac{Z}{h_3}\right) \tag{4.20}$$

The parameters of this model can be found in Table 4.3.

Absorption cross-section We assumed the cross-section for interstellar photoelectric absorption of Morrison & McCammon (1983), which is the model wabs implemented in XSPEC. These authors computed a functional form that fits the numerical results well regarding the effective cross-section per hydrogen atom as a function of energy:

$$\sigma(\varepsilon) = (c_0 + c_1\varepsilon + c_2\varepsilon^2)\varepsilon^{-3} \times 10^{-24}\,\mathrm{cm}^2 \tag{4.21}$$

where ε is the energy in keV. We list in Table 4.4 the coefficients of the analytical polynomial fit.

4.3.2 Neutron star properties

In the following we detail how some of the major features of the population of cooling neutron stars were simulated at the moment they are born after the supernova explosion.

Spatial distribution In order to place the newly born neutron stars in the Galactic model we followed closely the procedure adopted by Faucher-Giguère & Kaspi (2006), which is

Table 4.4: Parameters for the analytical fit of the effective cross-section for interstellar photoelectric absorption.

Energy range (keV)		c_0	c_1	c_2
	$\sigma(\varepsilon) = (c_0 + c_1\varepsilon + c_2\varepsilon^2)\varepsilon^{-3} \times 10^{-24}$ cm^2			
0.030 – 0.100	....	17.3	608.1	-2150.
0.100 – 0.284	....	34.6	267.9	-476.1
0.284 – 0.400	....	78.1	18.8	4.3
0.400 – 0.532	....	71.4	66.8	-51.4
0.532 – 0.707	....	95.5	145.8	-61.1
0.707 – 0.867	....	308.9	-380.6	294.0
0.867 – 1.303	....	120.6	169.3	-47.7
1.303 – 1.840	....	141.3	146.8	-31.5
1.840 – 2.471	....	202.7	104.7	-17.0
2.471 – 3.210	....	342.7	18.7	0.0
3.210 – 4.038	....	352.2	18.7	0.0
4.038 – 7.111	....	433.9	-2.4	0.75
7.111 – 8.331	....	629.0	30.9	0.0
8.331 – 10.000	....	701.2	25.2	0.0

Note: Coefficients c_0, c_1 and c_2 for Eq. (4.21); see text for details. *Reference:* Morrison & McCammon (1983).

briefly recalled here. The neutron star spatial location is specified by radial and vertical coordinates. The number of neutron stars as a function of Galactocentric radius follows the radial distribution suggested by Yusifov & Küçük (2004) for the population of radio pulsars:

$$\rho(R) = A\left(\frac{R + R_1}{R_\odot + R_1}\right)^{\alpha} \exp\left[-\beta\left(\frac{R - R_\odot}{R_\odot + R_1}\right)\right] \tag{4.22}$$

where R_1, α and β are model parameters listed in Table 4.5; A is a normalization constant.

This formula reflects the deficit of detected radio pulsars near the Galactic center, due to pulse broadening for relatively low-frequency radio surveys in the same volume as SgrA* (see Sect. 1.2.1 for a discussion of selection biases in radio surveys and Deneva et al. 2009a for a search of radio pulsars near the GC). The radial distribution per kpc^2 and cumulative distribution of neutron stars in the Milky Way can be seen in Fig. 4.4, for a normalization of 10^8 objects.

The angular distribution projected in the Galactic plane is not isotropical but rather follows the four logarithmic spiral arms parametrized by Eq. (4.7). The neutron star position in a given arm is spread around the arm centroid by applying isotropic X, Y translations. These translations on the plane are drawn from a normal distribution centered at zero with

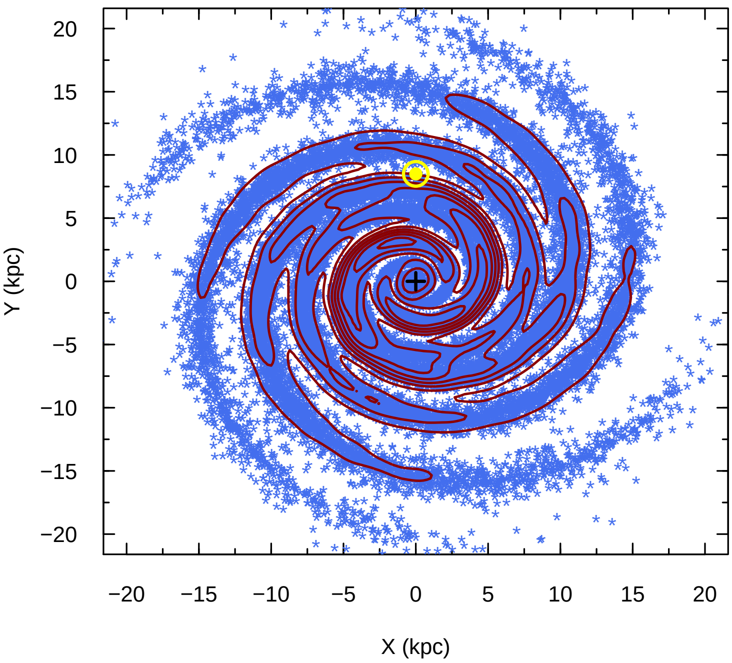

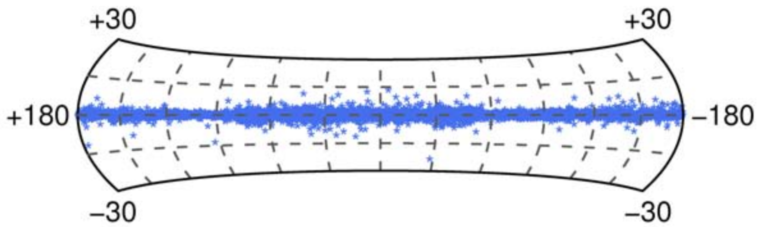

Figure 4.3: *Top:* Projected initial distribution of the modelled cooling INSs in the Galactic plane. The Sun location is marked in yellow while a cross at $X, Y = 0, 0$ shows the Galactic center. *Bottom:* Section of a Hammer-Aitoff projection in galactic coordinates of these newly born objects; $|b| \leq 30°$.

standard deviation equal to a factor of 0.07 times its original Galactocentric distance. The spatial distribution is also blurred in order to avoid artificial features near the GC (see Faucher-Giguère & Kaspi for details). These types of corrections are done so as to create a reasonably natural spatial initial distribution, which can be seen in Fig. 4.3.

The vertical distribution relative to the Galactic plane at birth is described by an exponential with scale height $z_0 = 50\,\text{pc}$; the neutron stars are uniformly distributed above and below the disk.

Table 4.5: Parameters for the initial spatial distribution of the INSs.

Parameter	Description	Value	Unit	Ref.
			Radial distribution	
R_1	Model parameter	0.55 ± 0.10	kpc	(a)
α	Model parameter	1.64 ± 0.11	...	(a)
β	Model parameter	4.01 ± 0.24	...	(a)
			Vertical distribution	
z_0	Scale height	50	pc	(b)

Note: See text for details. *Ref.:* (a) Yusifov & Küçük 2004, (b) Faucher-Giguère & Kaspi 2006.

Kinematic distribution The birth velocities are exponentially distributed with a three-dimensional mean speed of $380\,\mathrm{km\,s^{-1}}$. Such a distribution results from the study of Faucher-Giguère & Kaspi (2006) over accurate proper motion measurements of radio pulsars (Brisken et al. 2002; 2003); it describes well the observed population of isolated radio pulsars in spite of not being unique (see discussion in Sect. 4.2.2). We recalled our result of Chapter 2 that the spatial velocity distribution of the M7 do not seem to differ from that of young radio pulsars (Sect 2.6).

Birthrates We assumed that the population of cooling INSs is in a steady state and thus a constant birthrate is adopted during the lifetime of the Galaxy. The neutron star birthrate is also assumed to be the same in each of the spiral arms. In practice, the constant birthrate assumption is reasonable since only the objects younger than a few tens of million years – which are the ones still detectable through their thermal emission – are tracked by the model. The birthrate per area is therefore a function of the normalization constant A in Eq. (4.22). In our approach, the normalization is a free parameter in the model giving the total number of neutron stars in the Milky Way (see below).

Age distribution According to the constant birthrate assumption, the age distribution is chosen uniformly between zero and the age of the Galaxy, $t_G = 10\,\mathrm{Gyr}$. In this respect, the normalization constant A corresponds to the total number of neutron stars in the Galaxy. However, as mentioned above, only the objects younger than 1.3×10^7 yr, which is the time a neutron star with canonical mass and radius takes to cool down to $\sim 10^5$ K[7], are tested for detectability with the XMM-Newton EPIC pn detector.

Mass distribution For simplicity, all neutron stars in this preliminary version of the model are created with the same mass and radius, resulting in a gravitational acceleration

[7]Assuming the cooling curve of a magnetized neutron star composed of hadronic matter and with a non-decaying magnetic field of $B = 10^{14}$ G; `http://www.phas.ubc.ca/~heyl/cooling`.

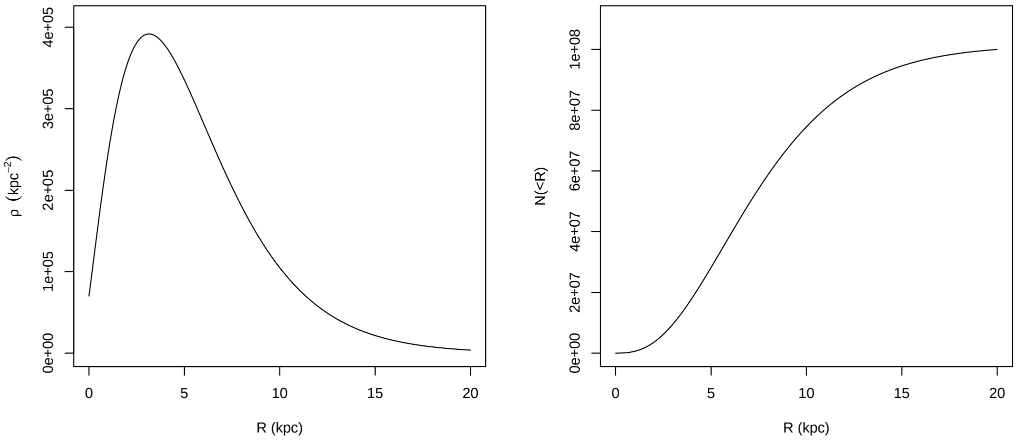

Figure 4.4: Initial radial and cumulative distribution of the modelled cooling neutron stars, for a normalization of $A \equiv N_{\rm tot} = 10^8$ neutron stars in the Milky Way.

of 10^{14} cm s^{-2} on the surface. If a canonical neutron star mass of 1.4 M⊙ is assumed, the radius is then 13.8 km and the gravitational redshift is $z_g \sim 0.20$. Since neutron star cooling is strongly dependent on mass, composition and magnetic field, this clearly corresponds to an oversimplification. We intend to implement a distribution of masses and cooling rates in future versions of the population synthesis model.

Emission properties We assumed that the radiation from the surface of the cooling INS is that of an isotropic blackbody, i.e.:

$$F_\nu^\infty = \frac{2\pi h}{c^2} \frac{\nu^3}{\exp(h\nu/kT_\infty) - 1} \tag{4.23}$$

Rewriting the integral in Eq. (4.3) in terms of energy, $\varepsilon = h\nu$, and assuming the black-body form above for F_ν^∞ and the diluted flux in Eq. (4.4), one gets:

$$S = \frac{2\pi}{h^3c^2}\left(\frac{R_\infty}{d_\star}\right)^2 \int_{\varepsilon_1}^{\varepsilon_2} \varepsilon^2 A(\varepsilon) \frac{\exp\left[-\sigma(\varepsilon) N_{\rm H}(r = d_\star, l, b)\right]}{\exp(\varepsilon/kT_\infty) - 1} d\varepsilon \tag{4.24}$$

where $d_\star$ is the neutron star distance to the Earth at present time, as T_∞ is the surface temperature taking into account the cooling evolution. As a function of the neutron star true emission radius $R_{\rm em}$ in Eq. (1.3), surface effective temperature $T_{\rm eff}$ in Eq. (1.2) and gravitational redshift z_g in Eq. (1.1), Eq. (4.24) above can be written:

$$S = \frac{2\pi}{h^3c^2}\left[\frac{R_{\rm em}(1+z_g)}{d_\star}\right]^2 \int_{\varepsilon_1}^{\varepsilon_2} \varepsilon^2 A(\varepsilon) \frac{\exp\left[-\sigma(\varepsilon) N_{\rm H}(r = d_\star, l, b)\right]}{\exp\left[\varepsilon(1+z_g)/kT_{\rm eff}\right] - 1} d\varepsilon \tag{4.25}$$

In the case of an isotropic emitter, $R_{\rm em} = R$, the gravitational radius of the neutron star.

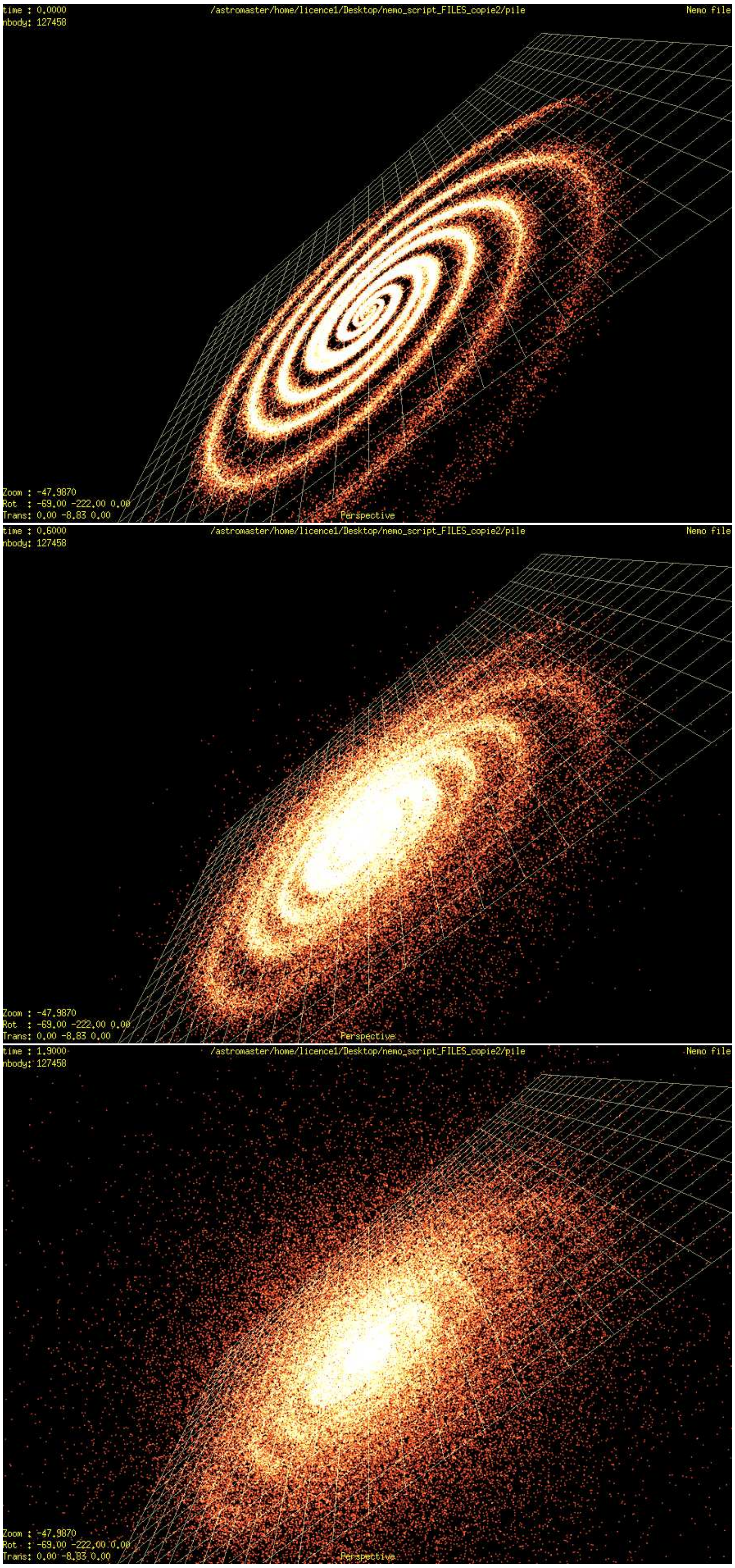

Figure 4.5: Spatial evolution of the neutron stars in the Galactic potential (we acknowledge A. Heidi and C. Boily for creating these plots with Nemo; http://bima.astro.umd.edu/nemo).

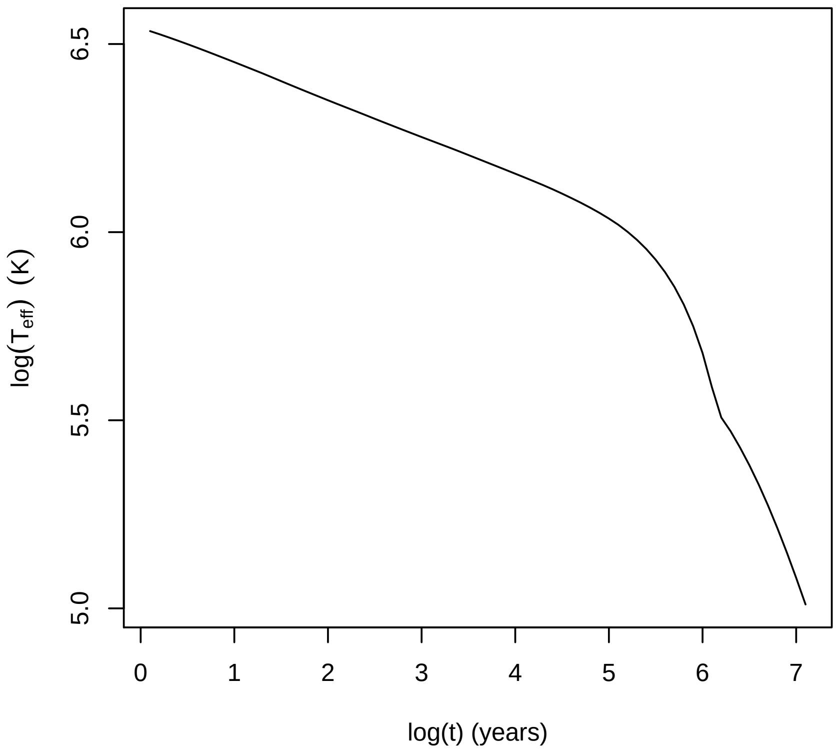

Figure 4.6: Adopted cooling curve for the synthetic neutron stars, assuming hadronic matter and a magnetic field of $B = 10^{14}$ G.

4.3.3 Neutron star evolution

The newly born neutron star receives a kick velocity and evolves in the Galactic potential during its lifetime as a thermally emitting source. We detail below how the spatial and thermal evolution of the synthetic cooling neutron stars were modelled.

Spatial evolution We assumed that the neutron star kick distribution is isotropic in three dimensional space. The speed modulus is exponentially distributed according to what is described in Sect. 4.3.2. The spatial motion of each neutron star younger than 1.3×10^7 yr is solved according to Eq. 4.2 for a total time according to its age. The spread in the initial spatial distribution is illustrated in Fig. 4.5.

Cooling Neutron star cooling is taken into account assuming hadronic matter and the effects of a non-decaying magnetic field of $B = 10^{14}$ G on the light-element atmosphere of a neutron star with a surface gravitational acceleration of $10^{14}\,\mathrm{cm\,s^{-2}}$ (Heyl 2000). With

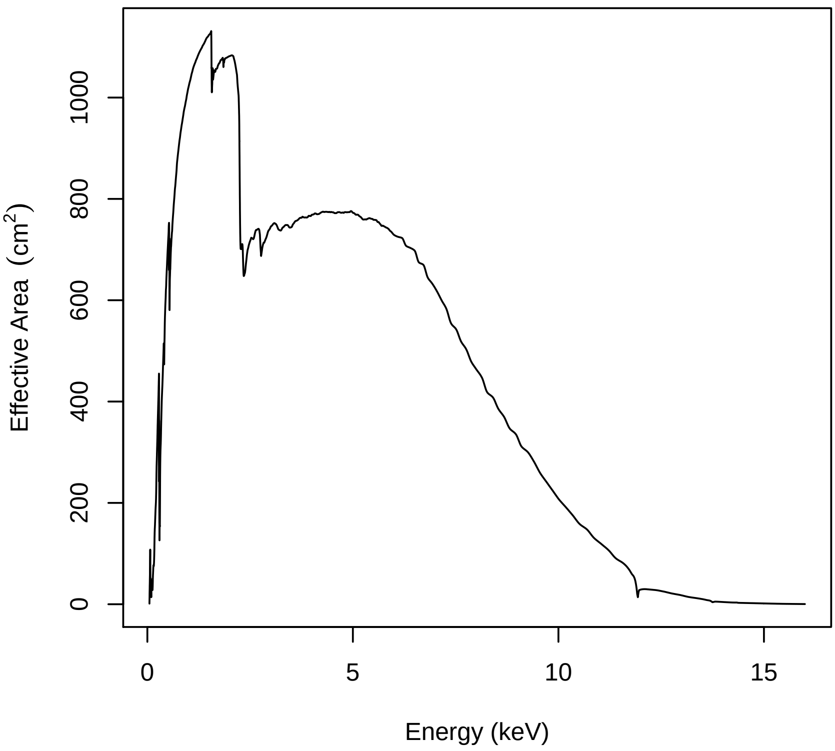

Figure 4.7: Effective area of the XMM-Newton EPIC pn camera considered in the population synthesis (on axis, medium filter).

this particular choice of cooling curve, we neglect the effects of the magnetic field decay as a heating source for the neutron star crust as discussed before. In addition, all synthetic neutron stars, having the same mass and composition, cool down at the same rate. The adopted cooling curve can be seen in Fig. 4.6.

4.3.4 Detectability with XMM-Newton

Once the thermal neutron star has evolved to its "current" position, all the parameters that determine its detectability by X-ray detectors are known. The last step in the simulation procedure consists in computing the source count rate as a function of energy band in the instrument detector of the mission of interest. We chose the XMM-Newton EPIC pn camera for consistency with our observational results obtained with the 2XMMp catalogue (Chapter 3). The EPIC pn sensitivity in the XMM-Newton energy pass-band 0.15 – 12 keV can be seen in Fig. 4.7, assuming on-axis observation and the medium filter; details are in Appendix B.1.1.

4.4 Simulation procedure

The first step in the simulation procedure consists of computing the number of neutron stars as a function of Galactocentric radius according to Eq. (4.22), which was done in steps of 10 pc from the Galactic center to a maximum radius of 20 kpc. In a given Galactocentric annulus, a random age between zero and the maximum age at which the star is still detectable as a thermal source, $t_{\rm cool} = 1.3 \times 10^7$ yr, is given to each synthetic neutron star. The simulation proceeds until the number of neutron stars to be created in the annulus is reached. For each neutron star, its azimuthal angle ϕ is then determined so that the neutron star position intersects a spiral arm in Eq. (4.7), which is randomly chosen between the four parametrized ones in the model (Table 4.1). Following what was described in Sect. 4.3.2, the neutron star radial position is then Gaussian-scattered isotropically around the arm centroid. A vertical distance relative to the plane is assigned to the neutron star so that the ensemble of sources is exponentially distributed above and below the disk with a scale height of $z_0 = 50$ pc.

The object receives a kick velocity with no preferential direction being defined; its three dimensional speed is exponentially distributed with mean $v_0 = 380\,{\rm km\,s^{-1}}$. The simulation next computes the object's current position by solving its equation of motion in (4.2). At this point in the procedure, a transformation of coordinates is performed in order to obtain the object's position in galactic coordinates. This position is then used to find the hydrogen column density as a function of distance to the source by solving the integral in Eq. (4.5), with the model $n(r, l, b)$ defined according to Sect. 4.3.1.

The last stage in the simulation procedure is to compute the source count rate as a function of energy band. For that, the code takes as parameters the object distance, $N_{\rm H}$ and age; by assuming the cooling curve, interstellar cross-section and instrumental effective area described before, the integral in Eq. (4.24) can be solved for the usual energy bands of XMM-Newton (Table B.3 in Appendix B.3.1). The simulation stops when the total number of neutron stars to be created in the Galaxy is reached, which in practice corresponds to 0.13% of the normalization constant A, the total number of neutron stars.

4.5 Preliminary results

We show in Fig. 4.8 the expected number of thermally emitting INSs as a function of the EPIC pn count rate resulting from our population synthesis model for different considered birthrate values. These plots are created by averaging the results of several trial simulations for each considered birthrate. For illustrative purposes only, we assumed whole sky coverage with XMM-Newton in order to compute the $\log N - \log S$ curve. In practice, the net area covered by the totality of XMM-Newton pointings is $420\,{\rm deg}^2$, considering the most complete compilation to date of the satellite observations for the purpose of serendipitous science (Appendix B.3.1). Moreover, the XMM-Newton pointings have different depths, so the area effectively covered by the satellite is more complex and has to be taken into account accordingly when comparing the theoretical $\log N - \log S$ curves with upper limits from catalogues.

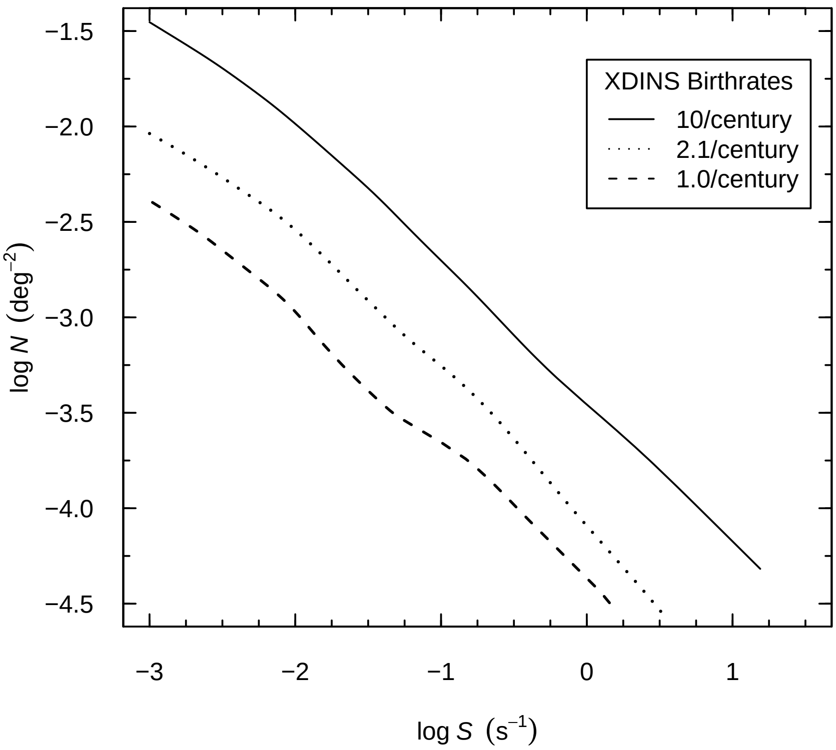

Figure 4.8: $\log N - \log S$ curves obtained with the preliminary version of the population synthesis model, assuming all-sky observation with the EPIC pn camera.

Recently, a birthrate of 2.1 ± 1.0 thermally emitting neutron stars born per century was suggested in the literature (Gill & Heyl 2007; see Sect. 1.5). These authors considered observational constraints from the RASS on the number of magnetars and XDINS in order to determine a limiting volume where these sources are detected by the survey up to a maximum distance. The number of progenitor OB stars in the volume is sought so as to find the relevant scalings. Finally, the spin-down ages of the XDINS provide the expected birthrates. The result is consistent with the lower limit obtained by Popov et al. (2006b) of 1 century^{-1}.

Considering the corresponding curve for $\beta = 2.1$ century^{-1}, our model gives a number of ~ 11 XDINS at a flux level $S_{\rm pn} > 0.2\,{\rm s}^{-1}$, corresponding to that of the faintest neutron star among the M7, RX J0420.0-5022. At the flux limit we applied in our search for thermally emitting INSs in the 2XMMp catalogue, a pn count rate of $10^{-2}\,{\rm s}^{-1}$, we expect from our results that ~ 120 XDINS are present over the whole sky. This translates into ~ 0.8 sources in the 2XMMp catalogue, a result that is in rough agreement with the one obtained by Posselt et al. (2008) for the same population and discussed in Chapter 3 (see

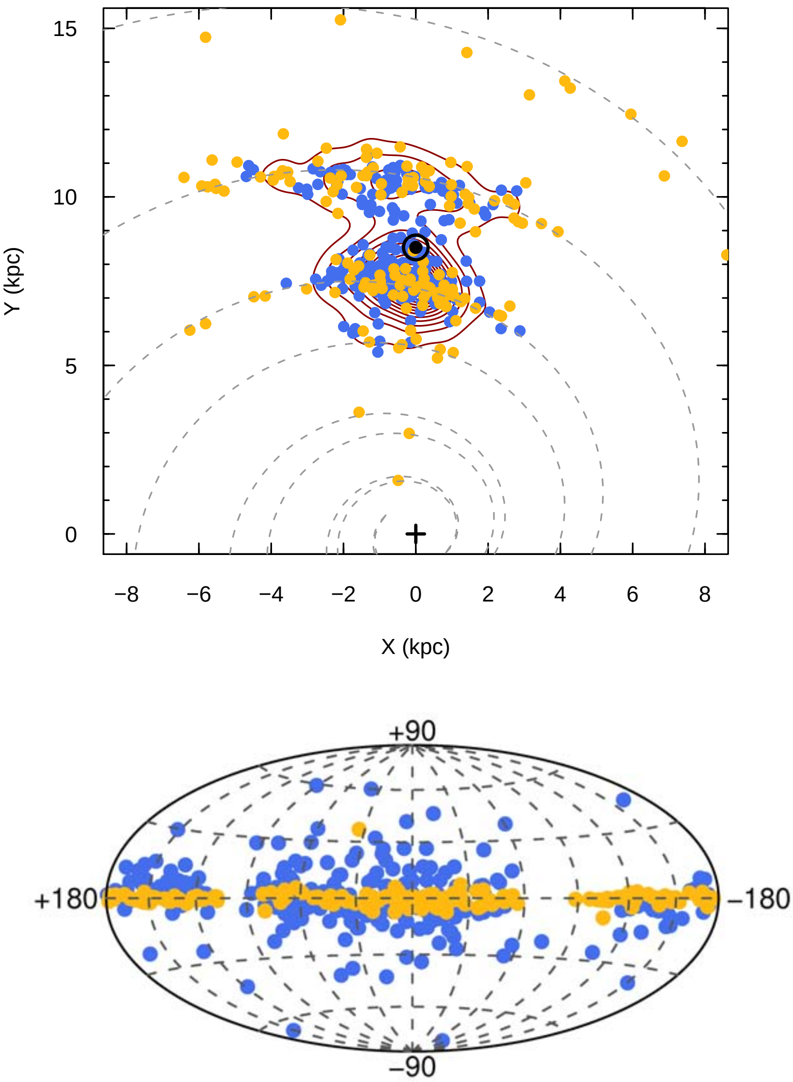

Figure 4.9: Spatial distribution of the modelled cooling INSs with EPIC pn counts above $10^{-2}\,\mathrm{s}^{-1}$ in the Galactic plane, for a normalized birthrate of 10 century^{-1}. Blue circles are neutron stars with blackbody temperatures $kT < 100$ eV while orange circles are those with higher temperatures. *Top:* Projected distribution on the Galactic plane. The Sun's location is marked in black while a cross at $X, Y = 0, 0$ shows the Galactic center. *Bottom:* Hammer-Aitoff projection in galactic coordinates of these "observed" objects.

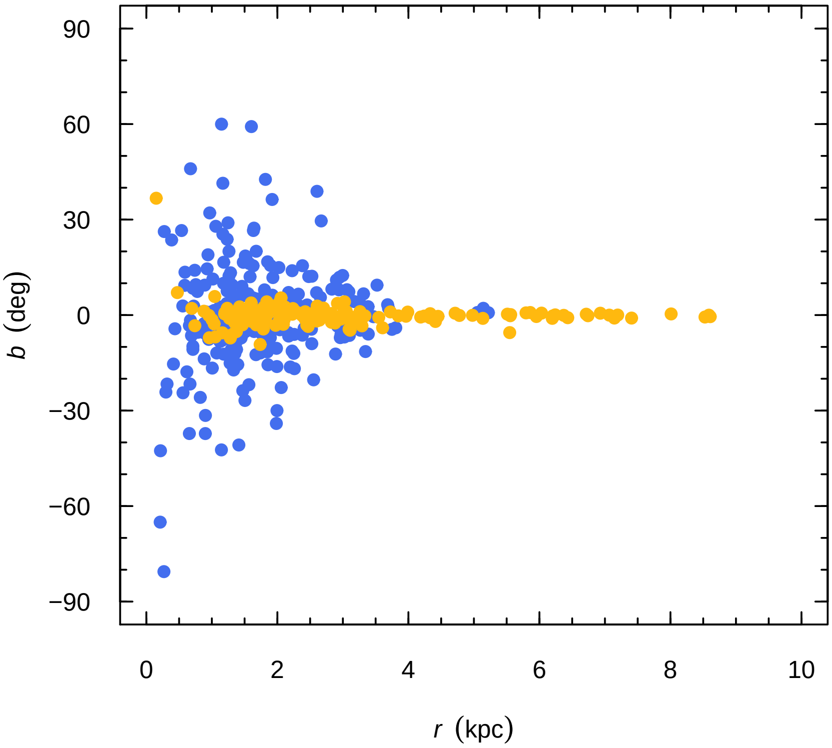

Figure 4.10: Galactic latitude of detected synthetic neutron stars as a function of distance from the Sun. EPIC pn counts are above $10^{-2}\,s^{-1}$, for a simulation with normalized birthrate of 10 century^{-1}. Neutron stars with blackbody temperatures $kT < 100\,eV$ are represented with blue circles while orange symbols are those with higher temperatures.

Sect. 3.6). We note however that, as it is, our $\log N - \log S$ curve is somewhat more steep than those obtained by these authors and hence our model predicts more sources at faint fluxes.

Although many of the assumptions considered in our model differ from those of Posselt et al., preventing a proper comparison, we estimate that the likely parameters controlling this discrepancy are the adopted cooling rates and, to a lower extent, the model for ISM distribution. Popov et al. (2005), Posselt et al. (2008) adopted a distribution of neutron star masses whereas in our simplified model all objects possess the same mass and therefore cool down at the same rate. In relation to the adopted set of cooling curves of Popov et al., Posselt et al., the synthetic neutron stars in our model lose thermal energy during the first 10^6 yr at a rate comparable with those of the lowest mass neutron stars in their model (which are the hottest for a given age). After ~ 1 Myr, while even these light-mass objects cool down very fast, reaching temperatures below few 10^4 K in 10^7 yr, our neutron

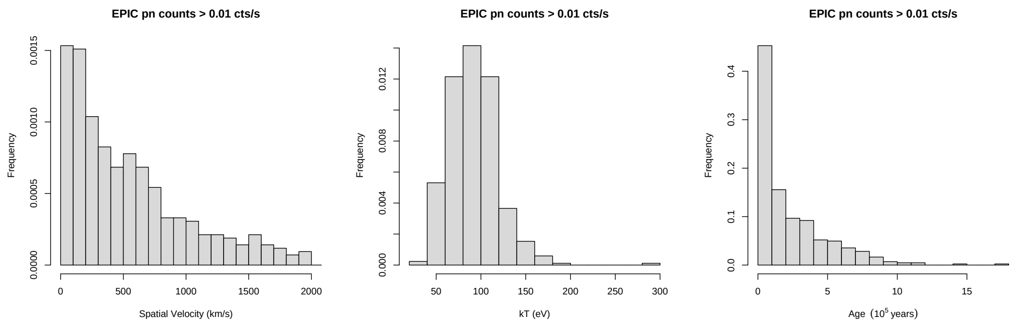

Figure 4.11: Velocity, kT and age distribution of INSs detected with EPIC pn count rates above $10^{-2}\,\mathrm{s}^{-1}$

stars are still somewhat hot due to the additional magnetic field heating of the envelope (see Fig. 4.6). This in principle explains why we detect more objects at faint fluxes. At the same time, we do not take into account the contributions of the Gould Belt or nearby OB associations in providing local remnants, i.e. close-by neutron stars which populate the bright end of the $\log N - \log S$ distribution.

The spatial distribution of the "observed" sample of thermal sources can be seen in Fig. 4.9, again assuming all-sky coverage. In this plot, we selected neutron stars with count rates above $10^{-2}\,\mathrm{s}^{-1}$ and highlighted those with blackbody temperatures above and below 100 eV. It is clear that, relative to the initial modelled distribution of progenitors in Fig. 4.3, it is the neutron stars in the immediate Solar vicinity that can be actually observed. At a distance scale typical of that of the M7, $d \lesssim 1$ kpc, we obtain that the typical temperatures, ages and 3-d velocities of the observable stars are $kT = 65 \pm 25$ eV, $\tau = (6.0 \pm 0.5) \times 10^5$ yr and $v_{3d} = 404 \pm 37\,\mathrm{km\,s^{-1}}$ (1σ). At greater distances the contributions from more distant spiral arms is apparent. In this case the neutron stars are consequently hotter and younger, as evident from the fact that they are still close to their birth places and concentrated in the plane. Indeed, our results show that at distances above 2.5 kpc nearly the totality of observed synthetic objects lies on the disk (Fig. 4.10). In Fig. 4.11 we show histograms of the distributions in age, temperature and spatial velocity of INSs detected with count rates above $10^{-2}\,\mathrm{s}^{-1}$.

4.6 Perspectives

The current version of our population synthesis model is preliminary yet has provided us with a sense of how these sources are expected to be born and to evolve in the Milky Way and what are the main sources of uncertainty involved in the population modelling of cooling neutron stars. We aim at developing our work further in order, firstly, to be able to compare its theoretical predictions with the upper limits derived by our work with the 2XMMp catalogue as well as its extensions, the 2XMMi and beyond; and secondly, by means of a more definitive version of the model, to constrain the important properties of the population of cooling neutron stars in the Galaxy, and thus derive more stringent estimates of their birthrates and of their expected density outside the Solar vicinity. Finally, the operation of the eROSITA survey in X-rays, which is expected to be launched in the near future, will probably have a great impact on the number of sources that can potentially be detected.

The main improvements planned for our model are the inclusion of a more realistic description of the absorbing interstellar material and a distribution of neutron star masses and cooling rates. For the first point, in collaboration with Bettina Posselt, we plan to incorporate her 3-d model for the interstellar photoelectric absorption, which considers the local clumpiness of the ISM at distances up to 230 pc. This will allow us to better account for the local effects that affect the detectability of nearby sources. For the second point, a distribution of masses will be included as well as a set of cooling curves. It would also be of great interest to include the effects of additional heating through magnetic field decay, so that the neutron star cooling would be determined not only by mass but also by the state of magnetization, an issue which was proven to dramatically change the neutron star thermal emission.

CHAPTER 5

Summary and outlook

We summarize below the main results obtained during the work on the thesis and their implications in addressing population properties of the group of seven nearby thermally emitting isolated neutron stars discovered by ROSAT, the *Magnificent Seven*. We also discuss how our results contribute to the overall understanding of the more general population of X-ray thermally emitting isolated neutron stars in the Milky Way.

5.1 Proper motion study of isolated neutron stars in X-rays

Chandra Observatory ACIS data obtained over a time interval of three to five years allowed us to either constrain or determine the proper motion of three of the *Magnificent Seven*. These sources have either too faint or dubious optical counterparts that prevent the conduction of proper motion investigations in the optical in a reasonable amount of time. We determined 2σ upper limits on the proper motions of sources RX J0806.4-4123 and RX J0420.0-5022 of $\mu < 87\,\mathrm{mas\,yr^{-1}}$ and $\mu < 113\,\mathrm{mas\,yr^{-1}}$, respectively. In the case of the *Magnificent Seven* RX J1308.6+2127, we measured for the first time the very significant displacement of the source, with $\mu = 213 \pm 14\,\mathrm{mas\,yr^{-1}}$, an unprecedented accuracy for X-ray observations. These results significantly limit the possible range of transverse velocities of these three sources and therefore provide valuable information on the properties of the ensemble of the *Magnificent Seven* as a group: within the limits imposed by the small number statistics, the distribution in transverse velocity of the *Magnificent Seven* does not appear statistically different from that of the radio pulsars. This indicates that the mechanism leading to the strong magnetic fields and long periods typical of these objects in relation to the bulk of the population of "standard" radio pulsars is, to first order, independent of that controlling the kick velocity.

The upper limit on the displacement on the sky of RX J0806.4-4123 hints at a slow relative velocity with respect to the interstellar medium. Moreover, this source is located in the gas-rich environment of the Galactic plane. In principle, these two conditions could favour a scenario where the X-ray luminosity (or a fraction of it) is produced by accretion from the interstellar medium onto the surface of the neutron star, an idea first proposed nearly 40 years ago. In the years following the discovery of the seven ROSAT sources, the accretion hypothesis was regarded as a strong candidate for the X-ray emission of these sources. However, as for the other neutron stars among the *Magnificent Seven*, we argue that accretion is unlikely to occur for the case of RX J0806.4-4123 and does not significantly contribute to its X-ray emission.

As it is, the thesis work doubles the number of radio-quiet thermally emitting neutron stars for which information on proper motion exists. Extensive simulations carried out with

MARX and the analysis of fields observed several times by Chandra confirm the feasibility of measuring proper motions at X-ray wavelengths with an accuracy approaching that of optical ground based observations.

We found that the likely transverse velocity of RX J1308.6+2127 is large, of the order of 400 to 800 $\mathrm{km\,s^{-1}}$ and could well be the largest of the six of the *Magnificent Seven* for which there exist both a measurement of the proper motion and an estimate of the distance. The receding radial velocities required for a birth close to the Galactic plane are of the order of 500 $\mathrm{km\,s^{-1}}$, suggesting space velocities as high as 1000 $\mathrm{km\,s^{-1}}$. RX J1308.6+2127 is therefore another example of a young cooling radio-quiet nearby neutron star which might be crossing the Galaxy as fast as the extreme cases of the radio pulsars, PSR B2011+38, B2224+65 and B1830-08.

The assumed present distance to RX J1308.6+2127 determines its possible travel time from nearby OB associations and from the Galactic plane in general. The analysis of all possible backward trajectories suggests that, for a present distance of between 400 and 800 pc, the most likely birth OB association is the Scutum OB2 A group located at 510 pc, whereas a birth in the nearby Upper Scorpius part of the Sco OB2 association would be possible if the present distance to the source were much less, around 260 pc. We also find that travel times from the Galactic plane or from one of the candidate OB associations depend sensitively on the assumed current distance to the source and range from less than ~ 1.2 Myr for a present distance in the range $400 - 800$ pc to less than 0.6 Myr for shorter distances. Although the still rather large uncertainties on the proper motion vector, current distance and the unknown radial velocity allow for longer flight times in some cases, the majority of the trajectories imply a kinematic age significantly younger than the spin-down time of 1.5 Myr. A similar discrepancy occurs for the *Magnificent Seven* RX J0720.4-3125 and RX J1856.5-3754.

5.2 The search for thermally emitting isolated neutron stars

Our search for new thermally emitting INSs in the 2XMMp catalogue revealed a number of interesting and previously unknown soft X-ray sources. A final list of 27 INS candidates, selected from among more than 72,000 X-ray sources, was presented in Chapter 3. Deep dedicated ESO-VLT and SOAR optical imaging conducted over the brightest end of our sample of candidates revealed likely optical counterparts for six of them which, based on blue optical colours and X-ray-to-optical flux ratios around 1 to 10, identify them as, most likely, AGN and CVs. We found that one source, 2XMM J010642.3+005032, has no evident optical candidate and hence is an interesting target for further optical and X-ray investigations.

The thesis work brought the long awaited discovery of a new thermally emitting isolated neutron star, 2XMM J104608.7-594306. In spite of many searches conducted over the past 10 years, no new candidate to be included in the select group of ROSAT sources had been identified so far, with the possible exception of the compact object nicknamed *Calvera*[1]. 2XMM J104608.7-594306 displays overwhelming evidence favouring an iden-

[1]However, *Calvera* displays properties that seem to be in contrast with an identification of a cooling neutron

tification with a cooling neutron star. Interestingly, it shows properties very similar to those of the *Magnificent Seven* although located at a greater distance. We have shown that 2XMM J104608.7-594306 displays purely thermal soft X-ray emission with no evidence for magnetospheric emission typical of radio pulsars detected at high energies. Furthermore, the source is possibly radio-quiet, is not associated with a supernova remnant, shows an X-ray flux which is constant over a timescale of several years and has no optical counterpart down to very deep limits. The present lower limit on the X-ray-to-optical flux ratio excludes standard classes of X-ray emitters. Its likely location in the Carina Nebula is in agreement with the most up-to-date expectations of population synthesis models and may provide valuable insights into the past star forming history of this giant HII region. Being slightly hotter, the source is expected to be more luminous and younger than the *Magnificent Seven* and thus perhaps still close to its birth place. Its X-ray temperature is however lower than that of the only rotating radio transient detected at high energies so far, RRAT J1819-1458, a source that displays X-ray properties similar to the *Magnificent Seven*. In this regard, 2XMM J104608.7-594306 is unique in the sense that it may represent an evolutionary missing link between the different classes of magnetars, radio-transient and radio-quiet isolated neutron stars.

This part of the thesis work affirms the use of the XMM-Newton catalogue of sources as an efficient tool to identify new thermally emitting INSs and other particular classes of soft X-ray sources. A similar search using the Chandra data with its excellent astrometric accuracy would be instrumental in selecting further sources, especially those located in the Galactic plane, where it is more likely to find new INS candidates.

5.3 Population synthesis of thermal isolated neutron stars

Our work in population synthesis, although preliminary in its current version, have provided us with a sense of how these sources are born and evolve in the Milky Way. Most importantly, it allowed us to experiment with the main uncertainties involved in the modelling of this population and to discover which ingredients have the greatest impact on the detectability of the studied thermal objects with current X-ray instruments. Our aim is to develop this model further and to compare its theoretical expectations with the observational results we obtained searching the XMM-Newton catalogue of sources for thermally emitting isolated neutron stars. Our final goal is to derive reliable estimates for the birthrate of thermally emitting sources, a crucial parameter for population studies of neutron stars, given the present discrepancy between the inferred birthrates of the different groups and the expected total number of neutron stars in the Galaxy. We also aim at constraining important properties of the Galactic population of *Magnificent Seven*-like objects and to investigate their possible links with other classes of isolated neutron stars.

star similar to the seven ROSAT sources.

Appendix A

Emission from cooling and accreting isolated neutron stars

Contents

A.1 Theory behind thermal emission of neutron stars

A.1.1 Introduction

One of the greatest interests in studying the thermal evolution of neutron stars is the possibility of constraining the equation of state (EoS) of stellar interior at very high densities through the confrontation of theory and observations. The EoS of dense matter not only fully determines the internal structure of neutron star, its maximum mass, radius, momentum of inertia, binding energy etc, but also plays an important role during the phenomena of both supernova and merger of compact objects. For reviews of the physics of neutron star interior, see e.g. Prakash et al. (1988), Lattimer & Prakash (2000; 2001), Haensel (2003), Weber et al. (2009); and references therein. A comprehensive overview of the role of observations in constraining neutron star physics can be found in Lattimer & Prakash (2007).

As far as EoS are concerned, the two most important neutron star properties are the stellar mass and radius. The neutron star maximum mass is a consequence of general relativity and is controlled by the stiffness of a given EoS, i.e. by how much matter can be compressed. Therefore, sufficiently large observed neutron star masses set significant upper limits to the allowed density range and provide effective constraints on the composition of dense matter and the structural properties of neutron stars. In particular, it can rule out some forms of the so-called exotic matter in neutron star interior (Sect A.1.2). Although there have been claims in recent years of measured neutron star masses in excess of $\sim 2\,M_\odot$ (e.g. Freire et al. 2008b;c, Webb & Barret 2007, Özel 2006), the still large observational uncertainties involved in these determinations – in particular, for the case of thermonuclear

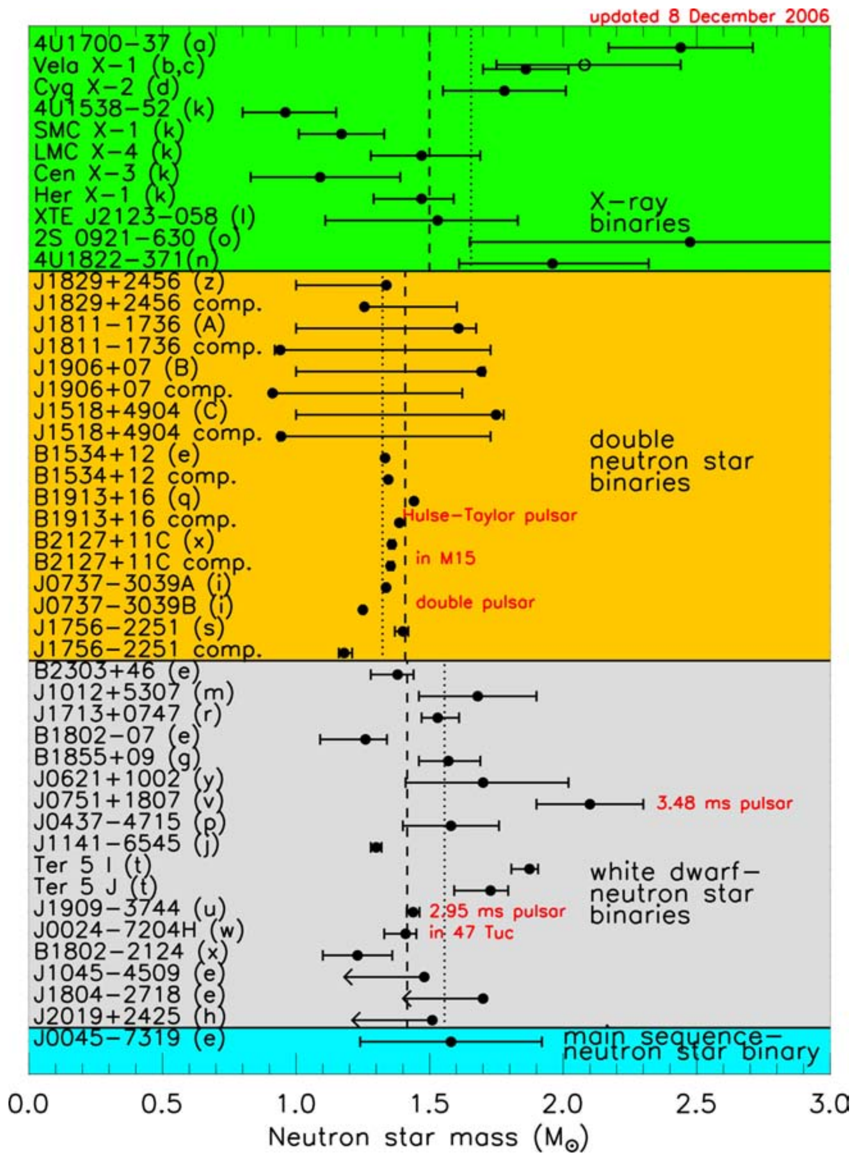

Figure A.1: Measured and estimated masses of neutron stars in radio binary pulsars (golden, silver and blue regions) and X-ray accreting binaries (green region; from Lattimer & Prakash 2007).

bursts in X-ray binaries and considering the effect of accretion in these systems – cannot definitely exclude the possibility of exotic constituents. In Fig. A.1 we show a plot of mass determinations of neutron stars in binary radio pulsars and X-ray accreting binaries. This is an updated version (as of December 2006) of the Thorsett & Chakrabarty (1999) plot in Fig. 4.2.

The neutron star radius is controlled by properties of the nuclear force at supranuclear densities. Whereas masses can be measured very accurately in radio pulsar binary systems through the determination of orbital parameters, radius measurements are far less precise.

Nonetheless, radii (or the mass-to-radius ratio M/R) can be inferred from e.g. rapidly rotating objects, gravitational redshifts, thermonuclear bursts on the surface of accreting neutron stars in binary systems, pulsar glitches, starquakes that occur after giant flares from soft γ-ray repeaters (SGRs), the thermal relaxation of the crust during periods of quiescence in-between X-ray bursts in low-mass X-ray binaries (LMXBs); in addition, from the observed thermal emission of cooling neutron stars.

The temporal evolution of the neutron star luminosity or temperature – or, in other words, its thermal behaviour – is strongly dependent on the internal composition and on the superfluid characteristics of its components. This is especially true for the first million years of the neutron star lifetime, when cooling is dominated by neutrino emission processes (Sect. A.1.3). Consequently, a rapidly cooling core would be revealed through relatively low surface temperatures measured for a given age, hence constraning the neutrino emissivity and interior matter composition. Here resides the importance of comparing cooling curves for different scenarios with the observed thermal emission of cooling neutron stars.

However, this is not a trivial task for several reasons. First of all, the detection of purely thermal radiation is a complicated problem. On the one hand, the thermal emission of young pulsars like the Crab (age $\lesssim 10^3$ yr) is obscured by the strong non-thermal emission of the processes occurring in the pulsar magnetosphere. On the other hand, the spectral energy distribution of old pulsars (age $\gtrsim 10^6$ yr) may be rather complex, showing, together with thermal emission from the surface, the contributions of hot polar caps that result from pulsar activity as well as of non-thermal components extending towards higher energies. This makes the extraction of the thermal radiation component from the observed spectra complicated and sometimes somewhat arbitrary. Therefore, neutron stars of intermediate age, $10^4 - 10^6$ yr, and with no significant magnetospheric emission, correspond very naturally to the ideal targets for constraining the several possible thermal scenarios.

From observations of thermally emitting sources, the redshifted surface effective temperature T_{eff}^{∞} and total bolometric flux F_{∞} are inferred. If the distance d to the source is known, then these quantities are used in order to derive the star radiation radius, according to:

$$R_{\infty} = d\left[\frac{F_{\infty}}{\sigma(T_{\text{eff}}^{\infty})^4}\right]^{1/2} \tag{A.1}$$

where σ is the Stefan-Boltzmann constant. The actual effective temperature and flux are related to the redshifted ones according to Eq. (1.2) and to:

$$F = (1 + z_g)^2 F_{\infty} \tag{A.2}$$

where z_g is the gravitational redshift, Eq. (1.1).

The radiation radius sets upper limits to both the neutron star mass and radius; hence, independent estimates of these quantities are required. As evident above, a distance estimate to the source is similarly needed as well as a good constraint of the interstellar hydrogen absorption in the line-of-sight, which can significantly modify the intrinsic shape of the source spectrum. In addition, details concerning the composition of the atmosphere and its magnetic field strength and structure are necessary ingredients in modelling the thermal emission (Sect. 1.3.2; see Zavlin 2009 for a review).

A.1.2 Neutron star interior

Neutron star structure can be divided into a thin atmosphere and four internal regions which are usually referred to as the envelope, the crust, the outer and the inner cores (Fig. A.2). The atmosphere is defined as the region where the density is less than $\sim 10^2\,\mathrm{g\,cm^{-3}}$. Its thickness is of only $0.1 - 10\,\mathrm{cm}$ and yet determines the properties of the emergent thermal photon flux. If the neutron star keeps its pre-collapse composition of the progenitor core, it is expected that the atmosphere will consist of iron. However, if any hydrogen is present, it must settle onto the outermost stellar layers (Sect. 1.3.2).

The matter in the envelope consists of condensed ions (atomic nuclei) and a gas of degenerate electrons. Magnetic fields in the envelope have a major influence on the electron thermal conductivity in the atmosphere, leading to significant surface temperature anisotropies. As the electron Fermi energy grows with increasing density, electron capture takes place and nuclei become richer in neutrons with the emission of neutrinos. The boundary between the crust and envelope is defined at a density corresponding to the *neutron dripping point*, at $\rho \sim 4 \times 10^{11}\,\mathrm{g\,cm^{-3}}$. The envelope has an estimated thickness of a few hundred meters.

In the crust, matter consists of a gas of free neutrons, electrons and nuclei. The fraction of neutrons increases inwards until the point where nuclei disappear at density $\sim 1.4 \times 10^{14}\,\mathrm{g\,cm^{-3}}$ (corresponding to half of the density of nuclear matter at saturation, ρ_0), about one kilometer from the boundary with the envelope. Below the crust lies the stellar core. At the lowest densities matter consists of a strongly non-ideal liquid of neutrons and protons, interacting via nuclear forces, electrons and possibly muons, all strongly degenerate. For densities up to about $2\rho_0$ the equation of state and composition of matter are reasonably well constrained by nuclear physics data and theory, while at higher densities they are much less certain. This point defines the boundary between the inner and outer core which, although it is not necessary, can be physically different. In massive stars, central densities can potentially be as high as $(10 - 15)\rho_0$ and therefore the inner core can reach a radius of several kilometers. In low mass stars, on the other hand, the inner core may be absent since the outer core extends to the center of the star. The composition of matter in the inner core is rather uncertain but in principle can consist of either nucleon matter (i.e. the constituents are basically the same as in the outer core) or of exotic matter, with the possible presence of hyperons, Bose-Einstein pion and kaon condensates and quarks, all of which are expected to appear under extreme circumstances of pressure and density.

Depending on the composition (and thus compressibility) of matter, different EoS are applied and different maximum masses for a given model are obtained. Generally speaking, very stiff EoS, with $M_{\rm NS}^{\rm max} \sim 2 - 2.5\,\mathrm{M}_\odot$, are only found for nucleon matter, whereas the appearance of a new phase tends to soften the EoS. In particular, the presence of exotic matter generally reduce the maximum mass appreciably.

For the sake of completeness, we also mention the hypothetical class of *strange stars*, which are mainly composed of strange quark matter under the assumption that this could

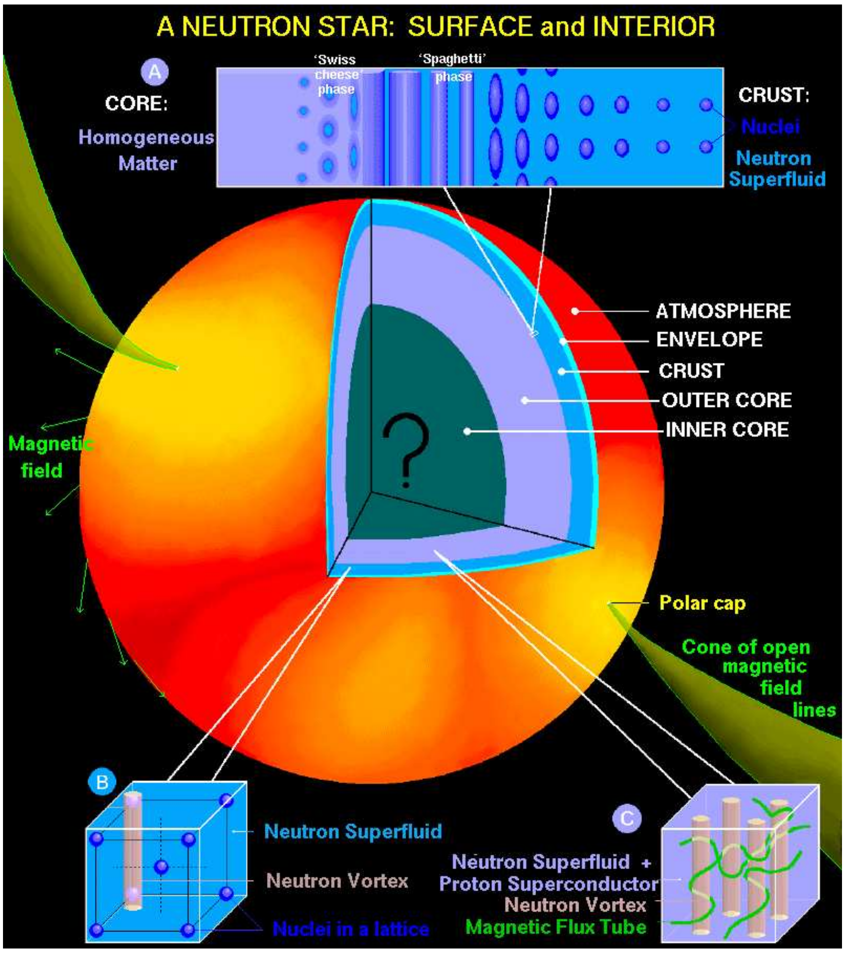

Figure A.2: Schematic view of the neutron star interior (from Dany Page's webpage at UNAM, http://www.astroscu.unam.mx/neutrones/NS-Picture/NS-Picture.html)

be a more fundamental or stable state of matter at high densities than nuclear matter. According to some models, the quark matter extends to the stellar surface; such objects are referred to as bare strange stars. Other descriptions favour a model where the strange star has a normal crust extending from the surface to the neutron dripping point. In general sense, strange stars can be very small and much more compact than "canonical" neutron stars for a given mass. A review of these objects can be found in Weber (2005).

A.1.3 Thermal evolution of neutron stars

The first ones to investigate the theory of neutron star cooling were Tsuruta & Cameron (1966), before the discovery of the first radio pulsar. The development of the theory was extensively reviewed in recent years and references can be found in Pethick (1992), Page (1998), Yakovlev et al. (1999), Page et al. (2004a), Yakovlev & Pethick (2004). In the following we recall the overall stages of neutron star thermal evolution and the physics

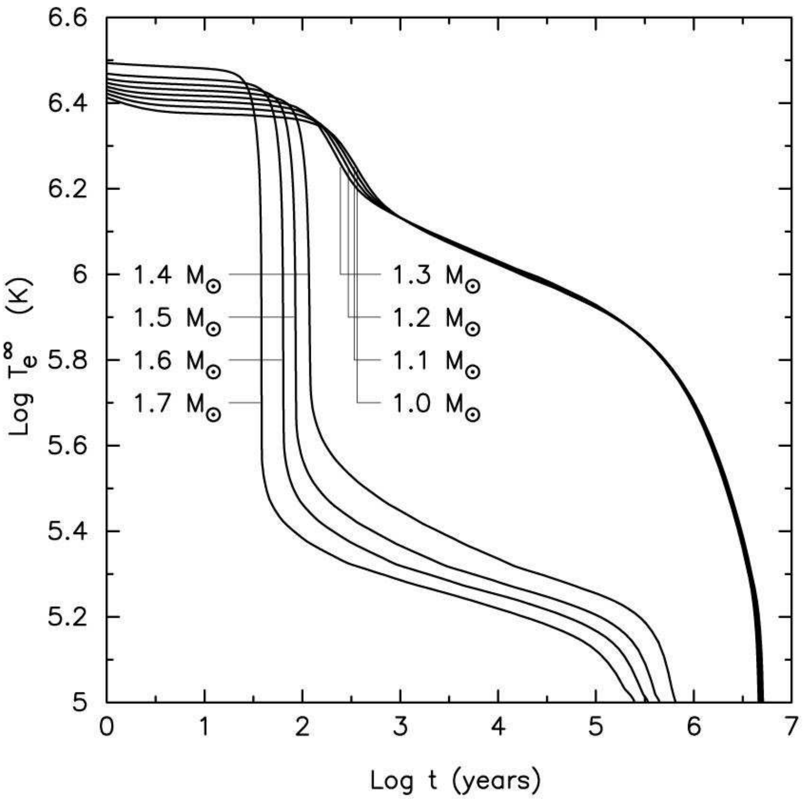

Figure A.3: Fast *vs.* standard cooling for neutron stars with different masses (from Page & Applegate 1992).

involved.

Following the supernova event, the newly formed neutron star is thought to possess a very high central temperature, $T_c \sim 10^{11}$ K and is at first opaque to neutrinos in a proto-neutron star stage. However, within a few days prodigious neutrino emission rapidly sets, proceeding to efficiently cool down the star to central temperatures of the order of 10^9 – 10^{10} K. At the very early stages of its life, the star is not in complete thermal equilibrium since the thermal relaxation time of the crust is of the order of 10 to 100 years. After this time, the stellar interior (at densities $\rho \gtrsim 10^{10}$ g cm^{-3}) becomes isothermal; the temperature gradient between the interior and the surface sets in the neutron star envelope. The star then cools by neutrino and photon emission at the expense of the thermal energy which is mainly stored in the core. Some heating mechanisms, like frictional heating of superfluid neutrons in the inner neutron star crust or some exothermal nuclear reactions, might contribute to reducing the cooling rate. In the first 10^5 years, the dominant cooling process is neutrino emission from the stellar interior (neutrino cooling era). After $\sim 10^6$ years, photon emission from the surface takes over as the main cooling mechanism, which then defines the photon cooling era.

Two different scenarios can determine the neutron star cooling behaviour once the surface temperature has cooled down to $\sim (1.5 - 3) \times 10^6$ K, which is after around 100 years. According to the *standard cooling scenario*, the temperature decreases gradually during the neutrino cooling era, down to around $(0.3 - 1) \times 10^6$ K, and then undergoes an exponential fall, reaching temperatures lower than $\sim 10^5$ K when the star is older than 10^7 years. This behaviour is a consequence of the *slow* neutrino ractions that operate in the neutron star core during the neutrino cooling era, among those are the modified Urca reactions. Slow neutrino reactions are expected to happen everywhere in the neutron star core, particularly in the lower density regime (hence in low mass neutron stars). Another slow neutrino emission process is via bremsstrahlung of neutrons and protons.

The other possible cooling scenario is the *fast cooling*, which is associated with higher central densities (more massive neutron stars) and/or the presence of exotic matter. In this scenario, the temperature sharply drops in the first hundred years, down to $(0.3 - 0.5) \times 10^6$ K, and then follows a more gradual decrease in the next years, reaching similar low temperatures at ages around 10^7 years as in the standard cooling scenario. The neutrino processes at work in the fast cooling are the direct Urca reactions; other direct Urca-like reactions may be in operation if pion/kaon condensates or quark matter are present. Since fast neutrino reactions, as the direct Urca, have density thresholds in order to take place, they are not expected to occur outside the inner core.

The two different cooling scenarios can be seen in the illustrative example of Fig. A.3, for a moderate EoS which allows direct Urca processes for neutron star masses above $1.35\,M_\odot$; star with lower masses undergo standard cooling. In fact, several effects can change this very general and simplified picture, with both scenarios being substantially affected by e.g. nucleon superfluidity and the magnetic field. The magnetic field influences the thermal conductivity of the surface layers and, in particular, makes it anisotropic (Sect. 4.2.3). In superfluid matter, on the other hand, when the temperature is low enough, baryons become "inactive" and do not take part in the nuclear reactions. The result is the suppression of e.g. Urca reactions although bremmstrahlung processes are unaffected. Moreover, other neutrino processes that are otherwise forbbiden in non-superfluid matter can then take place, such as the Cooper pairing of baryons.

A.2 Bondi-Hoyle accretion scenario

Ostriker, Rees, & Silk were the first ones to propose the idea that a sufficiently slowly moving and old isolated neutron star might accrete matter from the interstellar medium and become a source of soft X-rays. Such a possibility is exciting since it would allow the observation of a vast number of isolated sources that have exhausted their energy resources in the first 10−100 million years of their lives and which are therefore undetectable through cooling, rotational losses or magnetic field decay mechanisms. This hypothesis has been investigated usually assuming spherical Bondi-Hoyle accretion, which is recalled below (a recent review can be found in e.g. Edgar 2004). In the following we also briefly review the basic conditions under which accretion from the ISM might be possible, which has extensively been discussed in e.g. Treves et al. (2000), and references therein.

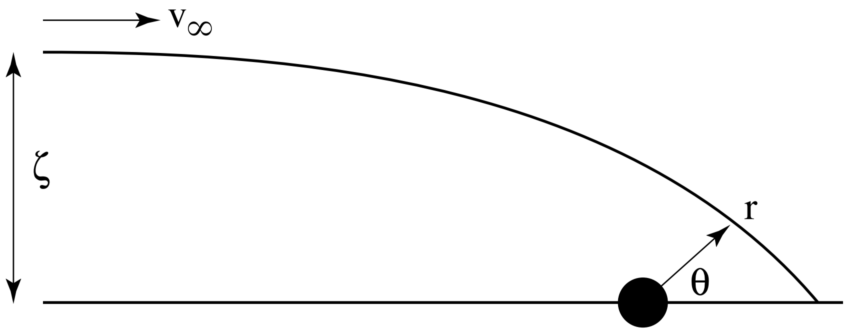

Figure A.4: Sketch of the Bondi-Hoyle accretion geometry (from Edgar 2004).

Spherical accretion The Bondi-Hoyle accretion theory concerns the supersonic motion of a point mass through an infinite gas cloud. The cloud is assumed to be uniform and effects of self-gravitation or ram pressure are neglected. The material surrounding the point mass is focused behind it and can be accreted due to gravity. The geometry of the problem originally solved by Bondi & Hoyle (1944) is shown in Fig. A.4. It consists of considering the ballistic orbits of test particles under the influence of the central gravitational field in order to define the maximum radius (or impact parameter) within which any test mass is accreted after it reaches the $\theta = 0$ axis in Fig. A.4. At this point, if:

$$\frac{1}{2}v_\infty^2 - \frac{GM}{r} < 0 \tag{A.3}$$

or, similarly, if the impact parameter ζ is such that:

$$\zeta < \zeta_0 = \frac{2GM}{v_\infty^2} \tag{A.4}$$

the test mass is bound to the central field and it is accreted. If it is considered that inside the critical radius the gas is supersonic and moves towards a free-fall solution then the mass flux is:

$$\dot{M} = \frac{2\pi G^2 M^2 \rho_\infty}{(v_\infty^2 + c_\infty^2)^{3/2}} \tag{A.5}$$

where ρ_∞ is the cloud mass density and c_∞ is the speed of sound of the surrounding material. This is known as the Bondi-Hoyle accretion rate. In usual units and as a function of the medium number density n, it can be written:

$$\dot{M} = 10^{11} n v_{10}^{-3}\,\mathrm{g\,s^{-1}} \tag{A.6}$$

where v_{10} is the neutron star velocity relative to the interstellar medium in units of $10\,\mathrm{km\,s^{-1}}$.

Accretion onto a spinning, magnetized isolated neutron star In the context of accretion onto old[1] isolated neutron stars, a number of conditions must be fulfilled before matter can reach the surface. These are better understood in terms of requirements made upon several scale lengths that determine the behaviour of the interaction of the neutron star with its surrounding medium. These scale lengths are the *accretion*, *corotation* and *Alfvèn radii*. The accretion radius is the above defined impact parameter ζ_0 in Eq. (A.4). It determines the region where the dynamics of the interstellar medium are dominated by the gravitational field of the neutron star. In usual units, it is of the form:

$$r_{\rm acc} = 3 \times 10^{14} m v_{10}^{-2} \ \text{cm} \tag{A.7}$$

where $m \equiv M/\mathrm{M}\odot$. The Alfvèn radius determines the boundary where the magnetic field dominates the motion of the infalling material:

$$r_{\rm alf} = \left(\frac{B^2 R^6}{\sqrt{2GM}\dot{M}} \right)^{2/7} \tag{A.8}$$

If the accretion rate is assumed to be the Bondi-Hoyle one, and with B, $\dot{M}$ and R in units of 10^{12} G, 10^{-11} g s^{-1} and 10^6 cm, respectively, then:

$$r_{\rm alf} = 2 \times 10^{10} \left(B_{12}^4 \dot{M}_{11}^{-2} R_6^{12} m^{-1} \right)^{1/7} \ \text{cm} \tag{A.9}$$

The corotation radius is the distance to the neutron star where its angular velocity is equal to the Keplerian angular velocity:

$$r_{\rm cor} = \left(\frac{GMP^2}{4\pi^2} \right)^{1/3} \tag{A.10}$$

which, again, can be written in more usual units as:

$$r_{\rm cor} = 2 \times 10^8 \left(mP^2 \right)^{1/3} \ \text{cm} \tag{A.11}$$

Following Treves et al. (2000), the first condition that must be fullfiled in order accretion to occur is that the accretion radius is larger than the Alfvèn radius. This corresponds to a requirement that the neutron star velocity should be smaller than:

$$v_{10} \lesssim \left(m^{8/7} B_{12}^{-4/7} n R_6^{-12/7} \right)^{1/5} \tag{A.12}$$

At the accretion radius the gravitational energy of the infalling material must exceed the energy of the momentum outflow produced by the rotating magnetic field. This is met when the neutron star has spun down to a period of:

$$P > P_{\rm cr} = 10 \times \frac{r_{\rm alf}}{10^{14} \ \text{cm}} \left(B_{12} \dot{M}_{11}^{-1/2} R_6^{3/2} m^{-1/8} \right)^{1/2} \ \text{s} \tag{A.13}$$

If $P < P_{\rm cr}$, the neutron star is said to be in the *ejector* phase. For neutron stars spinning slower than this critical value, the gravitational acceleration of the infalling material

[1] Young pulsars usually possess strong winds that prevent accretion to occur during the first 10 million years of the pulsar lifetime.

must then be higher than the centrifugal force at the corotation radius. This translates into another constraint to the neutron star spin period:

$$P > 10^3 \times B_{12}^{6/7} \dot{M}_{11}^{-1/2} m^{-1/2} \ \text{cm} \tag{A.14}$$

which, if not fullfiled, matter accumulates at the Alfvèn radius and the star is said to be in the *propeller* phase. Only by means of magnetic dipole radiation, this requirement cannot be achieved and the neutron star would have to lose rotational energy through additional mechanisms in order that accretion to be possible.

Appendix B

Telescopes, instruments and data sources

Contents

B.1 X-ray telescopes

B.1.1 XMM-Newton

The European Space Agency (ESA) XMM-Newton mission (Jansen et al. 2001) was launched in December 1999 and has a nominal lifetime of 10 years. It carries three co-aligned grazing-incidence X-ray telescopes, each comprising 58 nested Wolter type I mirror shells with a focal length of 7.5 m. This design provides a large collecting area over a wide energy band, the largest of all focusing X-ray satellites to date. A highly elliptical orbit offers continuous target visibility of up to 40 hours. Additionally to the X-ray telescopes, the observatory carries a co-aligned 30 cm diameter Optical Monitor (OM) telescope (Mason et al. 2001) which provides an imaging capability in three broad-band ultraviolet and optical filters, in wavelength range 1800 Å to 6000 Å. Two additional grism filters allow low dispersion spectroscopy in the optical/UV.

In total, there are six science instruments on board the satellite (including the OM) which can be operated simultaneously. One of the X-ray telescopes focuses photons directly on to an EPIC pn CCD imaging camera (Strüder et al. 2001). The other two telescopes have grating arrays which diffract approximately half of the incoming radiation onto their secondary foci, where are placed two reflection grating spectrometers (RGS; den

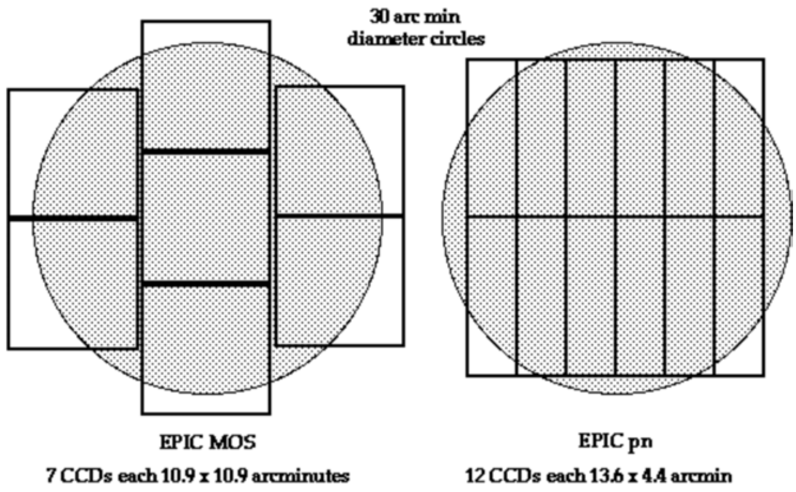

Figure B.1: Field-of-view and schematic layout of the EPIC MOS and pn cameras (from the XMM-Newton Users' Handbook).

Herder et al. 2001) intended for high resolution (resolving power $E/\Delta E \sim 100-800$) X-ray spectroscopy in the 0.33 – 2.5 keV range. The undeflected photons are focused on to two EPIC MOS imaging cameras (Turner et al. 2001). A basic description of the EPIC instruments is given below; more detailed information about the mission and its instruments can be found in the XMM-Newton Science Operations Centre (SOC) webpages[1,2,3].

EPIC instruments All three EPIC cameras have an identical forward section which contains a filter wheel, door, calibration source, radiation shielding, the interface to the spacecraft focal plane bulkhead, and the internal bulkhead that forms part of the camera vacuum enclosure. The rear part of each camera contains the CCDs and the cooling system and is different in construction for the MOS and pn cameras. A description of the stand-off section, which is identical for the two types of EPIC detectors, can be found in Turner et al. (2001).

The cameras acquire data nominally in the 0.1 – 15 keV energy range with a field-of-view (FoV) of $\sim 30'$ diameter (Fig. B.1). Each MOS CCD array consists of 7 identical $10.9' \times 10.9'$ front-illuminated (FI) chips. The central CCD is at the focal point on the optical axis of the telescope while the outer six are stepped towards the mirror to follow the focal plane curvature, and improve the focus for off-axis sources. The quantum efficiency is in range 0.2 – 10 keV, limiting the energy passband at its high energy end. As it is typical for FI CCDs, the low-energy response is poor below ~ 700 eV, due to the absorption in the electrode structure. The two MOS cameras are rotated by 90° with respect to each other. The pn camera consists of a single silicon array of 12 $13.6' \times 4.4'$ integrated devices which

[1] http://xmm.esac.esa.int

[2] http://xmm.esac.esa.int/external/xmm_user_support/documentation/uhb/index.html (XMM-Newton Users' Handbook)

[3] http://xmm.esac.esa.int/external/xmm_user_support/documentation/technical

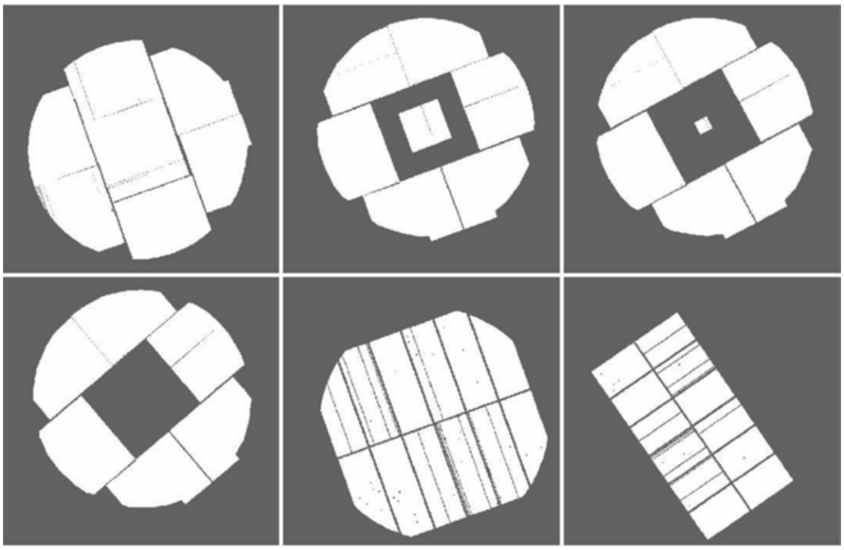

Figure B.2: Typical footprints of the different EPIC observing modes. *Top:* MOS full-window mode; MOS partial window W3 or W5 mode; MOS partial window W2 or W4 mode. *Bottom:* MOS fast uncompressed, fast compressed, or RFS mode; pn full-window mode; pn large-window mode (from Watson et al. 2009).

are operated in parallel. X-rays hit the detector from the rear side (back-illuminated, or BI, CCDs). Each CCD line is terminated by a readout amplifier. In contrast to the MOS detectors, the pn camera can detect photons with high efficiency up to 15 keV, due to its fully depleted layer of silicon.

The EPIC cameras can be used in a variety of different modes, with different time resolutions and saturation levels. Data acquisition can be carried out in *full-frame* and *extended full-frame* modes, where the full detector area is exposed, while only half of the detector is read out in the EPIC pn *large-window* mode. A single CCD is used for *small-window*, *timing* and *burst* modes. In the case of MOS, the outer ring of the CCDs always remain in standard imaging mode while the central CCD can be operated separately: in *partial-window* mode only part of the central CCD is read out, and in *fast* uncompressed and compressed modes the central CCD is in timing mode and produces no imaging data (see Fig. B.2). The cameras can be used with the filters *thick*, *medium* and *thin*, depending on the degree of optical blocking desired. These filters are needed in order to avoid contamination from IR, optical and UV photons in the EPIC detectors, which are also sensitive to these wavelengths.

The spectral and angular resolutions are moderate, with $E/\Delta E \sim 20-50$ and an on-axis FWHM of $\sim 6''$. The on-axis effective area for the pn camera is approximately $1400\,\mathrm{cm}^2$ at $1.5\,\mathrm{keV}$ and $600\,\mathrm{cm}^2$ at $8\,\mathrm{keV}$ while corresponding MOS effective areas are about $550\,\mathrm{cm}^2$ and $100\,\mathrm{cm}^2$, respectively. The combined effective area of the EPIC cameras can be seen in Fig. B.3, assuming that the cameras operate simultaneously using the same optical blocking filters. The energy resolution for the pn camera is $120\,\mathrm{eV}$ at $1.5\,\mathrm{keV}$ and $160\,\mathrm{eV}$ at

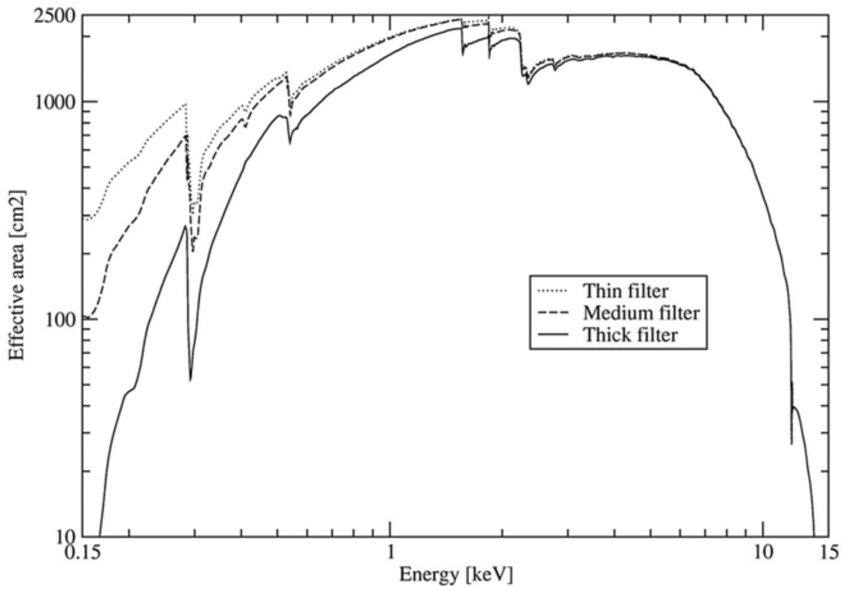

Figure B.3: Combined effective area of the EPIC cameras for the optical blocking filters *thin*, *medium* and *thick* (from the XMM-Newton Users' Handbook).

6 keV (FWHM), while for the MOS camera it is slightly better, with 90 eV and 135 eV, respectively. High time resolution (70 ms against 2.6 s for pn and MOS, respectively, in full-frame mode) is a consequence of the parallel readout of the pn camera.

The cameras were developed by the EPIC Consortium led by the Principal Investigator, M. J. L. Turner. The consortium comprises the following institutes: University of Leicester, University of Birmingham, CEA/Saclay, IAAP Tuebingen and MPE Garching, among others.

B.1.2 Chandra

The Chandra X-Ray Observatory (CXO; Weisskopf et al. 2000; 2002) combines an efficient high-resolution X-ray telescope with a suite of advanced imaging and spectroscopic instruments. The observatory was successfully launched on July 1999 and placed in a high elliptical orbit. The orbit allows for reasonably high observing efficiency, as the satellite spends most of the time well above the radiation belts and long continuous observations (~ 160 ks) are made possible by the orbital period of ~ 60 h. Chandra was designed to provide unprecedented advances over previous X-ray astronomy missions regarding spatial and spectral resolution. The High Resolution Mirror Assembly (HRMA; Schwartz et al. 2000) produces images with a half-power diameter of the point spread function (PSF) of $< 0.5''$. Both grating systems – the Low Energy Transmission Grating (LETG; Brinkman et al. 2000) and the High Energy Transmission Grating (HETG; Canizares et al. 2005) – offer resolving powers well in excess of 500 over much of their bandwidth which, together, cover the range from $\lesssim 0.1$ to 10 keV.

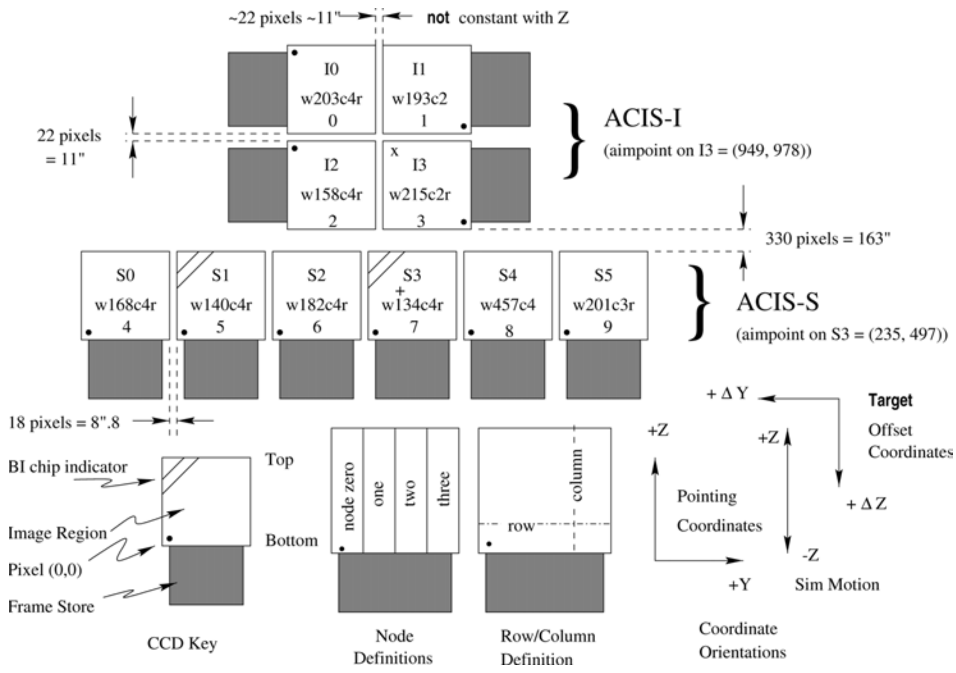

Figure B.4: Schematic layout of the ACIS detectors (from the Chandra Proposers' Guide).

The HRMA consists of a nested set of four Wolter type I grazing-incidence X-ray mirror pairs, with a focal length of 10 m. The Science Instrument Module (SIM) houses two focal instruments: the Advanced CCD Imaging Spectrometer (ACIS; see below) and the High Resolution Camera (HRC; Murray et al. 2000).

In spite of its superior aimpoint spatial resolution, the PSF broadens considerably for off-axis sources. This is primarily due to the separation between the detector plane and the effective focal plane, which is a strong function of both energy and off-axis angle. The degradation in image quality with off-axis angle in Chandra is more severe than in XMM-Newton, which (together with a smaller FOV) limits its applicability in producing serendipituous science (Chapter 3). The PSF distortion also impacts the proper motion studies carried out during the thesis (Chapter 2).

The HRC is comprised of two microchannel plate imaging detectors: HRC-I, designed for wide-field imaging, and HRC-S, which serves as a readout for the LETG. The HRC-I is placed at right angles to the optical axis, tangent to the focal surface. The HRC-S is made of three flat elements, the outer two of which are tilted to approximate the LETG Rowland circle. The HRC detectors have the highest spatial resolution on Chandra, matching the HRMA PSF most closely. Under certain circumstances, the HRC-S detector also offers the fastest time resolution (16 μs).

The HETG is intended for high resolution spectroscopy, achieving resolving power up to 1000 in energy range 0.4 – 10 keV. The LETG provides the highest spectral resolution on Chandra at soft (0.08 – 0.2 keV) energies. For a full description of the science instruments

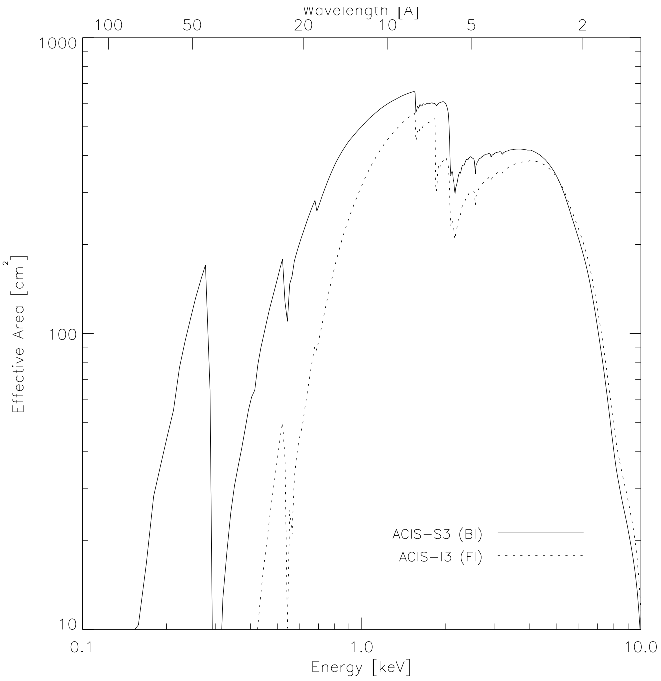

Figure B.5: Effective area of the BI and FI ACIS detectors (from the Chandra Proposers' Guide).

on board Chandra, we refer to the Chandra Proposers' Observatory Guide[4]. Below, the ACIS detectors are described in more detail.

ACIS detectors ACIS offers the capability to simultaneously acquire high-resolution images and moderate resolution spectra (Garmire et al. 2003). It contains 10 planar, 1024×1024 pixel CCDs; four arranged in a 2×2 array (ACIS-I), used for imaging, and six arranged in a $1{\times}6$ array (ACIS-S), used either for imaging or as a grating readout (Fig. B.4). The CCDs are flat but the chips in each array are positioned (tilted) to approximate the relevant focal surface – that of the HRMA, for ACIS-I, and that of the HETG Rowland circle, for ACIS-S. Two CCDs are back-illuminated (BI) and eight are front-illuminated (FI). The response of the BI devices extends to energies below that accessible to the FI chips. The chip average energy resolution of the BI devices is better than that of the FI devices. The FoV is $16.9' \times 16.9'$ and $8.3' \times 50.6'$ for ACIS-I and ACIS-S, respectively. The effective area is 50 cm^2 at 500 eV, 600 cm^2 at 1.5 keV and 40 cm^2 at 8 keV for the FI chips while corresponding effective areas are 110 cm^2, 700 cm^2 and 40 cm^2 for the BI chips, at these photon energies (Fig. B.5).

The efficiency of the ACIS instrument has been discovered to be slowly changing with time, most likely as a result of molecular contamination build-up on the optical blocking filter. The BI CCDs response extends to lower energies than the FI CCDs and the energy resolution is mostly independent of position. The low-energy response of the BI CCDs is

[4] http://cxc.harvard.edu/proposer/POG/html/index.html

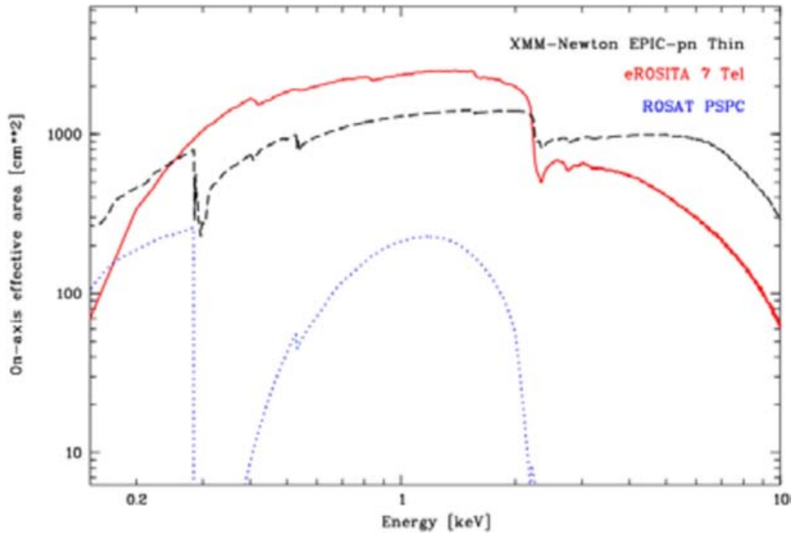

Figure B.6: On-axis effective area of the eROSITA detector (red line) compared with one XMM-Newton telescope (black) and ROSAT PSPC (blue). Extracted from http://www.aip.de/People/ASchwope/papers/eROSITA_SPIE_2006.pdf.

partially compromised by the contaminant build-up. The FI CCD response is more efficient at higher energies but the energy resolution varies with position due to radiation damage caused by protons reflecting through the telescope during radiation-zone passages in the early part of the mission.

The Instrument Principal Investigator for ACIS is Prof. G. Garmire (Pennsylvania State University). ACIS was developed by a collaboration between Penn State, the MIT Kavli Institute for Astrophysics and Space Research and the Jet Propulsion Laboratory, and was built by Lockheed Martin and MIT.

B.1.3 eROSITA

eROSITA (Extended Röntgen Survey with an Imaging Telescope Array[5]) will be one out of three main instruments on the Russian new Spectrum-RG mission, which is expected to be launched in 2012. The other two instruments are the wide-field X-ray monitor Lobster (Leicester University, UK) and the X-ray concentrator ART (IKI, Russia). eROSITA is the successor of the ROSAT mission, the first X-ray imaging telescope to perform an all-sky survey at soft X-ray energies (0.1 – 2.4 keV). While Chandra and XMM-Newton have spectral ranges extending to 10 keV – which is substantially wider range than that of ROSAT – these observatories can only perform pointed observations covering a small portion of the sky. The basic idea behind the mission is to extend the ROSAT All-Sky Survey (Voges et al. 1999) towards higher energies, with unprecedented spectral and angular resolution for an all-sky survey.

[5] http://www.mpe.mpg.de/projects.html#erosita

The camera will operate on board of Spectrum-RG, a medium size satellite that will be put into a 600 km equatorial orbit with a Soyuz-2 rocket. The X-ray optics consists of 7 modules with 54 mirror shells each and a baffle in front of each module. Relative to a single mirror system, this configuration will allow a shorter focal length and smaller shells and therefore reduced instrumental background and pile-up level when observing bright sources. The detector is based on the EPIC pn camera developed for XMM-Newton (Meidinger et al. 2006). Relative to pn, the CCD has been extended by a frame store area allowing a fast shift from the image (data) array. This aims at reducing the number of out-of-time (OOT) events, i.e. the photons that are recorded during read-out. The pixel size has also been reduced relative to pn to 75 μm, in order to be better adjusted for the resolution of the eROSITA telescope. At higher energies, the use of 6 inch silicon wafers with a thickness of 450 μm is expected to improve the detector quantum efficiency. The CCD has 256×256 pixels and a field-of-view of $41.3' \times 41.3'$. The channels are read out in parallel and the integration time is 50 ms. The total collecting area of the detector at 1.5 keV is 2470 cm^2 and the spectral resolution is 130 eV at 6 keV; the total energy range is 0.2 – 12 keV.

The scientific goals of the X-ray mission is to perform, in addition to pointed observations, an all-sky survey which will consist of a continuous scan with one revolution per orbit, an extragalactic survey with variable scan speed and a deep survey in pointing mode. The effective area of eROSITA is about twice that of one of the XMM-Newton telescopes below 2keV, whereas it is three times smaller at higher energies. This is a consequence of the small focal lenght-to-aperture ratio of the eROSITA mirrors. A comparison of the on-axis effective area of eROSITA with XMM-Newton and ROSAT can be seen in Fig. B.6. The angular resolution, $< 20''$ averaged over the FoV, is better than that of ROSAT due to the smaller FoV and the better spatial resolution of the frame store pn CCD relative to the ROSAT PSPC. Furthermore, the duration previewed for the all-sky survey is four years and the exposure time per FoV is 1.3 ks, which will increase the sensitivity to approximately 30 times that reached by ROSAT. It is expected that 3.2×10^6 AGN and 85×10^3 clusters of galaxies in the extragalactic sky can be detected.

eROSITA is developed by the Max-Planck-Institute for Extraterrestrial Physics (MPE) in Munich, Germany.

B.1.4 Comparison between some X-ray observatories

A comparison of basic properties of some past and present X-ray missions is provided in Table B.1.

B.2 Optical telescopes

B.2.1 ESO-VLT

The European Southern Observatory Very Large Telescope (ESO-VLT) consists of an array of four 8.2 m telescopes operating at the Paranal Observatory on Cerro Paranal, Atacama desert in Chile, at an altitude of 2,635 m. The four telescopes can work independently or in

Table B.1: Comparison of basic properties of some selected (past and present) X-ray missions.

Observatory	Detector	Ener. Range (keV)	Eff. Area (cm^2)	Ang. Resol. (arcsec)	Ener. Resol. (eV)	Frame Time (s)	FoV (arcmin)	Target Visib. (hour)
XMM-Newton	EPIC pn	0.13 – 15	1227	6	55	73.4×10^{-3}	30	36.7
	EPIC MOS	0.3 – 10	922	6	55	2.6	30	
	RGS	0.4 – 2.5	185	–	2.9	4.8/9.6	–	
Chandra	ACIS BI	0.1 – 10	615	1	100	3.2	17	44.4
	ACIS FI	0.4 – 10	385	1	56	3.2	17	
	HRC	0.08 – 10	215	< 0.5	–	16×10^{-6}	31	
	HETG	0.6 – 10	10	–	1.0	–	–	
	LETG	0.1 – 6	55	–	5.4	–	–	
Suzaku	XRS	0.3 – 12	100	limited	6.5	–	17	0.72
	XIS	0.2 – 12	1600	< 90	50	8	17.8	
ROSAT	PSPC	0.1 – 2.4	210	15	500	130×10^{-6}	114	1.3
	HRI	0.1 – 2.4	80	2	–	16×10^{-6}	38	

Note: Effective area and energy resolution at 1 keV; angular resolution in FWHM. Time resolution is nominal full-frame mode. Orbital visibility outside the particle-radiation dominated zone.

combined mode. In this latter mode the VLT provides the total light-collecting power of a 16 m single telescope. The telescopes may also be used in interferometric mode providing high-resolution imaging. The useful wavelength range extends from the near-UV up to 25 μm in the mid-IR. It can operate in either Cassegrain, Nasmyth or Coudé focus, with a large set of different science instruments, performing high-resolution and multi-object spectroscopy and high-resolution imaging. Below are described the basic properties of the FORS (FOcal Reducer low/dispersion Spectrograph, Appenzeller et al. 1998) detectors, used for follow-up optical investigations in this work. Detailed information about the telescopes and science instruments can be found in the ESO-VLT webpages[6].

FORS The FORS instruments have been developed under ESO contract by the Landessternwarte Heidelberg, the University Observatory of Göttingen, and the University Observatory of Munich. FORS is the visual and near-UV low-dispersion spectrograph of the ESO-VLT, designed to operate in wavelength range 330 – 1100 nm. Two versions of FORS have been built, FORS1 and FORS2. The instrument provides an image scale of $0.25''$ pixel^{-1} (or $0.125''$ pixel^{-1} with the high resolution collimator) in the standard readout mode (2×2 binning). Two spatial resolutions and hence field sizes can be selected by exchange of the collimators. The resulting field-of-view is $6.8' \times 6.8'$ with the standard resolution collimator (SR) and $4.2' \times 4.2'$ with the high resolution collimator (HR). FORS1 is mounted on Unit Telescope UT2 (Kueyen) and is equipped with a mosaic of two 2 k $\times$ 4 k E2V CCDs, with a pixel size of 15 μm. These CCDs provide much higher response in the blue and UV wavelength range below 600 nm, but suffers from severe fringing above 650 nm. FORS2 is installed on UT1 (Antu) and is optimized for the red band with a very low level of fringes, thanks to a mosaic of two 2 k $\times$ 4 k MIT CCDs (with 15 μm pixels). The response in the UV (below 400 nm) is significantly decreased. The detectors are flat; the gap between the two chips is about 480 μm. FORS1 has a polarimetric capability while FORS2 allows multi-object spectroscopy with exchangable masks and has a high time resolution mode. More information can be found in the FORS manuals[7].

B.2.2 SOAR

The Southern Astrophysical Research Telescope (SOAR; Krabbendam et al. 2004) is a 4.1 m aperture optical and near-IR telescope located on Cerro Pachón, Chile, at 2,738 m elevation. It is operated by a consortium including the countries of Brazil and Chile, Michigan State University, the Cerro Tololo Inter-American Observatory (CTIO) and the University of North Carolina at Chapel Hill. The first-light instruments were designed to allow optical and near-IR imaging and mid to low-resolution spectroscopy (Cecil 2000). In the following, the main features of the SOAR Optical Imager (SOI; Schwarz et al. 2004), used in this work, are described.

SOI The SOI consists of a mini-mosaic of two E2V 2 k $\times$ 4 k CCDs located at its focal plane, a focal reducer camera, two filter cartridges, and a linear Atmospheric Dispersion

[6] http://www.eso.org/sci/facilities/lpo
[7] http://www.eso.org/sci/facilities/paranal/instruments/fors/doc

Table B.2: Comparison between versions of the XMM-Newton serendipitous catalogue of X-ray sources.

Version	Release Date	N_{obs}	N_{det}	Coverage (deg^2)	Mean Flux ($\mathrm{erg\,s^{-1}\,cm^{-2}}$)	Positional Accur. (C.L.)
1XMM	2003-04-07	585	28,279	50	3.0×10^{-14}	$< 2''$ (68%)
2XMMp	2006-07-24	2400	123,170	285	2.4×10^{-14}	$< 2''$ (68%)
2XMM	2007-08-22	3491	191,870	360	2.5×10^{-14}	$< 5''$ (99%)
2XMMi	2008-08-20	4117	221,012	420	2.5×10^{-14}	$< 5''$ (99%)

Note: N_{obs} and N_{det} stand for number of observations used in the compilation of the catalogue and number of unique detected sources, respectively. The sky coverage takes overlaps into account. Flux is measured in the total EPIC energy band (0.2 – 12 keV).

Corrector (ADC). The two CCDs in SOI are mounted with their long sides parallel and spaced 102 pixels apart, resulting in a $7.8''$ gap between the individual CCD images. The instrument was designed to produce precision photometry and to fully exploit the expected high image quality of the SOAR telescope over a $5.5' \times 5.5'$ field-of-view (pixel scale $0.077''$ pixel^{-1}), with high throughput down to the atmospheric cut-off, and close reproduction of photometric pass-bands throughout 310 – 1050 nm.

B.3 Data bases

B.3.1 The 2XMMp catalogue

Catalogue description The 2XMMp catalogue is the pre-release of the second catalogue of serendipitous X-ray sources from the ESA's XMM-Newton Observatory, compiled by the Survey Science Centre (SSC[8]) and released on 2006 July 24. It consists essentially of a subset of the full 2XMM catalogue (which was released one year later) and contains source detections drawn from 2400 EPIC observations carried out between 2000 February 4 and 2006 April 20. The data sets that originated the catalogue were all made public by at most 2006 May 31; however, not all public observations available by the time of its compilation were considered[9]. The included observations were selected only on the basis of their public availability and suitability for serendipitous science; therefore, they do not consist of a set homogeneous data. The 2XMMp catalogue surpass by a factor 4 to 6 its predecessor, 1XMM, in absolute number of observations, unique detected sources and sky coverage. It has been exceeded by the later versions of the second serendipitous catalogue, 2XMM and 2XMMi (see Table B.2). All versions of the XMM-Newton catalogue can be accessed from the following webpage: `http://xmmssc-www.star.le.ac.uk/Catalogue`.

[8]`http://xmmssc-www.star.le.ac.uk`

[9]Observations that exhibited deficiencies in the automatic processing and thus required visual screening were left out of the catalogue compilation. These were included later in the next releases of the 2XMM catalogue.

Table B.3: Energy bands used in the processing of the XMM-Newton catalogue.

Band ID	Energy Band (keV)	Band ID	Energy Band (keV)	Band ID	Energy Band (keV)
1	0.2 – 0.5	2	0.5 – 1.0	3	1.0 – 2.0
4	2.0 – 4.5	5	4.5 – 12.0	Total	0.2 – 12.0

The total area of the fields is $\sim 400\,\mathrm{deg}^2$; however, taking account of the substantial overlaps between observations, the net sky coverage is $\sim 285\,\mathrm{deg}^2$. The catalogue contains 153,105 X-ray source detections which relate to 123,170 unique X-ray sources. The median flux (in the total energy band 0.2 – 12 keV) of the catalogue detections is $\sim 2.4 \times 10^{-14}\,\mathrm{erg\,cm^{-2}\,s^{-1}}$; 20% of the sources have fluxes below $1 \times 10^{-14}\,\mathrm{erg\,cm^{-2}\,s^{-1}}$. The positional accuracy is generally $< 2''$ (68% confidence radius). The flux values from the three EPIC cameras are overall in agreement to $\sim 2\%$, for on-axis sources, and $\sim 6\%$, for off-axis ones. In the following the main aspects of the catalogue pipeline compilation are briefly described. A full description can be found in the catalogue User Guide[10] and webpage[11]. We also refer to Watson et al. (2009) for a detailed account of the data processing and creation steps of the 2XMM catalogue.

Pipeline processing The Observation Data Files (ODF) – i.e. a collection of raw data files created from the satellite telemetry – are processed in order to create calibrated science event lists that are subsequently filtered for time intervals of low background activity. This is done using a threshold optimised for point source detection. Then the "useful" scientific exposures within an observation are selected on the basis of their exposure times, instrument modes etc. X-ray images and exposure maps in several energy bands (See Table B.3) are next generated from the calibrated files; these are used for source detection and subsequent source parametrisation. The resulting source lists are then cross-correlated with a variety of archival catalogues, images databases and other archival resources. Binned data products, as spectra and light curves, are automatically generated for sources with a sufficient number of detected photons (EPIC counts greater than 500). The final step is the application of automatic and visual screening procedures to check for any problems in the data products. A schematic view of the processing flow can be visualized in Fig. B.7.

[10] http://xmmssc-www.star.le.ac.uk/Catalogue/2XMMp/UserGuide_2xmmp.html
[11] http://xmmssc-www.star.le.ac.uk/Catalogue/xcat_public_2XMMp.html

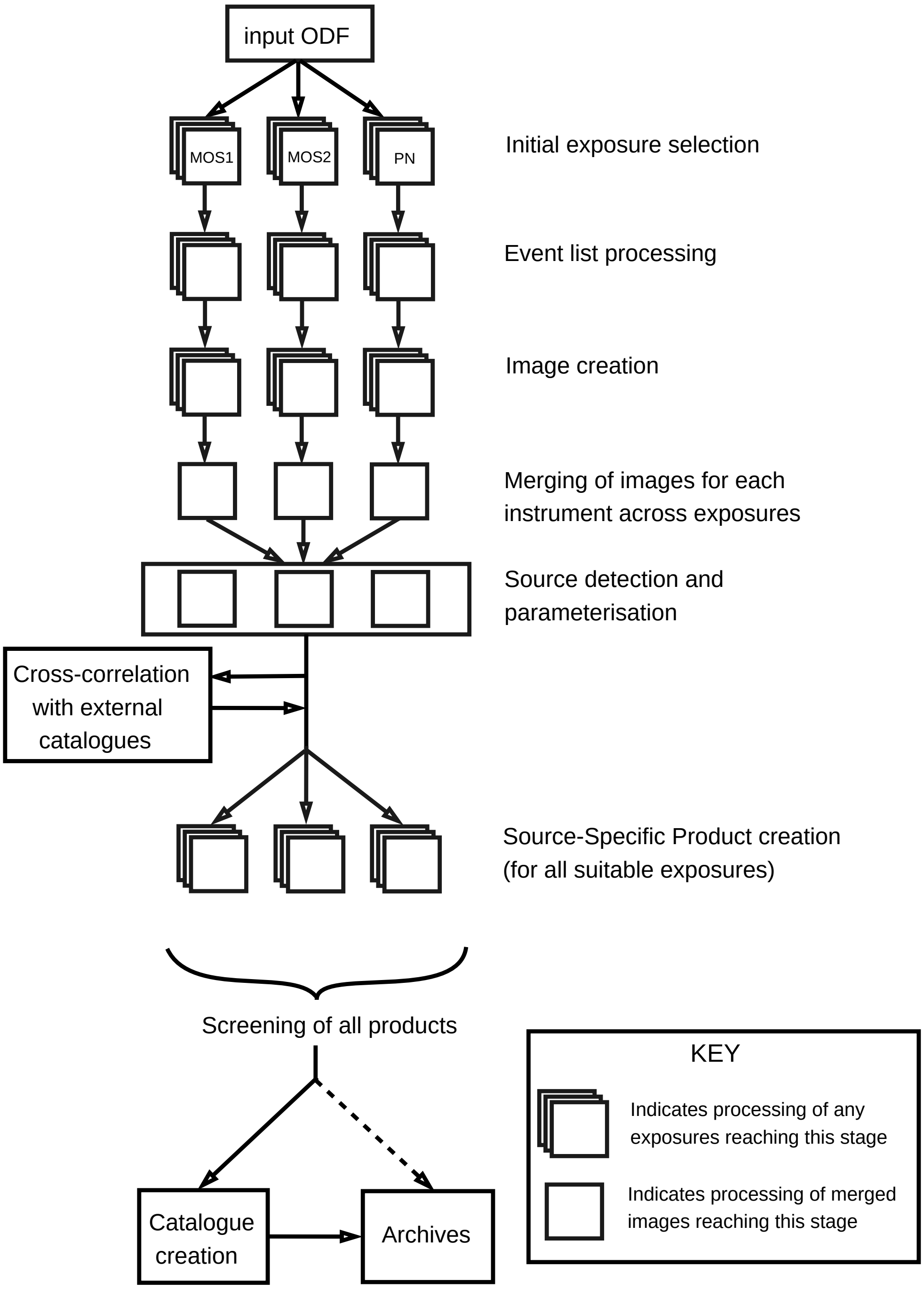

Figure B.7: Processing flow of the 2XMMp catalogue pipeline (from Watson et al. 2009).

APPENDIX C

Additional figures and tables

Contents

Chapter 2

We show in Figs. C.1 to C.4 and C.5 to C.6 the optical finding charts centered on the positions of the background X-ray sources that were used as reference for the ACIS-I and ACIS-S simulations.

Tables C.3 to C.5 list the properties of the X-ray sources detected in the archival Chandra observations of LALA Cetus, PKS 0312-770 and FIELD-142549+353248, used as test runs for the frame matching algorithm in ACIS-I mode. Tables C.6 to C.8 list the ones detected in the test fields in ACIS-S configuration: 3C 33, 3C 325 and MG J0414+0534. The observations in ACIS-I mode were filtered in the 0.5 – 5 keV energy band and were subjected to detection with wavdetect using a threshold of 10^{-6}. In ACIS-S we used the 0.3 – 10 keV and a threshold of 10^{-5}. Only the central CCD chips were considered (ccd_id = 0 – 3 for ACIS-I and ccd_id = 6 – 7 for ACIS-S). The tables list the sources common to both epochs within 1″; coordinates and net counts refer to the "first epoch" observation (see Table 2.8). The archival Chandra "first epoch" images of the fields of these quasars and AGN, filtered in the energy bands listed above, can be seen in Figs. C.7 to C.9. In Tables C.1 and C.2 are the mean number of common sources and frame errors obtained by matching the repeated Chandra observations.

In Fig. C.10 is shown the 2002 and 2005 images of RX J0806.4-4123 and RX J0420.0-5022 overlayed to the first epoch contours. The positions of both neutron stars in the two epoch Chandra observations are consistent within one Gaussian standard deviation.

Chapter 3

Fig. C.11 shows the optical and X-ray finding charts of the intermediate mass black hole found in the 2XMM data by Farrell et al. (2009).

C.1 Figures

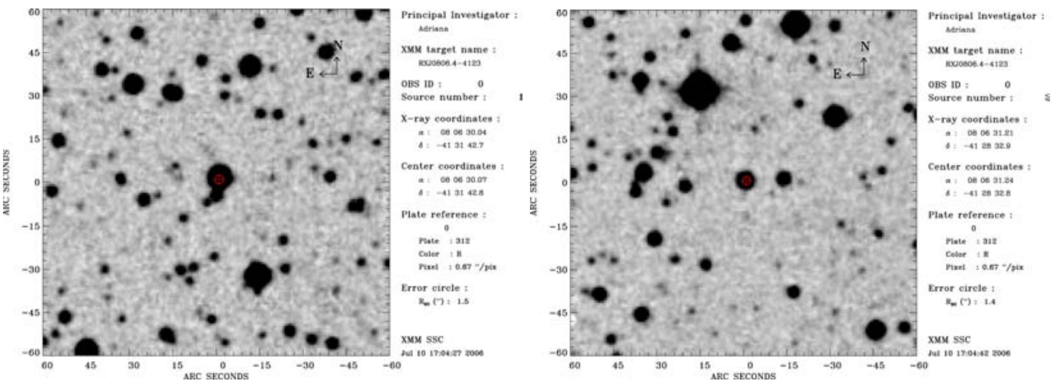

Figure C.1: *Chapter 2*. Optical finding charts of the background reference sources used in the simulations of the ACIS-I field (RX J0806.4-4123).

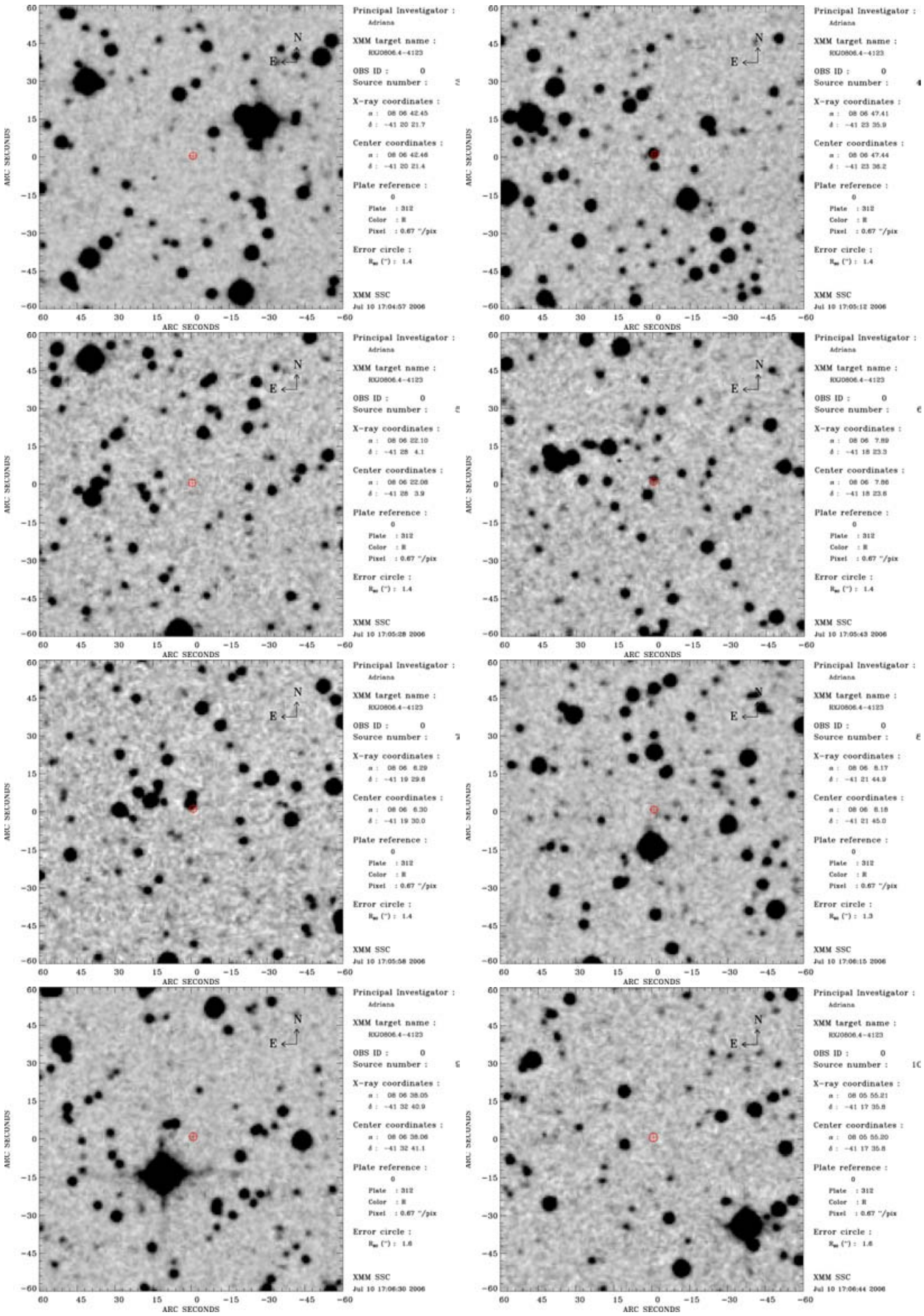

Figure C.2: *Chapter 2*. Optical finding charts of the background reference sources used in the simulations of the ACIS-I field (RX J0806.4-4123; *continued*).

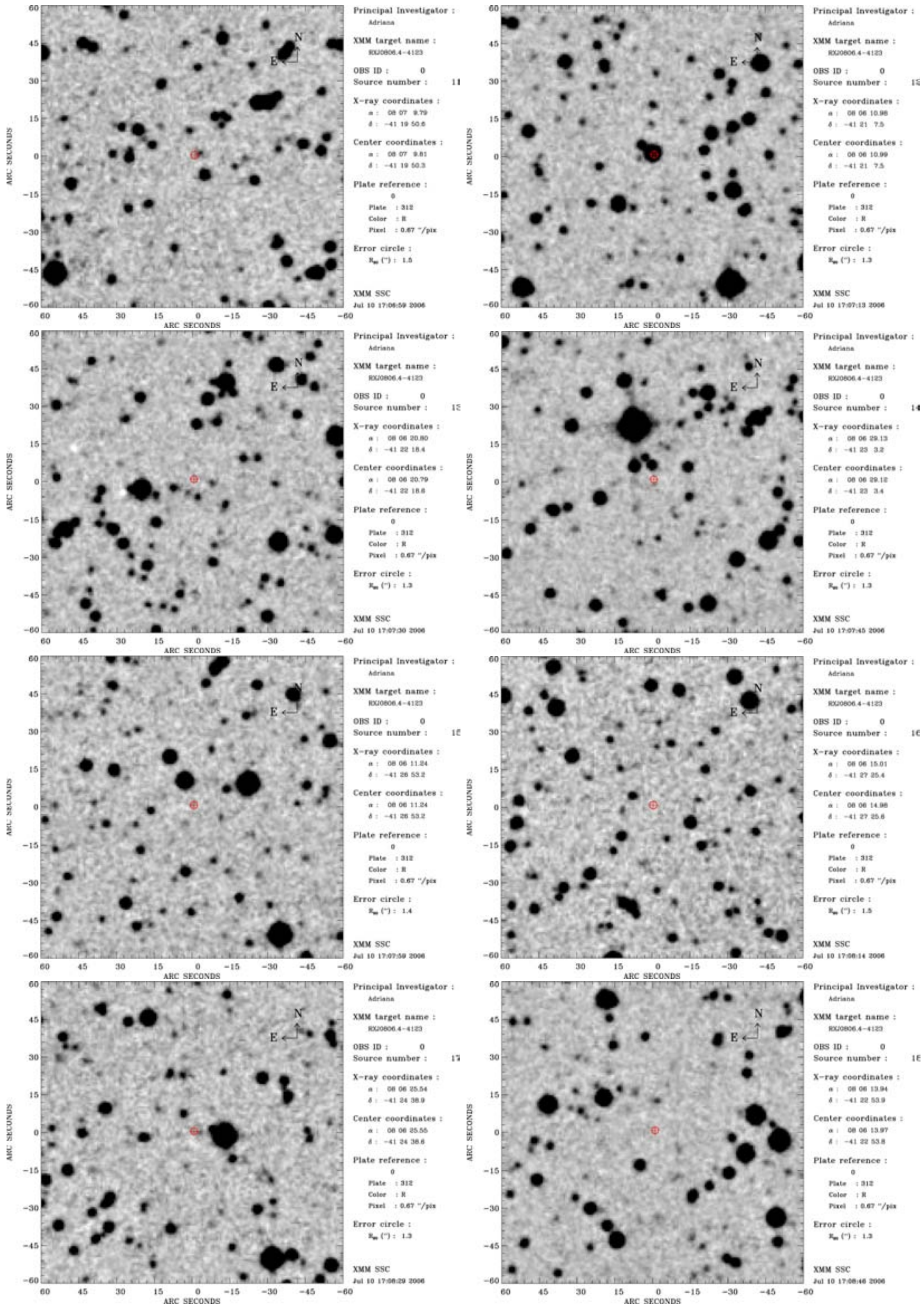

Figure C.3: *Chapter 2*. Optical finding charts of the background reference sources used in the simulations of the ACIS-I field (RX J0806.4-4123; *continued*).

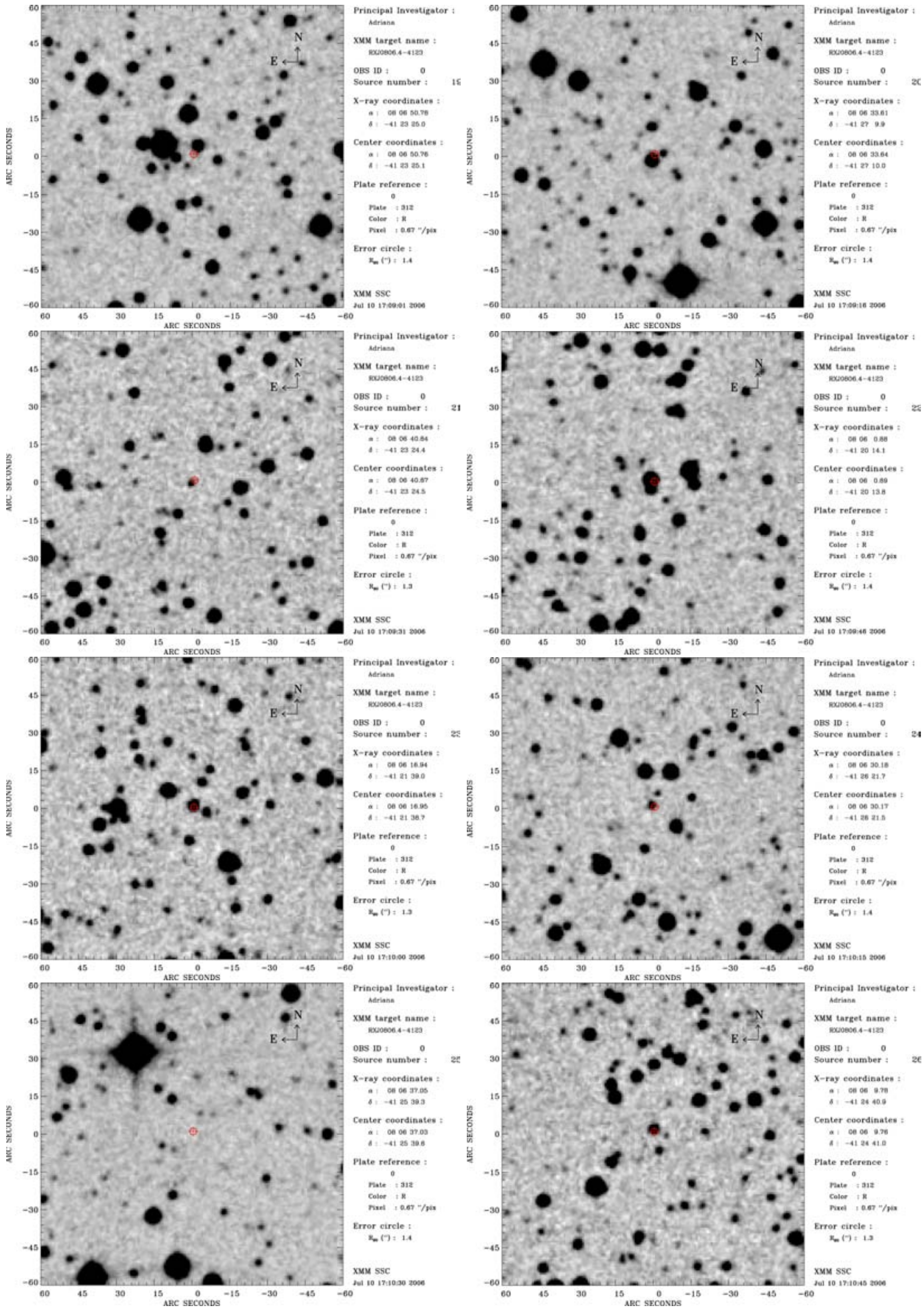

Figure C.4: *Chapter 2*. Optical finding charts of the background reference sources used in the simulations of the ACIS-I field (RX J0806.4-4123; *end*).

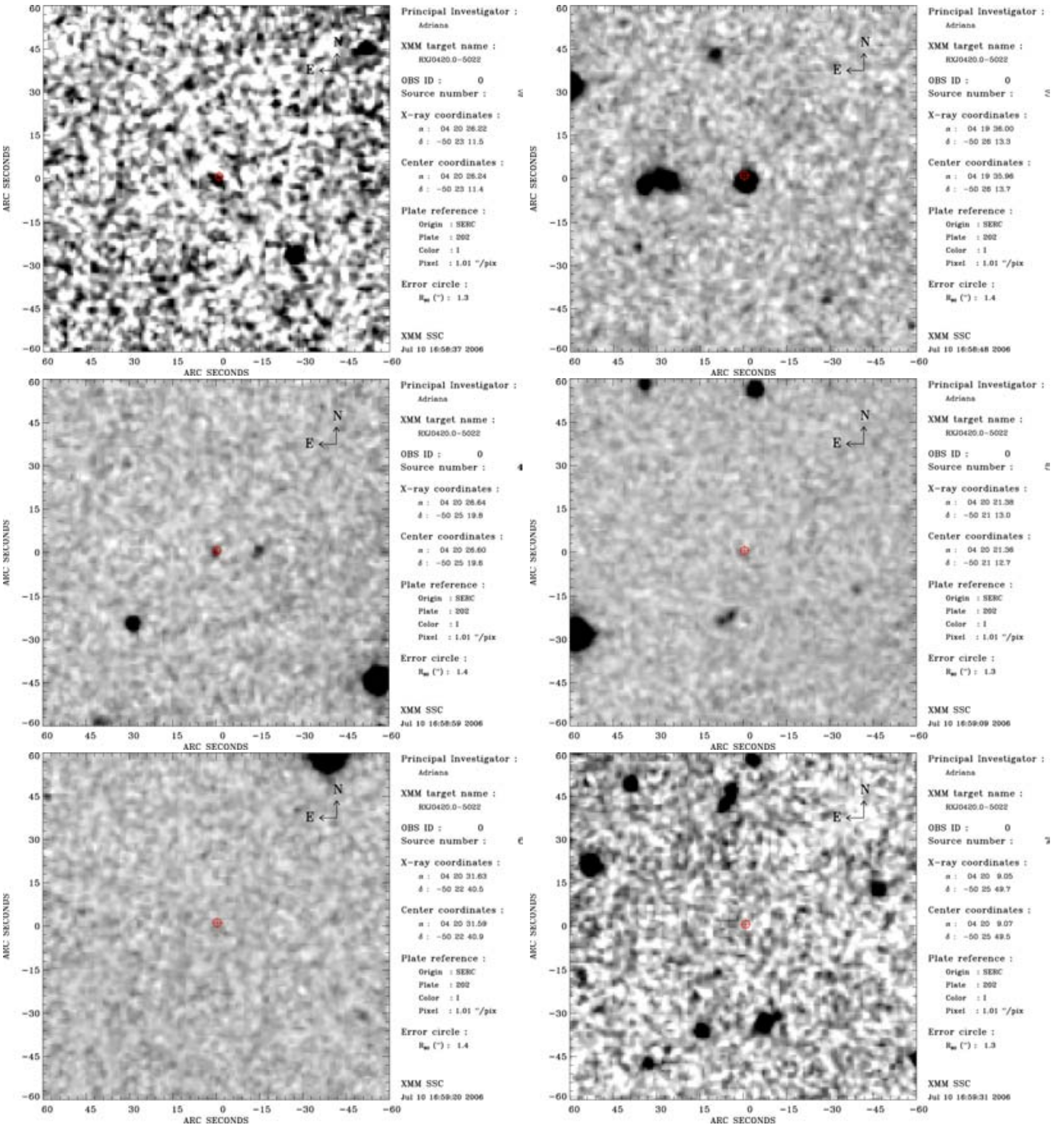

Figure C.5: *Chapter 2*. Optical finding charts of the background reference sources used in the simulations of the ACIS-S field (RX J0420.0-5022).

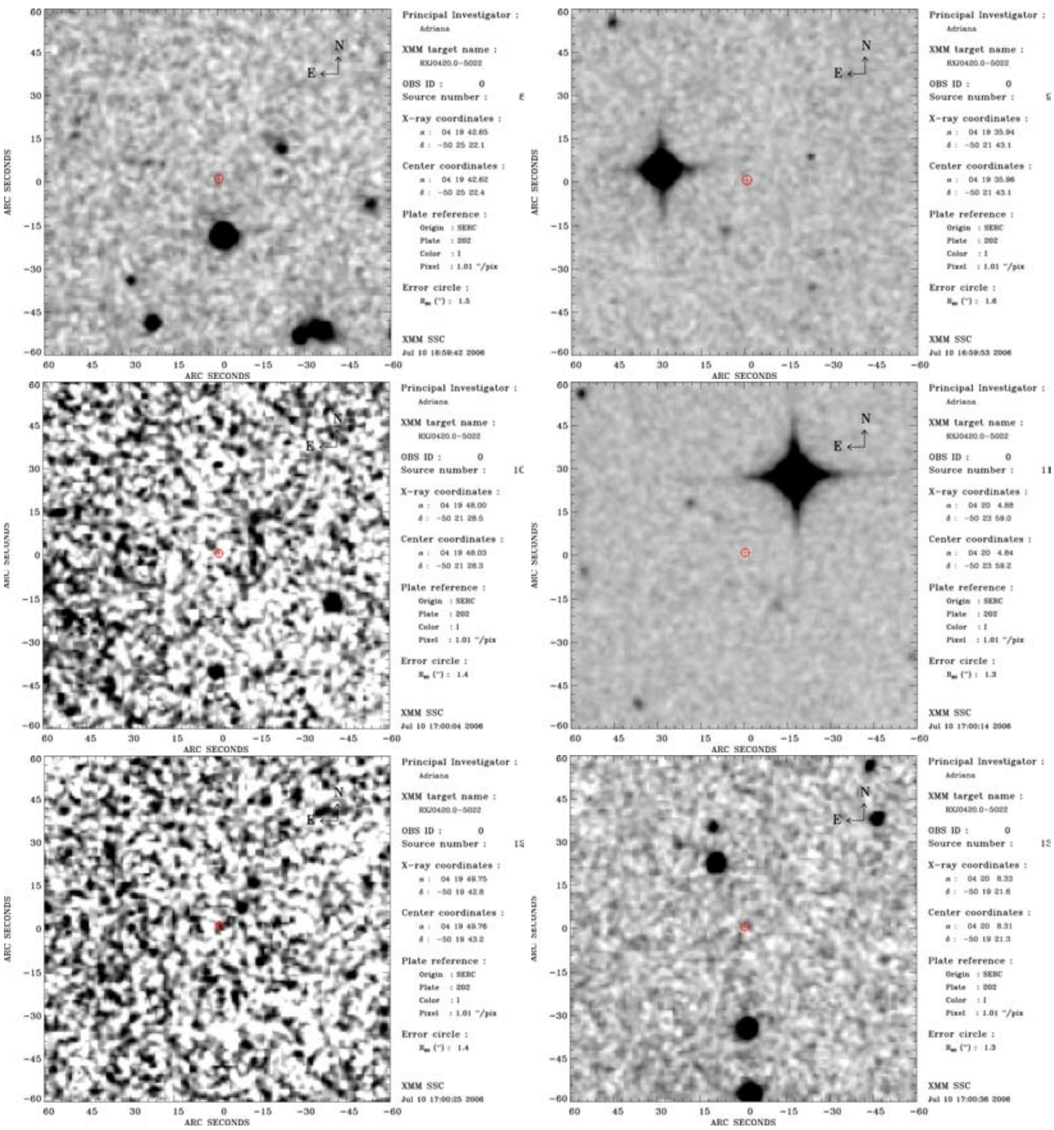

Figure C.6: *Chapter 2*. Optical finding charts of the background reference sources used in the simulations of the ACIS-S field (RX J0420.0-5022; *end*).

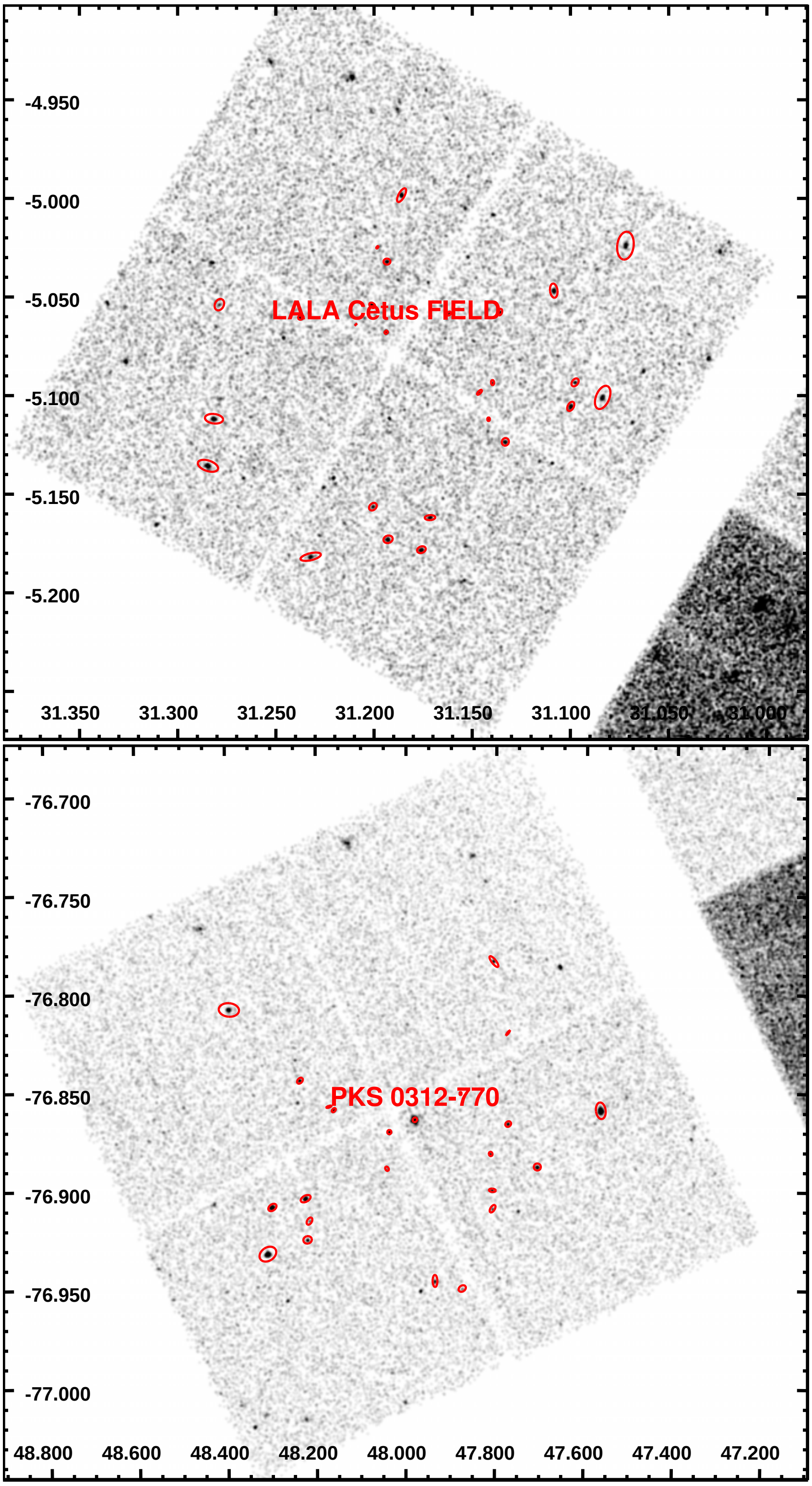

Figure C.7: *Chapter 2*. ACIS images of the fields of LALA Cetus and PKS 0312-770, both in ACIS-I configuration, with the positions of reference sources and central target highlighted by ellipses (corresponding to 3σ of their wavdetect errors). The images were smoothed using a Gaussian filter of 2 pixels in size and binned.

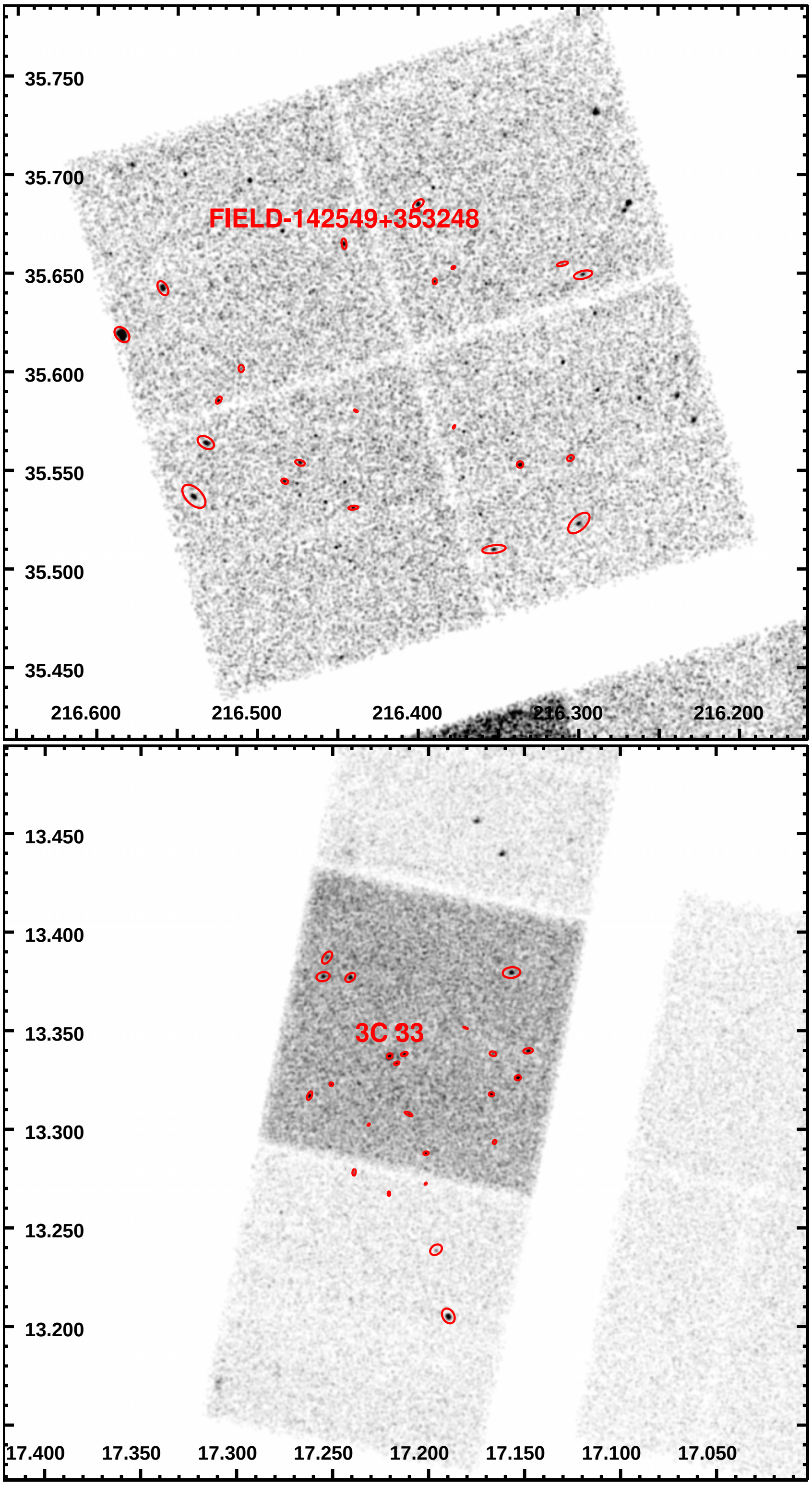

Figure C.8: *Chapter 2*. ACIS images of the fields 142549+353248 (ACIS-I) and 3C 33 (ACIS-S) *(continued).*

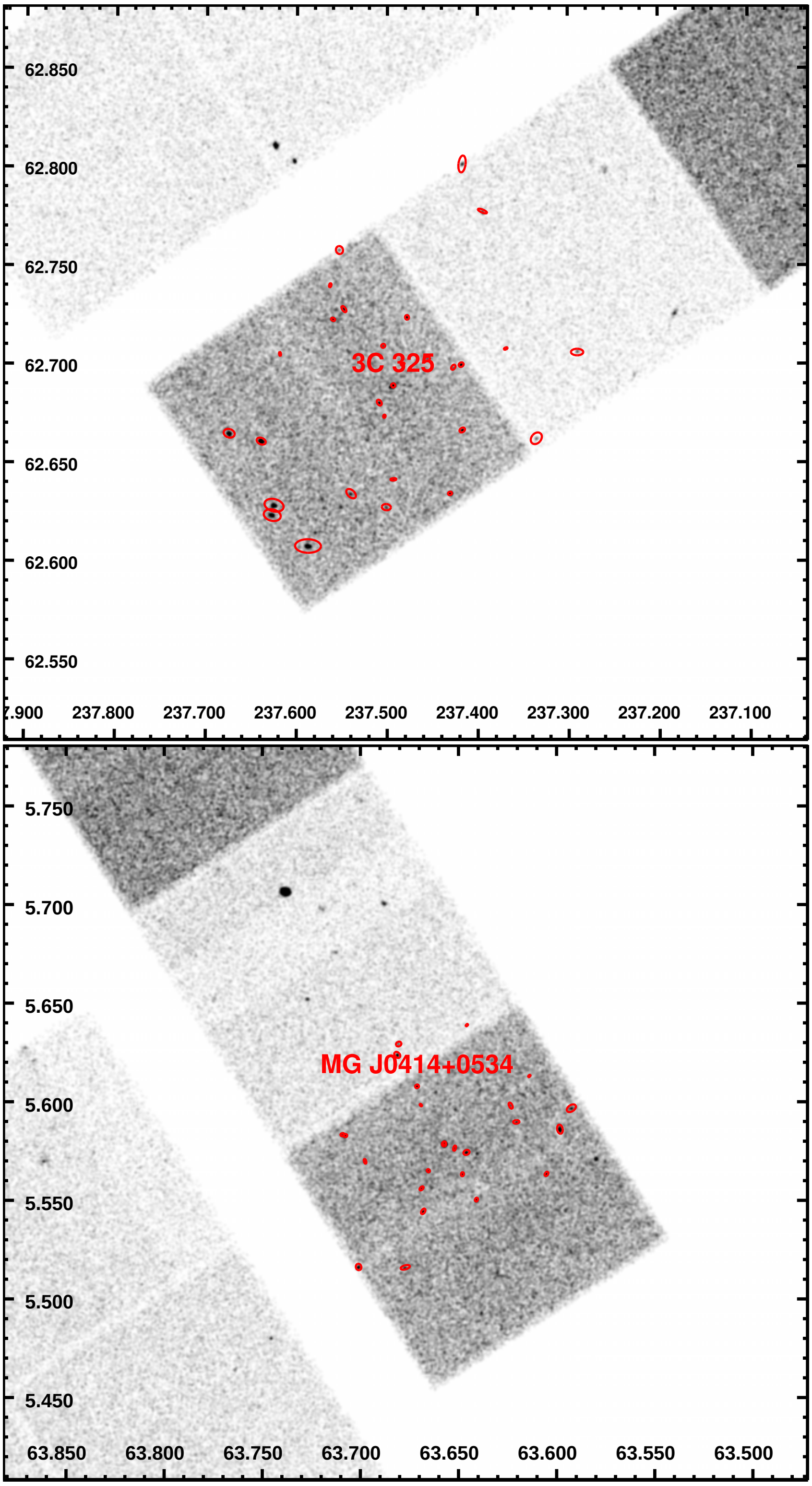

Figure C.9: *Chapter 2*. ACIS images of the fields of 3C 325 and MG J0414+0534 (both in ACIS-S configuration; *end*).

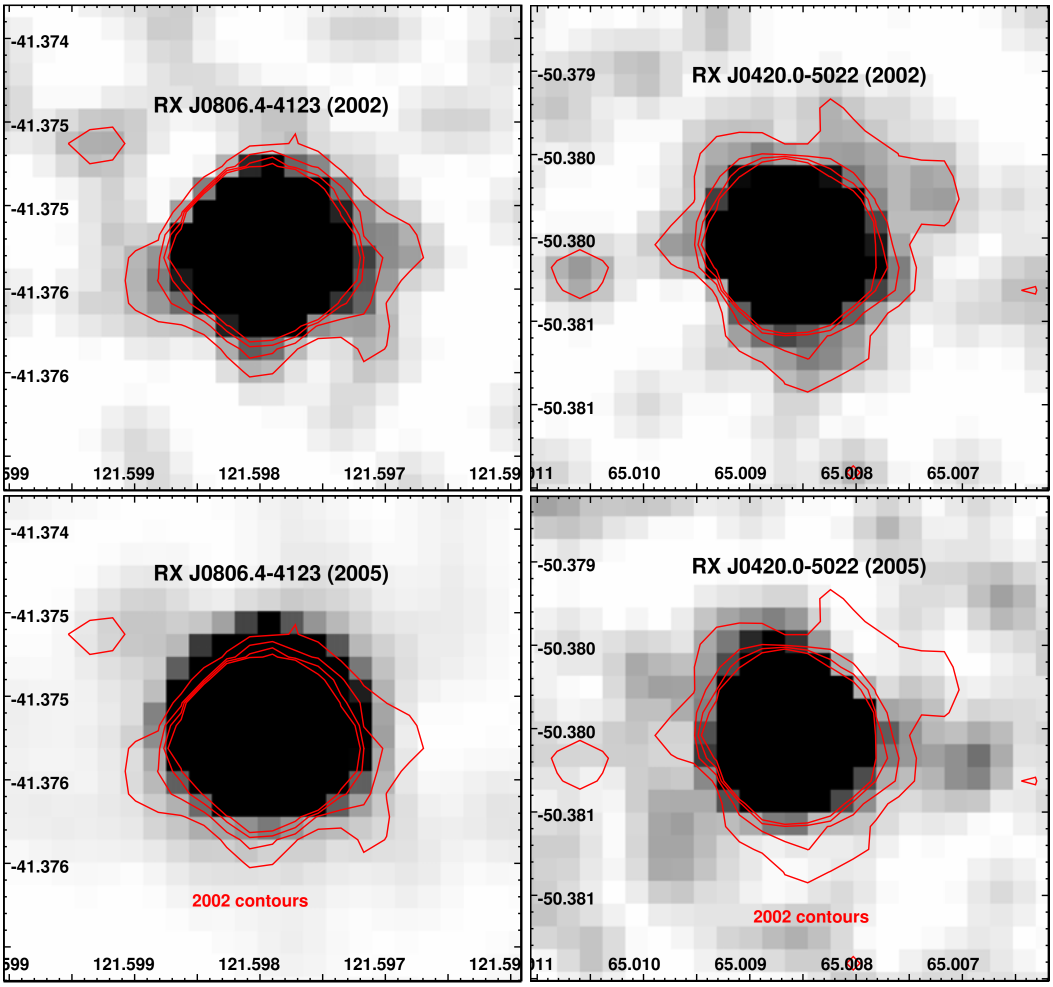

Figure C.10: *Chapter 2*. Upper limits on the displacements of RX J0806.4-4123 and RX J0420.0-5022 in a three-year time span. The positions of the neutron stars in the two epochs are consistent with one Gaussian standard deviation. The first epoch contours are superposed to the 2002 (top) and 2005 (bottom) images of the sources. Images are zoomed by a factor of 32 and were smoothed using a Gaussian filter of size 2 pixels.

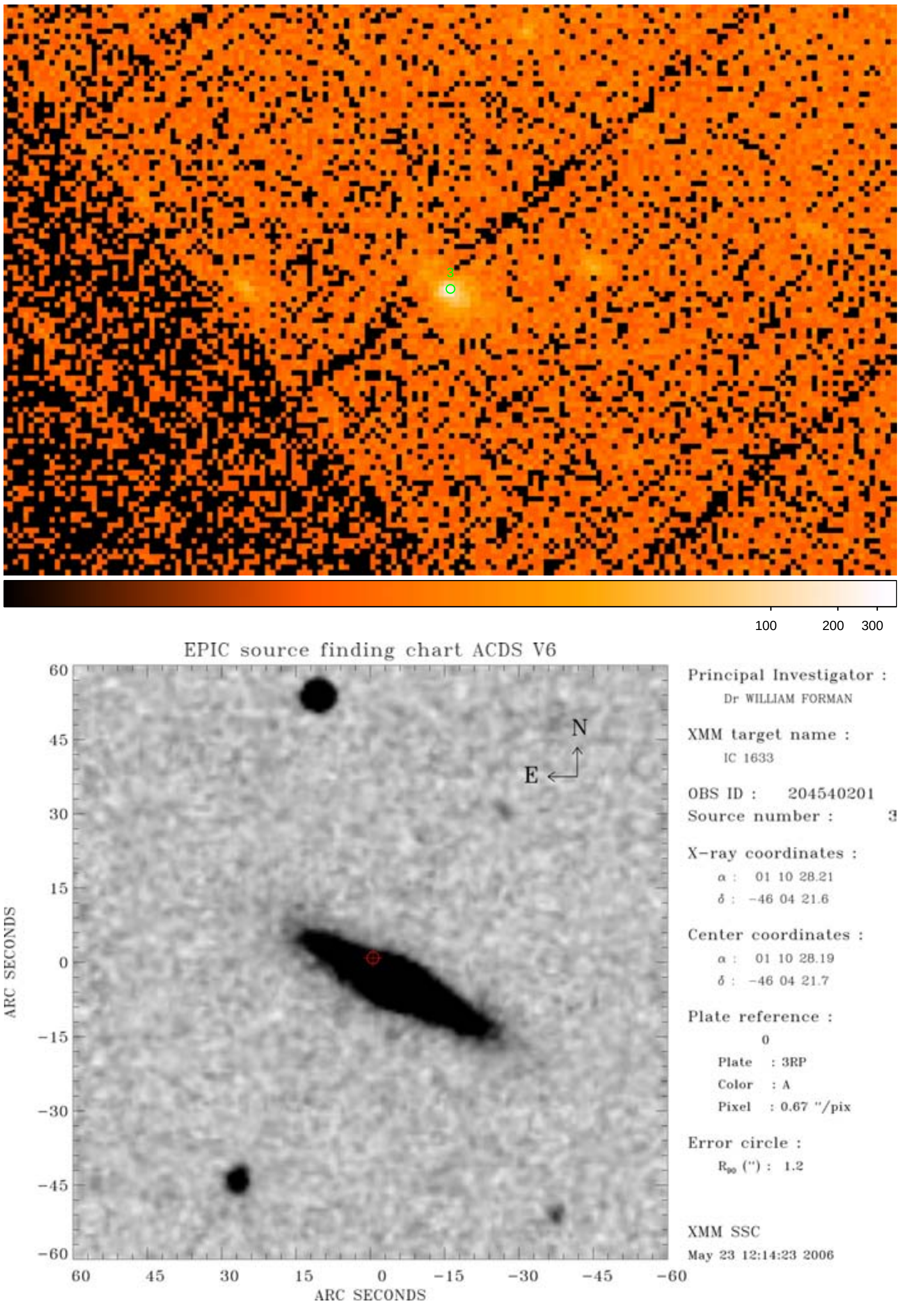

Figure C.11: X-ray and optical finding charts of the intermediate mass black hole discovered in ESO 243-09 (Farrell et al. 2009).

C.2 Tables

Table C.1: *Chapter 2*. Number of reference sources common to both epoch observations, as a function of detection algorithm and randomization state, in the Chandra test fields.

Pixel	ACIS-I		ACIS-S	
Randomization	celldetect	wavdetect	celldetect	wavdetect
applied	24.7 ± 1.5	26.2 ± 1.1	16.4 ± 0.4	19.2 ± 0.4
not applied	26.0 ± 1.6	32.1 ± 2.0	16.0 ± 0.4	21.1 ± 0.6

Note: Results averaged over all energy bands and detection thresholds used for a given ACIS observing configuration. Errors are 1σ.

Table C.2: *Chapter 2*. Frame error as a function of detection algorithm, randomization state and energy band in the Chandra test fields.

Pixel	ACIS-I		ACIS-S	
Randomization	celldetect	wavdetect	celldetect	wavdetect
applied	0.106(26)	0.102(18)	0.109(7)	0.089(12)
not applied	0.099(23)	0.088(20)	0.100(9)	0.091(15)
Energy	ACIS-I		ACIS-S	
Band (keV)	celldetect	wavdetect	celldetect	wavdetect
0.3 – 10	0.100(22)	0.092(18)	0.104(10)	0.089(15)
0.3 – 5	0.097(24)	0.092(18)	0.104(11)	0.089(12)
0.5 – 5	0.098(23)	0.090(20)	0.103(11)	0.088(16)
0.3 – 3	0.106(24)	0.100(21)	0.110(12)	0.090(9)
0.5 – 2	0.11(3)	0.100(22)	0.112(10)	0.096(16)

Note: Results are averaged over all configurations for a given ACIS observing configuration. Errors are 1σ and units are arcsec.

Table C.3: *Chapter 2*. Sources in the Chandra test fields. LALA Cetus (ACIS-I).

α (deg)	δ (deg)	Counts (160 ks)	Off-axis (arcmin)	α (deg)	δ (deg)	Counts (160 ks)	Off-axis (arcmin)
31.193831(12)	−5.067904(19)	61 ± 7	1.35	*Central target*			
31.200903(20)	−5.054261(18)	64 ± 8	2.27	31.2322(4)	−5.18172(5)	19 ± 4	6.32
31.28149(7)	−5.11174(4)	46 ± 7	6.01	31.13586(3)	−5.05766(4)	16 ± 4	3.39
31.28458(8)	−5.13562(5)	41 ± 7	6.66	31.18598(6)	−4.99838(9)	14 ± 4	5.38
31.10847(3)	−5.046803(6)	34 ± 6	5.13	31.20057(6)	−5.15636(6)	9 ± 3	4.21
31.09982(3)	−5.10547(5)	33 ± 6	5.11	31.09764(6)	−5.09332(7)	8 ± 3	5.15
31.13313(3)	−5.12349(4)	30 ± 5	3.69	31.27876(9)	−5.05389(11)	7.3 ± 2.8	6.04
31.08356(7)	−5.10093(11)	27 ± 6	6.03	31.141684(28)	−5.11201(4)	6.9 ± 2.6	2.89
31.19285(4)	−5.17290(4)	27 ± 5	5.11	31.13964(3)	−5.09340(5)	6.8 ± 2.6	2.65
31.17586(4)	−5.17816(4)	26 ± 5	5.42	31.14629(6)	−5.09834(6)	4.7 ± 2.2	2.31
31.19343(3)	−5.03207(3)	24 ± 5	3.41	31.16180(4)	−5.05844(5)	4.7 ± 2.2	2.21
31.23728(3)	−5.060379(26)	24 ± 5	3.61	31.19831(3)	−5.02480(3)	3.9 ± 2.0	3.89
31.07199(8)	−5.02397(14)	23 ± 5	7.70	31.16373(3)	−5.07079(11)	2.9 ± 1.7	1.58
31.17148(6)	−5.161903(29)	23 ± 4	4.48	31.20928(3)	−5.06400(4)	2.9 ± 1.7	2.10

Note: Equatorial coordinates, detected counts and off-axis angles as observed in the first epoch observation; errors are 1σ.

Table C.4: *Chapter 2*. Sources in the Chandra test fields. PKS 0312-770 (ACIS-I).

α (deg)	δ (deg)	Counts (12 ks)	Off-axis (arcmin)	α (deg)	δ (deg)	Counts (12 ks)	Off-axis (arcmin)
47.980048(11)	−76.864189(26)	2336 ± 49	0.34	*Central target*			
47.56524(5)	−76.859253(19)	547 ± 24	5.92	48.23623(18)	−76.84424(4)	15 ± 4	3.36
48.30978(14)	−76.932137(28)	193 ± 15	6.02	47.81069(12)	−76.88144(3)	13 ± 3	2.86
48.29912(9)	−76.908467(19)	140 ± 12	4.99	47.93476(16)	−76.94590(9)	12 ± 3	5.20
48.03717(4)	−76.870411(10)	129 ± 11	0.78	48.17200(21)	−76.857530(21)	8 ± 3	2.35
48.22459(11)	−76.904100(19)	106 ± 10	4.03	47.80600(24)	−76.90920(7)	8 ± 3	3.94
48.3935(4)	−76.80819(5)	40 ± 7	6.22	48.21614(27)	−76.91548(7)	6.6 ± 2.6	4.42
47.70629(15)	−76.88795(3)	33 ± 6	4.32	48.04242(20)	−76.88901(5)	5.7 ± 2.4	1.80
48.16109(9)	−76.859267(21)	31 ± 5	2.20	47.87828(11)	−76.85086(4)	4.8 ± 2.2	1.75
47.77175(16)	−76.86624(3)	20 ± 4	3.12	47.77295(21)	−76.82001(6)	4.8 ± 2.2	3.93
47.80482(25)	−76.78387(7)	17 ± 4	5.31	47.8736(4)	−76.94972(8)	4.6 ± 2.2	5.62
48.22055(26)	−76.92498(5)	15 ± 4	4.90	48.1615(4)	−76.806731(29)	3.8 ± 2.0	3.90
47.80666(21)	−76.899883(24)	15 ± 4	3.53				

Note: Equatorial coordinates, detected counts and off-axis angles as observed in the first epoch observation; errors are 1σ.

Table C.5: *Chapter 2*. Sources in the Chandra test fields. FIELD-142549+353248 (ACIS-I).

α (deg)	δ (deg)	Counts (120 ks)	Off-axis (arcmin)	α (deg)	δ (deg)	Counts (120 ks)	Off-axis (arcmin)
216.389624(4)	+35.64611(5)	10 ± 3	2.90	*Central target*			
216.584817(29)	+35.618994(24)	329 ± 22	8.70	216.44042(10)	+35.53129(3)	10 ± 3	4.41
216.33649(3)	+35.553186(28)	44 ± 6	4.47	216.52436(6)	+35.58584(6)	9 ± 3	5.74
216.55932(7)	+35.64255(4)	34 ± 7	7.81	216.30504(8)	+35.55645(6)	6.2 ± 2.6	5.66
216.39988(6)	+35.68528(5)	33 ± 6	5.13	216.51038(7)	+35.60187(8)	5.6 ± 2.4	4.99
216.446265(29)	+35.66517(5)	33 ± 5	4.33	216.30990(16)	+35.65494(5)	5.5 ± 2.4	5.81
216.53977(12)	+35.53703(11)	30 ± 6	7.45	216.43889(6)	+35.58049(3)	4.8 ± 2.2	1.90
216.53239(12)	+35.56431(7)	19 ± 4	6.43	216.37800(6)	+35.65314(4)	4.7 ± 2.2	3.50
216.35273(19)	+35.51026(5)	15 ± 4	6.02	216.40139(4)	+35.60951(3)	3.9 ± 2.0	0.65
216.29982(17)	+35.52348(13)	15 ± 4	6.99	216.37204(7)	+35.54691(3)	3.8 ± 2.0	3.63
216.47362(9)	+35.55408(4)	12 ± 3	4.22	216.37757(4)	+35.57237(5)	3.8 ± 2.0	2.22
216.29703(18)	+35.64939(7)	10 ± 3	6.17	216.38773(9)	+35.61346(4)	2.9 ± 1.7	1.27
216.48310(7)	+35.54471(4)	10 ± 3	4.94	216.40421(3)	+35.53602(6)	2.9 ± 1.7	3.84

Note: Equatorial coordinates, detected counts and off-axis angles as observed in the first epoch observation; errors are 1σ.

Table C.6: *Chapter 2*. Sources in the Chandra test fields. 3C 33 (ACIS-S).

α (deg)	δ (deg)	Counts (20 ks)	Off-axis (arcmin)	α (deg)	δ (deg)	Counts (20 ks)	Off-axis (arcmin)
17.220265(4)	+13.337278(4)	1315 ± 37	1.78	*Central target*			
17.167255(16)	+13.317895(11)	103 ± 10	2.66	17.25071(4)	+13.32291(4)	16 ± 4	2.42
17.153459(19)	+13.326219(15)	97 ± 10	3.57	17.25293(6)	+13.38719(8)	16 ± 4	5.28
17.18971(4)	+13.20544(5)	85 ± 11	6.32	17.238838(25)	+13.27823(4)	14 ± 3	2.40
17.262016(18)	+13.317161(28)	71 ± 8	2.97	17.19613(9)	+13.23902(8)	10 ± 3	4.27
17.24083(4)	+13.37709(3)	57 ± 7	4.44	17.16644(5)	+13.33840(4)	10 ± 3	3.20
17.215596(20)	+13.351843(22)	51 ± 7	2.60	17.21045(4)	+13.30792(4)	7 ± 3	0.09
17.14811(4)	+13.339882(23)	50 ± 7	4.17	17.16562(4)	+13.29367(5)	5.5 ± 2.4	2.84
17.15679(7)	+13.37957(4)	46 ± 7	5.33	17.22068(3)	+13.26743(5)	4.7 ± 2.2	2.52
17.21266(3)	+13.338265(20)	34 ± 6	1.78	17.18076(6)	+13.35154(3)	4.6 ± 2.2	3.15
17.216635(28)	+13.333554(18)	29 ± 5	1.52	17.20153(3)	+13.27253(3)	3.9 ± 2.0	2.24
17.201332(29)	+13.287956(18)	29 ± 5	1.38	17.202898(21)	+13.34537(6)	3.7 ± 2.0	2.26
17.25502(7)	+13.37751(5)	22 ± 5	4.84	17.23122(4)	+13.30247(4)	2.7 ± 1.7	1.18

Note: Equatorial coordinates, detected counts and off-axis angles as observed in the first epoch observation; errors are 1σ.

Table C.7: *Chapter 2*. Sources in the Chandra test fields. 3C 325 (ACIS-S).

α (deg)	δ (deg)	Counts (30 ks)	Off-axis (arcmin)	α (deg)	δ (deg)	Counts (30 ks)	Off-axis (arcmin)
237.493425(13)	+62.689340(6)	351 ± 19	0.56	*Central target*			
237.63929(3)	+62.661020(11)	409 ± 21	4.88	237.53993(14)	+62.63443(6)	13 ± 4	4.05
237.62491(10)	+62.62849(3)	99 ± 11	5.70	237.55306(11)	+62.75796(6)	13 ± 3	4.23
237.58742(14)	+62.60785(3)	99 ± 11	6.07	237.50105(14)	+62.62760(4)	13 ± 4	4.14
237.67469(8)	+62.664945(29)	80 ± 9	5.69	237.48300(6)	+62.700157(23)	12 ± 3	0.27
237.62690(11)	+62.62349(3)	74 ± 9	5.95	237.49703(8)	+62.68842(5)	12 ± 3	0.67
237.41839(4)	+62.699867(17)	58 ± 7	1.68	237.29009(20)	+62.70614(5)	11 ± 3	5.23
237.56005(5)	+62.722834(17)	48 ± 7	2.75	237.49323(11)	+62.641716(19)	10 ± 3	3.28
237.41723(5)	+62.666717(21)	43 ± 6	2.44	237.45591(10)	+62.70277(4)	9 ± 3	0.75
237.43075(5)	+62.634590(19)	42 ± 6	3.91	237.50457(8)	+62.70942(3)	9 ± 3	1.06
237.47826(4)	+62.723842(20)	41 ± 6	1.67	237.42703(8)	+62.69856(5)	8 ± 3	1.43
237.50889(6)	+62.68062(3)	24 ± 5	1.23	237.39461(19)	+62.77774(4)	6 ± 3	5.42
237.41719(9)	+62.80163(9)	21 ± 5	6.56	237.36908(9)	+62.708014(28)	5.8 ± 2.4	3.11
237.33541(15)	+62.66246(7)	16 ± 4	4.43	237.45618(6)	+62.688785(28)	5.7 ± 2.4	0.76
237.50326(4)	+62.673711(23)	16 ± 4	1.49	237.61868(5)	+62.70524(5)	4.3 ± 2.2	3.88
237.54805(7)	+62.72802(4)	15 ± 4	2.70	237.56325(7)	+62.74012(6)	3.7 ± 2.0	3.51
237.48872(9)	+62.69072(4)	15 ± 4	0.41				

Note: Equatorial coordinates, detected counts and off-axis angles as observed in the first epoch observation; errors are 1σ.

Table C.8: *Chapter 2*. Sources in the Chandra test fields. MG J0414+0534 (ACIS-S).

α (deg)	δ (deg)	Counts (30 ks)	Off-axis (arcmin)	α (deg)	δ (deg)	Counts (30 ks)	Off-axis (arcmin)
63.657359(3)	+5.578563(4)	1339 ± 37	0.59	*Central target*			
63.657200(6)	+5.579073(5)	289 ± 17	0.57	63.62055(4)	+5.589802(22)	18 ± 4	2.59
63.598305(12)	+5.586095(19)	209 ± 14	3.91	63.668830(27)	+5.556102(27)	17 ± 4	1.82
63.656822(12)	+5.578576(12)	144 ± 12	0.61	63.59249(6)	+5.59673(5)	16 ± 4	4.30
63.681209(22)	+5.623785(22)	57 ± 7	2.48	63.68049(4)	+5.62929(3)	15 ± 4	2.77
63.665381(12)	+5.565052(12)	57 ± 7	1.26	63.605147(28)	+5.56345(3)	13 ± 3	3.75
63.640845(14)	+5.550415(18)	45 ± 6	2.54	63.669181(22)	+5.598332(23)	12 ± 3	0.80
63.671128(17)	+5.607844(16)	41 ± 6	1.37	63.62340(3)	+5.59806(5)	11 ± 3	2.51
63.70090(3)	+5.51624(3)	38 ± 6	4.74	63.651989(26)	+5.57649(5)	9 ± 3	0.91
63.707735(24)	+5.582922(19)	37 ± 6	2.63	63.697619(23)	+5.56980(4)	9 ± 3	2.24
63.645936(29)	+5.574339(23)	33 ± 6	1.27	63.67712(9)	+5.51605(4)	7 ± 3	4.27
63.667980(23)	+5.544449(28)	30 ± 5	2.51	63.64574(4)	+5.63889(4)	2.8 ± 1.7	3.34
63.648002(18)	+5.563289(24)	26 ± 5	1.66	63.61388(4)	+5.61310(4)	2.7 ± 1.7	3.39
63.709159(28)	+5.583358(22)	20 ± 4	2.71	63.61631(4)	+5.60378(5)	1.7 ± 1.4	3.02

Note: Equatorial coordinates, detected counts and off-axis angles as observed in the first epoch observation; errors are 1σ.

APPENDIX D

Acronym list

The following list is a description of the set of acronyms and abbreviations used in this document (Table D.1).

Table D.1: List of acronyms and abbreviations used in this work.

Acronym	Description
	Astrophysics
AGN	Active Galactic Nucleus
AXP	Anomalous X-ray Pulsar
CCO	Central Compact Object
CV	Cataclysmic Variable
HMXB	High-Mass X-ray Binary
INS	Isolated Neutron Star
ISM	Interstellar Medium
LMC	Large Magellanic Cloud
LSR	Local Standard of Rest
LMXB	Low-Mass X-ray Binary
M7	The ROSAT-discovered "Magnificent Seven"
MSP	Millisecond Pulsar
PSR	Pulsating Source of Radio (Pulsar)
PWN	Pulsar Wind Nebula
RRAT	Rotating Radio Transient
SGR	Soft Gamma-ray Repeater
SN	Supernova
SMC	Small Magellanic Cloud
SNR	Supernova Remnant
XDINS	X-ray Dim Isolated Neutron Star
	Chandra
ACIS	Advanced CCD Imaging Spectrometer
ACIS-I	ACIS Imaging Array
ACIS-S	ACIS Spectroscopic Array
AXAF	Advanced X-Ray Astrophysics Facility (≡ Chandra)
CALDB	Calibration Data Base
Chandra	Chandra X-Ray Observatory
CIAO	Chandra Interactive Analysis of Observations

Continue on next page...

Table D.1 – Continued

Acronym	Description
CXC	Chandra X-Ray Center
HETG	High Energy Transmission Grating
HRC	High Resolution Camera
HRMA	High Resolution Mirror Assembly
LETG	Low Energy Transmission Grating
MARX	Model of AXAF Response to X-rays
OBF	Optical Blocking Filter
SDP	Standard Data Processing
SIM	Scientific Instrument Module
TE	Timed Exposure
	ESO-VLT and SOAR
ESO	European Southern Observatory
ESO-VLT	ESO Very Large Telescope
FORS	FOcal Reducer low/dispersion Spectrograph
HR	High Resolution (collimator)
SOAR	Southern Astrophysical Research Telescope
SOI	SOAR Optical Imager
SR	Standard Resolution (collimator)
UT	Unit Telescope
	XMM-Newton
ACDS	Astronomical Catalogue Data Subsystem
EPIC	European Photon Imaging Camera
EPIC MOS	EPIC MOS CCD camera
EPIC pn	EPIC pn CCD camera
MOS	Metal Oxide Semiconductor
ODF	Observation Data Files
RFS	Refresh Frame Store
SAS	Science Analysis Software
SOC	Science Operation Center
SSC	Survey Scinece Centre
XMM-Newton	X-ray Multi-Mirror Mission
	General
ADU	Analog to Digital Unit
ADC	Atmospheric Dispersion Corrector
ARF	Ancillary Response Function
BI	Back-Illuminated
CCD	Charge Coupled Device
CTE	Charge Transfer Efficiency
CTI	Charge Transfer Inefficiency
Dec	Declination

Continue on next page...

Table D.1 – Continued

Acronym	Description
DM	Dispersion Measure
EoS	Equation of State
EW	Equivalent Width
GTI	Good Time Interval
FFT	Fast Fourrier Transform
FI	Front-Illuminated
FITS	Flexible Image Transport System
FoV	Field-of-View
FWHM	Full Width Half Maximum
IR	Infrared
JD	Julian Day
LOS	Line-of-Sight
mas	milliarcsecond
MHD	Magnetohydrodynamics
MJD	Modified Julian Date
OOT	Out-of-time
PH	Pulse Height
PHA	Pulse Height Amplifier (or Amplitude)
PI	Pulse Invariant
PSF	Point Spread Function
QE	Quantum Efficiency
QPO	Quasi Periodic Oscillation
RMF	Redistribution Matrix Function
rms	Root Mean Squared
S/N	Signal-to-Noise
SED	Spectral Energy Distribution
UT	Universal Time
UV	Ultraviolet
ZAMS	Zero-Age Main Sequence
	Satellites, Institutions and Softwares
2MASS	Two Micron All Sky Survey
ATNF	Australia Telescope National Facility
ASCA	Advanced Satellite for Cosmology and Astrophysics
BSC	RASS Bright Source Catalogue
CGRO	Compton Gamma-Ray Observatory (≡ Compton)
Compton	Compton Gamma-Ray Observatory
CTIO	Cerro Tololo Inter-American Observatory
DSS	Digital Sky Survey
ESA	European Space Agency
Einstein	Einstein Observatory

Continue on next page…

Table D.1 – Continued

Acronym	Description
eROSITA	Extended Röntgen Survey with an Imaging Telescope Array
EUVE	Extreme Ultraviolet Explorer
Fermi	Fermi γ-Ray Space Telescope
FIRST	The Faint Images of the Radio Sky at Twenty centimeters
FSC	RASS Faint Source Catalogue
GBGC	Green Bank Globular Cluster survey
GLAST	Gamma-ray Large Area Space Telescope (≡ Fermi)
GSC	The Guide Star Catalog
HEAO-2	High Energy Astrophysical Observatory (≡ Einstein)
HEASARC	High Energy Astrophysics Science Archive Research Center
HRI	ROSAT High Resolution Imager
HST	Hubble Space Telescope (≡ Hubble)
Hubble	Hubble Space Telescope
INTEGRAL	International Gamma-Ray Astrophysics Laboratory
IRAF	Image Reduction and Analysis Facility
IRAS	Infrared Astronomical Satellite
MIDAS	ESO Munich Image Data Analysis System
MIT	Massachusetts Institute of Technology
MPE	Max-Planck-Institut für Extraterrestrische Physik
NASA	National Aeronautics and Space Administration
NOAO	National Optical Astronomy Observatory
NRAO	National Radio Astronomy Observatory
NVLA	The NRAO Very Large Array
NVSS	The NRAO VLA Sky Survey
PIMMS	Portable, Interactive Multi-Mission Simulator
PA	Parkes Perseus Arm Survey
PALFA	Parkes Arecibo L-band Feed Array
PH	Parkes High Latitude Survey
PMPS	Parkes Multibeam Pulsar Survey
PSC	IRAS Point Source Catalogue
PSPC	ROSAT Position Sensitive Proportional Counter
RASS	ROSAT All-Sky Survey
ROSAT	Roentgen Satellite
RXTE	Rossi X-ray Timing Explorer
SAO	Smithsonian Astrophysical Observatory
SAS-1	Small Astronomy Satellite 1 (≡ Uhuru)
SDSS	Sloan Digital Sky Survey
SHL	Swinburne High Latitude Survey
SIL	Swinburne Intermediate Survey
Uhuru	Uhuru Satellite

Continue on next page…

Table D.1 – Continued

Acronym	Description
USNO	The United States Naval Observatory
VLA	Very Large Array
VLBA	Very Large Baseline Array
XIS	X-ray Imaging Spectrometer (Suzaku)
XRONOS	General purpose timing analysis package
XRS	X-ray Spectrometer (Suzaku)
XSPEC	X-ray Spectral fitting package
XSTAR	Spectral analysis tool

Bibliography

Abdo, A. A., Ackermann, M., Atwood, W. B., et al. 2009, ApJ, 696, 1084 4

Adelman-McCarthy, J. K., Agüeros, M. A., Allam, S. S., et al. 2006, ApJS, 162, 38 87, 98

Agüeros, M. A., Anderson, S. F., Margon, B., et al. 2006, AJ, 131, 1740 xvii, xxi, 87, 88

Aguilera, D. N., Pons, J. A., & Miralles, J. A. 2007, astro-ph/0710.4914, 710 161

Aguilera, D. N., Pons, J. A., & Miralles, J. A. 2008, ApJ, 673, L167 35, 36, 83, 145, 161

Akgün, T., Link, B., & Wasserman, I. 2006, MNRAS, 365, 653 22

Alpar, M. A. 2001, ApJ, 554, 1245 30

Appenzeller, I., Fricke, K., Fürtig, W., et al. 1998, The Messenger, 94, 1 109, 208

Arnaud, K. 2004, in Bulletin of the American Astronomical Society, Vol. 36, Bulletin of the American Astronomical Society, 934–+ 63, 95

Arnaud, K. A. 1996, in Astronomical Society of the Pacific Conference Series, Vol. 101, Astronomical Data Analysis Software and Systems V, ed. G. H. Jacoby & J. Barnes, 17–+ 63, 95

Arzoumanian, Z., Chernoff, D. F., & Cordes, J. M. 2002, ApJ, 568, 289 152, 158

Atlee, D. W. & Mathur, S. 2009, ApJ, submitted, astro-ph/0901.3566 146

Baade, W. & Zwicky, F. 1934, Proceedings of the National Academy of Science, 20, 254 1

Barcons, X., Carrera, F. J., Ceballos, M. T., et al. 2007, A&A, 476, 1191 143, 147

Becker, W. 2009, in Astrophysics and Space Science Library, Vol. 357, Astrophysics and Space Science Library, ed. W. Becker, 91–140 32

Becker, W. & Aschenbach, B. 2002, in Neutron Stars, Pulsars, and Supernova Remnants, ed. W. Becker, H. Lesch, & J. Trümper, 64–+ 10

Becker, W. & Pavlov, G. 2002, Pulsars and isolated neutron stars (Kluwer Academic Publishers), 721–+ 5, 32

Becker, W. & Truemper, J. 1997, A&A, 326, 682 31

Bessell, M. S. 2005, ARA&A, 43, 293 125

Bhattacharya, D. & van den Heuvel, E. P. J. 1991, Phys. Rep., 203, 1 27

Bhattacharya, D., Wijers, R. A. M. J., Hartman, J. W., & Verbunt, F. 1992, A&A, 254, 198 27, 152

Bienaymé, O., Soubiran, C., Mishenina, T. V., Kovtyukh, V. V., & Siebert, A. 2006, A&A, 446, 933 77

Bilir, S., Karaali, S., & Tunçel, S. 2005, Astronomische Nachrichten, 326, 321 121

Binney, J. & Tremaine, S. 1987, Galactic dynamics, ed. J. Binney & S. Tremaine 162, 168

Blaauw, A. 1961, Bull. Astron. Inst. Netherlands, 15, 265 80

Blaes, O. & Madau, P. 1993, ApJ, 403, 690 10, 11

Blaes, O., Warren, O., & Madau, P. 1995, ApJ, 454, 370 127, 128, 145

Boella, G., Butler, R. C., Perola, G. C., et al. 1997, A&AS, 122, 299 5

Boller, T., Brandt, W. N., & Fink, H. 1996, A&A, 305, 53 146

Bondi, H. & Hoyle, F. 1944, MNRAS, 104, 273 196

Bowyer, S. & Malina, R. F. 1991, Advances in Space Research, 11, 205 5

Bradt, H., Rappaport, S., Mayer, W., et al. 1969, Nature, 222, 728 2

Bradt, H. V., Rothschild, R. E., & Swank, J. H. 1993, A&AS, 97, 355 5

Brinkman, B. C., Gunsing, T., Kaastra, J. S., et al. 2000, in Society of Photo-Optical Instrumentation Engineers (SPIE) Conference Series, Vol. 4012, Society of Photo-Optical Instrumentation Engineers (SPIE) Conference Series, ed. J. E. Truemper & B. Aschenbach, 81–90 202

Brisken, W. F., Benson, J. M., Goss, W. M., & Thorsett, S. E. 2002, ApJ, 571, 906 158, 173

Brisken, W. F., Fruchter, A. S., Goss, W. M., Herrnstein, R. M., & Thorsett, S. E. 2003, AJ, 126, 3090 158, 173

Bromley, B. C., Kenyon, S. J., Brown, W. R., & Geller, M. J. 2009, ApJ, submitted, astro-ph/0907.5567 155

Bronfman, L., Casassus, S., May, J., & Nyman, L.-Å. 2000, A&A, 358, 521 155

Buccheri, R., Bennett, K., Bignami, G. F., et al. 1983, A&A, 128, 245 139

Burgay, M., Joshi, B. C., D'Amico, N., et al. 2006, MNRAS, 368, 283 7

Burwitz, V., Haberl, F., Neuhäuser, R., et al. 2003, A&A, 399, 1109 13, 21, 136

Burwitz, V., Zavlin, V. E., Neuhäuser, R., et al. 2001, A&A, 379, L35 13

Camilo, F., Ransom, S. M., Halpern, J. P., & Reynolds, J. 2007, ApJ, 666, L93 29

Camilo, F., Ransom, S. M., Halpern, J. P., et al. 2006, Nature, 442, 892 29

Canal, R. & Gutiérrez, J. 1997, in Astrophysics and Space Science Library, Vol. 214, White dwarfs, ed. J. Isern, M. Hernanz, & E. Garcia-Berro, 49–+ 155

Canizares, C. R., Davis, J. E., Dewey, D., et al. 2005, PASP, 117, 1144 202

Cappellaro, E., Evans, R., & Turatto, M. 1999, A&A, 351, 459 6

Cappellaro, E., Turatto, M., Tsvetkov, D. Y., et al. 1997, A&A, 322, 431 6

Cardelli, J. A., Clayton, G. C., & Mathis, J. S. 1989, ApJ, 345, 245 125

Cardone, V. F., Piedipalumbo, E., & Tortora, C. 2005, MNRAS, 358, 1325 167, 168

Cash, W. 1979, ApJ, 228, 939 134

Cecil, G. N. 2000, in Society of Photo-Optical Instrumentation Engineers (SPIE) Conference Series, Vol. 4008, Society of Photo-Optical Instrumentation Engineers (SPIE) Conference Series, ed. M. Iye & A. F. Moorwood, 83–93 208

Chang, P. & Bildsten, L. 2003, ApJ, 585, 464 21

Chang, P. & Bildsten, L. 2004, ApJ, 605, 830 21

Chatterjee, S. & Cordes, J. M. 2002, ApJ, 575, 407 18, 127, 128

Chatterjee, S. & Cordes, J. M. 2004, ApJ, 600, L51 81

Chatterjee, S., Cordes, J. M., Lazio, T. J. W., et al. 2001, ApJ, 550, 287 158

Chatterjee, S., Vlemmings, W. H. T., Brisken, W. F., et al. 2005, ApJ, 630, L61 81

Chevalier, R. A. & Emmering, R. T. 1986, ApJ, 304, 140 86

Chieregato, M., Campana, S., Treves, A., et al. 2005, A&A, 444, 69 xvii, xxi, 88

Chiu, H.-Y. & Salpeter, E. E. 1964, Physical Review Letters, 12, 413 2

Churchwell, E., Babler, B. L., Meade, M. R., et al. 2009, PASP, 121, 213 165

Cocke, W. J., Disney, M. J., & Taylor, D. J. 1969, Nature, 221, 525 2

Cole, T. W. 1969, Nature, 221, 29 2

Colpi, M., Campana, S., & Treves, A. 1993, A&A, 278, 161 10

Comella, J. M., Craft, Jr., H. D., Lovelace, R. V. E., Sutton, J. M., & Tyler, G. L. 1969, Nature, 221, 453 2

Condon, J. J., Cotton, W. D., Greisen, E. W., et al. 1998, AJ, 115, 1693 87

Corbel, S., Chapuis, C., Dame, T. M., & Durouchoux, P. 1999, ApJ, 526, L29 30

Cordes, J. M. 1993, in Astronomical Society of the Pacific Conference Series, Vol. 36, Planets Around Pulsars, ed. J. A. Phillips, S. E. Thorsett, & S. R. Kulkarni, 43–60 22

Cordes, J. M. & Chernoff, D. F. 1998, ApJ, 505, 315 86

Cordes, J. M. & Lazio, T. J. W. 2002, ArXiv Astrophysics e-prints 86, 158

Cordes, J. M., Romani, R. W., & Lundgren, S. C. 1993, Nature, 362, 133 81

Cordes, J. M. & Shannon, R. M. 2008, ApJ, 682, 1152 31

Cumming, A. 2008, in American Institute of Physics Conference Series, Vol. 1068, American Institute of Physics Conference Series, ed. R. Wijnands, D. Altamirano, P. Soleri, N. Degenaar, N. Rea, P. Casella, A. Patruno, & M. Linares, 152–159 27

Cutri, R. M., Skrutskie, M. F., van Dyk, S., et al. 2003, 2MASS All Sky Catalog of point sources., ed. R. M. Cutri, M. F. Skrutskie, S. van Dyk, C. A. Beichman, J. M. Carpenter, T. Chester, L. Cambresy, T. Evans, J. Fowler, J. Gizis, E. Howard, J. Huchra, T. Jarrett, E. L. Kopan, J. D. Kirkpatrick, R. M. Light, K. A. Marsh, H. McCallon, S. Schneider, R. Stiening, M. Sykes, M. Weinberg, W. A. Wheaton, S. Wheelock, & N. Zacarias 98

Dame, T. M. & Thaddeus, P. 2008, ApJ, 683, L143 165

Danner, R. 1998, A&AS, 128, 331 12

Davies, J. C., Hunt, G. C., & Smith, F. G. 1969, Nature, 221, 27 2

de Boer, H. 1991, in IAU Symposium, Vol. 144, The Interstellar Disk-Halo Connection in Galaxies, ed. H. Bloemen, 333–336 169, 170

de Luca, A. 2008, in American Institute of Physics Conference Series, Vol. 983, 40 Years of Pulsars: Millisecond Pulsars, Magnetars and More, ed. C. Bassa, Z. Wang, A. Cumming, & V. M. Kaspi, 311–319 24

De Luca, A., Caraveo, P. A., Esposito, P., & Hurley, K. 2009, ApJ, 692, 158 19, 42, 67

De Luca, A., Caraveo, P. A., Mereghetti, S., Negroni, M., & Bignami, G. F. 2005, ApJ, 623, 1051 136

De Luca, A., Caraveo, P. A., Mereghetti, S., Tiengo, A., & Bignami, G. F. 2006, Science, 313, 814 34

De Luca, A., Mereghetti, S., Caraveo, P. A., et al. 2004, A&A, 418, 625 33, 34

de Ruiter, H. R., Arp, H. C., & Willis, A. G. 1977, A&AS, 28, 211 120

de Vaucouleurs, G. 1948, Annales d'Astrophysique, 11, 247 166

de Vries, C. P., Vink, J., Méndez, M., & Verbunt, F. 2004, A&A, 415, L31 22, 23

de Zeeuw, P. T., Hoogerwerf, R., de Bruijne, J. H. J., Brown, A. G. A., & Blaauw, A. 1999, AJ, 117, 354 78

den Hartog, P. R., Hermsen, W., Kuiper, L., et al. 2006, A&A, 451, 587 30

den Herder, J. W., Brinkman, A. C., Kahn, S. M., et al. 2001, A&A, 365, L7 199

Deneva, J. S., Cordes, J. M., & Lazio, T. J. W. 2009a, ApJ, 702, L177 171

Deneva, J. S., Cordes, J. M., Mc Laughlin, M. A., et al. 2009b, ApJ, 703, 2259 30

Dickey, J. M. & Lockman, F. J. 1990, ARA&A, 28, 215 108, 141, 169, 170

Diehl, R., Halloin, H., Kretschmer, K., et al. 2006, Nature, 439, 45 6, 37

Dillon, M., Gänsicke, B. T., Aungwerojwit, A., et al. 2008, MNRAS, 386, 1568 121

Dodson, R., Legge, D., Reynolds, J. E., & McCulloch, P. M. 2003, ApJ, 596, 1137 158

Durney, B. 1969, Nature, 222, 1260 2

Earn, D. J. D. 1996, ApJ, 465, 91 167

Edgar, R. 2004, New Astronomy Review, 48, 843 195, 196

Edwards, R. T., Bailes, M., van Straten, W., & Britton, M. C. 2001, MNRAS, 326, 358 7

Elias, F., Cabrera-Caño, J., & Alfaro, E. J. 2006, AJ, 131, 2700 80

Emmering, R. T. & Chevalier, R. A. 1989, ApJ, 345, 931 152

Farrell, S. A., Webb, N. A., Barret, D., Godet, O., & Rodrigues, J. M. 2009, Nature, 460, 73 103, 104, 148, 213, 224

Faucher-Giguère, C.-A. & Kaspi, V. M. 2006, ApJ, 643, 332 7, 37, 145, 152, 158, 162, 163, 165, 166, 170, 172, 173

Ferlet, R., Vidal-Madjar, A., & Gry, C. 1985, ApJ, 298, 838 169

Ferrario, L. & Wickramasinghe, D. 2006, MNRAS, 367, 1323 152

Ferrario, L. & Wickramasinghe, D. 2008a, MNRAS, 389, L66 162

Ferrario, L. & Wickramasinghe, D. T. 2008b, in American Institute of Physics Conference Series, Vol. 968, Astrophysics of Compact Objects, ed. Y.-F. Yuan, X.-D. Li, & D. Lai, 194–196 154

Figer, D. F., Najarro, F., Geballe, T. R., Blum, R. D., & Kudritzki, R. P. 2005, ApJ, 622, L49 30

Fox, D. B. 2004, ArXiv Astrophysics e-prints; astro-ph/0403261 88

Freire, P. C. C., Ransom, S. M., Bégin, S., et al. 2008a, ApJ, 675, 670 7

Freire, P. C. C., Ransom, S. M., Bégin, S., et al. 2008b, ApJ, 675, 670 189

Freire, P. C. C., Wolszczan, A., van den Berg, M., & Hessels, J. W. T. 2008c, ApJ, 679, 1433 189

Fritz, G., Henry, R. C., Meekins, J. F., Chubb, T. A., & Friedman, H. 1969, Science, 164, 709 2

Fruscione, A., McDowell, J. C., Allen, G. E., et al. 2006, in Society of Photo-Optical Instrumentation Engineers (SPIE) Conference Series, Vol. 6270, Society of Photo-Optical Instrumentation Engineers (SPIE) Conference Series 49

Fukugita, M., Ichikawa, T., Gunn, J. E., et al. 1996, AJ, 111, 1748 121

Gaensler, B. M., McClure-Griffiths, N. M., Oey, M. S., et al. 2005, ApJ, 620, L95 155

Gaensler, B. M., McLaughlin, M., Reynolds, S., et al. 2007, Ap&SS, 308, 95 31

Gaensler, B. M. & Slane, P. O. 2006, ARA&A, 44, 17 127

Garmany, C. D. 1994, PASP, 106, 25 79

Garmire, G. P., Bautz, M. W., Ford, P. G., Nousek, J. A., & Ricker, Jr., G. R. 2003, in Society of Photo-Optical Instrumentation Engineers (SPIE) Conference Series, Vol. 4851, Society of Photo-Optical Instrumentation Engineers (SPIE) Conference Series, ed. J. E. Truemper & H. D. Tananbaum, 28–44 204

Gehrels, N., Chincarini, G., Giommi, P., et al. 2004, ApJ, 611, 1005 6, 88

Gehrels, N. & Michelson, P. 1999, Astroparticle Physics, 11, 277 6

Georgelin, Y. M. & Georgelin, Y. P. 1976, A&A, 49, 57 166

Geppert, U. 2009, in Astrophysics and Space Science Library, Vol. 357, Astrophysics and Space Science Library, ed. W. Becker, 319–352 159, 160

Geppert, U., Küker, M., & Page, D. 2004, A&A, 426, 267 77, 161

Geppert, U., Küker, M., & Page, D. 2006, A&A, 457, 937 161

Getman, K. V., Flaccomio, E., Broos, P. S., et al. 2005, ApJS, 160, 319 55

Ghez, A. M., Salim, S., Weinberg, N. N., et al. 2008, ApJ, 689, 1044 165

Giacconi, R., Branduardi, G., Briel, U., et al. 1979, ApJ, 230, 540 5

Giacconi, R., Kellogg, E., Gorenstein, P., Gursky, H., & Tananbaum, H. 1971, ApJ, 165, L27+ 5

Gies, D. R. & Bolton, C. T. 1986, ApJS, 61, 419 80

Gill, R. & Heyl, J. 2007, MNRAS, 381, 52 37, 179

Glendenning, N. 1996, Compact Stars. Nuclear Physics, Particle Physics and General Relativity., ed. N. Glendenning 159

Gold, T. 1968, Nature, 218, 731 2

Gold, T. 1969, Nature, 221, 25 2

Gonthier, P. L., Van Guilder, R., & Harding, A. K. 2004, ApJ, 604, 775 152

Gonzalez, M. E., Kaspi, V. M., Camilo, F., Gaensler, B. M., & Pivovaroff, M. J. 2007, Ap&SS, 308, 89 34

Gotthelf, E. V., Halpern, J. P., & Seward, F. D. 2005, ApJ, 627, 390 158

Grindlay, J. E. & Bogdanov, S. 2009, in Astrophysics and Space Science Library, Vol. 357, Astrophysics and Space Science Library, ed. W. Becker, 165–179 27

Grupe, D., Beuermann, K., Thomas, H.-C., Mannheim, K., & Fink, H. H. 1998, A&A, 330, 25 146

Gunn, J. E. & Ostriker, J. P. 1970, ApJ, 160, 979 19

Gutiérrez, J., Canal, R., & García-Berro, E. 2005, A&A, 435, 231 155

Haberl, F. 2004a, Advances in Space Research, 33, 638 45

Haberl, F. 2004b, Memorie della Societa Astronomica Italiana, 75, 454 12

Haberl, F. 2005, in 5 years of Science with XMM-Newton, ed. U. G. Briel, S. Sembay, & A. Read, 39–44 12

Haberl, F. 2007, Ap&SS, 308, 181 xvii, xxi, 12, 13, 16, 17, 83

Haberl, F., Motch, C., Buckley, D. A. H., Zickgraf, F.-J., & Pietsch, W. 1997, A&A, 326, 662 12

Haberl, F., Motch, C., & Pietsch, W. 1998, Astronomische Nachrichten, 319, 97 12, 45

Haberl, F., Motch, C., Zavlin, V. E., et al. 2004a, A&A, 424, 635 13, 16, 45, 46

Haberl, F., Pietsch, W., & Motch, C. 1999, A&A, 351, L53 12, 46

Haberl, F., Schwope, A. D., Hambaryan, V., Hasinger, G., & Motch, C. 2003, A&A, 403, L19 13, 16, 45

Haberl, F., Turolla, R., de Vries, C. P., et al. 2006, A&A, 451, L17 22

Haberl, F. & Zavlin, V. E. 2002, A&A, 391, 571 45, 46

Haberl, F., Zavlin, V. E., Trümper, J., & Burwitz, V. 2004b, A&A, 419, 1077 13, 16

Haensel, P. 2003, in EAS Publications Series, Vol. 7, EAS Publications Series, ed. C. Motch & J.-M. Hameury, 249–+ 189

Hakkila, J., Myers, J. M., Stidham, B. J., & Hartmann, D. H. 1997, AJ, 114, 2043 169

Hamaguchi, K., Corcoran, M. F., Ezoe, Y., et al. 2009, ApJ, 695, L4 147

Hambaryan, V., Hasinger, G., Schwope, A. D., & Schulz, N. S. 2002, A&A, 381, 98 45

Harding, A. K. 2009, in Astrophysics and Space Science Library, Vol. 357, Astrophysics and Space Science Library, ed. W. Becker, 521–542 27

Harrison, P. A. & Lyne, A. G. 1993, MNRAS, 265, 778 86

Hartman, J. W., Bhattacharya, D., Wijers, R., & Verbunt, F. 1997, A&A, 322, 477 152

Heger, A., Fryer, C. L., Woosley, S. E., Langer, N., & Hartmann, D. H. 2003, ApJ, 591, 288 153, 155

Heger, A., Woosley, S. E., & Spruit, H. C. 2005, ApJ, 626, 350 158

Helfand, D. J., Gotthelf, E. V., & Halpern, J. P. 2001, ApJ, 556, 380 19

Helfand, D. J. & Tademaru, E. 1977, ApJ, 216, 842 86

Helou, G. & Walker, D. W., eds. 1988, Infrared astronomical satellite (IRAS) catalogs and atlases. Volume 7: The small scale structure catalog, Vol. 7 87

Hernquist, L. 1990, ApJ, 356, 359 166

Hessels, J. W. T., Ransom, S. M., Kaspi, V. M., et al. 2008, in American Institute of Physics Conference Series, Vol. 983, 40 Years of Pulsars: Millisecond Pulsars, Magnetars and More, ed. C. Bassa, Z. Wang, A. Cumming, & V. M. Kaspi, 613–615 30

Hessels, J. W. T., Ransom, S. M., Stairs, I. H., et al. 2006, Science, 311, 1901 7

Hessels, J. W. T., Stappers, B. W., Rutledge, R. E., Fox, D. B., & Shevchuk, A. H. 2007, A&A, 476, 331 148

Hewish, A., Bell, S. J., Pilkington, J. D., Scott, P. F., & Collins, R. A. 1968, Nature, 217, 709 2, 85

Heyl, J. 2000, in KITP Conference: Spin, Magnetism and Cooling of Young Neutron Stars 176

Heyl, J. S. & Kulkarni, S. R. 1998, ApJ, 506, L61 xviii, xxii, 16, 36, 83

Hillier, R. R., Jackson, W. R., Murray, A., Redfern, R. M., & Sale, R. G. 1970, ApJ, 162, L177+ 2

Hills, J. G. 1983, ApJ, 267, 322 157

Ho, W. C. G., Kaplan, D. L., Chang, P., van Adelsberg, M., & Potekhin, A. Y. 2007, Ap&SS, 308, 279 18, 21, 145, 163

Ho, W. C. G. & Lai, D. 2004, ApJ, 607, 420 18

Hobbs, G., Lorimer, D. R., Lyne, A. G., & Kramer, M. 2005, MNRAS, 360, 974 19, 81, 86, 145, 158

Hohle, M. M., Haberl, F., Vink, J., et al. 2009, A&A, 498, 811 22, 24

Hoogerwerf, R., de Bruijne, J. H. J., & de Zeeuw, P. T. 2001, A&A, 365, 49 80

Hou, L. G., Han, J. L., & Shi, W. B. 2009, A&A, 499, 473 165

Hui, C. Y. & Becker, W. 2006, A&A, 457, L33 42

Hulse, R. A. & Taylor, J. H. 1975, ApJ, 195, L51 28, 157

Humphreys, R. M. 1978, ApJS, 38, 309 78

Hurley, K. 2009, in Astrophysics and Space Science Library, Vol. 357, Astrophysics and Space Science Library, ed. W. Becker, 575–588 24

Ikhsanov, N. R. 2007, Ap&SS, 308, 137 145

Jacoby, B. A. 2005, PhD thesis, California Institute of Technology, United States – California 7

Jansen, F., Lumb, D., Altieri, B., et al. 2001, A&A, 365, L1 199

Jones, D. I. & Andersson, N. 2001, MNRAS, 324, 811 22

Kaplan, D. L. 2008, in American Institute of Physics Conference Series, Vol. 983, 40 Years of Pulsars: Millisecond Pulsars, Magnetars and More, ed. C. Bassa, Z. Wang, A. Cumming, & V. M. Kaspi, 331–339 xviii, xxii, 12, 14, 20, 22, 36

Kaplan, D. L., Chatterjee, S., Gaensler, B. M., & Anderson, J. 2008, ApJ, 677, 1201 19

Kaplan, D. L., Chatterjee, S., Hales, C. A., Gaensler, B. M., & Slane, P. O. 2009a, AJ, 137, 354 19, 42, 67

Kaplan, D. L., Esposito, P., Chatterjee, S., et al. 2009b, MNRAS, accepted, astro-ph/0908.3819 32

Kaplan, D. L., Kulkarni, S. R., & van Kerkwijk, M. H. 2002a, ApJ, 579, L29 13, 45

Kaplan, D. L. & van Kerkwijk, M. H. 2005a, ApJ, 628, L45 xvii, xxi, 17, 19, 22, 83

Kaplan, D. L. & van Kerkwijk, M. H. 2005b, ApJ, 635, L65 xvii, xxi, 17, 19, 45, 83

Kaplan, D. L. & van Kerkwijk, M. H. 2009, ApJ, 692, L62 xvii, xxi, 18, 19, 136

Kaplan, D. L., van Kerkwijk, M. H., & Anderson, J. 2002b, ApJ, 571, 447 xvii, xxi, 15, 18, 41, 43, 77, 81

Kaplan, D. L., van Kerkwijk, M. H., & Anderson, J. 2007, ApJ, 660, 1428 xvii, xxi, 15, 41, 43, 44, 77, 81, 83

Kaplan, D. L., van Kerkwijk, M. H., Marshall, H. L., et al. 2003, ApJ, 590, 1008 13

Kaspi, V. M., Roberts, M. S. E., & Harding, A. K. 2004, ArXiv Astrophysics e-prints 10, 134

Keane, E. F. & Kramer, M. 2008, MNRAS, 391, 2009 37, 153

Keane, E. F., Ludovici, D. A., Eatough, R. P., et al. 2009, MNRAS, accepted, astro-ph/0909.1924 30, 31, 37

Kiel, P. D. & Hurley, J. R. 2009, MNRAS, 395, 2326 152

Kiel, P. D., Hurley, J. R., Bailes, M., & Murray, J. R. 2008, MNRAS, 388, 393 152

Kleinmann, S. G., Lysaght, M. G., Pughe, W. L., et al. 1994, Ap&SS, 217, 11 88

Klose, S., Henden, A. A., Geppert, U., et al. 2004, ApJ, 609, L13 30

Kluźniak, W. & Ruderman, M. 1998, ApJ, 505, L113 159

Kniffen, D. A. 1990, in Astrophysics and Space Science Library, Vol. 166, IAU Colloq. 123: Observatories in Earth Orbit and Beyond, ed. Y. Kondo, 63–+ 5

Kondratiev, V. I., Burgay, M., Possenti, A., et al. 2008, in American Institute of Physics Conference Series, Vol. 983, 40 Years of Pulsars: Millisecond Pulsars, Magnetars and More, ed. C. Bassa, Z. Wang, A. Cumming, & V. M. Kaspi, 348–350 xvii, xxi, 15, 146

Kondratiev, V. I., McLaughlin, M. A., Lorimer, D. R., et al. 2009, ApJ, accepted, astro-ph/0907.0054 xvii, xxi, 15, 36, 146

Krabbendam, V. L., Heathcote, S., Schumacher, G., et al. 2004, in Society of Photo-Optical Instrumentation Engineers (SPIE) Conference Series, Vol. 5489, Society of Photo-Optical Instrumentation Engineers (SPIE) Conference Series, ed. J. M. Oschmann, Jr., 615–624 208

Kuiper, L., Hermsen, W., Cusumano, G., et al. 2001, A&A, 378, 918 3

Kuiper, L., Hermsen, W., & Mendez, M. 2004, ApJ, 613, 1173 30

Kulkarni, S. R. & van Kerkwijk, M. H. 1998, ApJ, 507, L49 13

Lai, D. 2001, Reviews of Modern Physics, 73, 629 xvii, xxi, 17

Lai, D., Chernoff, D. F., & Cordes, J. M. 2001, ApJ, 549, 1111 19

Lallement, R., Welsh, B. Y., Vergely, J. L., Crifo, F., & Sfeir, D. 2003, A&A, 411, 447 169

Landau, L. 1932, Phys. Z. Sowjetunion, 1, 285 1

Landolt, A. U. 1992, AJ, 104, 340 113

Large, M. I., Vaughan, A. E., & Mills, B. Y. 1968, Nature, 220, 340 2

Lasker, B. M. 1976, ApJ, 203, 193 2

Lattimer, J. M. & Prakash, M. 2000, Phys. Rep., 333, 121 189

Lattimer, J. M. & Prakash, M. 2001, ApJ, 550, 426 189

Lattimer, J. M. & Prakash, M. 2007, Phys. Rep., 442, 109 189, 190

Letcavage, R., Rutledge, R. E., Fox, D. B., & Shevchuk, A. H. 2009, in American Astronomical Society Meeting Abstracts, Vol. 213, American Astronomical Society Meeting Abstracts, 470.03–+ 88, 148

Leutenegger, M. A., Kahn, S. M., & Ramsay, G. 2003, ApJ, 585, 1015 144

Lewin, W. H. G. & van der Klis, M. 2006, Compact stellar X-ray sources, ed. W. H. G. Lewin & M. van der Klis 5

Lewin, W. H. G., van Paradijs, J., & van den Heuvel, E. P. J. 1997, X-ray Binaries, ed. W. H. G. Lewin, J. van Paradijs, & E. P. J. van den Heuvel 5

Link, B. 2003, in Astronomical Society of the Pacific Conference Series, Vol. 302, Radio Pulsars, ed. M. Bailes, D. J. Nice, & S. E. Thorsett, 241–+ 22

Liu, Q. Z., van Paradijs, J., & van den Heuvel, E. P. J. 2006, A&A, 455, 1165 5

Liu, Q. Z., van Paradijs, J., & van den Heuvel, E. P. J. 2007, A&A, 469, 807 5

Lorimer, D. R. 2005, Living Reviews in Relativity, 8, 7 85

Lorimer, D. R. 2008, Living Reviews in Relativity, 11, 8 28, 29

Lorimer, D. R., Bailes, M., & Harrison, P. A. 1997, MNRAS, 289, 592 86, 158

Lorimer, D. R., Faulkner, A. J., Lyne, A. G., et al. 2006, MNRAS, 372, 777 7

Lyne, A. G. 2008, in American Institute of Physics Conference Series, Vol. 983, 40 Years of Pulsars: Millisecond Pulsars, Magnetars and More, ed. C. Bassa, Z. Wang, A. Cumming, & V. M. Kaspi, 561–566 7, 143

Lyne, A. G. & Lorimer, D. R. 1994, Nature, 369, 127 86

Lyne, A. G., Manchester, R. N., Lorimer, D. R., et al. 1998, MNRAS, 295, 743 163

Lyne, A. G., McLaughlin, M. A., Keane, E. F., et al. 2009, MNRAS, accepted, astro-ph/0909.1165 32, 146

Lyne, A. G., Ritchings, R. T., & Smith, F. G. 1975, MNRAS, 171, 579 163

Maccacaro, T., Gioia, I. M., Zamorani, G., et al. 1982, ApJ, 253, 504 147

MacFadyen, A. I., Woosley, S. E., & Heger, A. 2001, ApJ, 550, 410 155

Madau, P. & Blaes, O. 1994, ApJ, 423, 748 10

Malofeev, V. M., Malov, O. I., & Teplykh, D. A. 2007, Ap&SS, 308, 211 15

Manchester, R. N. 2009, in Astrophysics and Space Science Library, Vol. 357, Astrophysics and Space Science Library, ed. W. Becker, 19–39 7

Manchester, R. N., Hobbs, G. B., Teoh, A., & Hobbs, M. 2005, AJ, 129, 1993 7, 143

Manchester, R. N., Lyne, A. G., Camilo, F., et al. 2001, MNRAS, 328, 17 7

Mason, K. O., Breeveld, A., Much, R., et al. 2001, A&A, 365, L36 199

Mateos, S., Saxton, R. D., Read, A. M., & Sembay, S. 2009, A&A, 496, 879 138

Mateos, S., Warwick, R. S., Carrera, F. J., et al. 2008, A&A, 492, 51 122, 147

McLaughlin, M. 2009, in Astrophysics and Space Science Library, Vol. 357, Astrophysics and Space Science Library, ed. W. Becker, 41–66 24

McLaughlin, M. A., Lyne, A. G., Keane, E. F., et al. 2009, MNRAS, accepted, astro-ph/0908.3813 31, 146

McLaughlin, M. A., Lyne, A. G., Lorimer, D. R., et al. 2006, Nature, 439, 817 24, 30

McLaughlin, M. A., Rea, N., Gaensler, B. M., et al. 2007, ApJ, 670, 1307 xviii, xxii, 32, 146

McLaughlin, M. A., Stairs, I. H., Kaspi, V. M., et al. 2003, ApJ, 591, L135 34

McLean, B. J., Greene, G. R., Lattanzi, M. G., & Pirenne, B. 2000, in Astronomical Society of the Pacific Conference Series, Vol. 216, Astronomical Data Analysis Software and Systems IX, ed. N. Manset, C. Veillet, & D. Crabtree, 145–+ 88, 98

McMahon, R. G., Irwin, M. J., & Maddox, S. J. 2000, VizieR Online Data Catalog, 1267, 0 98

Medin, Z. & Lai, D. 2007, MNRAS, 382, 1833 21

Meidinger, N., Andritschke, R., Hälker, O., et al. 2006, in Society of Photo-Optical Instrumentation Engineers (SPIE) Conference Series, Vol. 6276, Society of Photo-Optical Instrumentation Engineers (SPIE) Conference Series 206

Mereghetti, S. 2008, A&A Rev., 15, 225 24, 28

Mignani, R. P., de Luca, A., & Caraveo, P. A. 2004, in IAU Symposium, Vol. 218, Young Neutron Stars and Their Environments, ed. F. Camilo & B. M. Gaensler, 391–+ 5

Mignani, R. P., Motch, C., Haberl, F., et al. 2009, A&A (accepted); astro-ph/0906.5480 13, 46

Mitsuda, K., Bautz, M., Inoue, H., et al. 2007, PASJ, 59, 1 6

Mizutani, M., Onaka, T., & Shibai, H. 2002, A&A, 382, 610 145

Monet, D. G. 1998, in Bulletin of the American Astronomical Society, Vol. 30, Bulletin of the American Astronomical Society, 1427–+ 87, 93

Monet, D. G., Levine, S. E., Canzian, B., et al. 2003, AJ, 125, 984 96

Morrison, R. & McCammon, D. 1983, ApJ, 270, 119 170, 171

Motch, C. 2001, X-ray Astronomy: Stellar Endpoints, AGN, and the Diffuse X-ray Background, 599, 244 12

Motch, C., Guillout, P., Haberl, F., et al. 1997, A&AS, 122, 201 12, 53, 147

Motch, C. & Haberl, F. 1998, A&A, 333, L59 13

Motch, C., Haberl, F., Zickgraf, F.-J., Hasinger, G., & Schwope, A. D. 1999, A&A, 351, 177 12

Motch, C., Michel, L., & Pineau, F. X. 2007a, in Astronomical Society of the Pacific Conference Series, Vol. 376, Astronomical Data Analysis Software and Systems XVI, ed. R. A. Shaw, F. Hill, & D. J. Bell, 699–+ 99

Motch, C., Pires, A. M., Haberl, F., & Schwope, A. 2007b, Ap&SS, 308, 217 xv, xix, xxiii, 42, 76, 252, 253, 254

Motch, C., Pires, A. M., Haberl, F., Schwope, A., & Zavlin, V. E. 2008, in American Institute of Physics Conference Series, Vol. 983, 40 Years of Pulsars: Millisecond Pulsars, Magnetars and More, ed. C. Bassa, Z. Wang, A. Cumming, & V. M. Kaspi, 354–356 42, 76

Motch, C., Pires, A. M., Haberl, F., Schwope, A., & Zavlin, V. E. 2009, A&A, 497, 423 xv, xvii, xix, xxi, xxiii, 18, 20, 42, 46, 76, 81, 252, 253, 254

Motch, C., Sekiguchi, K., Haberl, F., et al. 2005, A&A, 429, 257 41, 44, 45

Motch, C., Zavlin, V. E., & Haberl, F. 2003, A&A, 408, 323 18, 21, 41, 43, 145

Muno, M. P., Clark, J. S., Crowther, P. A., et al. 2006, ApJ, 636, L41 30, 155

Muno, M. P., Gaensler, B. M., Nechita, A., Miller, J. M., & Slane, P. O. 2008, ApJ, 680, 639 144

Murray, S. S., Austin, G. K., Chappell, J. H., et al. 2000, in Society of Photo-Optical Instrumentation Engineers (SPIE) Conference Series, Vol. 4012, Society of Photo-Optical Instrumentation Engineers (SPIE) Conference Series, ed. J. E. Truemper & B. Aschenbach, 68–80 203

Narayan, R. & Ostriker, J. P. 1990, ApJ, 352, 222 86

Neuhäuser, R. 2001, Astronomische Nachrichten, 322, 3 18, 41, 42, 43

Neuhäuser, R. & Trümper, J. E. 1999, A&A, 343, 151 12

Nomoto, K. & Kondo, Y. 1991, ApJ, 367, L19 154

Ogelman, H. & Tepedelenlioglu, E. 2005, ArXiv Astrophysics e-prints 42

Oppenheimer, J. R. & Volkoff, G. M. 1939, Physical Review, 55, 374 2

Ostriker, J. P. & Gunn, J. E. 1969, ApJ, 157, 1395 2

Ostriker, J. P., Rees, M. J., & Silk, J. 1970, Astrophys. Lett., 6, 179 10, 12, 85, 195

Özel, F. 2006, Nature, 441, 1115 189

Pacini, F. 1967, Nature, 216, 567 2

Pacini, F. 1968, Nature, 219, 145 2

Paczynski, B. 1990, ApJ, 348, 485 11

Page, D. 1998, in NATO ASIC Proc. 515: The Many Faces of Neutron Stars., ed. R. Buccheri, J. van Paradijs, & A. Alpar, 539–+ 193

Page, D. & Applegate, J. H. 1992, ApJ, 394, L17 194

Page, D., Geppert, U., & Küker, M. 2007, Ap&SS, 308, 403 145

Page, D., Lattimer, J. M., Prakash, M., & Steiner, A. W. 2004a, ApJS, 155, 623 18, 193

Page, K. L., Schartel, N., Turner, M. J. L., & O'Brien, P. T. 2004b, MNRAS, 352, 523 146

Panzera, M. R., Campana, S., Covino, S., et al. 2003, A&A, 399, 351 88

Patsis, P. A., Contopoulos, G., & Grosbol, P. 1991, A&A, 243, 373 168, 169

Pavlov, G. G., Sanwal, D., & Teter, M. A. 2004, in IAU Symposium, Vol. 218, Young Neutron Stars and Their Environments, ed. F. Camilo & B. M. Gaensler, 239–+ 24

Pavlov, G. G., Shibanov, Y. A., Zavlin, V. E., & Meyer, R. D. 1995, in The Lives of the Neutron Stars, ed. M. A. Alpar, U. Kiziloglu, & J. van Paradijs, 71–+ 134

Pavlov, G. G., Teter, M. A., Kargaltsev, O., & Sanwal, D. 2003, ApJ, 591, 1157 42

Pavlov, G. G., Zavlin, V. E., & Sanwal, D. 2002, in Neutron Stars, Pulsars, and Supernova Remnants, ed. W. Becker, H. Lesch, & J. Trümper, 273–+ 21

Pérez-Azorín, J. F., Pons, J. A., Miralles, J. A., & Miniutti, G. 2006, A&A, 459, 175 21, 145, 161

Perna, R., Narayan, R., Rybicki, G., Stella, L., & Treves, A. 2003, ApJ, 594, 936 145

Pethick, C. J. 1992, Reviews of Modern Physics, 64, 1133 193

Petit, V., Wade, G. A., Drissen, L., & Montmerle, T. 2008, in American Institute of Physics Conference Series, Vol. 983, 40 Years of Pulsars: Millisecond Pulsars, Magnetars and More, ed. C. Bassa, Z. Wang, A. Cumming, & V. M. Kaspi, 399–403 30

Pineau, F.-X., Derriere, S., Michel, L., & Motch, C. 2008, in American Institute of Physics Conference Series, Vol. 1082, American Institute of Physics Conference Series, 15–21 120

Pires, A. M. & Motch, C. 2008, in American Institute of Physics Conference Series, Vol. 983, 40 Years of Pulsars: Millisecond Pulsars, Magnetars and More, ed. C. Bassa, Z. Wang, A. Cumming, & V. M. Kaspi, 363–365 xxiii, 136

Pires, A. M., Motch, C., & Janot-Pacheco, E. 2009a, A&A, 504, 185 xvi, xix, xxiii, 89, 252, 253, 254

Pires, A. M., Motch, C., Turolla, R., Treves, A., & Popov, S. B. 2009b, A&A, 498, 233 xv, xix, xxiii, 89, 252, 253, 254

Pons, J. A., Link, B., Miralles, J. A., & Geppert, U. 2007a, Physical Review Letters, 98, 071101 34

Pons, J. A., Pérez-Azorín, J. F., Miralles, J. A., & Miniutti, G. 2007b, Ap&SS, 308, 247 35, 161

Popov, S., Grigorian, H., Turolla, R., & Blaschke, D. 2006a, A&A, 448, 327 38, 161

Popov, S. B., Colpi, M., Prokhorov, M. E., Treves, A., & Turolla, R. 2000a, ApJ, 544, L53 38, 152

Popov, S. B., Colpi, M., Prokhorov, M. E., Treves, A., & Turolla, R. 2003, A&A, 406, 111 xviii, xxii, 38, 39, 87, 152

Popov, S. B., Colpi, M., Treves, A., et al. 2000b, ApJ, 530, 896 143, 162, 169

Popov, S. B. & Prokhorov, M. E. 2007, Soviet Physics Uspekhi, 50, 1123 152

Popov, S. B., Turolla, R., & Possenti, A. 2006b, MNRAS, 369, L23 83, 179

Popov, S. B., Turolla, R., Prokhorov, M. E., Colpi, M., & Treves, A. 2005, Ap&SS, 299, 117 38, 144, 152, 164, 169, 181

Posselt, B., Popov, S. B., Haberl, F., et al. 2007, Ap&SS, 308, 171 xvii, xxi, 15, 45, 46, 77, 81

Posselt, B., Popov, S. B., Haberl, F., et al. 2008, A&A, 482, 617 83, 90, 94, 143, 144, 146, 148, 152, 155, 169, 179, 181

Possenti, A. 2007, in From Planets to Dark Energy: the Modern Radio Universe. October 1-5 2007, The University of Manchester, UK. Published online at SISSA, Proceedings of Science, p.23 7

Poveda, A., Ruiz, J., & Allen, C. 1967, Boletin de los Observatorios Tonantzintla y Tacubaya, 4, 86 80

Prakash, M., Lattimer, J. M., & Ainsworth, T. L. 1988, Physical Review Letters, 61, 2518 189

Predehl, P. & Schmitt, J. H. M. M. 1995, A&A, 293, 889 62, 125

Ramsay, G. & Cropper, M. 2004, MNRAS, 347, 497 146

Ramsay, G., Cropper, M., Wu, K., et al. 2004, MNRAS, 350, 1373 146

Ransom, S. M., Gaensler, B. M., & Slane, P. O. 2002, ApJ, 570, L75 21

Ransom, S. M., Hessels, J. W. T., Stairs, I. H., et al. 2005, Science, 307, 892 7

Rea, N., McLaughlin, M. A., Gaensler, B. M., et al. 2009, ApJ, 703, L41 32, 146

Redman, S. L. & Rankin, J. M. 2009, MNRAS, 395, 1529 31

Reichen, M., Lanz, T., Golay, M., & Huguenin, D. 1990, Ap&SS, 163, 275 78

Reynolds, S. P., Borkowski, K. J., Gaensler, B. M., et al. 2006, ApJ, 639, L71 31

Richards, G. T., Fan, X., Schneider, D. P., et al. 2001, AJ, 121, 2308 121

Ruphy, S., Robin, A. C., Epchtein, N., et al. 1996, A&A, 313, L21 167, 168

Ruprecht, J., Balazs, B. A., & White, R. E. 1981, Catalogue of star clusters and associations. Supplement 1. Part A: Introduction; Supplement 1. Part B1: New data for open clusters; Part B2: New data for associations, globular clusters and extragalactic objects (Budapest: Akademiai Kiado, 1981) 78

Rutledge, R. E., Fox, D. B., & Shevchuk, A. H. 2008, ApJ, 672, 1137 88, 148

Rutledge, R. E., Fox, D. W., Bogosavljevic, M., & Mahabal, A. 2003, ApJ, 598, 458 xvii, xxi, 87, 94, 143, 148

Schlegel, D. J., Finkbeiner, D. P., & Davis, M. 1998, ApJ, 500, 525 62, 96, 143

Schneider, D. P., Hall, P. B., Richards, G. T., et al. 2005, AJ, 130, 367 104

Schwartz, D. A., David, L. P., Donnelly, R. H., et al. 2000, in Society of Photo-Optical Instrumentation Engineers (SPIE) Conference Series, Vol. 4012, Society of Photo-Optical Instrumentation Engineers (SPIE) Conference Series, ed. J. E. Truemper & B. Aschenbach, 28–40 202

Schwarz, H. E., Ashe, M. C., Boccas, M., et al. 2004, in Society of Photo-Optical Instrumentation Engineers (SPIE) Conference Series, Vol. 5492, Society of Photo-Optical Instrumentation Engineers

(SPIE) Conference Series, ed. A. F. M. Moorwood & M. Iye, 564–573 109, 208

Schwope, A., Hasinger, G., Lehmann, I., et al. 2000, Astronomische Nachrichten, 321, 1 45

Schwope, A. D., Erben, T., Kohnert, J., et al. 2009, A&A, 499, 267 13

Schwope, A. D., Hambaryan, V., Haberl, F., & Motch, C. 2005, A&A, 441, 597 21, 77, 83

Schwope, A. D., Hambaryan, V., Haberl, F., & Motch, C. 2007, Ap&SS, 308, 619 13, 16, 17, 45, 77

Schwope, A. D., Hasinger, G., Schwarz, R., Haberl, F., & Schmidt, M. 1999, A&A, 341, L51 12, 45, 143, 147

Shevchuk, A. S. H., Fox, D. B., & Rutledge, R. E. 2009, ArXiv Astrophysics e-prints; astro-ph/0907.4352 88, 148

Shklovsky, I. S. 1967, ApJ, 148, L1+ 2, 5

Smith, N. 2006, ApJ, 644, 1151 144

Smith, N. & Brooks, K. J. 2007, MNRAS, 379, 1279 144, 145, 147

Spitkovsky, A. 2006, ApJ, 648, L51 162

Staelin, D. H. & Reifenstein, E. C. 1968, Science, 162, 1481 2

Stetson, P. B. 1987, PASP, 99, 191 116

Stocke, J. T., Morris, S. L., Gioia, I. M., et al. 1991, ApJS, 76, 813 147

Stollman, G. M. 1987, A&A, 178, 143 152

Stone, R. C. 1991, AJ, 102, 333 80

Story, S. A., Gonthier, P. L., & Harding, A. K. 2007, ApJ, 671, 713 152

Strüder, L., Briel, U., Dennerl, K., et al. 2001, A&A, 365, L18 199

Tauris, T. M. & Manchester, R. N. 1998, MNRAS, 298, 625 163

Taylor, J. H. & Cordes, J. M. 1993, ApJ, 411, 674 86, 157

Thompson, C. & Beloborodov, A. M. 2005, ApJ, 634, 565 30

Thompson, C. & Duncan, R. C. 1993, ApJ, 408, 194 30, 159

Thompson, D. J., Fichtel, C. E., Kniffen, D. A., & Ogelman, H. B. 1975, ApJ, 200, L79 2

Thorsett, S. E. & Chakrabarty, D. 1999, ApJ, 512, 288 156, 157, 190

Tiengo, A. & Mereghetti, S. 2007, ApJ, 657, L101 18

Tody, D. 1986, in Presented at the Society of Photo-Optical Instrumentation Engineers (SPIE) Conference, Vol. 627, Society of Photo-Optical Instrumentation Engineers (SPIE) Conference Series, ed. D. L. Crawford, 733–+ 110

Toropina, O. D., Romanova, M. M., Toropin, Y. M., & Lovelace, R. V. E. 2003, ApJ, 593, 472 145

Treves, A. & Colpi, M. 1991, A&A, 241, 107 10, 11

Treves, A., Turolla, R., Zane, S., & Colpi, M. 2000, PASP, 112, 297 12, 82, 162, 195, 197

Trümper, J. 1984, Advances in Space Research, 3, 483 5

Tsuruta, S. & Cameron, A. G. W. 1966, Canadian Journal of Physics, 44, 1863 193

Turner, M. J. L., Abbey, A., Arnaud, M., et al. 2001, A&A, 365, L27 200

Turolla, R. 2009, in Astrophysics and Space Science Library, Vol. 357, Astrophysics and Space Science Library, ed. W. Becker, 141–163 13

van Kerkwijk, M. H. & Kaplan, D. L. 2007, Ap&SS, 308, 191 xvii, xxi, 16, 17, 18, 22, 41, 43, 81

van Kerkwijk, M. H. & Kaplan, D. L. 2008, ApJ, 673, L163 xvii, xxi, 18, 19, 83

van Kerkwijk, M. H., Kaplan, D. L., Durant, M., Kulkarni, S. R., & Paerels, F. 2004, ApJ, 608, 432 13, 15, 16, 17

van Kerkwijk, M. H., Kaplan, D. L., Pavlov, G. G., & Mori, K. 2007, ApJ, 659, L149 22

van Kerkwijk, M. H. & Kulkarni, S. R. 2001, A&A, 380, 221 18, 127

Vivekanand, M. & Narayan, R. 1981, Journal of Astrophysics and Astronomy, 2, 315 86

Voges, W., Aschenbach, B., Boller, T., et al. 1999, A&A, 349, 389 5, 87, 148, 205

Voss, R., Diehl, R., Hartmann, D. H., et al. 2009, å (accepted); astro-ph/0907.5209 152

Vranesevic, N., Manchester, R. N., Lorimer, D. R., et al. 2004, ApJ, 617, L139 7, 158

Wainscoat, R. J., Cohen, M., Volk, K., Walker, H. J., & Schwartz, D. E. 1992, ApJS, 83, 111 8, 166

Wallace, P. T., Peterson, B. A., Murdin, P. G., et al. 1977, Nature, 266, 692 2

Walter, F. M. 2001, ApJ, 549, 433 18, 41, 43

Walter, F. M. & Lattimer, J. M. 2002, ApJ, 576, L145 43

Walter, F. M. & Matthews, L. D. 1997, Nature, 389, 358 13

Walter, F. M., Wolk, S. J., & Neuhäuser, R. 1996, Nature, 379, 233 11, 12

Wang, C., Lai, D., & Han, J. L. 2006a, ApJ, 639, 1007 83

Wang, Z., Chakrabarty, D., & Kaplan, D. L. 2006b, Nature, 440, 772 30

Watson, M. G., Schröder, A. C., Fyfe, D., et al. 2009, A&A, 493, 339 90, 201, 210, 211

Webb, N. A. & Barret, D. 2007, ApJ, 671, 727 189

Weber, F. 2005, Progress in Particle and Nuclear Physics, 54, 193 193

Weber, F., Negreiros, R., & Rosenfield, P. 2009, in Astrophysics and Space Science Library, Vol. 357, Astrophysics and Space Science Library, ed. W. Becker, 213–245 189

Weisskopf, M. C., Brinkman, B., Canizares, C., et al. 2002, PASP, 114, 1 202

Weisskopf, M. C., Tananbaum, H. D., Van Speybroeck, L. P., & O'Dell, S. L. 2000, in Society of Photo-Optical Instrumentation Engineers (SPIE) Conference Series, Vol. 4012, Society of Photo-Optical Instrumentation Engineers (SPIE) Conference Series, ed. J. E. Truemper & B. Aschenbach, 2–16 202

Weltevrede, P., Stappers, B. W., Rankin, J. M., & Wright, G. A. E. 2006, ApJ, 645, L149 31, 37

White, R. L., Becker, R. H., Helfand, D. J., & Gregg, M. D. 1997, ApJ, 475, 479 88

Widrow, L. M. & Dubinski, J. 2005, ApJ, 631, 838 166, 168

Wielen, R. 1977, A&A, 60, 263 53

Winkler, C., Courvoisier, T. J.-L., Di Cocco, G., et al. 2003, A&A, 411, L1 6

Winkler, P. F. & Petre, R. 2007, ApJ, 670, 635 42

Woods, P. M. & Thompson, C. 2006, Soft gamma repeaters and anomalous X-ray pulsars: magnetar candidates (Compact stellar X-ray sources), 547–586 24

Woosley, S. E., Arnett, W. D., & Clayton, D. D. 1973, ApJS, 26, 231 6

Woosley, S. E. & Weaver, T. A. 1986, ARA&A, 24, 205 6

Woosley, S. E. & Weaver, T. A. 1995, ApJS, 101, 181 6

Wright, A. E., Griffith, M. R., Burke, B. F., & Ekers, R. D. 1994, ApJS, 91, 111 143

Yakovlev, D. G., Levenfish, K. P., & Shibanov, Y. A. 1999, Soviet Physics Uspekhi, 42, 737 193

Yakovlev, D. G. & Pethick, C. J. 2004, ARA&A, 42, 169 193

Yusifov, I. & Küçük, I. 2004, A&A, 422, 545 171, 173

Zahn, J.-P., Brun, A. S., & Mathis, S. 2007, A&A, 474, 145 158

Zampieri, L., Campana, S., Turolla, R., et al. 2001, A&A, 378, L5 xxi, 12, 89, 143

Zane, S., Cropper, M., Turolla, R., et al. 2005, ApJ, 627, 397 13, 16, 143

Zane, S., de Luca, A., Mignani, R. P., & Turolla, R. 2006, A&A, 457, 619 41, 45, 81

Zane, S., Haberl, F., Cropper, M., et al. 2002, MNRAS, 334, 345 xviii, xxii, 36

Zane, S., Mignani, R. P., Turolla, R., et al. 2008, ApJ, 682, 487 13

Zane, S. & Turolla, R. 2006, MNRAS, 366, 727 21

Zane, S., Turolla, R., & Drake, J. J. 2004, Advances in Space Research, 33, 531 145

Zane, S., Turolla, R., Stella, L., & Treves, A. 2001, ApJ, 560, 384 xvii, xxi, 16

Zane, S., Turolla, R., Zampieri, L., Colpi, M., & Treves, A. 1995, ApJ, 451, 739 169

Zavlin, V. E. 2007, Ap&SS, 308, 297 27

Zavlin, V. E. 2009, in Astrophysics and Space Science Library, Vol. 357, Astrophysics and Space Science Library, ed. W. Becker, 181–211 163, 192

Zavlin, V. E. & Pavlov, G. G. 2002, in Neutron Stars, Pulsars, and Supernova Remnants, ed. W. Becker, H. Lesch, & J. Trümper, 263–+ 17

Zavlin, V. E., Pavlov, G. G., & Shibanov, Y. A. 1996, A&A, 315, 141 134

Zhang, B., Gil, J., & Dyks, J. 2007, MNRAS, 374, 1103 31

Zhang, W., Woosley, S. E., & Heger, A. 2008, ApJ, 679, 639 157

Zhao, H. 1996, MNRAS, 278, 488 167

Zhu, W., Kaspi, V. M., Gonzalez, M. E., & Lyne, A. G. 2009, ApJ, accepted, astro-ph/0909.0962 34

Zissell, R. E. 2000, Journal of the American Association of Variable Star Observers (JAAVSO), 28, 149 114

Population study of radio-quiet and thermally emitting isolated neutron stars

Abstract:
The main objective of the thesis is to study the properties of the Galactic population of radio-quiet and thermally emitting isolated neutron stars (INSs). This is done by studying further the existing neutron star sample of nearby seven sources, known as the "Magnificent Seven" (M7), as well as by searching for new candidates and constraining possible populations. During the thesis, we investigated the proper motions of three of the faintest M7 in X-rays with the satellite Chandra. This work allowed us to constrain the neutron star displacement in two cases as well as to accurately determine the high proper motion of a third source, for the first time in X-rays with a significance approaching 10 standard deviations (Motch, Pires, Haberl, & Schwope, 2007, Ap&SS, 308, 217; Motch, Pires, Haberl, Schwope, & Zavlin, 2009, A&A 497, 423). The search of new INS candidates in the serendipitous catalogue of the XMM-Newton Observatory, with more than $120,000$ X-ray sources, had as well the aim to constrain the spatial density of thermally emitting sources located beyond the solar vicinity. This work allowed the long awaited discovery of a new thermally emitting INS with properties similar to those of the seven nearby sources discovered by ROSAT (Pires, Motch, Turolla, Treves, & Popov, 2009, A&A 498, 233). Moreover, deep optical observations with SOAR and the ESO-VLT have been obtained during the thesis work in order to optically identify a handful of INS candidates that have been selected among more than $72,000$ sources (Pires, Motch, & Janot-Pacheco, 2009, A&A, 504, 185). Finally, population synthesis of Galactic thermally emitting INSs allows constraining the global properties of this population based on the whole sample of XMM-Newton observations. By estimating the density of similar sources at more remote distances in the Milky Way, the final objective is to determine whether the spatial density derived from the group of seven nearby sources is a local anomaly caused by the Sun's current location near regions of active stellar formation of the Gould Belt.
Keywords: stars: neutron – X-rays: individual: RX J0806.4-4123, RX J0420.0-5022, RX J1308.6+2127, 2XMM J104608.7-594306 – Catalogs

Estudo de população de estrelas de nêutrons isoladas emissoras de raios X e silenciosas em rádio

Resumo:
O objetivo da tese é estudar as propriedades da população Galáctica de estrelas de nêutrons isoladas com emissão térmica em raios X mas silenciosas em rádio. Isto é feito investigando-se a amostra existente de sete fontes próximas, conhecidas como "Magnificent Seven" (M7), assim como através da procura por novos candidatos e restringindo possíveis cenários e populações. Durante a tese, nós investigamos os movimentos próprios de três das mais fracas fontes em raios X com o satélite Chandra. Este trabalho nos permitiu restringir o deslocamento da estrela de nêutrons em dois casos assim como medir com grande precisão o alto valor de movimento próprio de uma terceira fonte, pela primeira vez em raios X com uma significância alcançando 10 desvios-padrão (Motch, Pires, Haberl, & Schwope, 2007, Ap&SS, 308, 217; Motch, Pires, Haberl, Schwope, & Zavlin, 2009, A&A 497, 423). A procura por novos candidatos a estrelas de nêutrons isoladas no catálogo de fontes do satélite XMM-Newton, com mais de $120,000$ fontes de raios X, teve igualmente como objetivo restringir a densidade espacial de fontes com emissão térmica situadas além da vizinhança solar. Este trabalho levou à aguardada descoberta de uma nova estrela de nêutrons isolada em processo de resfriamento, a qual exibe propriedades similares às sete fontes descobertas pelo ROSAT (Pires, Motch, Turolla, Treves, & Popov, 2009, A&A 498, 233). Mais ainda, observações óticas profundas com os telescópios SOAR e ESO-VLT foram obtidas durante a tese de maneira a identificar no óptico a amostra mais brilhante de candidatos a estrelas de nêutrons, os quais foram selecionados entre mais de $72,000$ fontes (Pires, Motch, & Janot-Pacheco, 2009, A&A, 504, 185). Finalmente, a síntese de população de estrelas de nêutrons isoladas Galácticas permite restringir as propriedades globais da população com base na amostra total de observações em raios X realizadas com o satélite XMM-Newton. Estimando-se a densidade de fontes similares a maiores distâncias na Via Láctea, o objetivo final é determinar se a densidade espacial derivada do grupo de sete estrelas próximas corresponde a uma anomalia local causada pela proximidade do Sol em relação a regiões de ativa formação estelar do Cinturão de Gould.
Palavras-chave: estrelas de nêutrons – raios X: indivíduo: RX J0806.4-4123, RX J0420.0-5022, RX J1308.6+2127, 2XMM J104608.7-594306 – Catálogos

Etude des populations d'étoiles à neutrons isolées détectées par leur rayonnement X thermique

Résumé:

La présente thèse de doctorat porte sur la population d'étoiles à neutrons isolées thermiques dénuées d'émission radio dans la Galaxie. Les propriétés de cette population sont étudiées par l'analyse de l'échantillon connu des sept sources, d'une part, et d'autre part par la recherche de nouveaux candidats et par la modélisation de cette population supposant plusieurs scénarios évolutifs possibles. Les mouvements propres de trois sources parmi les plus faibles sources ont été étudiés avec le satellite Chandra pendant la thése. Ce travail a permis de contraindre le déplacement de l'étoile à neutrons dans deux cas pour les sources RX J0806.4-4123 et RX J0420.0-5022, et a mis en évidence pour la première fois dans le domaine des rayons X le mouvement propre d'une troisième source, RX J1308.6+2127, avec une précision jamais obtenue avant (Motch, Pires, Haberl, & Schwope, 2007, Ap&SS, 308, 217; Motch, Pires, Haberl, Schwope, & Zavlin, 2009, A&A 497, 423). La recherche de nouveaux candidats étoile à neutrons isolée dans le catalogue du satellite de rayons X XMM-Newton, avec plus de 120 mille sources, a eu également comme but de contraindre la densité spatiale des sources X thermiques situées à grandes distances. Ce travail a mené à la découverte très attendue d'une nouvelle étoile à neutrons isolée, 2XMM J104608.7-594306, présentant des propriétés similaires à celles des sept sources découvertes par ROSAT (Pires, Motch, Turolla, Treves, & Popov, 2009, A&A 498, 233). En outre, des observations optiques profondes avec les telescopes ESO-VLT et SOAR ont été utilisées pour identifier optiquement l'échantillon des candidats étoile à neutrons qui ont été séléctionnés parmi plus de 72 milles sources (Pires, Motch, & Janot-Pacheco, 2009, A&A, 504, 185). Finalement, le travail de modélisation de la population d'étoiles à neutrons isolées thermiques de la Galaxie permet de contraindre les propriétés globales de cette population à partir du relevé constitué par l'ensemble des observations faites par le satellite XMM-Newton. Ce travail a pour but de déterminer si la densité spatiale déduite du groupe de sept étoiles proches est une anomalie causée par notre position actuelle proche des zones actives de formation récente d'étoiles de la ceinture de Gould en estimant la densité des sources similaires dans la Voie Lactée à plus grande distance.

Mots clés: étoiles à neutrons – rayons X: individu: RX J0806.4-4123, RX J0420.0-5022, RX J1308.6+2127, 2XMM J104608.7-594306 – Catalogs